Ore genetic study of the Ostra polymetallic mineralization (Eastern Carpathians, Romania)

Árpád Ádámcsik[1], Boglárka B. Balázs[1], István Márton[2], Szabolcs Orbán[3], Gabriella B. Kiss[1]
[1]*Eötvös Loránd University, Faculty of Sciences, Institute of Geography and Geosciences, Department of Mineralogy*
[2]*Dundee Precious Metals Inc*
[3]*Goldron Geoconsulting Ltd*

Abstract. The Ostra polymetallic mineralization is hosted in the metamorphic formations of the Tulgheș Lithogroup from the alpine Bucovinian Nappes of the Crystalline-Mesozoic Zone in the Eastern Carpathians (Romania). The polymetallic mineralization consists of pyrite, chalcopyrite, sphalerite, galena, fahlore, marcasite and barite. In terms of spatial distribution, the massive sulfides are most commonly associated with the porphyroid rocks in the examined outcrops, which were discovered through barite exploitation. During the present study, two different massive sulfide lenses from the topographically upper and lower part of the mine were studied in details. Based on whole rock geochemistry, the studied ores are unusually Pb-Zn-rich, compared to other VMS deposits, though its noble metal content normalized to primitive mantle shows similar characteristics than Cyprus-type VMS. With the help of mineral chemical analyses as well as fluid inclusion study, the formation conditions were also determined: temperature decrease from the proximal (>250°C) to distal (<200°C) parts of the massive sulfide lens. Besides, compositional differences in the ore minerals as well as in the paragenesis were recorded among the proximal and distal, as well as lower and upper massive sulfide lenses.

1 Introduction

The polymetallic mineralization from Ostra is located in the Eastern Carpathians, Romania. The Eastern Carpathians host a series of volcanogenic massive sulfide (VMS) deposits which were important sources of copper and barite during the mid-1900's. The massive sulfide bodies, located within the Tulgheș Lithogroup, were known since decades, but no modern ore genetic research was carried out. Ostra was actively mined during the mid-1900's, but mining started to decay by the start of early 2000's. Ostra was mainly mined for barite with no real interest in the underlying massive sulfide bodies. The geologically correlating, nearby occurrences (e.g., Leșul Ursului, Mănăila) have a proven [Cu (±Au-Pb-Zn-Ag-Ba)] content, which could give a new approach to the belt scaled exploration (Damian et al. 2023). Barite mining was the main target of the exploited area, unfortunately grade and tonnage data for the base metals is not available. Active mining of the Mănăila-Cârlibaba deposits is taking place in the northern part of this VMS belt.

The study area is located in the western part of the Eastern Carpathians, which is built up (from west to east) by the Crystalline–Mesozoic Zone, the flysch zone, and the molasses zone. The mineralization is hosted in the rocks of the low-grade metamorphic Tulgheș Lithogroup which is a part of the Crystalline-Mesozoic Zone, which structurally belongs to the Eastern Dacides (Săndulescu 1984). The Crystalline-Mesozoic Zone is made up of several Alpine tectonic units, with eastern vergence, overthrusted in the Austrian tectogenesis. This zone is overlain by a Permian-Mesozoic sedimentary cover (Balintoni et al. 2009). The main lithologies which built up the Tulgheș Lithogroup of the Crystalline-Mesozoic Zone are the following: psammite (sericite quartzites, sericite-chlorite schists); graphitic sediments (sericite-chlorite±graphite schists, graphitic metacherts±Mn deposits, carbonate rocks); volcanic rocks (felsic metavolcanics±Kuroko-type base metal deposits, sericite-chlorite schists); mix series of sericite-chlorite schists, greenschists, acid metavolcanics, metacherts, carbonate rocks (Munteanu & Tatu 2003). The main mineralizations of the polymetallic belt accumulated in the Tulgheș Lithogroup are grouped into three districts, as follows (from north to south): Borșa-Vișeu District, Fundu Moldovei-Leșul Ursului District, Bălan-Fagul Cetății District (Damian et al. 2023). The Ostra mineralization forms part of the central-positioned Fundu Moldovei-Leșul Ursului District.

2 Methodology

Field mapping (Fig.1.) and sample collection were completed in 2022 in order to understand the outcrop-scaled structural features and geometries of the mineralization. Based on macroscopic observations, 18 samples (out of 78) were chosen for further detailed analyses.

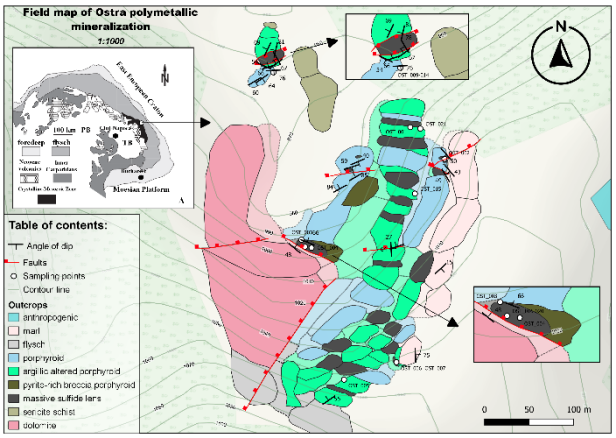

Figure 1. Field map of the studied area in the Ostra polymetallic mineralization, highlighting the two massive sulfide lenses studied in details, in higher resolution. A. The location of the Crystalline-Mesozoic Zone in the Carpathians (PB - Pannonian Basin, TB - Transylvanian Basin) map modified after (Munteanu et al. 2004).

The rock samples were taken from an abandoned open-pit mine, aiming to cover various lithological units, alteration assemblages and sulfide paragenesis. Besides, two chosen sections (comprising of a massive sulfide lens and its altered host rock) were sampled in details, representing two different topographic highs of the mine (Fig. 2).

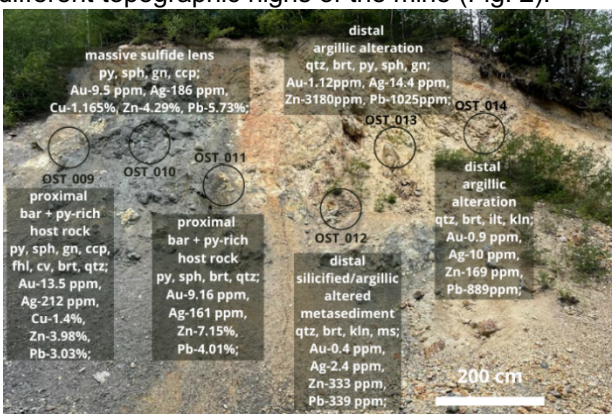

Figure 2. Photo of the sampling profile of the lower massive sulfide lens and its altered host rock. Sampling locations as well as the basic characteristics of the collected samples are also shown, for the massive sulfide lens and its proximal and distal alteration halo (py-pyrite, sph-sphalerite, gn-galena, ccp-chalcopyrite, fhl-fahlore, cv-covellite, brt-barite, qtz-quartz, kln-kaolinite, ms-muscovite, ilt-illite).

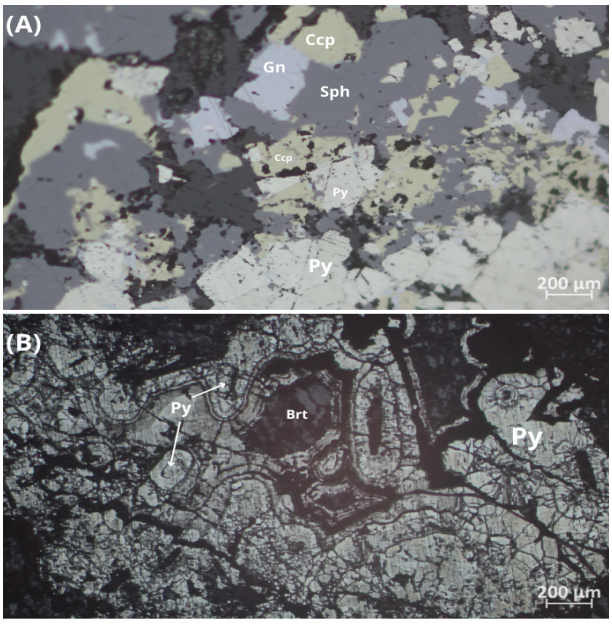

Figure 3. Plane-polarized reflected light photo of representative mineral assemblages from Ostra mineralization. (A) massive sulfide sample, with euhedral grains of pyrite, intergrowth with chalcopyrite, sphalerite, and galena; (B) pyrite with collomorphic texture (py-pyrite, sph-sphalerite, gn-galena, ccp-chalcopyrite, cv-covellite, brt-barite).

Detailed petrography was carried out on standard polished 30 µm thin sections (13 samples) and block sections (5 samples) using a Nikon Alphaphot polarizing microscopes at the Department of Mineralogy, Eötvös Loránd University (ELTE), Budapest, Hungary. These detailed petrographic studies were complemented with SEM-EDS observations at the Department of Petrology and Geochemistry, ELTE, on an Amray 1830I scanning electron microscope.

Argillic alteration of the host rock was examined with a Siemens D5000 X-ray diffraction equipment, to identify the clay minerals. Measurements were carried out at the Department of Mineralogy (ELTE).

The chemical compositions of sulfide minerals were determined using a JXA-8530F Field Emission Electron Probe Microanalyzer (EPMA). The analyses were carried out at the Earth Science Institute, Slovak Academy of Sciences (Banská Bystrica, Slovakia). The analyzed points were selected using the backscattered electron (BSE) images. The measurements were performed on polished carbon-coated sections using an acceleration voltage of 20 kV and a 15 nA beam current, 1-3 µm beam diameter (depending on the size of the grain). Trace element compositions were measured in pyrite, sphalerite, chalcopyrite, galena, fahlore and barite.

The whole rock geochemical analyses were conducted by ALS in Loughrea, Ireland, where rock sample compositions were determined by using fusion decomposition followed by ICP-AES measurement and four acid digestion followed by ICP-MS measurement of the 75 µm grain-sized pulverized material (for detailed documentation, see the ALS brochure). Samples that exceeded detection limits for elements of interest like Au, were reanalyzed using 30-g fire assay with gravimetric finish (ALS Geochemistry method Au-GRA21).

Fluid inclusion petrography was carried out on doubly polished 100-130 µm thick sections with an Olympus BH2 type microscope, while microthermometry was performed with a Linkam FT IR 600 stage mounted on an Olympus BX51 microscope, at the Department of Mineralogy (ELTE).

3 Results and their interpretations

3.1 Field Description, Petrography and Mineralogy

During field mapping, we have identified several massive sulfide lenses, which were always associated to the metamorphosed porphyroid rocks. Argillic alteration of the immediate host rock is common. Barite occurs in two textural and paragenetic relationships: it can be either associated with distal parts of the massive sulfide lenses, or it can form massive bodies (without sulfides) in the porphyroid rock. This porphyroid host rock consists mostly of a very complex textured grey to creamy white coloured rock, with a breccia-like appearance, including some cross-cutting barite veins. The samples are described as a porphyroid rock.

The massive sulfide lenses consist mostly of pyrite, chalcopyrite, sphalerite, galena, covellite, fahlore and marcasite, but leading to its distal parts, gangue minerals (coarse grained, euhedral barite,

rare fine-grained quartz) may also occur in them (Fig. 3). One massive sulfide sample from the higher topographic level of mine is described as a silica – pyrite-rich breccia, where the fractures have been partially filled with pyrite. The size of the massive sulfide lenses is commonly around 2-3 x 10 m.

The petrographical analyses confirm that massive sulfide samples are dominated by pyrite (often with collomorphic texture) together with sphalerite, galena, chalcopyrite and fahlore (Fig. 3). In some pyrite, galena-filled fractures were found, while the presence of covellite was observed, which partially replaced chalcopyrite or galena. The gangue minerals are barite and quartz. The distal samples are characterized by predominantly quartz and barite with disseminated sulfides.

X-ray powder diffraction analyses have shown that the alteration halo of the massive sulfide lenses is different in the lower and upper levels of the mine. In case of the lower benches of the pit, proximal alteration zone contains kaolinite group clay minerals, while the distal zone consists mostly of illite group clay minerals. As a contrary, at higher elevation, in case of the proximal zone, dickite, alunite and K-feldspar occur, while in the distal alteration zone, kaolinite group minerals were found.

3.2 Mineral chemistry

Pyrite, sphalerite, chalcopyrite, galena, fahlore and barite were studied with EPMA. Pyrite appears in the massive sulfide rocks as part of a compact, pyrite-rich polymetallic ore, where pyrite can be found mostly in the form of subhedral equigranular grains, associated with the rest of above-mentioned sulfides. Pyrite grains are rimmed by chalcopyrite, sphalerite and galena. Electron microprobe analysis indicates minor amounts of Sb, Zn, Ni, Co, Ag and Au in the pyrite, and a relatively high amount of As, Cu and Pb. The pyrite is rich in As (from 0.1 up to 5 wt.%), but Ag and Au are insignificant. Compositional zonation (due to variable Sb and As content) as well as tiny galena inclusions are observed in pyrite on BSE images. Based on Se content in pyrite, the ore-forming temperature (T) was estimated (Keith et al. 2018). The massive sulfide lens studied at the lower level of the mine formed at about 270±10 °C.

Sphalerite is the second most abundant mineral of the pyrite-rich polymetallic ore. It mostly appears in the form of anhedral crystals arranged in the open spaces between the pyrite grains, intergrown sometimes with chalcopyrite, galena and fahlore. Electron microprobe analysis indicates sphalerite with low Sb, Cd and Cu content, but systematically higher Fe content occurs in the proximal part of the massive sulfide lens. Sphalerite from the proximal part of the massive sulfide lens contained significantly higher amount of Fe (up to 8.1 wt.%), compared to the distal ore (0.6-1.2 wt.%). This suggests lower formation temperature for the distal ores, and higher (>200 °C) formation temperature for the proximal one, which is in good agreement with the pyrite thermometry results.

Galena is present also in our samples, intergrown with sphalerite and chalcopyrite. Fahlore is a common mineral in the lower massive sulfide lens, while it occurs only sporadically in the upper level of the mine. Galena and fahlore show compositional differences according to their location in the massive sulfide lens: distal galena contained elevated Zn (up to 1%), while distal fahlore was characterized by elevated Hg (up to 12.9%) and low Sb. The Ag content of the deposit is connected to the fahlore, no other Ag-bearing mineral was observed. Based on the composition of fahlore, tennantite, is occurring in the studied samples (most often Cu-rich tennantite) (Fig. 4).

Chalcopyrite forms anhedral grains that border mostly pyrite or sphalerite, galena, and contains fahlore inclusions. Chalcopyrite is sometimes present with covellite. Electron microprobe analyses indicates minor amounts in Pb, Zn and Au in the crystal structure of chalcopyrite.

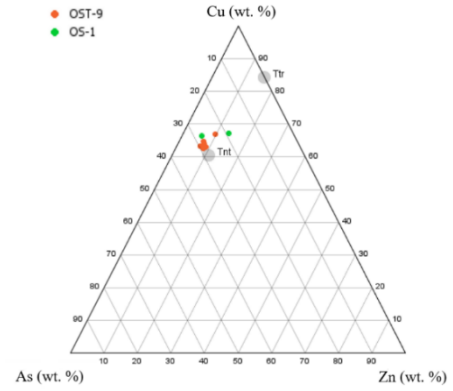

Figure 4. As-Cu-Zn ternary diagram for tennantite of the Ostra deposit. (orange dots - proximal massive sulfide samples; green dots - distal massive sulfide samples; tnt – tennantite, ttr - tetrahedrite)

3.3 Whole rock geochemistry

In terms of geochemistry, it can be said that there are significant differences between the values obtained along the two studied massive sulfide lenses. The most significant observations occur in the distribution of precious metal, such as gold or silver, and base metal content, such as copper, lead, and zinc.

Gold content of the lower massive sulfide lens can reach up to 13 ppm, while it barely reaches 1.2 ppm in the upper massive sulfide lens. The Ag content also differs significantly, with a 174.25 ppm mean value, where in the lower massive sulfide lens is up to 212 ppm and only 21.1 ppm in the higher one.

There are significant differences in the base metal content as well; such as copper (between 1.1-1.4% in the lower, and <134 ppm in the upper massive sulfide lens), lead (up to 5.73% in the lower massive sulfide lens compared to <338 ppm in the upper one) and zinc (7.15% in the lower massive sulfide lens and <294 ppm in upper one). Regardless

the structural position, studying the Cu:Zn:Pb ratio, the samples are rich in Pb and Zn (Fig. 5.). High Fe and S content of the higher massive sulfide lens prove its richness in pyrite.

As previous studies did not address the deposit type of the Ostra mineralization, we tried to examine this aspect, too. Based on studies of the nearby occurrences of the same belt (Damian et al. 2023), the VMS origin seems to be a geologically reasonable option. The observed textural features (i.e., the Ostra mineralization is associated with a porphyroid host rock, roughly with argillic alteration and with a few massive sulfide lenses) also support this assumption.

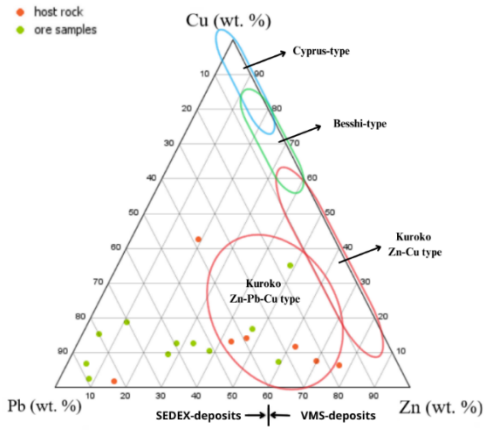

Figure 5. Ternary diagram of the base metal ratio of our samples. (orange dots - host rock; green dots - massive sulfide ore samples). The VMS/SEDEX ternary plot, and the reference fields for VMS types is after Ciftci (2019).

3.4 Fluid inclusion

Fluid inclusions of barite in the distal parts of the massive sulfide lens were studied in details. Our petrographycal observations suggest, that barite formed partly syngenetically with the sulfides, though its crystallization lasted longer. Based on our preliminary results, the primary fluid inclusions (occurring in growth zones or in the spongy cores of the baryte crystals), revealed a homogeneous parent fluid, which can be modelled in a NaCl-H_2O system. Despite the small size of the primary liquid + vapour fluid inclusions (usually 3-7 μm), their chemical composition and physical properties can be determined: Th (LV-L) = 145-185°C (i.e., minimum formation temperature due to homogeneous conditions of the parent fluid) and 3.7-5.3 NaCl equiv. wt.% salinity was confirmed. This minimum formation temperature data is in good agreement with the low Fe content of the syngenetic sphalerite grains. The slightly higher salinity compared to modern seawater values can be the result of fluid-rock interaction during the hydrothermal fluid circulation in the oceanic crust.

4 Conclusions

In the present preliminary research, we applied the combination of field observation, whole rock geochemistry and fluid inclusion studies. The electron microprobe analyses on Ostra samples provide important information about the ore-forming conditions and geochemical variations.

In conclusion, the field mapping and petrographic analyses performed on the studied area have provided important information regarding the structural features and geometries of the mineralization. The massive sulfide lenses were found to be associated with a low-grade metamorphic porphyroid rocks, and argillic alteration occurred in the immediate host rock. Barite occurred either in association with the distal parts of the massive sulfide lenses or in the porphyroid rocks also.

The VMS origin is a geologically and texturally reasonable option for the genesis of the deposit at Ostra. Furthermore, significant differences were observed between the studied massive sulfide lenses of the mine; in the metal content, as well as mineral paragenesis, suggesting a somewhat different evolution for the different parts of the deposit.

Studying the formation conditions of a single massive sulfide lens, a temperature decrease from proximal to distal parts is clearly observed, together with compositional variations.

Overall, this information provides valuable insights into the geological and geochemical characteristics of the mineralization and helps further exploration and evaluation activities.

Acknowledgements

This research was supported by a student research grant from the Hugh E. McKinstry Fund of the Society of the Economic Geologists. Trip to Banská Bystrica to perform EPMA analyses was supported by the Talent Support Council of ELTE Eötvös Loránd University, Budapest.

References

Ciftci, E. (2019): Volcanogenic Massive Sulfide (VMS) Deposits of Turkey. Modern Approaches in Solid Earth Sciences, p. 427-495.

Damian, G., Apopei, A.I., Buzatu, A., Maftei, A.E., Damian, F. (2023): New Mineral Occurrences in Massive Sulfide Deposits from Mănăila, Eastern Carpathians, Romania. Minerals 13:111.

Keith, M., Smith, D.J., Jenkin, G.R.T., Holwell, D.A., Dye, M.D. (2018): A review of Te and Se systematics in hydrothermal pyrite from precious metal deposits: Insights into ore-forming processes. Ore Geology Reviews 96:269-282.

Munteanu, M., Marincea, S., Kasper, H.U., Zak, K., Alexe, V., Trandafir, V., Saptefrati, G., Mihalache, A. (2004): Black chert-hosted manganese deposits from the Bistritei Mountains, Eastern Carpathians (Romania): petrography, genesis and metamorphic evolution. Ore Geology Reviews 24:45-65.

Munteanu, M., Tatu, M. (2003): The East-Carpathian Crystalline-Mesozoic Zone (Romania): Paleozoic Amalgamation of Gondwana- and East European Craton-derived Terranes. Gondwana Research 6:185-196

Săndulescu, M. (1984): Geotectonica României. Editura Tehnică.

The value of resampling – application of a generalised geochemical exploration model at Golden Grove VMS, Australia

Mark Arundell[1], Lucas Williams[2]
[1]IMEx Consulting, Orange, NSW, Australia
[2]29Metals Ltd Golden Grove Operations Pty Ltd, WA, Australia

Abstract. Sampling of bottom of hole historic Rotary Air Blast (RAB) drilling combined with multi-element analysis over three deposits in the Golden Grove area has led to the development of a generalised geochemical model revealing the position of the footwall/hangingwall contact and a distinct pathfinder signature proximal to mineralisation. The results from this initial pilot sampling program provided motivation for a belt wide program of reanalysis of historic bottom of hole drill samples. The geochemical model has been applied to areas under deep transported cover and led to the development of new robust prospects as well as a review of the lithostratigraphy.

1 Introduction

The Gossan Hill, Scuddles and Gossan Valley VMS deposits occur on the NE flank of the Warriedar Fold Belt (Figure 1), in the Golden Grove Domain, with an age of about 3.0Ga. The Golden Grove Domain has a layered stratigraphy that is laterally continuous over some 30km. Within this, the Golden Grove Formation is a layered rhyodacitic volcaniclastic succession that underlies and hosts the VMS deposits. Dacitic and rhyodacitic volcanics of the Scuddles Formation are the main rock types of the hanging wall. Bedded tuffaceous volcaniclastic rocks of the Golden Grove Formation are subdivided into six members, based on facies, grain-size variation, abundance of volcanic quartz grains and bedding characteristics (Frater, 1983; Sharpe and Gemmell, 2001, 2002).

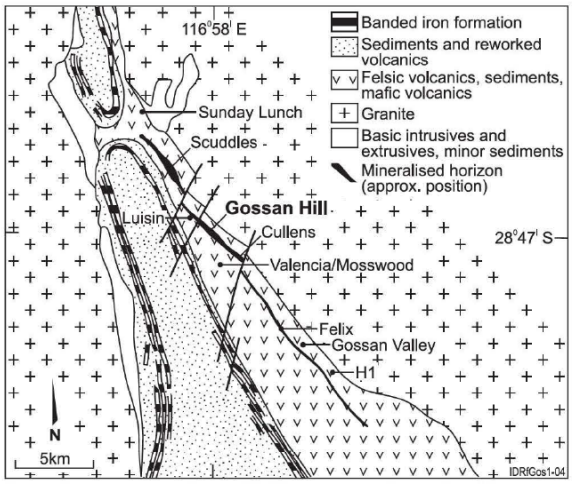

Figure 1. Regional geology of Golden Grove area (after Smith, 2003)

The Golden Grove Formation shows quartz, Fe-rich chlorite and lesser muscovite alteration. At Gossan Hill, alteration zones surround the deposit and are characterized by chlorite and ankerite-siderite (with FeO and MgO enrichment), grading stratigraphically upwards into intense silicification. Regional deformation has resulted in EW compression, minor faulting, cleavage, schistosity and boudinage of the rocks (Smith, 2003)

2 Discovery History and Mineralisation

Outcropping gossans were recognized and sampled in 1971 on what is now Gossan Hill. Five diamond drill holes tested the gossans in 1972 and four of the holes intersected significant base metal sulphides (about 1-3.5% Cu and Zn). Although, difficulties in assessing the geometry of the deposit were recognised, a resource of 15 Mt at 3.4% Cu was defined. The non-outcropping Scuddles deposit was discovered 4 km to the north of Gossan Hill in 1979. The geometry of the Scuddles deposit turned out to be relatively straightforward and much of the focus at Golden Grove then centred on delineation and development of Scuddles. The most comprehensive exploration activity has been over the Gossan Hill to Scuddles area (Figure 1) (Smith, 2003).

At the mine scale, a steep west dipping horizon of thinly bedded chert and tuff, within the Golden Grove Formation, hosts the Zn mineralisation at both Gossan Hill and Scuddles and is underlain by coarse felsic volcaniclastic rocks. The Gossan Hill deposit consists of a number of lenses of Zn and Cu mineralisation, extending over a strike of 400m and a width of 20m. The Cu ore occurs in magnetite-rich volcaniclastic rocks stratigraphically below the Zn ore. An oxidised near surface Au-Ag resource overlies the Zn sulphide lenses and an oxide Cu resource overlies the Cu sulphide lenses (Normandy, 1999).

3 Multi-element geochemistry

Since the discovery of Gossan Hill ~50 years ago, the Golden Grove area has been subject to intensive and systematic geological, geochemical and geophysical exploration. A number of other prospects (e.g. Gossan Valley, Felix) have been discovered associated with the “mineralised horizon” (Figure 1).

In the period between 2004 and 2014, near surface geochemical exploration had largely been neglected. Prior historic RAB (Rotary Air Blast) drilling, with associated bottom of the hole geochemical sampling, well covered the prospective stratigraphy. However, most of these samples had only been analysed for Cu, Pb, Zn and Au.

A program of systematic sampling of drillcore for low detection level multi-element geochemistry had been in place since ~2003 which enabled identification of primary rock pathfinders and alteration.

Interpretation of this multi-element drillhole data (Halley 2014a) noted that proximal footwall alteration at Gossan Valley carried a distinct Mo-Bi signature with lesser amounts of As and Sb. In the hangingwall, As values were elevated but it was interpreted not to be associated with the VMS alteration.

The advent of low-level detection ICP-MS combined with four acid digestion methods was considered to offer an opportunity to determine whether historic shallow (e.g. RAB) drill samples could offer new insights into the near surface metal pathfinder, alteration and lithogeochemistry of the Golden Grove deposits – particularly given the above signature noted at Gossan Valley.

A pilot program was conducted in 2014 where ~80 bottom of hole RAB pulp samples were reanalysed from each of the Scuddles, Gossan Hill and Gossan Valley deposits. Samples were selected on a nominal 320m north-south by 80m east-west grid centred on the deposit.

Interpretation of these new data by Halley (2014b) noted the Mo and Bi anomalies associated with the Gossan Hill deposit were spatially restricted and the values for As and Sb were considered low for a VMS system. Elevated Cd and In concentrations were also noted at Gossan Hill and high Ba and Tl at Scuddles.

In 2017, the 2014 pilot program datasets were reassessed in order to determine whether the resampling of bottom of hole RAB material should be extended away from the three known deposits. This reassessment led to the development of a Generalised Geochemical Model (Figure 2) based on all three deposits – Scuddles, Gossan Hill and Gossan Valley.

The pathfinder signature for copper mineralisation in the hangingwall dacite unit consisted of As, Bi, Mo, Sb, Sn W and Se. The zinc mineralisation pathfinder signature was As, In, Sb and Se. Also, a Pb and Tl signature was noted south and proximal to zinc mineralisation in the upper footwall position.

It was also noted that the extent of the hangingwall pathfinder anomaly was controlled by the geometry of the dacite unit. A thin hangingwall dacite produced a laterally extensive pathfinder anomaly proximal to the hangingwall contact that largely mirrored the distribution of the dacite. A thicker hangingwall dacite "dome" produced a less laterally extensive anomaly but a broader pathfinder anomaly into the hangingwall unit.

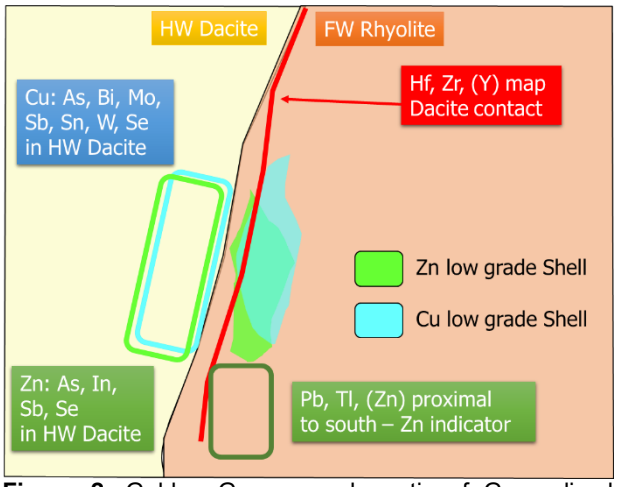

Figure 2. Golden Grove – schematic of Generalised Geochemical Model

The contact between the footwall units (dominantly rhyolitic) and the hanging wall units (dacitic) – the "mineralised horizon" of Figure 1 – could be mapped by the distribution of Hf, Zr and Y.

The Golden Grove mining leases contain ~35km strike extent of the "mineralised horizon" with thickening transported cover blanketing this key position to the south-east of the Gossan Valley deposit.

This area, shown as H1 on Figure 1, contained a number of historic RAB drillholes but very limited deeper Reverse Circulation (RC) percussion and/or diamond drillholes. Also, historic analysis of the RAB drilling was largely confined to Cu, Pb, Zn and Au. Fortunately, the majority of drill sample pulps from historic drilling at Golden Grove had been stored on site and thus could be retrieved for reanalysis.

Interpretation of the results of this reanalysis at H1 is presented in Figure 3.

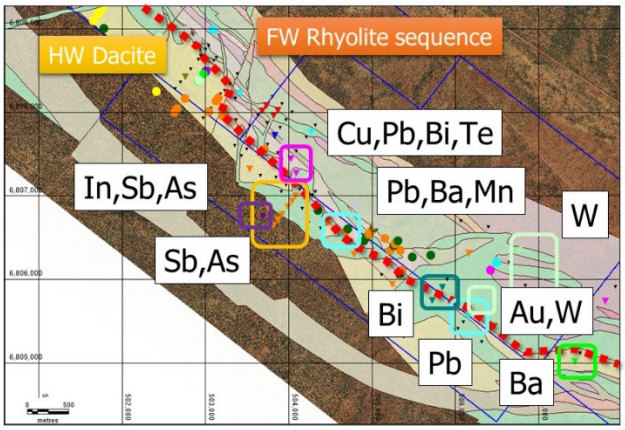

Figure 3. H1 area. Interpreted multi-element geochemistry on interpreted geology and aerial photograph. Green: dolerite; yellow: hangingwall Dacite & Red/pale green footwall Rhyolite units

The identification of a multi-point Sb/As/In anomaly in an interpreted hangingwall position was considered promising. However, the logged bottom

of hole lithology was dolerite (green on Figure 3) for most of the anomalous Sb/As samples which, previously, would have been interpreted to indicate that these are “false” anomalies. The dolerite is dated as Proterozoic and thus postdates and is known to crosscut mineralisation as dykes and sills. Review of data from another area identified that although dolerite may have been recorded as the end of hole lithology it is likely that the RAB drilling technique has been unable to penetrate far into this hard rock type and thus this Sb/As anomalous bottom of hole interval is more likely to be hosted in highly weathered (clay) hangingwall dacite. The presence of Cu/Pb/Bi/Te anomalous concentrations in the samples in an adjacent footwall position further indicates the high prospectivity of this area.

The presence of a Bi anomaly occurring at the interpreted position of the “mineralised horizon” with anomalous Pb proximal is also considered encouraging. Although bedrock is interpreted to be dolerite (Figure 3), the presence of these pathfinders and a Au, W anomaly in the footwall necessitates that this area be re-assessed.

Re-sampling in the H1 area was conducted by targeting the full strike extent of the “mineralised horizon” and generated multiple new targets. The integration of geological observations was critical in the interpretation of the geochemical data in order to rigorously prioritise potential targets.

4 Conclusions

Storage of historic drill samples may seem an unnecessary luxury but the ability to re-analyse old samples using new techniques offering not just more elements but significant lower detection limits provide the ability to generate new targets in what may be perceived to be a mature exploration terrain. Systematic sampling & multi-element analysis of bottom of hole samples over known deposits enabled a Generalised Geochemical Model to be developed and new prospects have been developed based on this model.

At Golden Grove, multi-element reanalysis has enabled “new” robust targets to be developed in the “Shallow”. This has challenged the paradigm of the area being a mature terrain and the necessity of “Deep” exploration.

Acknowledgements

Golden Grove Operations Pty Ltd, a wholly owned subsidiary of 29Metals Limited, is thanked for permission to publish this work. This paper owes much gratitude to the excellent foundational work conducted by previous explorers, research students and consultants, in particular, geochemists Cliff Stanley and Scott Halley.

References

Frater, K.M., 1983. Geology of the Golden Grove Prospect, Western Australia: a volcanogenic massive sulfide-magnetite deposit. Economic Geology, 78: 875-919.

Halley, 2014a. Golden Grove Geochemistry. MMG Golden Grove unpublished report.

Halley, 2014b. Golden Grove RAB Geochemistry. MMG Golden Grove unpublished report.

Normandy Golden Grove Operations, 1999. Scuddles and Gossan Hill Archaean VHMS deposits . Hand out and field excursion guide, 26 pp plus figures

Sharpe, R. and Gemmell, J. B., 2002. The Archean Cu-Zn magnetite rich Gossan Hill volcanic-hosted massive sulphide deposit, Western Australia: genesis of a multistage hydrothermal system. Economic Geology, 97:517-539.

Sharpe, R. and Gemmell, J.B., 2001. Alteration characteristics of the Archean Golden Grove Formation at the Gossan Hill deposit, Western Australia: Induration as a focusing mechanism for mineralizing hydrothermal fluids . Economic Geology, 96: 1239-1262.

Smith, R. E., 2003. Gossan Hill Cu-Zn-Au Deposit, Golden Grove, Western Australia. Regolith Expression of Australian Ore Systems, CRC LEME.

Stanley, C.R., and Radford, N., 2003. Lithogeochemical Exploration in Deep Regolith at the Golden Grove Volcanic Hosted Massive Sulphide Deposit, Western Australia. IGES 2003, Dublin, Ireland.

Serpentinization of the Ronda Massif (Spain): structural control and fluid origin, a framework for metal mobility

Bastien Audran[1], Philippe Boulvais[1], Yannick Branquet[1], Pierre Gautier[1], Marc Ulrich[2], Guillaume Raymond[3], George Beaudoin[3], Daniel Layton-Matthews[4], Rémi Coltat[5], Evelyne Leduc[4], Maëlys Bevan[1]

[1] Géosciences Rennes, UMR 6118, University of Rennes, 35042 Rennes, France

[2] IPGS-EOST, UMR 7516, University of Strasbourg, Strasbourg, France

[3] Département de géologie et de génie géologique, Centre de recherche sur la géologie et le génie des ressources minérales (E4m), Université Laval, Québec, G1V 0A6, Canada

[4] Queen's Facility for Isotope Research, Department of Geology and Geological Engineering, Queen's University, 36 Union Street, Kingston, Ontario, Canada K7L 3N6

[5] Instituto Andaluz de Ciencias de la Tierra (IACT)-CSIC, Universidad de Granada, Granada, Spain

Abstract. Serpentinization is a hydrothermal transformation of ultramafic rocks which leads to metal mobility. The Ronda peridotite Massif (Andalusia, Spain) represents the largest body of subcontinental peridotites exposed at the Earth's surface. No comprehensive work on serpentinization has been conducted so far, notably because most research has focussed on the high-temperature deformation and petrology of mantle rocks. In the Massif, serpentinization rate varies from a few percent to 100%. We identified three steps of serpentinization. The first one (lizardite 1) is pervasively developed within the peridotite with common mesh-texture. The second forms corridors of lizardite 2, chrysotile and magnetite. The third is associated with cataclasis and consists of polygonal serpentine veins (plus minor chrysotile) and magnetite. Structural analysis allows identifying a regional tectonic context for the cataclasis-associated serpentinization which corresponds to a multi-directional horizontal stretching and vertical shortening direction (i.e. near pure flattening). The different stages of serpentinization show comparable isotopic compositions, with $\delta^{18}O$ values of ~ +5.0‰ and δD of ~ -79‰, suggesting that they were developed under sub-identical conditions of fluid-rock interactions (fluid sources, temperature of formation and fluid/rock ratio). This study provides the framework in which metals can be mobilized during serpentinization.

1. Introduction

Serpentinization is a hydrothermal transformation of ultramafic rocks, such as the Sub-Continental Lithospheric Mantle (SCLM) which represents a reservoir of metals (e.g., Cu, Zn, Co, Ni, Cr, PGE, V, Ti, Au). During their exhumation, the mantle rocks are affected by various hydrothermal processes which can lead to economically viable metal deposits (e.g., seafloor massive sulfides; Patten et al. 2022). Despite some works (Deschamps et al. 2013; Lawley et al. 2020), the characteristics of metal mobilities during serpentinization still remain poorly constrained, notably the related spatial scales. Different approaches can be developed to address this issue: experimentation, modelling, chemical and mineralogical characterization directly on the seafloor or on terrestrial samples (such as the Ronda Massif, Spain).

The Ronda massif is the largest remnant of SCLM in the world. It is partially serpentinized and is thus perfectly suitable to characterize metal mobilities at various scales (from the centimetre to the multi-kilometres scale). To date, studies on the serpentinization of the Ronda peridotite remains scarce (Pedrera et al. 2016).

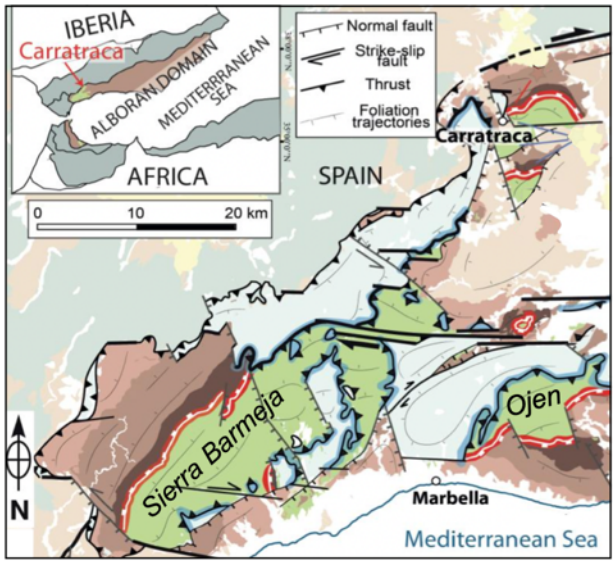

Figure 1. Simplified tectonic map of the Ronda peridotite Massifs (green), thrusts (blue), Crust–Mantle extensional shear zone (red) (modified after Frasca et al. 2017).

To constrain the mobility of metals during serpentinization taking the Ronda Massif as a case study, we first present the main serpentinization stages, then the structures along which serpentinization occurred. We also present stable oxygen and hydrogen isotope data, to discuss the origin of the serpentinizing fluids.

2. Geological context

The Ronda Massif is located in the western Betic Cordilleras (Spain) (Figure 1). The Massif is composed of peridotites with different facies: isotropic to mylonitic, containing garnet, spinel or plagioclase, with dykes of pyroxenite of various types. Structural and petrographic studies have shown the parallelism between the foliation in the SCLM and in the overlying continental crust (Figure 1). The Massif and associated crust were thrusted towards the north-west on the 'external zones' (i.e. upper continental crust; see Frasca et al. 2017) during a Cenozoic compressional event (Figure 1). However, the mechanism and the timing of thrusting have been subjects of controversy for decades, with

various proposed models (e.g., extension, compression or transpression alone; polyphased tectonic; Mesozoic or Cenozoic in age). Geochronological studies performed within the lower crust, close to the crust/mantle boundary, revealed dominant deformation during the Variscan orogen, with an Alpine overprint. Later, some felsic magmas, dated between 19 and 22 Ma intruded the SCLM Massifs (U-Pb on zircon: Esteban et al. 2011; Frasca et al. 2017). A potential source of these granitic magmas can be the underthrusted units which underwent a dynamothermal metamorphism during the thrusting of the Ronda SCLM units (Esteban et al. 2011; Tubia et al. 2012).

Pedrera et al. (2016) described two main types of serpentinization: (1) common mesh-texture and (2) veins of either antigorite or lizardite. These authors associated the latter type to the felsic intrusions during Cenozoic polyphased tectonic event.

3. Method

This study is mainly focused on the largest mantellic massif, the Sierra Barmeja (Figure 1). Sampling was regularly distributed to perform a large-scale characterization of mineralogy, serpentinization rate and stable isotope distribution.

The mineralogy of serpentine polytypes has been determined by Raman spectroscopy which allows discrimination of lizardite/polygonal serpentine from antigorite and chrysotile.

The structural context of serpentinization has been accessed through systematic fault kinematic analysis based on serpentine shear veins bearing slickenfibers in 17 measurements stations. We used the right dihedra method which allows calculating the stretching and shortening axes.

A total of 32 samples have been selected for a stable isotope study of oxygen and hydrogen. These samples correspond to 12 whole rocks (WR) of serpentinized peridotite (lizardite ± chrysotile), 3 serpentinized corridors (lizardite + chrysotile) and 17 veins of serpentine (polygonal serpentine ± chrysotile). For each sample, we separated magnetite from serpentine by hand magnet. In order to estimate the serpentinization temperature, the $\delta^{18}O$ values of 2 magnetite-serpentine pairs have been measured. The $\delta^{18}O$ and δD values are reported relative to VSMOW, with an accuracy of ±0.2‰ and ±1.5‰, respectively.

4. Results and discussion

4.1 Steps of serpentinization

Three steps of serpentinization have been identified in the Sierra Barmeja Massif.

The first step presents a typical massive aspect with brown patina (Figure 2A), a result of weathering. It consists of brown lizardite (liz 1) developed as mesh-texture with remnants of olivine and pyroxene. Olivine crystals are fractured and partially replaced by a pseudomorphic lizardite 1, with rare magnetite grains. Pyroxene crystals are only fractured and mostly preserved from serpentinization. The serpentinization rate is highly variable, with a noticeable increase towards the edges of the massif which corresponds to large fault zones (Figure 1).

The second step is easily identified as white banded veins (or corridors), the white colour being due to weathering (Figure 2B). The serpentinized corridors are typically a few centimetres wide to establish fully serpentinized zones. Pyroxene within the corridors is transformed into bastite. In the centre of the corridors, pyroxene is even partially dissolved and replaced by lizardite (liz 2). This lizardite is white in thin section, always associated with magnetite veinlets/ribbons (Figure 3), and discontinuous chrysotile veins. The contacts between liz 1 and liz 2 are either sharp or gradual.

The third serpentinization step is associated with cataclasis (Figure 2C). The thickness of the cataclasites is variable, ranging from pluri-decametric to metric. Clasts are metric to sub-

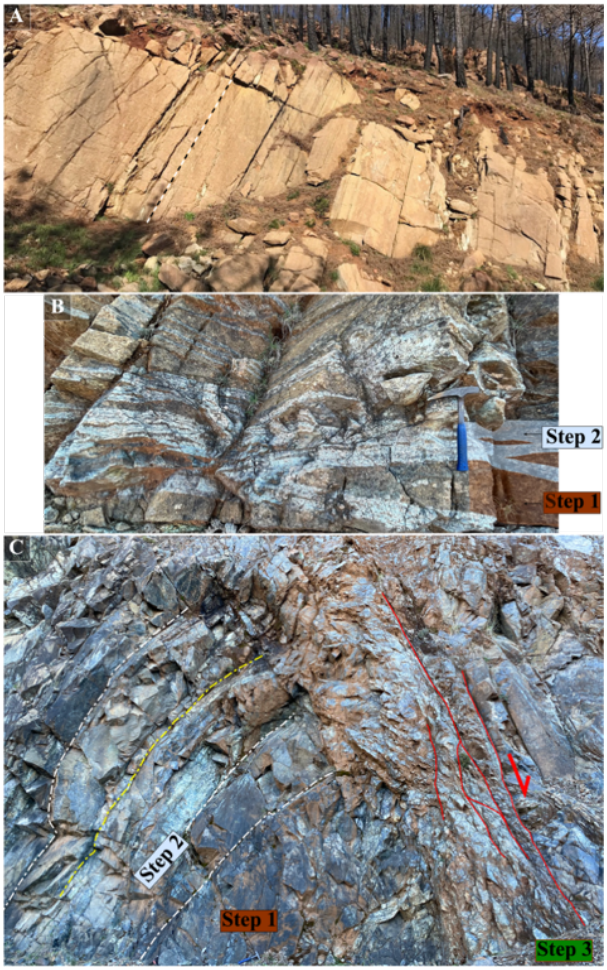

Figure 2. Serpentinization steps in outcrops. **(A)** First step corresponding to massive brown peridotites partially serpentinized in mesh-texture with mantellic HT foliation (dashed line); **(B)** second step characterized by multi-centimetre white band corresponding to serpentinized corridors with remnants of step 1 partially serpentinized peridotite; **(C)** the third serpentinization step results in metre-thick cataclastic zones with normal sense of shear (red lines). Step 2 corridors (white lines) and centimetric-scale felsic dyke (yellow line) are shown.

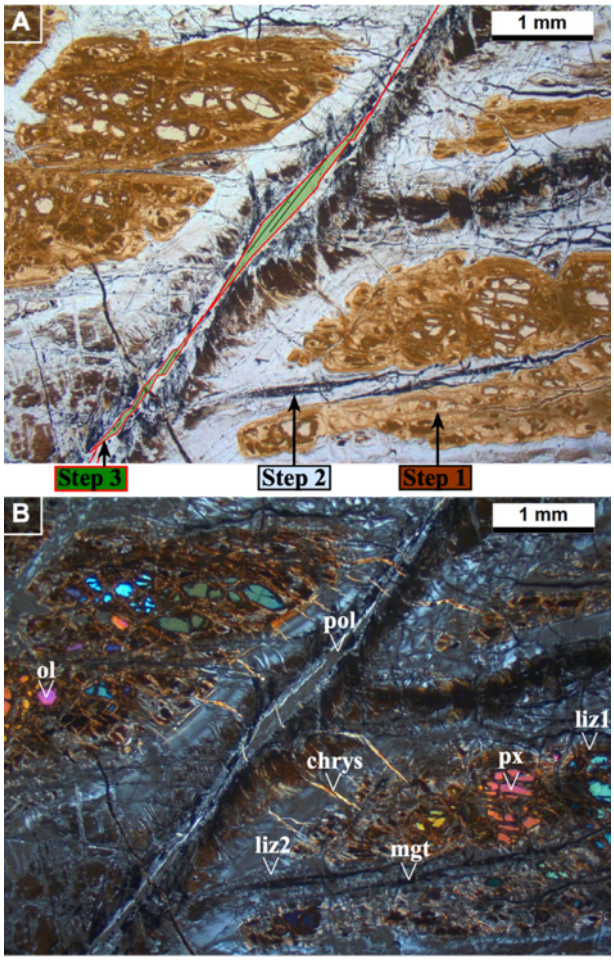

Figure 3. The three steps of serpentinization in thin section **(A)** in plane polarized light and **(B)** in cross-polarized. Remnants of brown, mesh-textured liz 1 with olivine (ol) and pyroxene (px) (i.e. step 1) are crosscut by lizardite 2 (i.e. step 2); liz 2 is associated with magnetite (mgt) veinlets; subsequently, a shear vein filled with polygonal serpentine (pol, in green on A) developed (i.e. step 3) and intersected liz 2; this vein is associated with magnetite crystallisation and is crosscut by chrysotile (chrys) tension gash.

centimetric in size and are often sub-rounded. Deformed bands are characterised by the development of green serpentine (mainly polygonal serpentine) filling veins. Different types of veins are encountered: shear (or hybrid shear-extensional) veins with slickenfibers and extensional veins (i.e. tension gashes with serpentine fibres normal to wallrocks). The main veins are composed of polygonal serpentine mixed with chrysotile (Figure 3). Veins are associated with a metasomatic halo in the host serpentinized peridotite. Within halos, pyroxenes are transformed into bastite, and clusters of magnetite crystals appear in the rim of vein. Locally chrysotile tension gashes cut through green serpentine veins (Figure 3).

4.2 Structural analysis of step 3 serpentine veins

The network of green serpentine shear veins indicates generally a normal sense of shear (e.g., Figure 2C). Nearly four hundred serpentine slickenfibers were measured and analyzed, site by site, throughout the Sierra Barmeja massif. Some dominant trends in vein orientation at the station scale (e.g., N-S, NW-SE, NE-SW, E-W) have been observed, without bulk predominant orientation at the massif scale. With the exception of station 3, where only limited data is available, all sites present a sub-vertical shortening. The horizontal stretching direction varies from site to site (Figure 4A).

When considering the whole massif as a single station, orientation and plunge of shear veins are heterogenous (Figure 4B). However, contouring of pression/tension calculated axes yields a pattern similar to that of individual stations i.e. vertical shortening and horizontal stretching during a near pure flattening deformation (Figure 4C). Therefore, step 3 serpentinization might occur at a Sierra Barmeja massif scale during an extension tectonic event.

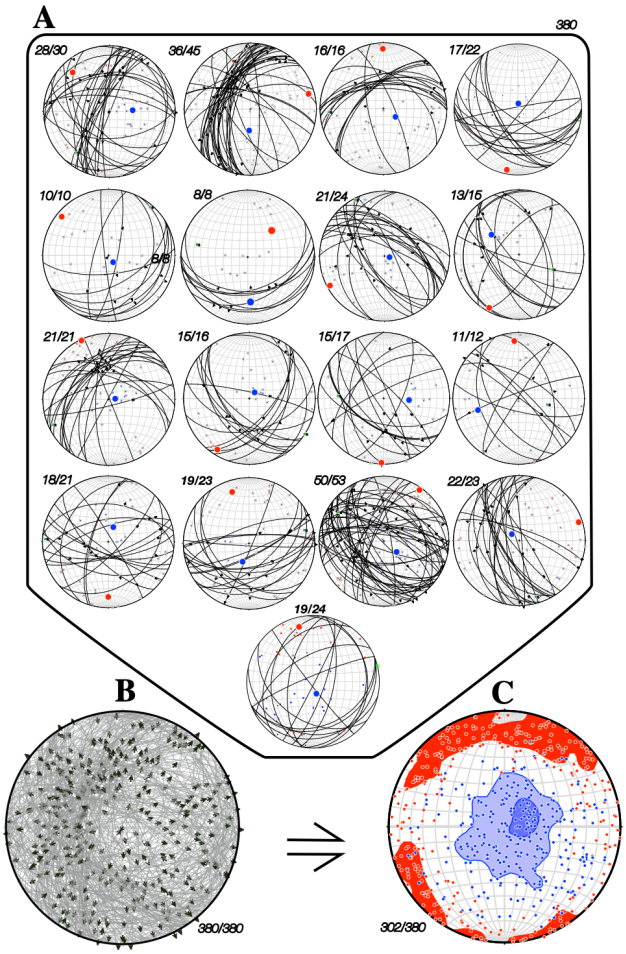

Figure 4. Stereoplots (Schmidt's lower hemisphere) of the step 3 serpentine veins measured throughout the Sierra Barmeja **(A)** stereograms of 17 stations, great circles are vein planes with kinematics (arrow), calculated mean shortening axis (blue circle) and stretching axis (red circle); **(B)** stereogram gathering all data (380) with their kinematics; **(C)** calculated stereogram of compatible shear veins with stretching (red) and shortening (blue) axes with contouring which yields an oblate ellipsoid (R=0.88) suggestive a pure flattening strain.

4.3 Oxygen and hydrogen isotope compositions

The $\delta^{18}O$ values as a whole range between +2.9‰ to +8.7‰ with most values around ~ 5.0‰ (Figure 5). The δD values are between -33‰ and -96‰ with most values around ~ -79‰.

More specifically, serpentinized peridotites of step 1 have homogeneous $\delta^{18}O_{WR}$ values around ~ +5.3‰. The measured values do not correlate with the intensity of serpentinization (from ~35 to 90% in the analysed samples). It seems that two sub-groups can be identified on the basis of their δD_{WR} values around -75‰ and -90‰, respectively.

Serpentinized corridors (liz 2) have δD values between -71‰ and -76‰, similarly to the first sub-group of liz 1. Their $\delta^{18}O$ values range between +2.9‰ to +5.5‰.

The $\delta^{18}O$ and δD values of step 3 serpentine are scattered around the values of the serpentinized peridotites and corridors, which may result from some variation of the conditions of serpentinization (low fluid/rock ratio, variable temperatures).

Two serpentine-magnetite pairs give a $\Delta^{18}O$ value of +10.1‰ and +10.7‰, which yields a temperature of equilibrium of 180 ± 50°C, using the fractionation factor of Früh-Green et al. (1996).

From these results, consistent with the main mineralogical features of serpentinization in the Ronda Massif, it seems unlikely that seawater was involved during serpentinization. Rather, crustal fluids can be proposed for all steps of serpentinization, the fairly comparable isotopic compositions pleading for a continuum of serpentinization rather than for discrete serpentinization events.

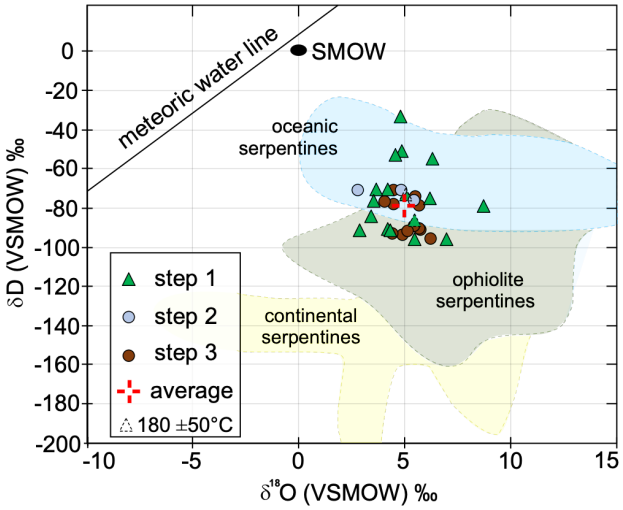

Figure 5. $\delta^{18}O$ vs. δD diagram of serpentinites from the Sierra Barmeja massif. The blue, green and yellow domains represent the isotopic compositions of oceanic, ophiolite and meteoric serpentines, respectively (Früh-Green et al. 2001).

5. Conclusion

The peridotites of the Ronda Massif (Spain) have undergone three steps of serpentinization. Pervasive lizardite 1 serpentinization occurs throughout the Massif. The second step is more localised and consists of corridors of lizardite 2, chrysotile and magnetite. The third step is marked by both polygonal serpentine and magnetite veins occurring within cataclastic zones. This syn-step 3 cataclastic deformation occurred during a regional-scale extensional tectonic event characterized by multi-directional horizontal stretching (near pure flattening strain). All serpentinization steps share similar isotopic signatures with average values of ~+5‰ and ~ -79‰ for $\delta^{18}O$ and δD, respectively. Crustal-derived fluids are favoured for serpentinization, which is thought to have occurred at temperatures around 180 ± 50°C.

Acknowledgements

This work is part of Bastien Audran PhD thesis. Thanks are due to the CNRS-SYSTER French program for financing field work and analyses.

References

Deschamps, F., Godard, M., Guillot, S., Hattori, K., (2013) Geochemistry of subduction zone serpentinites: A review. Lithos 178, p. 96–127. https://doi.org/10.1016/j.lithos.2013.05.019

Esteban, J.J., Cuevas, J., Tubía, J.M., Sergeev, S., Larionov, A., (2011) A revised Aquitanian age for the emplacement of the Ronda peridotites (Betic Cordilleras, southern Spain). Geol. Mag. 148, p. 183–187. https://doi.org/10.1017/S0016756810000737

Frasca, G., Gueydan, F., Poujol, M., Brun, J.-P., Parat, F., Monié, P., Pichat, A., Mazier, S., (2017) Fast switch from extensional exhumation to thrusting of the Ronda Peridotites (South Spain). Terra Nova 29, p. 117–126. https://doi.org/10.1111/ter.12255

Früh-Green, G.L., Plas, A., Lécuyer, C., (1996) Petrologic and stable isotope constraints on hydrothermal alteration and serpentinization of the epr shallow mantle at hess deep (site 895). Ocean Drilling Program, Vol. 147, p. 255–291 https://doi.org/10.2973/odp.proc.sr.147.1996

Früh-Green, G.L., Scambelluri, M., Vallis, F., (2001) O–H isotope ratios of high-pressure ultramafic rocks: implications for fluid sources and mobility in the subducted hydrous mantle. Contrib Mineral Petrol 141, p. 145–159. https://doi.org/10.1007/s004100000228

Lawley, C.J.M., Petts, D.C., Jackson, S.E., Zagorevski, A., Pearson, D.G., Kjarsgaard, B.A., Savard, D., Tschirhart, V., (2020) Precious metal mobility during serpentinization and breakdown of base metal sulphide. Lithos 354–355, 105278. https://doi.org/10.1016/j.lithos.2019.105278

Patten, C.G.C., Coltat, R., Junge, M., Peillod, A., Ulrich, M., Manatschal, G., Kolb, J., (2022) Ultramafic-hosted volcanogenic massive sulfide deposits: an overlooked sub-class of VMS deposit forming in complex tectonic environments. Earth-Science Reviews 224, 103891. https://doi.org/10.1016/j.earscirev.2021.103891

Pedrera, A., Galindo-Zaldívar, J., Acosta-Vigil, A., Azor, A., González-Menéndez, L., Rodríguez-Fernández, L.R., Ruiz-Constán, A., (2016) Serpentinization-driven extension in the Ronda mantle slab (Betic Cordillera, S. Spain). Gondwana Research 37, p. 205–215. https://doi.org/10.1016/j.gr.2016.05.008

Tubía, J.M., Cuevas, J., Esteban, J.J., (2013) Localization of deformation and kinematic shift during the hot emplacement of the Ronda peridotites (Betic Cordilleras, southern Spain). Journal of Structural Geology 50, p. 148–160. https://doi.org/10.1016/j.jsg.2012.06.010

Formation of large mound-shaped sulfide deposit on axial volcanic ridge – A case from the Wocan-1 hydrothermal field, Carlsberg Ridge

Yiyang Cai[1,2,3], Yejian Wang[1], Sven Petersen[2], Xiqiu Han[1,3]
[1] *Key Laboratory of Submarine Geosciences, Second Institute of Oceanography, Ministry of Natural Resources, Hangzhou 310012, China*
[2] *GEOMAR, Helmholtz Centre for Ocean Research Kiel, Kiel 24148, Germany*
[3] *School of Oceanography, Shanghai Jiao Tong University, Shanghai, 200030, China*

Abstract. The hydrothermally active Wocan-1 mound is a nearly circular mound, ~260 m wide and ~50 m high, located on the northwestern slope of an axial volcanic ridge in Carlsberg Ridge. Seafloor observations and sampling indicate a large variability of venting styles as a result of local permeability control. High temperature black smokers are widely distributed over the summit area with significant metal flux indicating limited subseafloor seawater mixing. Clear vent fluids as well as diffuse fluid venting is common in the central and northern areas suggesting subseafloor metal precipitation. Copper-rich sulfides are most abundant in the summit region and along its eastern slope with chalcopyrite and atacamite being major minerals, whereas pyrite and anhydrite are the major minerals in the northern margin area. Sulfur isotope ratios reveal a larger contribution of entrained seawater in the central and the northern areas, when compared to southern area. The increase of $\delta^{34}S$ is related to recrystallization of primary sulfides in the presence of fluids with abundant sulfate-derived sulfur. The active Wocan-1 mound is larger than the well-known TAG active mound on the Mid-Atlantic Ridge indicating that axial volcanic ridges also have the potential to host large sulfide deposit.

1 Introduction

Large seafloor massive sulfide deposits at mid-ocean ridges are often related to off-axis tectonic massifs, ocean core complexes, or associated with detachment faults. They are only rarely observed on axial volcanic ridges. The Wocan-1 hydrothermal field on the axial volcanic ridge of the slow-spreading Carlsberg Ridge is one exception that was recently discovered.

Wocan-1 was discovered in 2013 during the Chinese DY 28th cruise. Previous studies confirmed the presence of abundant high-temperature mineralization at Wocan (Wang et al. 2017). Age dating of nearby sediment cores has revealed an intense activity over the past ~ 1070 years, with the oldest known mineralization dating back to 10,604 ± 67yr BP and the field is currently considered to be in a mature stage of hydrothermal activity (Qiu et al. 2021). In addition, the approximate area covered by hydrothermal precipitates at Wocan (~ 420 m x 320 m; Wang et al. 2017) suggests it is a comparable in scale to some of the largest off-axis vent fields known (German et al., 2016).

In 2017, during the DY 38th Cruise, further investigations were carried out by the manned submersible Jiaolong at Wocan-1. Detailed seafloor observation, high-resolution topographic mapping and accurate sampling have been undertaken, which allows further insights into the processes shaping the Wocan-1 mound. We report here on the variability of venting styles at Wocan-1, the associated mineralization types, their mineralogy, and sulfur isotope compositions and describe the causes for their spatial and temporal variations. Results from this study will contribute to a better understanding of the formation processes of large sulfide deposits on mid-ocean ridges and of the potential of axial volcanic ridges to host economically interesting sulfide deposits.

2 Geological background

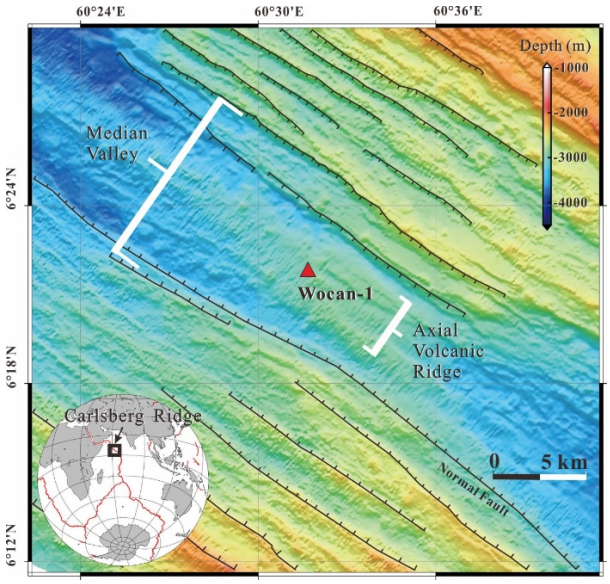

Figure 1. Bathymetric and structural map of the survey area over Carlsberg Ridge and location of the active Wocan-1 hydrothermal field (Wang et al. 2017).

The Carlsberg Ridge (CR), separating the Indian and Somalia tectonic plates in the northwest Indian Ocean, is a slow spreading mid-ocean ridge with a full spreading rate of 22-32 mm/yr (Kamesh Raju et al. 2008). The Wocan Ridge is a NW-SE oriented axial volcanic ridge in the median valley of a symmetrical-spreading mid-ocean ridge segment of the Carlsberg Ridge (Wang et al. 2017). The ridge

extends for ~28 km and covers a total area of about 220 km^2. Wocan Ridge is wide at its center and narrows at the ends, especially in the northwest, where the ridge is linearly extended. Based on TV-sled, TV-grab and manned submersible observations, two sites of hydrothermal mineralization care now recognized. The hydrothermally active Wocan-1 field is located on the Wocan Ridge at 6°22' N, 60°31' E in a water depth of 2970 ~ 3120 m. The Wocan-2 hydrothermal site is located ~1.7 km to the northwest of Wocan-1. It lacks active black smokers, but low-temperature diffuse flow is present.

3 Method

3.1 Seafloor observations and mapping

Four dives with more than 40 hours bottom time have been undertaken by the manned submersible Jiaolong in the Wocan-1 hydrothermal field and its surrounding areas. The topography was derived based on data obtained by bathymetric side-scan sonar (HRBSSS) system of the submersible which surveyed ~80 m above the seafloor at a speed of ~2 knots (Wang et al. 2021). Underwater acoustic communication devices transmitted positioning data obtained by a POSIDONIA USBL on the supporting mother ship, allowing for the determination of the initial position of the integrated navigation system. The submersibles Doppler Velocity Log provided information on the velocity over ground. Motion sensor IXSEA Octans provided data on attitude and heading. Both of them were used to supplement the HRBSSS data and to aid navigation.

3.2 Analytical methods

Textural interpretations and mineral identification were based on polished thin sections analyses at the Second Institute of Oceanography, Ministry of Natural Resources (SIOMNR), Hangzhou, China. The thin sections were examined under a polarizing microscope using reflected and transmitted light.
In-situ sulfur isotope analyses were taken on 135 spots in six samples. Chemical laser-ablation spot-analyses (N=95) on sulfide minerals were performed on a Neptune Plus MC-ICP-MS (Thermo Fisher Scientific, Bremen, Germany) equipped with a Geolas HD excimer ArF laser ablation system (Coherent, Göttingen, Germany) at the Wuhan SampleSolution Analytical Technology Co., Ltd, Hubei, China using the technique described by Hu et al. (2015) and Fu et al. (2016). Ion-probe analyses on 40 sulfide spots were performed by the Sensitive High-Resolution Ion MicroProbe SI (SHRIMP-SI) at Research School of Earth Sciences (RSES), Australian National University, using the technique described by Ireland et al. (2014).

4 Result

The hydrothermally active Wocan-1 mound is located on the northwestern slope of an axial volcanic ridge. The nearly circular mound is ~260 m wide and ~50 m high (Figure 2). The size, the abundant sulfide outcrops, and the abundance of mass wasting all over the mound surface indicate long-lasting hydrothermal activity at Wocan-1.

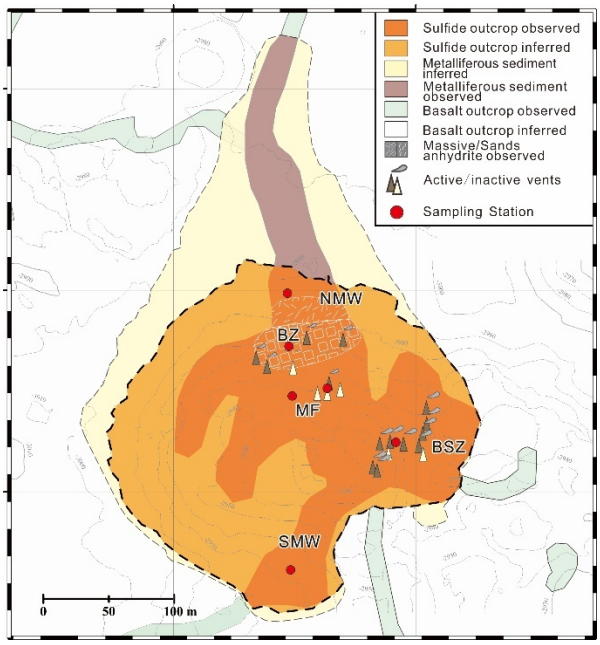

Figure 2. Geological map of the Wocan-1 active mound, interpreted from the high-resolution bathymetry, surface samples, and video surveys. BSZ=Black Smoker Zone, MF= Mulberry Forest, BZ= Beehive Zone, SMW= Southern Mass Wasting, NMW= Northern Mass Wasting.

4.1 Active vents and mass wasting

There are three distinct active vent sites on this mound, distributed over the summit area and along the northern and eastern slopes of the mound. The largest active vent site, the Black Smoker Zone (BSZ), is located near the summit and along the southeastern slope of the mound. The second area of active venting, Mulberry Forest (MF), occurs ~70 m further to the northwest, is located on a gentle slope, and consists of a dense group of chimneys resembling organ pipes. Most of the chimneys at this site are inactive with only a few active vents being present, which currently vent clear fluids. Finally, the Beehive Zone (BZ), which is furthest to the north, is constructed of beehive chimneys usually standing on top of small mounds mainly composed of massive pyrite and anhydrite.

Extensive mass wasting has been observed on the surface and along the margins of the Wocan-1 mound. The most significant mass wasting is documented at the northern margin of the mound (site NMW) with sulfide talus extending up to ~50 m away from the mound with many oxidized sulfide blocks. Anhydrite sand is also abundant in the north (Figure 3). Further down slope, fine-grained metalliferous sediments extend for a further ~200 m

in flatter areas. On the southern slope another mass wasting area is apparent (site SMW) and extends for 100 m from the summit of the mound to the bottom (Figure 2). Within the SMW area, sulfide blocks are commonly coated by atacamite and greenish sediments are also observed indicating the presence of Cu-rich material in this area.

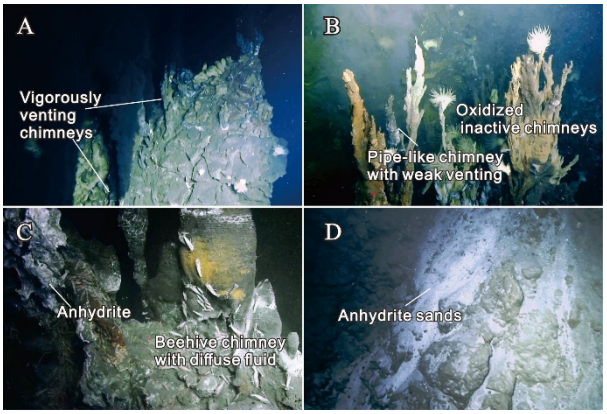

Figure 3. A. Vigorously venting black smoker complex, field of view ~5 m; B. Pipe-like chimneys with weak venting, field of view ~3 m; C. Beehive chimneys with diffuse fluid, field of view ~2 m; D. Anhydrite sand on the northern slope of the mound, field of view ~5 m.

4.2 Mineralogy of the chimneys and massive sulfides

In this study, samples from Wocan-1 mound have been classified into 1) Cu-rich chimneys, 2) Fe-rich massive sulfides and 3) massive anhydrite-pyrite. The sample types are not evenly distributed over the mound: Cu-rich chimney fragments were collected from the central and southern vent sites (BSZ, SMW and MF), while massive pyrite and massive anhydrite-pyrite samples were mainly obtained from northern areas (BZ and NMW).

Cu-rich chimney fragments collected from the central and southern vent sites are mainly composed of chalcopyrite, sphalerite, pyrite, marcasite and minor covellite, often filled with opal-CT. Based on the texture and paragenesis, pyrite can be distinguished into three types: Main stage, euhedral pyrite-I, subhedral pyrite forming the early or late stages (pyrite-II and pyrite-III), and a colloform pyrite-IV that forms at lower temperatures in the early and late stages of hydrothermal precipitation. Similarly, marcasite forms three distinct types: subhedral marcasite (both early or late stage; mrc-I, mrc-II) and colloform marcasite-III. Pyrite-I is always euhedral in texture and can be found as a core to massive chalcopyrite. High temperature chalcopyrite is commonly rimed by sphalerite and both can be replaced by later stage, subhedral pyrite and marcasite (py-III and mrc-II). Sphalerite inclusions in mrc-III and py-II are commonly observed. Colloform marcasite (mrc-III) and pyrite (py-IV) co-precipitate in the outmost layer of the sample. Covellite and opal-CT occur in the late paragenetic sequence and form in the pore space of the sulfides. Covellite may also form or as a weathering product during the warning stages of hydrothermal activity, as documented from a sample collected from the apron of SMW, where chalcopyrite was replaced by covellite in the outmost layer and atacamite is occurring on the surface of the sample.

Fe-rich massive sulfides and massive anhydrite-pyrite samples are abundant at BZ and NMW. Nodular pyrite aggregates are common in a matrix of anhydrite and massive pyrite with individual pyrite grains reaching more than 1 mm in size. Massive pyrite and nodular pyrite are generally dense and strongly recrystallized with indications of sequential overgrowth layers with rare chalcopyrite residual inclusion (Figure 4D). Chalcopyrite is rare in these samples and may overgrow early bornite or is present as fine-grained chalcopyrite set in an anhydrite matrix.

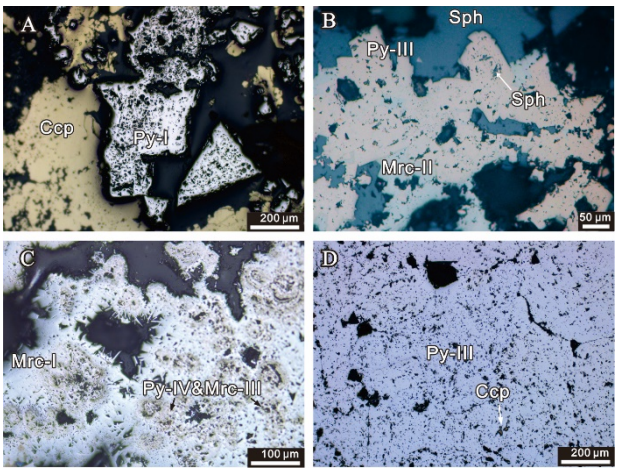

Figure 4. Microscopic features of selected samples of the Wocan-1 mound. A. Euhedral pyrite as a core of subhedral chalcopyrite; B. Recrystallized pyrite and marcasite with sphalerite being present as inclusions and overgrowths; C. Colloform pyrite and marcasite rimed by marcasite microlite; D. Strongly recrystallized pyrite with indications of sequential overgrowth layers with rare chalcopyrite residual inclusion.

4.3. Sulfur isotope

In-situ sulfur isotope analyses of six pyrite- and marcasite-bearing samples from BSZ, MF, BF and NMW. Overall, the $\delta^{34}S$ ratios of Wocan-1 pyrite and marcasite range from -1.60 ~ 5.04‰ ($\delta^{34}S_{ave}$ =2.1‰, n = 135). The $\delta^{34}S$ values vary between pyrite and marcasite in different types from various areas.

In samples from BSZ site and SMW, δ34S values of pyrite range from 0.35 ~2.98‰ ($\delta^{34}S_{ave}$ = 1.60‰, n = 24). Lighter and even negative values have been observed in marcasite ($\delta^{34}S_{ave}$ = 1.17‰, n = 22), and documented the lowest $\delta^{34}S$ value of -1.60‰. In samples from the MF site, $\delta^{34}S$ values of pyrite range from 0.22 ~ 5.00‰ ($\delta^{34}S_{ave}$ = 2.69‰, n = 26). Only pyrite was analysed in samples from the BF and NMW sites and it shows a narrow range of $\delta^{34}S$ values ranging from 2.78 ~ 4.27‰ with an average $\delta^{34}S$ value of 3.56‰ (n = 20).

5 Discussion and conclusion

Significant differences in fluxes of discharged fluids and transported metals have been observed between BSZ, MF and BZ. High temperature black smokers with significant loss of metal to the water column indicates limited subseafloor fluid mixing (Jamieson et al. 2014). In contrast hot, clear fluids and diffuse fluids at MF and BZ are free of metal-rich black smoke, suggesting metal precipitation prior to venting and the accumulation of minerals within the mound or beneath the seafloor by mixing with abundant seawater.

Areas such as BSZ, MF, and SMW are enriched in high-temperature Cu-rich mineral assemblages composed mainly of chalcopyrite with subordinate sphalerite and pyrite. This suggests the presence of a high-temperature upflow zone. It is, however, difficult to explain why pyrite is particularly abundant in the northern margin of the mound. Weathering processes, recrystallization, and changes in the fluid composition could all be responsible for the enrichment of pyrite in this area (Webber et al. 2015; Petersen et al. 2000; Hannington et al. 1995). Traces of growth layering are present with the samples, as are nodular pyrite aggregates in massive anhydrite-pyrite. This texture is similar to that reported for the active TAG mound, suggesting that pyrite from the BZ and NMW has experienced similar recrystallisation processes. It should be noted, that chalcopyrite and sphalerite are particularly low in such samples from Wocan-1 when compared to similar samples from TAG, implying that the fluid composition is relatively Cu- and Zn-poor. It is likely, that these nodular breccias at Wocan-1 have been stripped of most of the Cu and Zn during recrystallization.

The mean $\delta^{34}S$ values of pyrite varies between different areas: $\delta^{34}S_{BSZ\&SMW}$ = 1.60‰ < $\delta^{34}S_{MF}$ = 2.69‰ < $\delta^{34}S_{BZ\&NMW}$ = 3.56‰. Using a simple two-endmember mixing model (Ono et al. 2007), it can be calculated that the contribution of seawater-derived sulfur differs between the sites and is increased by 6% and 10% in the central and the northern areas when compared to the southern sites. Recrystallization during late-stage mixing of hydrothermal fluids with abundant entrained seawater-derived sulfur as evidenced by the abundance of anhydrite have led to this increase of $\delta^{34}S$ values.

Wocan-1 is a large deposit when compared to other sulfide occurrences at axial volcanic ridges. The mound diameter, the intense mass wasting, evidence for recrystallization of primary sulfides and seawater ingress into the mound point to long-lasting, multi-staged history of venting at this site. This and the abundance of Cu-rich material may indicate that sulfide deposits at axial volcanic ridges should be reconsidered as potential exploration targets for economically interesting mineralization.

References

Fu J, Hu Z, Zhang W, Yang L, Liu Y, Li M, Zong K, Gao S, Hu S (2016) In situ sulfur isotopes (delta(34)S and delta(33)S) analyses in sulfides and elemental sulfur using high sensitivity cones combined with the addition of nitrogen by laser ablation MC-ICP-MS. Analytica chimica acta 911: 14–26

Hannington MD, Jonasson IR, Herzig PM, Petersen S (1995) Physical and Chemical Processes of Seafloor Mineralization at Mid-Ocean Ridges. In: Humphris SE, Zierenberg RA, Mullineaux LS, Thomson RE (ed) Geophysical Monograph Series. American Geophysical Union, Washington DC, pp 115–157

Hu Z, Zhang W, Liu Y, Gao S, Li M, Zong K, Chen H, Hu S (2015) "Wave" signal-smoothing and mercury-removing device for laser ablation quadrupole and multiple collector ICPMS analysis: application to lead isotope analysis. Analytical chemistry 87: 1152–1157

Ireland TR, Schram N, Holden P, Lanc P, Ávila J, Armstrong R (2014) Charge-mode electrometer measurements of S-isotopic compositions on SHRIMP-SI. International Journal of Mass Spectrometry 359: 26–37.

Jamieson J, Hannington M, Petersen S, Tivey M (2014) Volcanogenic Massive Sulfides. In: Harff J, Meschede M, Petersen S, Thiede J (ed) Encyclopedia of Marine Geosciences. Springer Netherlands, Dordrecht, pp 1–9

Kamesh R, Chaubey AK, Amarnath D, Mudholkar A (2008) Morphotectonics of the Carlsberg Ridge between 62°20′ and 66°20′E, northwest Indian Ocean. Marine Geology 252: 120–128.

Ono S, Shanks WC, Rouxel OJ, Rumble D (2007) S-33 constraints on the seawater sulfate contribution in modern seafloor hydrothermal vent sulfides. Geochimica et Cosmochimica Acta 71: 1170–1182

Petersen S, Herzig PM, Hannington MD (2000) Third dimension of a presently forming VMS deposit: TAG hydrothermal mound, Mid-Atlantic Ridge, 26°N. Mineral. Deposita 35: 233–259

Qiu Z, Han X, Li M, Wang Y, Chen X, Fan W, Zhou Y, Cui R, Wang L (2021) The temporal variability of hydrothermal activity of Wocan hydrothermal field, Carlsberg Ridge, northwest Indian Ocean. Ore Geology Reviews: 103999

Wang Y, Han X, Petersen S, Frische M, Qiu Z, Li H, Li H, Wu Z, Cui R (2017) Mineralogy and trace element geochemistry of sulfide minerals from the Wocan Hydrothermal Field on the slow-spreading Carlsberg Ridge, Indian Ocean. Ore Geology Reviews 84: 1–19

Wang Y, Han X, Zhou Y, Qiu Z, Yu X, Petersen S, Li H, Yang M, Chen Y, Liu J, Wu X, Luo H (2021) The Daxi Vent Field: An active mafic-hosted hydrothermal system at a non-transform offset on the slow-spreading Carlsberg Ridge, 6°48′N. Ore Geology Reviews 129: 103888

Webber AP, Roberts S, Murton BJ, Hodgkinson MR (2015) Geology, sulfide geochemistry and supercritical venting at the Beebe Hydrothermal Vent Field, Cayman Trough. Geochem Geophys Geosyst 16: 2661–2678

Zong T, Han X, Liu J, Wang Y, Qiu Z, Li H, Yu X (2019) H_2O in basaltic glasses from the slow-spreading Carlsberg Ridge: Implications for mantle source and magmatic processes. Lithos 332–333: 274–286.

Origin of Fe-Ca metasomatism at oceanic core complexes: implications for the formation of seafloor massive sulphide deposits (MARK area, 23°N)

R. Coltat[1,2], M. Andreani[3], C. Patten[4], M. Godard[5], B. Debret[6], J. Escartin[2]
[1]*Instituo Andaluz de Ciencias de la Tierra, IACT, CSIC-UGR, Armilla, Granada, Spain*
[2]*Laboratoire de Géologie, UMR 8538, Département de Géosciences, ENS Paris, PSL Research University, Paris, France*
[3]*Laboraoire de Géologie de Lyon, UMR 5672, ENS, Université Lyon 1, Lyon, France*
[4]*Institute of applied geochemistry, Chair for Geochemistry and Economic Geology, KIT, Karlsruhe, Germany*
[5]*Géosciences Montpellier, CNRS, Université de Montpellier, Montpellier, France*
[6]*Institut de Physique du Globe de Paris, CNRS UMR 7154, Paris, France*

Abstract. At (ultra)slow-spreading ridges, the circulation of hot, acidic, reduced and metal-rich fluids triggers the formation of ultramafic-hosted seafloor massive sulphides deposits (UM-SMSs). These sites display a great variability from site to site, making it difficult to build a simple genetic model. They may notably be associated with Fe-Ca metasomatism, as observed in fossil mineralized systems, thus with possible genetic implications for the formation of mineralized systems. Similar Fe-Ca metasomatism is reported in mantle rocks drilled at the Mid-Atlantic Ridge Kane (MARK) area, offering access to the vertical dimension beneath an oceanic core complex to unravel the nature and geometry of deep magmato-hydrothermal processes.
At MARK, mantle rocks record complex melt-rock and fluid-rock interactions. Magma channelling and interactions with peridotite enrich mantle silicates in Fe, Co and Zn. Subsequent hydrothermal alteration produces metamorphic mineral assemblages (e.g., amphibole, clinopyroxene, chlorite, talc, ilvaite, hydro-garnet, serpentine) and is responsible for Cu leaching. It occurs during early mantle exhumation and is followed by the serpentinization of the massif during progressive mantle denudation. Considering the lithological heterogeneity at (ultra)slow-spreading ridges, metal enrichment in mantle rocks through melt-rock interactions may be widespread, eventually accounting for metal endowment at UM-SMS

1 Introduction

Mid-Oceanic Ridges (MORs) are the locus of hydrothermal circulations leading to intense chemical and thermal exchanges between the oceanic lithosphere and the oceans (Alt, 1995). This results in a variability of altered rocks and hydrothermal fluids that vent at the seafloor (e.g., Schwarzenback and Steele-Mclnnis, 2020). Among them, UM-SMSs form when hot (e.g., 300-350°C), acidic, reduced and metal-rich fluids mix with ambient seawater in ultramafic dominated environments, leading to the formation of Cu-Zn-Co-(Au-Ag) mineralizations (Fouquet et al., 2010).

However, the structural, mineralogical and geochemical variability from site to site (Fouquet et al., 2010) is coupled to the difficulty to access the vertical dimension beneath UM-SMSs. This results in limited constraints on the nature and geometry of deep hydrothermal circulations, and thus on a simple genetic model. This can be partly resolved by focusing on fossil mineralized systems exposed in Alpine ophiolites and that share similarities with UM-SMSs, although they are closely associated with (Fe)-Ca silicates and are interpreted as deep portions beneath UM-SMSs (e.g., Coltat et al., 2019). This suggests that Fe-Ca metasomatism could have genetic links with the formation of UM-SMSs, and that is not documented at MORs due to the restricted access to the vertical dimension. This can be partly addressed through drill cores at exhumed mantle domes.

Here, we focus on the MARK area, an oceanic core complex (OCC) where mantle rocks showing evidence of Fe-Ca metasomatism have been drilled during ODP Leg 153 (Cannat et al., 1995). We performed a petrographic and geochemical on mantle rocks to provide i) temporal and spatial constraints on Fe-Ca metasomatism, and ii) quantify the associated chemical mobilities and their implication for UM-SMS formation.

2 Geological setting

The southern zone of the Kane fracture zone is referred to as the MARK area (23°N, Fig. 1). This segment is asymmetric, with development of an OCC on the western flank (Dick et al., 2010), and block-faulted basaltic pillow lavas on the eastern flank (Cannat et al, 1995). A volcanic ridge at the axial valley hosts the active Snake Pit hydrothermal field.

Mantle rocks were recovered at ODP site 920, 40 km south to the Kane transform at ~3300 meters below sea level (23°20.32'N, Fig. 1B). The holes 920B and 920D reached 126 and 200 meters below seafloor, with a cumulative recovery of 38 and 47%, respectively. Serpentinized harzburgites with minor dunite layers and gabbro veins were recovered.

Structural observations of serpentinite veins indicate hydrothermalism and alteration associated with mantle exhumation (Andreani et al., 2007). The presence of unusual Fe-Ca silicates (e.g., ilvaite, hydro-andradite and diopside) accompanied with sulphides and oxides (Gaggero et al., 1997) also suggests high temperature hydrothermal activity. After petrographic analyses, this occurs during early serpentinization (Gaggero et al., 1997)

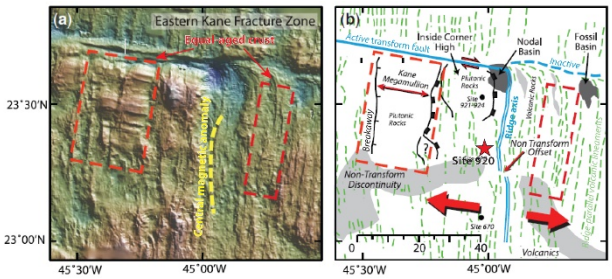

Figure 1. (A) Shaded relief bathymetric map of the Mid-Atlantic Ridge Kane area and (B) tectonic interpretation of the Kane megamullion (after Dick et al., 2010).

3 Methods

We focused on nineteen samples covering different types of petrographic facies: serpentinized peridotites, altered magmatic rocks intruding serpentinized peridotites, serpentinized peridotite-magmatic dykelets contacts, serpentine-chlorite-amphibole-talc veins, clinopyroxene-rich alteration zones and veins, and calcite-bearing veins cutting through serpentinized peridotites. This sample set is representative of the variability in hydrothermal signatures observed in mantle rocks at MARK.

Mineralogical assemblages have been determined through microscope observations and SEM analyses. EPMA and LA-ICP-MS analyses were carried out on mantle and metamorphic mineral phases from 16 samples to constrain their geochemical compositions. Finally, bulk rock geochemical compositions of sixteen mantle and magmatic rocks were measured using ICP-MS technique.

4 Results and interpretation

4.1 Petrography of the MARK mantle and magmatic rocks

The host rocks represent either serpentinized peridotites (SP) or magmatic dykelets intruding the former. Serpentinization is variable, generally less advanced near magmatic intrusions where pyroxene may be preserved. Further away, mantle silicates (olivine and pyroxenes) are almost fully replaced by serpentine, forming mesh and bastite textures. Magmatic rocks represent rodingitized and clinopyroxene-rich dykelets and oxide gabbro. They present advanced alteration with common chlorite, hydro-grossular and clinopyroxene assemblages in the rodingitized dykelet (Fig. 2A). In oxide gabbro, amphibole forms after clinopyroxene, albite after plagioclase and chlorite after Fe-Ti oxides (Fig. 2B).

At the contact with magmatic dykelets, the peridotite is altered (a few mm to few cm in size) and contains metamorphic Fe-Ca-rich assemblages including amphibole, chlorite, talc, clinopyroxene, serpentine and minor ilvaite and hydro-andradite in apparent textural equilibrium (Fig. 2C). Ilvaite forms directly at the expense of pristine Fe-rich mantle olivine (Fig. 2D) suggesting that serpentinization was not achieved during Fe-Ca metasomatism. This is supported by the presence of late serpentine veins cutting through these contacts.

Serpentinized peridotites also contain different types of veins, mm to cm thick. The veins and its serpentinized peridotite host rock are hereafter referred to as PP1, PP2 and CP. The first type (PP1) is made of amphibole (tremolitic to pargasitic composition), chlorite, talc, serpentine ± clinopyroxene assemblages with locally minor titanite.

A second type (PP2) represents clinopyroxene-rich veins, where coarse clinopyroxene grains are partially amphibolitized (Fig. 2E) and enclosed in a matrix made of tiny amphibole (tremolitic to pargasitic composition), serpentine and chlorite grains. Locally the proportion of clinopyroxene in mantle rock increases, defining a pervasive zone made of tiny imbricated clinopyroxene lathes associated with amphibole and phyllosicliates.

Finally, the third type of vein cutting through serpentinized peridotite (CP) represents calcite-bearing veins and is either made of hydro-andradite, diopside, serpentine, calcite, pyrrhotite assemblages (Fig. 2F) or serpentine, calcite, Cu-sulfides veins. While sulfides represent less than 5% in both veins, they suggest metal mobilization during the formation of calcite-bearing veins.

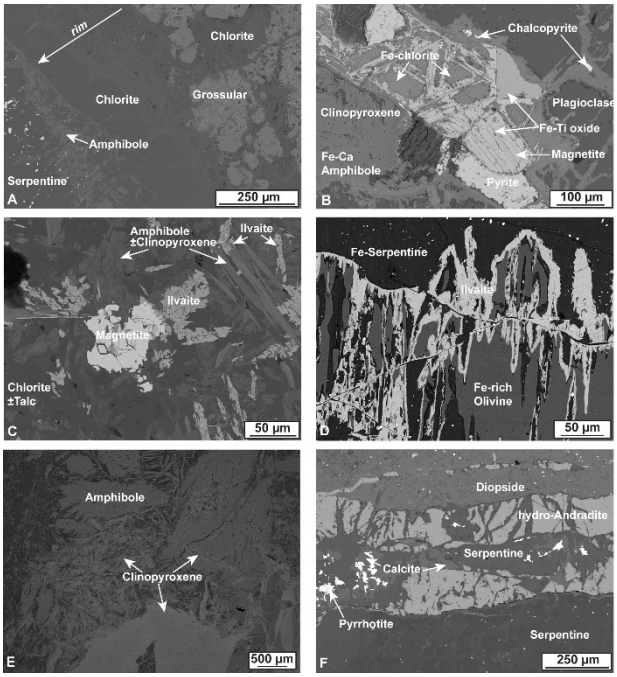

Figure 2. SEM pictures of magmatic and mantle rocks of ODP site 920 (A) Rodingitized magmatic dykelet-peridotite contact showing chlorite enrichment towards the rim of the dykelet. (B) Amphibolitized oxide gabbro. Amphibole and Fe-chlorite form at the expense of clinopyroxene and Fe-Ti oxides, respectively. (C) Ilvaite replacing magnetite and associated with amphibole in a fine-grained matrix of chlorite+talc. (D) Ilvaite replacing olivine and surrounded by a matrix of Fe-serpentine. (E) Clinopyroxene-amphibole-serpentine-chlorite vein cutting through the serpentinized peridotite (PP2). (F) Vein made of hydro-andradite, clinopyroxene, pyrrhotite, calcite and serpentine cutting through a serpentinized peridotite (CP).

4.2 Bulk rock and *in-situ* olivine geochemistry

The different samples investigated present heterogenous chemical compositions that commonly lie between the poles defined by the serpentinized peridotites and mafic rocks, locally overlapping the MARK pyroxenes (Fig. 3). The CaO content is low in SP, comparable to country serpentinized peridotites, and increases in other samples according to the presence of Ca-bearing mineral phases in these samples (Fig. 3A). PP1 and PP2 have higher FeO content compared to other samples (Fig. 3B).

SP and CP display low REE compositions comparable to country serpentinized peridotites, with a strong Eu positive anomaly and a local concave-up shape (Fig. 3C). The magmatic dykelet-peridotite contact, apart from the positive Eu anomaly, displays REE compositions that mimic those of the oxide gabbro. Finally, PP1 and PP2 are generally enriched in REE and display a positive to negative Eu anomaly compared to SP, but show REE patterns and compositions similar to those of MARK pyroxenites (Fig. 3D). This suggests that veins forming PP1 and PP2 are former pyroxenite veins intruding mantle rocks, which subsequently underwent hydrothermal alteration that produced the observed metamorphic mineral assemblages. The variable REE compositions can be ascribed to the mixing, in various proportions, between pyroxenite and peridotite components.

PP1 and PP2 are depleted in Cu compared to country serpentinized peridotites (Fig. 3E). This cannot be explained by pyroxenite-peridotite mixing as pyroxenite contains more Cu than peridotite. Hence, this suggests that Cu is removed from the rock during hydrothermal alteration. However, Zn is little sensitive to hydrothermal alteration because of the homogenous Zn content of our samples. Only one CP is enriched in Cu and Zn compared to other samples, accordingly to the presence of sulphide in this sample (Fig. 3E, F).

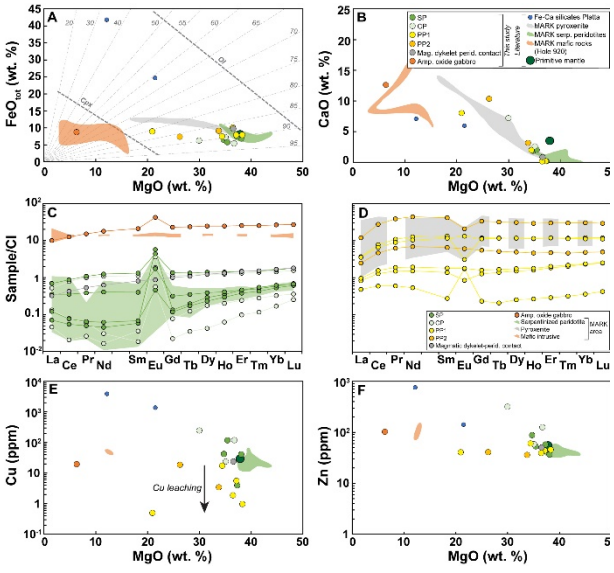

Figure 3. Bulk rock major, trace and rare earth element chemical compositions of mantle and mafic rocks of the ODP site 920 compared with data from the literature (Burgath et al., 1997; Cannat et al., 1997; Casey, 1997; Coltat et al., 2019). CI composition are from McDonough and Sun (1995).

Olivine in mantle rocks at MARK displays variable FeO and MgO contents, with higher FeO content in grains at the contact with magmatic dykelets compared to grains away from these contacts (Fig. 4A). This results in a strong decrease of the Mg# which is accompanied with the decrease of the NiO content and the increase of the Co and Zn contents (Fig. 4B-D).

Similar major element systematics were reported at MARK and ascribed to melt-rock interactions during magma channelling in the lithospheric mantle (Cannat et al., 1997). This suggests that melt-rock interactions may drastically modify the metal (Fe, Co, Zn) budget of mantle rocks.

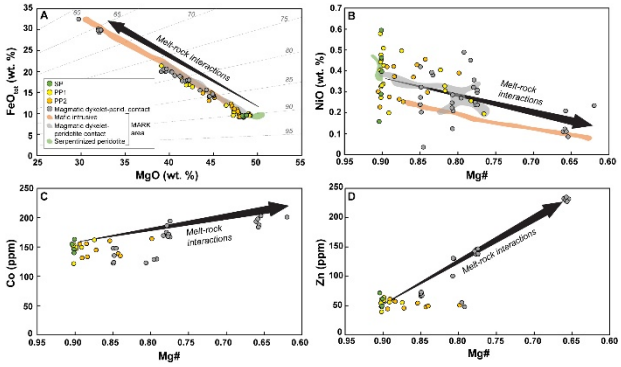

Figure 4. Major and trace element compositions of olivine of the ODP site 920 at MARK compared with data from the literature (Cannat et al., 1997).

4.3 Magmato-hydrothermal history at MARK

Several lines of petrographic and geochemical evidences plead for complex magmato-hydrothermal processes at MARK. These are synthetized in Figure 5.

First, mantle rocks are intruded by magma injections leading to melt-rock interactions with mantle silicates and enrichment of Fe, Co and Zn. As olivine at the contact with magmatic dykelets does not present evidence for recrystallization, magma channelling has to occur in a fresh, non-serpentinized mantle at depth.

In a second stage, fluid circulation along the lithological interfaces produces secondary hydrous Fe-Ca metamorphic assemblages. Ti thermometry of amphibole (Liu et al., 2021) suggests a ~420-830°C temperature formation range, agreeing with the 425 ± 75°C range estimated for the stability of ilvaite-hydro-andradite-diopside assemblages (Gustafson, 1974). Such high temperatures inhibit pervasive serpentinization (Allen and Seyfried, 2003). Fe is likely brought through former melt-rock interactions while Ca may derive from the dissolution of primary magmatic silicates (clinopyroxene,

plagioclase) or seawater-derived hydrothermal fluid. Cu is leached during this stage.

Finally, progressive mantle exhumation and cooling in a brittle regime potentially promotes thermal cracking, and allows seawater entrainment and pervasive serpentinization of the peridotite footwall as well as formation of calcite-bearing veins at temperature <400°C, locally accompanied with metal-bearing fluids.

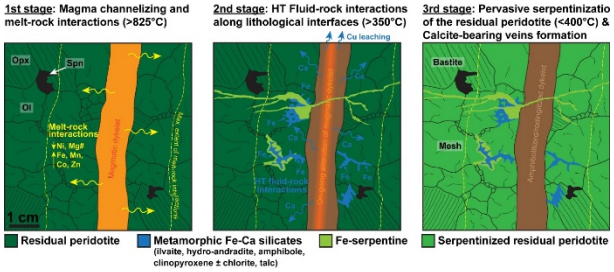

Figure 5. Schematic sketch showing the progressive melt-rock and late fluid-rock interactions leading to Fe-Ca metasomatism and serpentinization of mantle rocks of the ODP site 920

5 Conclusions

Mantle rocks at MARK record complex melt-rock and fluid-rock interactions. A petrographic and geochemical tracing carried out on mantle rocks allowed to identify i) magma channelling through mantle rocks and Fe, Co, Zn enrichment in mantle silicates through melt-rock interactions, ii) subsequent fluid circulation along lithological interfaces, prior to serpentinization, and formation of metamorphic mineral assemblages and responsible for Cu leaching iii) late serpentinization at decreasing temperatures.

This indicates that melt-rock and fluid-rock interactions may control important melt mobilities in exhumed mantle rocks, even if those are very limited at MARK. However, at slow-spreading ridges where important magma bodies may percolate through and interact with mantle rocks, those processes likely have strong implications for the metal budget of the oceanic lithosphere, while accounting for the chemical variability observed at ultramafic-hosted seafloor massive sulphide deposits.

Acknowledgements

This work was funded through an IODP-France (OPE-2021-93) and CNRS-INSU grants to R. Coltat and J. Escartin. Analyses by LA-ICPMS at LERA are supported by the DFG fund INST121384/213-1 FUGG to C. Patten.

References

Allen, D.E., Seyfried Jr., W.E., 2003. Compositional controls on vent fluids from ultramafic-hosted hydrothermal systems at mid-ocean ridges: An experimental study at 400°C, 500 bars. Geochimica et Cosmochimica Acta 67, 1531–1542. https://doi.org/10.1016/S0016-7037(02)01173-0

Andreani, M., Mével, C., Boullier, A.-M., Escartín, J., 2007. Dynamic control on serpentine crystallization in veins: Constraints on hydration processes in oceanic peridotites. Geochemistry, Geophysics, Geosystems 8, 24. https://doi.org/10.1029/2006GC001373

Burgath, K.-P., Marchig, V., Mussallam, K., 1997. 29. Data report: Mineralogic, structural, and chemical variability of mantle sections from Holes 920B and 920D. Proc. ODP. Sci. Results College Station, Texas 153.

Cannat, M., Chatin, F., Whitechurch, H., Ceuleneer, G., 1997. 11. Gabbroic rocks trapped in the upper mantle at the Mid-Atlantic Ridge, in: Proc. Ocean Drill. Program Sci. Results. pp. 243–264.

Cannat, M., Karson, J. a., Miller, D.J., Party, S.S., 1995. ODP Leg 153 MARK Initial Report. Proceedings ODP Initial Reports 153.

Casey, J.F., 1997. Comparison of major-and trace-element geochemistry of abyssal peridotites and mafic plutonic rocks with basalts from the MARK region of the Mid-Atlantic Ridge, in: Proceedings of the Ocean Drilling Program. Scientific Results. pp. 181–241.

Coltat, R., Branquet, Y., Gautier, P., Campos Rodriguez, H., Poujol, M., Pelleter, E., McClenaghan, S., Manatschal, G., Boulvais, P., 2019. Unravelling the root zone of ultramafic-hosted black smokers-like hydrothermalism from an Alpine analog. Terra Nova 31, 549–561. https://doi.org/10.1111/ter.12427

Dick, H.J.B., Johan Lissenberg, C., Warren, J.M., 2010. Mantle melting, melt transport, and delivery beneath a slow-spreading ridge: The paleo-MAR from 23°15′N to 23°45′N. Journal of Petrology 51, 425–467. https://doi.org/10.1093/petrology/egp088

Fouquet, Y., Cambon, P., Etoubleau, J., Charlou, J.L., Ondréas, H., Barriga, F.J.A.S., Cherkashov, G., Semkova, T., Poroshina, I., Bohn, M., Donval, J.P., Henry, K., Murphy, P., Rouxel, O., 2010. Geodiversity of Hydrothermal Processes Along the Mid-Atlantic Ridge and Ultramafic-Hosted Mineralization: A New Type of Oceanic Cu-Zn-Co-Au Volcanogenic Massive Sulfide Deposit. Geophysical Monograph Series 188, 321–367.

Gaggero, L., Cortesogno, L., Gazzotti, M., 1997. 30. Data reports: Oxides, sulfides, and asociated phases in veins and hydrothermally aletred peridotitic rocks. Proceedings of the Ocean Drilling Program, Scientific Results 153, 523–529.

Gustafson, W.I., 1974. The Stability of Andradite, Hedenbergite, and Related Minerals in the System Ca-Fe-Si-O-H. Journal of Petrology 15, 455–96.

Liao, Y., Wei, C., Rehman, H.U., 2021. Titanium in calcium amphibole: Behavior and thermometry. American Mineralogist 106, 180–191. https://doi.org/10.2138/am-2020-7409

McDonough, W.F., Sun, S. s., 1995. The composition of the Earth. Chemical Geology 120, 223–253. https://doi.org/10.1016/0009-2541(94)00140-4

Schwarzenbach, E.M., Steele-MacInnis, M., 2020. Fluids in submarine mid-ocean ridge hydrothermal settings. Elements: An International Magazine of Mineralogy, Geochemistry, and Petrology 16, 389–394.

A new vision of the geodynamic evolution of the Iberian Pyrite Belt: VHMS in an intra-arc basin

Fernando Tornos1, Carmen Conde[1], Caio R. de Mello[2], Colombo C. G. Tassinari[2]
[1]Instituto de Geociencias (IGEO, CSIC-UCM), C/Severo Ochoa, 7, 28040 Madrid, Spain
[2]Institute of Geosciences, University of Sao Paulo, Brazil

Abstract. The Iberian Pyrite Belt (IPB) is the largest sulfur anomaly on the earth's crust, dominantly in the form of giant bodies of volcanogenic massive sulfides. VHMS deposits at the IPB are usually interpreted as formed in an intra-continental basin on the northward subducting plate and prior to continent-continent collision. Geochronology, lithogeochemistry and isotope geochemistry suggest that the Iberian Pyrite Belt formed in an intra- to back-arc setting above a southward verging subduction zone in a scenario more similar to other felsic-siliciclastic VMS belts worldwide. The original features of the arc are partially eroded during later oblique continent-continent collision.

1 Introduction

The Iberian Pyrite Belt (IPB) is the largest VHMS district in the world, with more than 1900 Mt of pyrite-rich massive sulfides and large underlying stockworks. It is located in SW Iberia, within the northern part of the South Portuguese Zone. The massive sulfides were deposited in a continental marine basin and interbedded with felsic volcanic rocks and shale during late Devonian to Early Carboniferous times. Here, we propose that the geodynamic scenario is identical to that of other felsic-siliciclastic VHMS systems with the mineralization formed in continental intra-arc marine basin prior to continent-continent collision.

2 Geological setting

The formation of the IPB reflects the evolution from a siliciclastic sequence deposited in a passive continental margin into a classical volcanic arc dominated by calc-alkaline felsic magmatism but with more accessory andesite and basalt (Volcano-Sedimentary [VS] Complex). The VS Complex was deposited in one or more E-W trending basins in which tilted blocks controlled both the depth and type of sedimentation. Along with the volcanic rocks, the sequence includes large amounts of felsic mass flows, shale and chemical sediments (Oliveira, 1990; Moreno, 1996). Systematic mapping and geochronology show that there is not a unique sequence for the whole IPB and it is made by stacked dome complexes of intermediate to felsic composition interbedded with pillowed flows and subvolcanic sills of basalt. The sequence and the style of mineralization change from south to north. In the southern part of the belt there is abundant shale interbedded with the volcanic rocks. Most VMS are exhalative to sub-exhalative within anoxic bottoms and formed in a short time span of less than 1 Ma at the Devonian-Carboniferous boundary and in relationship with catastrophic events during the onset of volcanism (Menor-Salvan et al. 2010). In the northern part of the Belt, shales are scarce and massive sulfides are found replacing porous and reactive felsic rocks such as hyaloclastite and pumice- and glass-rich mass flows (Tornos 2006). The age of these deposits is more than 10 Ma younger, early Tournaisian, than the shale hosted. Rio Tinto is the only deposit that has both deep replacive mineralization on felsic volcanic rocks and exhalative mineralization on shale (de Mello et al. 2022).

Volcanism is rooted in subvolcanic plutonic complexes that are geochemically similar and broadly coeval with the volcanism. The VS Complex is capped by the Baixo Alentejo Flysch (BAF) Group, a turbidite package, 2500 m thick, dated as late Visean to Serpukhovian age. The BAF is interpreted to be synchronous with the southward progradation of the Variscan tectonic front during continent-continent collision.

The IPB was affected by the Variscan orogeny with a thin-skinned deformation defined by the existence of large south-verging thrusts in a ramp and flat geometry (Silva, 1990). Late in this Orogeny a calc-alkaline magmatism was emplaced, which was dated between 330 ± 3 and 328 ± 3 Ma (Kramm et al. 1991; Onézime et al 2003, respectively). Regionally, the volcanic rocks were affected by very low to low grade regional metamorphism (Schermerhorn 1975; Munhá 1990; Sánchez España 2000).

3 Geochemistry

Volcanic rocks of the VS Complex include small amounts of dominantly tholeiitic basalt with Zr/Y ratios below 4.5. They trace primitive melts of mantle derivation that arrived to the upper crust. Their probably more voluminous underplating in the lower to intermediate crust induced partial melting and rise of large amounts of intermediate to felsic magmatic rocks with a calk-alkaline affiliation (Zr/Y>7; $[La/Yb]_n$<5.5) and compositions controlled by fractional crystallization in similar magmatic chambers (Silva et al. 1990; Tornos et al. 2005; Conde and Tornos 2020). However, it looks like that only the most Zr-depleted dacite and/or rhyodacite is related to the VMS deposits (<380 µg/g; Conde and Tornos 2020). The volcanic sequence also includes significant amounts of andesite, especially in the northern part of the Belt and located close to the footwall of the VS Complex. Geochemically, andesite shows negative Nb anomalies and Th-Rb-

Y values similar to those of volcanic arcs (Pearce et al. 1984). This suggests that volcanism in the Pyrite Belt is not bimodal as has been previously proposed by Soriano (1997), Mitjavila et al. (1997), Leistel et al. (1998) and others.

The shale in the southern part of the belt has $^{87}Sr/^{86}Sr_i$ values of 0.685 to 0.711 and εNd_i values of -14.4 to -8.4, indicating that the Sr in shale did not equilibrate with ambient seawater. Both Nd and Sr seem to be inherited from a old continental crust.

Volcanic rocks have εNd_i values indicative of a more juvenile source. Andesite to rhyolite have, as expected, somewhat lower εNd_i values (-4.6 to +2.8) than the associated basalt (-1.8 to +5).

The isotopic composition of the massive sulfides in the southern part of the Belt (εNd_i, -11.2 to +5.4; $^{87}Sr/^{86}Sri$, 0.7067-0.7155) show that hydrothermal fluids are equilibrated with the underlying Phyllite-Quartzite (PQ) Group and/or a radiogenic basement with little or no input from volcanic rocks. The high $^{87}Sr/^{86}Sr$ initial ratios well above seawater also suggest that the ore forming fluids were either basinal brines or seawater with long residence times (Tornos, 2006).

εNd_i values of the massive sulfides in the northern IPB (-7.2 to +2.5) are more akin to those of the volcanic rocks and reflect either inheritance from the host rocks or derivation of the hydrothermal fluids from underlying felsic igneous rocks. Nevertheless, the Sr isotope values are similar in both the volcanic and shale hosted massive sulfides indicating a old crustal provenance and extensive interchange with basinal-derived fluids.

4 Geochronology

U-Pb zircon ages show that the formation of the IPB took place in a rather long time span of ca. 35 Ma (see Fig 1) and probably evidencing a migration of the arc from South to North (Rosa et al., 2009). The oldest recorded volcanism is 374±2 Ma at Neves Corvo (Oliveira et al. 2013) and extends to 338.3±2 Ma in the northern part of the IPB (this work). Mineralization seems also prograde northwards, with the shale-hosted deposits being of uppermost Devonian age (ca. 360 Ma) and the volcanic-hosted deposits being on average of Early Tournaisian age. Systematic dating of the felsic volcanic rocks associated with the replacive massive sulfides suggest ages of mineralization between 355.3±3.7 Ma and 347±2 Ma (Fig 1).

Queerly, the andesite has not yielded primary zircon nor growth zones but has abundant inherited zircon of 540 to 470 Ma age, indicating the existence of an early Paleozoic magmatism beneath the cropping out IPB.

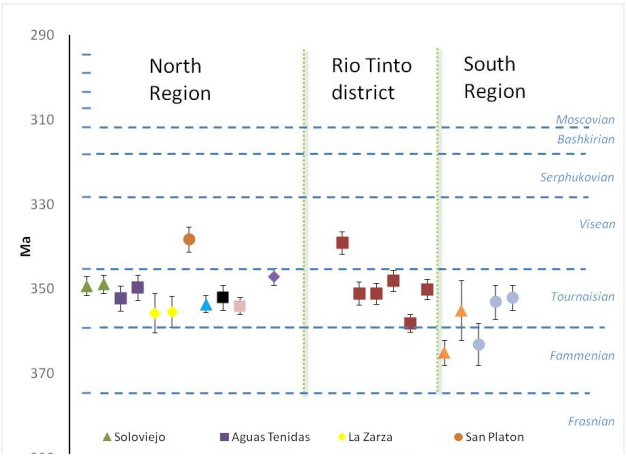

Figure 1. Geochronology of felsic volcanic rocks in the Pyrite Belt – most of them host the VMS deposits.

The South Portuguese Zone was an exotic terrane (Avalonia?) that during Variscan times collided with the Iberian Autochthonous Terrane that was part of Gondwana (Nance et al. 2010; Díez et al. 2016). Most studies agree that the IPB was an intracontinental pull-apart marine basin forming on the northward subducting plate prior to collision and in response to oblique subduction (Munhá et al. 1986; Quesada 1991; Onézime 2003). This scenario is at odds with the geodynamic scenario of felsic-siliciclastic massive sulfides, all formed in magmatic arcs overriding the subducting plate (Franklin et al 2005).

Geochemistry of volcanic rocks, and especially of andesite, and zonation are more consistent with that of a magmatic arc than with an intraplate setting.

Our envisaged scenario includes the formation of a back-arc basin at ca. 360 Ma in relationship with southward oblique subduction of the Gondwana plate beneath Avalonia (Fig 2). First felsic volcanism was responsible of the denudation of large amounts of vascular plants and, indirectly, instauration of anoxic brine pools. Here, mixing of deep hydrothermal fluids equilibrated with the basement with modified seawater rich in H_2S due to the microbial reduction of seawater sulfate promoted the formation of the giant shale-hosted deposits (Menor-Salvan et al. 2010). Nd-Sr isotope geochemistry suggests that venting fluids are not modified seawater equilibrated with volcanic as in most VMS districts but basinal/metamorphic equilibrated with underlying (meta-)sediments.

The best physical scenario is the onset of convective hydrothermal cells during the early stages that involved the circulation of metal-rich and sulfide-poor basinal/metamorphic water. These fluids were later replaced in the cells by seawater, something that inhibited the formation of mineralization (Conde 2016).

5 Geotectonic setting and discussion

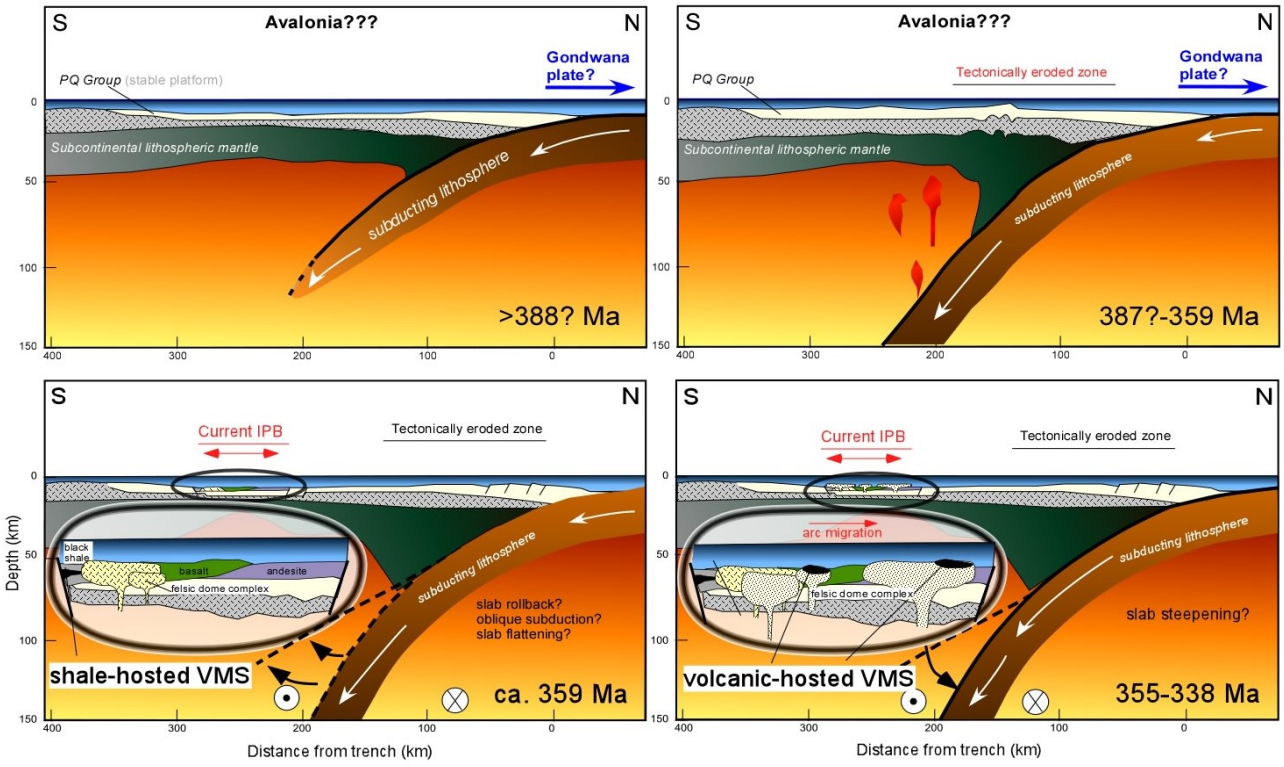

Figure 2. Schematic diagram of the geodynamic evolution of the Iberian Pyrite Belt.

Further northward migration of the arc due to slab flattening or rollback was accompanied by extension, increase in the volume of volcanism and extrusion of andesite followed by dominantly felsic rocks in a scenario similar to that of Taupo (Cole et al. 1990; de Ronde et al 2001). There was a second event of VMS formation that was directly related with felsic volcanism and specially with the Zr-poor dacite-rhyolite. Here, hydrothermal fluids have more negative εNd_i values and seem to be equilibrated with the felsic volcanic rocks or their subvolcanic roots. However, we have not found evidences of the involvement of magmatic-hydrothermal fluids in the system. If so, their key contribution to the metal budget would have been masked by mixing with non-magmatic hydrothermal fluids (de Ronde et al. 2001).

The geodynamic scenario is similar to that proposed for the Bathurst Camp (van Staal et al 1992, 2003) or the Kuroko district (Yamada et al 2011). What makes different the IPB from these districts is the existence of a thick continental basement and the dominance of shale during the early stages of basin formation; these features probably control the origin of fluids and the environment of deposition of the earliest mineralization.

Further closure of the IPB during continent-continent collision at Later Visean (Onézime 2003) was followed by major strike-slip deformation along the suture and tectonic erosion of most of the magmatic arc, remnants of which are now conserved in the highly deformed and lithologically heterogeneous northern IPB (Fig 2).

4 Conclusions

Integration of geological and metallogenic data with geochronology, isotope geochemistry and lithogeochemistry suggest that the Iberian Pyrite Belt formed in an evolving back to intra-arc continental basin on the overriding plate of a southward verging subduction zone, a geodynamic setting similar to that of all the other VMS deposits formed in active margins.

Acknowledgements

We are grateful for discussions with César Casquet, Juan Gomez Barreiro and José Ramon Martinez Catalán. This research is supported by the Exploration Information System (EIS) project of Horizon Europe (contract 101057357).

References

Cole JW (1990) Structural control and origin of volcanism in the Taupo volcanic zone New-Zealand. Bull Volcanol 52: 445-459.

Conde C, Tornos F (2020) Geochemistry and architecture of the host sequence of the massive sulfides in the northern Iberian Pyrite Belt. Ore Geol Rev 127.

Conde C (2016) Geology and hydrothermal evolution of massive sulphides of the Iberian Pyrite Belt. Doctoral Thesis, Salamanca (Spain). Universidad de Salamanca: 379.

de Mello CR, Tornos F, Conde C, Tassinari CCG et al (2022) Geology, Geochemistry, and Geochronology of the Giant Rio Tinto VMS Deposit, Iberian Pyrite Belt, Spain. Econ Geol 117:1149-1177.

de Ronde CEJ, Baker ET, Massoth GJ et al (2001) Intra-oceanic subduction-related hydrothermal venting, Kermadec volcanic arc, New Zealand. Earth Planet Sci Lett 193: 359-369.

Díez RD, Arenas R, Pereira MF et al (2016) Tectonic evolution of Variscan Iberia: Gondwana–Laurussia collision revisited. Earth-Sci Rev 162: 269-292.

Franklin JM, Lydon JW, Sangster DF (1981) Volcanic-associated massive sulfide deposits. Econ Geol 75: 485-627

Kramm U, Giese U, Zhuravlev D, Walter R (1991) Isotope equilibration of magmatic and metamorphic rocks of the Aracena Metamorphic Belt, in XI Reunion sobre la Geologia del Oeste Peninsular, Univ. of Seville, Huelva, Spain.

Leistel JM, Marcoux E, Thiéblemont E et al (1998) The volcanic-hosted massive sulphide deposits of the Iberian Pyrite Belt. Miner Deposita 33: 2-30.

Menor-Salvan C, Tornos F, Fernández-Remolar D, Amils R (2010) Association between catastrophic paleovegetation changes during Devonian-Carboniferous boundary and the formation of giant massive sulphide deposits. Earth Planet Sci Lett 299: 398-408.

Mitjavila J, Martí J, Soriano C (1997) Magmatic evolution and tectonic setting of the Iberian Pyrite Belt volcanism. J Petrology 38: 727–755.

Moreno C, Sierra S, Sáez R (1996) Evidence for catastrophism at the Famenian-Dinantian boundary in the Iberian Pyrite Belt. Recent Advences. In: Strogen P., Somerville D, Jones G Ll (Eds.) Lower Carboniferous geology. Geological Society, London, Special Publication 107: 153-162.

Munhá J (1990) Metamorphic evolution of the south Portuguese/Pulo do Lobo zone. In Dallmeyer RD, Martinez Garcia E, (Eds) Pre-Mesozoic evolution of Iberia: Berlin, New York, Springer Verlag, p. 363–368.

Munhá J, Oliveira JT, Ribeiro A et al (1986) Beja-Acebuches Ophiolite: characterization and geodynamic significance. Maleo, Bol. Inf. Soc. Geol. Port. 2: 1–31.

Nance RD, Gutiérrez-Alonso G, Keppie JD et al (2010) Evolution of the Rheic Ocean. Gond Res 17: 194-222.

Oliveira JT, Relvas J, Pereira Z et al (2013) O Complexo Vulcano-Sedimentar de Toca da Moura-Cabrela (Zona de Ossa Morena): evolução tectono-estratigráfica e mineralizações associadas. In: Dias R, et al (Eds., Geologia de Portugal: 621–645.

Oliveira JT (1990) South Portuguese Sone: introduciton. Stratigraphy and synsedimentary tectonism. In: Dallmeyer RD, Martínez García E (Eds.) PreMesozoic Geology of Iberia. Springer Verlag: 333-347.

Onézime J, Charvet J, Faure M et al (2003) A new geodynamic interpretation for the South Portuguese Zone (SW Iberia) and the Iberian Pyrite Belt genesis. Tectonics 22: 1–17.

Pearce JA, Harris NBW, Tindle AG (1984) Trace element discrimination diagrams for the tectonic interpretation of granitic rocks. J Petrology 25: 956–983.

Quesada C (1991) Geological constraints on the Paleozoic tectonic evolution of the tectonostratigraphic terranes in the Iberian Massif, Tectonophysics 185: 225-245.

Rosa DRN, Finch AA, Andersen T, Inverno CMC (2009) U–Pb geochronology and Hf isotope ratios of magmatic zircons from the Iberian Pyrite Belt. Mineral. Petrol. 95: 47–69.

Sánchez España FJ (2000) Mineralogía y geoquímica de los yacimientos de sulfuros masivos en el área Nor- Oriental de la Faja Pirítica Ibérica, San Telmo-San Miguel-Peña del Hierro), Norte de Huelva, España. Unpublished Doctoral Thesis, Universidad del País Vasco: 307.

Schermerhorn LJG (1975) Spilites, regional metamorphism and subduction in the Iberian Pyrite Belt., somecomments, Geologie en Mijnbouw 54: 23-35.

Soriano C (1997) Evolución geodinámica de la Faja Pirítica Ibérica, Zona Sud Portuguesa. Ph.D. Thesis. Universitat de Barcelona: 328.

Silva JB, Oliveira JT, Ribeiro A (1990) Structural outline of the South Portuguese Zone. In: Dallmeyer RD, Martínez García E (Eds.) Pre-Mesozoic Geology of Iberia. Springer-Verlag, Verlin: 348–362.

Tornos F (2006) Environment of formation and styles of volcanogenic massive sulfides: The Iberian Pyrite Belt. Ore Geol Rev 28: 259–307.

Tomos F, Casquet C, Relvas J (2005) The metalogenesis of transpressional orogens: the Variscan of SW Iberia. Ore Geol Rev 27: 133-163

Valenzuela A, Donaire T, Pin C et al (2011) Geochemistry and U-Pb dating of felsic volcanic rocks in the Riotinto-Nerva unit, Iberian Pyrite Belt, Spain: crustal thinning, progressive crustal melting and massive sulphide genesis. J Geol Society 168: 717-731.

van Staal CR, Wilson RA, Rogers N et al (2003) Geology and tectonic history of the Bathurst Supergroup, Bathurst Mining Camp and its relationships to coeval rocks in southwestern New Brunswick and adjacent Maine - A synthesis. Econ Geol, Monograph 11: 37-60.

van Staal CR, Fyffe LR, Langton JP, McCutcheon SR (1992) The Ordovician Tetagouche Group, Bathurst camp, northern New Brunswick, Canada: History, tectonic setting, and distribution of massive- sulfide deposits. Expl Min Geology: 93–103

Yamada R, Yoshida R (2011) Relationships between Kuroko volcanogenic massive sulfide (VMS) deposits, felsic volcanism, and island arc development in the northeast Honshu arc, Japan. Miner Deposita 46: 1-18.

The San Miguel deposit, Iberian Pyrite Belt: reconstructing a sub-seafloor replacive VMS

Carmen Conde[1], Fernando Tornos[1] , Miguel Polo[2]
[1]Instituto de Geociencias (IGEO, CSIC-UCM), C/Severo Ochoa, 7, 28040 Madrid, Spain
[2]Emerita Resources. Av. De la Constitución 23, 41004, Sevilla, Spain

Abstract. San Miguel is perhaps the most outstanding example of volcanogenic massive sulfides in the Pyrite Belt, showing excellent exposures of replacive massive sulfides and overlying gossan. Detailed geological and structural studies show that the mineralization has replaced a permeable horizon of volcanic breccias of dacitic composition and is rooted in a extensional syn-volcanic fault

1 Introduction

The San Miguel volcanogenic massive sulfide (VMS) is perhaps one of the best examples worldwide of massive sulfides being formed by the replacement of volcanic rocks when hydrothermal fluids channelized along an extensional fault crosscut reactive/permeable layers (Fig. 1).

San Miguel is located in the northern Iberian Pyrite Belt, in the southward overturned and thrusted limb of an E-W trending antiform. The mine was worked during the Roman Empire, with the works oriented to the exploitation of gold and silver that were enriched in the contact of the gossan and the underlying massive sulfides; this enriched layer includes clays with native gold (< 7 g/t) and several hundred ppm of silver in the form of argentojarosite (Fig. 2). The mine was reactivated in ca. 1851 when extracted Cu and pyrite, used for hydrosulfuric acid; it closed in 1960 (Pinedo-Vara, 1963). Afterwards, some of the remaining gossan has been mined for Au.

2 Geological setting

The Iberian Pyrite Belt (IPB) is one of the most outstanding mineral belts on Earth, being the largest crustal sulfur anomaly and hosting a significant proportion of the giant VMS. It had a total estimated pre-mining tonnage of 1900 Mt of massive sulphides and a larger tonnage of (sub-) economic stockwork (Tornos, 2006). The massive sulfides are hosted in the Volcano-Sedimentary Complex (VS Complex), a heterogeneous and up to 1,300 m thick sequence

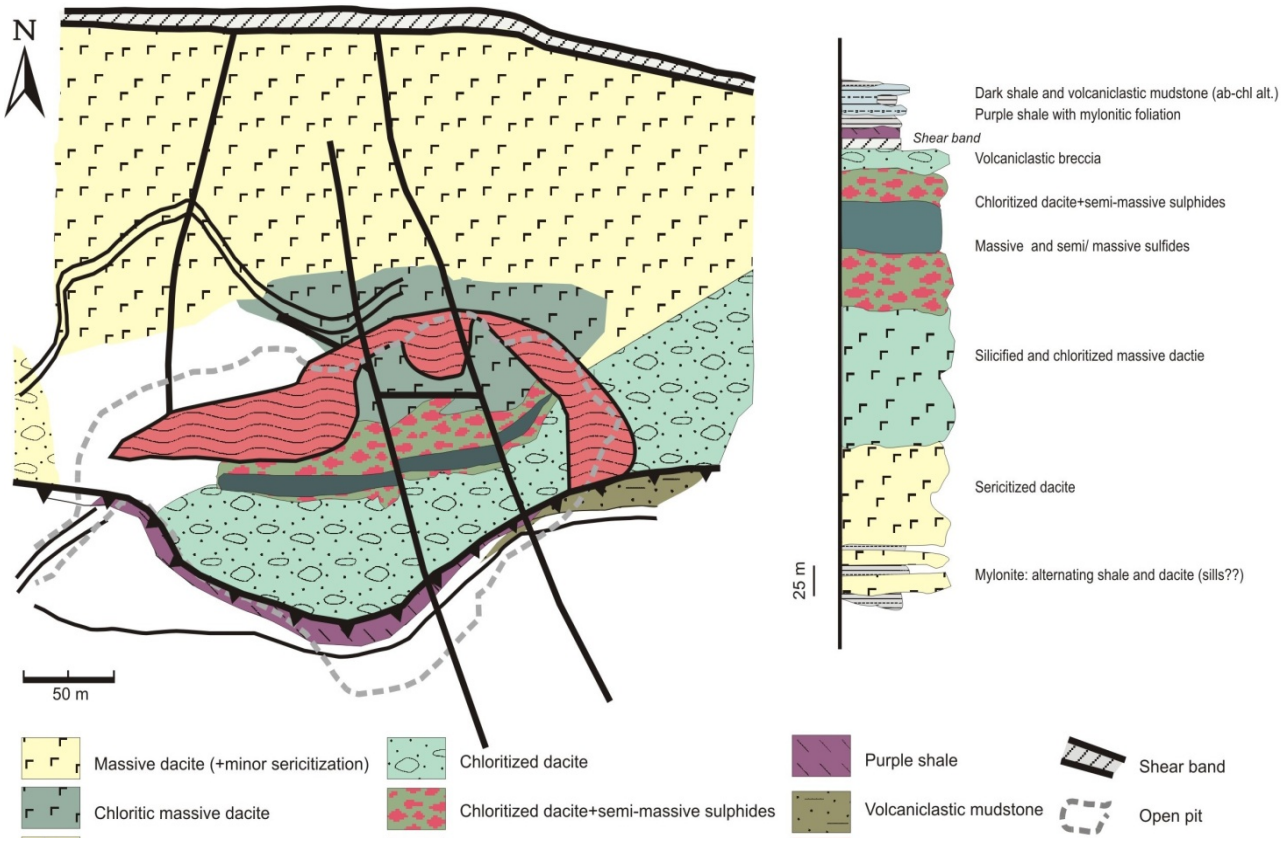

Figure 1. Geologic map of the open pit and simplified lithostratigraphic sequence of the San Miguel Mine showing the main volcanic rocks and hydrothermal alteration (modified of Tornos and Velasco 2007).

deposited in a continental intra- to back-arc marine basin (Tornos et al. 2023); its age is Late Devonian to Early Late Visean (Oliveira, 1990) The VS Complex is dominated by large felsic (dacite-rhyolite) dome complexes and interlayered pumice- and glass-rich mass flows and related volcaniclastic rocks. Shale is common, especially in the southern part of the Belt (Soriano et al 1999, Tornos 2006, Rosa 2007, Valenzuela et al. 2011, Conde and Tornos 2020). The sequence also includes pillowed lava flows and subvolcanic sills of basalt as well as andesite domes, which are especially abundant in the northern part of the belt. Basalt show an alkaline to continental tholeiitic affinity (Munha 1983; Mitjavila et al. 1997; Thieblemont et al. 1998) The intermediate to felsic rocks are low-Al high-Nb calc-alkaline and define an almost continuous trend.

The VS Complex is overlain by the Baixo Alentejo Flysch (BAF) Group, a synorogenic turbiditic sequence up to 2,500 m thick and dated as late Visean to Serpukhovian age and interpreted as result of the growth of a foreland basin during the onset of the Variscan orogeny.

The Variscan deformation is related with continent-continent collision and produced south-ward verging folds and thrusts. Related metamorphism is of very low- to low-grade metamorphism (Schermerhorn 1975; Munhá 1990; Sánchez España 2000). Metamorphism was followed by major I-type plutonism (Schutz et al. 1987; Thiéblemont et al. 1998).

The VMS deposits occur either as (sub-) exhalative stratiform bodies interbedded with shale above the lowermost felsic volcanic rocks (Late Famennian) or replacing felsic volcanic rocks and of early Tournaisian age (Tornos et al. 2023). In both cases, massive sulfides form large lenses with an extensive underlying stockwork. Massive sulfides are dominated by pyrite with lesser amounts of sphalerite, chalcopyrite and galena (Marcoux et al. 1996; Tornos 2006). When exposed subaerially, they are capped by well-preserved gossans and usually small cementation zones (Velasco et al. 2013).

3 San Miguel geology

The San Miguel Mine host several subvertical orebodies, being the largest one exposed in a small ellipsoidal open pit some 200 m in length (Fig 2a). When unaltered, the host rock is a thick felsic unit including coherent quartz-feldspar-phyric dacite interbedded with lenses of a breccia with fragments of a similar composition and a more fine grained supporting groundmass that probably correspond to in-situ and transported hyaloclastite; these layers are interbedded with more polymictic mass flows including coherent dacite, pumice-rich fragments and hyaloclastite supported by glass- and pumice-rich sandstone. The total thickness of this unit is ca. 300 m. U-Pb dating of the dacite has yielded an age of 352 ± 3Ma. Laterally, these rocks grade into a zone of distal phyllic (quartz-sericite) alteration and a pervasive proximal alteration that has replaced the volcanics by chlorite, quartz and pyrite (Fig. 2b). The VS Complex is overthrusted by a more detritic unit. The contact includes up to 1 m of mylonite with fragments of volcanic rock and shale. It grades into 4-6 m of shale and a metre thick unit of feldspar-bearing volcaniclastic mudstone and sandstone with fragments of fine-grained volcanic rocks that resemble peperite. These rocks are overlain by the Baixo Alentejo Flysch Group. Rocks in the allocthonous unit show sub-horizontal S_0 and S_1 but near the thrust plane they are almost obliterated by a younger subvertical crenulation associated with tights folds with subvertical axial plane.

The conspicuous purple colour of this hanging wall unit could be due to shallow marine oxidation, similar to that of a regional marker horizon (Routhier et al 1980, IGME 1982, Oliveira 1990) or due to syn-tectonic oxidation (Conde and Tornos 2020) related with the circulation of oxic waters during Variscan times.

3.1 The replacive mineralization

The massive sulfides are exposed in the northern part of the pit; they consist of a E-W trending subvertical lens, dipping ca. 70°S. In detail, they include coarse-grained pyrite intergrown with chlorite (brunsvingite-diabanite) and hydrothermal quartz (Polo 2022); the rock includes abundant inherited magmatic phenocrysts, giving a texture similar to that described by Doyle & Allen (2003) in the Maurliden deposit and unequivocally showing that sulfides replaced a porphyritic volcanic rock. The rock also includes magmatic zircon inherited from the protolith. The ratio between sulfides and silicates outlines a differential erosion that highlights the presence of ghosts of an ancient fragmental rock (Fig. 2c) that could well be an autoclastic breccia or a hyaloclastite. The fragments show a E-W subhorizontal foliation perpendicular to the orientation of the lens. In detail, there is a gradation from pyrite-poor footwall to pyrite-chlorite supporting ghosts of altered dacite and massive chlorite-bearing massive sulfides with inherited quartz phenocrysts (Fig. 2c).

The footwall of the massive sulfides includes a sub-horizontal fracture infilled with pyrite that has a sharp to replacive contacts with the dacite (Fig. 2d). If restored to the assumed original, horizontal, position, this structure should be vertical and, thus, probably corresponds to a tensional feeder zone to the San Miguel VMS system. The alignment of the fragments situated near the structure, also originally vertical, is also consistent with vertical fluid flow.

Figure 2. Representative photographs of the San Miguel massive sulfide. (a) Landscape of the NE wall of the open pit showing the mineralized sequence and the overthrusted siliciclastic unit. (b) Photograph of the so called "stockwork" but interpreted as semi-massive sulfides cementing a volcanic breccia. (c) Volcanic breccia partially replaced by pyrite and chlorite but showing oriented remnants of the fragments. (d) Feeder structure infilled with pyrite and located along in a normal fault that puts in contact massive and brecciated dacite.

4 Discussion

The San Miguel Mine has been traditionally interpreted as a stockwork zone grading into overlying exhalative massive sulfides. However, this study suggests that the mineralization is replacive on felsic volcanic rocks and the formation of the massive sulfides is probably controlled by variations in the permeability and reactivity of the host sequence. What was interpreted as a stockwork is the footwall of the mineralization and the breccia-like structure are primary structures enhanced by alteration. The San Miguel mine does not have a stockwork underlying the mineralization but a fault-controlled feeder zone (Fig. 2d). This scenario is probably more common than usually recorded in VMS systems (Doyle & Allen 2003; Tornos et al. 2015). It is unlikely that massive sulfides form and are preserved in high energy systems such as during the dynamic growth of felsic domes – any exhalative body will not have time to grow and would have been destroyed by mass flows or magmatic/hydrothermal explosions. It is much more likely that the VMS formed after the growth of the volcanic complex, something that also facilitates its preservation. Replacive VMS systems on volcaniclastic felsic rocks has been recently recorded by submarine drilling in the Okinawa Trough (Nozaki et al. 2021).

The envisaged model includes the upflow of hydrothermal fluids along a tensional fault till arrive to permeable/reactive rocks that were probably capped by impermeable rocks such as shale or coherent volcanic rocks. Reaction of the hot and metal-carrying fluids with cooler modified seawater probably rich in reduced sulfate should have promoted the precipitation of sulfides and chloritization of the host rocks. What remains intriguing is the geochemical mechanism that ultimately drives the dissolution of the Al-rich phases, leaving a rock composed by pyrite, few remnants of quartz phenocrysts and magmatic zircon.

Acknowledgements

We are grateful for discussions with F. Velasco. This research is supported by the Exploration Information System (EIS) project of Horizon Europe (contract 101057357).

References

Conde C, Tornos F (2020) Geochemistry and architecture of the host sequence of the massive sulfides in the northern Iberian Pyrite Belt. Ore Geol Rev 127.

Doyle MG, Allen RL, (2003) Subsea-floor replacement in volcanic-hosted massive sulfide deposits. Ore Geology Reviews 23: 183-222.

IGME (1982) Síntesis Geológica de la Faja Pirítica del SO de España IGME, Madrid: 106.

Marcoux E, Leistel JM (1996) Mineralogy and geochemistry of massive sulphide deposits. Iberian Pyrite Belt. Bol Geol Minero 107: 117-126.

Mitjavila J, Martí J, Soriano C (1997) Magmatic evolution and tectonic setting of the Iberian Pyrite Belt volcanism. J Petrology 38: 727–755.

Munhá J (1990) Metamorphic evolution of the south Portuguese/Pulo do Lobo zone. In Dallmeyer RD, Martinez Garcia E, (Eds) Pre-Mesozoic evolution of Iberia: Berlin, New York, Springer Verlag, p. 363–368.

Munhá J, (1983) Hercynian magmatism in the Iberian Pyrite Belt. Memorias Servicio Geologico Portugal 29: 39-81.

Nozaki T, Nagase T, Takaya Y, Yamasaki T et al (2021) Subseafloor sulphide deposit formed by pumice replacement mineralisation. Scientific Reports 11:8809. doi: 10.1038/s41598-021-87050-z.

Oliveira JT (1990) South Portuguese Sone: introduciton. Stratigraphy and synsedimentary tectonism. In: Dallmeyer RD, Martínez García E (Eds.) PreMesozoic Geology of Iberia. Springer Verlag: 333-347.

Polo M (2022) Cartografía y evolución mineralógica de la alteración hidrotermal en la mina San Miguel (Faja Pirítica Ibérica). Universidad de Madrid.

Pinedo-Vara I (1963) Piritas de Huelva. Su historia, minería y aprovechamiento. Summa Editorial, Madrid, 1003 pp.

Rosa CJP (2007) Facies Architecture of the Volcanic Sedimentary Complex of the Iberian Pyrite Belt, Portugal and Spain. Ph.D. thesis. University of Tasmania: 357.

Routhier P, Aye F, Boyer C, Lecolle M et al (1980) Le ceinture sud-iberique aamas sulfures dans sa partie espagnole mediane. Memoire BRGM 94, 265 pp.

Sánchez España FJ (2000) Mineralogía y geoquímica de los yacimientos de sulfuros masivos en el área Nor- Oriental de la Faja Pirítica Ibérica, San Telmo-San Miguel-Peña del Hierro), Norte de Huelva, España. Unpublished Doctoral Thesis, Universidad del País Vasco: 307.

Schermerhorn LJG (1975) Spilites, regional metamorphism and subduction in the Iberian Pyrite Belt., somecomments, Geologie en Mijnbouw 54: 23-35.

Schutz W, Ebneth J, Meyer KD (1987) Trondhjemites, tonalites and diorites in the South Portuguese Zone and their relations to the vulcanites and mineral deposits of the Iberian Pyrite Belt. Geologische Rundschau 76: 201-212.

Soriano D, Martí J (1999) Facies analysis of volcano-sedimentary successions hosting massive sulfide deposits in the Iberian Pyrite Belt, Spain. Econ. Geol. 94, 867–882.

Thieblemont D, Pascual E, Stein G (1998) Magmatism in the Iberian Pyrite Belt: petrological constraints on a metallogenic model. Miner Deposita 33: 98-110.

Tornos F (2006) Environment of formation and styles of volcanogenic massive sulfides: The Iberian Pyrite Belt. Ore Geol Rev 28: 259–307.

Tornos F, Conde C (2023) A new vision of the geodynamic evolution of the Iberia Pyrite Belt: VHMS in a intra-arc basin. 17th SGA Biennial Meeting “Mineral Resources in a Changing World. (Under submission)

Tornos F, Peter JM, Allen RL, Conde C (2015) Controls on the siting and style of volcanogenic massive sulphide deposits Ore Geol Rev 68: 142-163.

Velasco F, Herrero JM, et al (2013) Supergene features and evolution of gossans capping massive sulphide deposits in the Iberian Pyrite Belt. Ore Geol Rev 53: 181-203.

Valenzuela A, Donaire T, Pin C et al (2011) Geochemistry and U-Pb dating of felsic volcanic rocks in the Riotinto-Nerva unit, Iberian Pyrite Belt, Spain: crustal thinning, progressive crustal melting and massive sulphide genesis. J Geol Society 168: 717-731.

VMS mineralization, recent developments, and the big remaining questions

Y. Michelle DeWolfe[1]
[1]*Mount Royal University*

Abstract. Volcanogenic massive sulfide (VMS) deposits are an important source for base and precious metals globally (Lydon, 1984; Ohmoto, 1996; Franklin et al., 2005; Hannington, 2014). Although Phanerozoic rocks contain 72% of the world's VMS tonnage, the Proterozoic accounts for ~20% of global VMS tonnage, and the Archean Eon, 8% (Mercier-Langevin, 2014). Though ore-forming processes and environments of VMS deposits are generally well understood (Allen et al., 2002, 2011; Franklin et al., 2005; Galley et al., 2007) new advances in our understanding of VMS systems continue to be made. Discovering these typically small but high-grade deposits remains a significant challenge, especially in strongly deformed and metamorphosed rocks that characterize many Precambrian volcanic belts, and understanding metal endowment variations in particular (e.g., Archean deposits tend to have higher metal endowment) remains largely elusive.

Comparative studies with modern seafloor massive sulfide (SMS) deposits, have been crucial in attempting to answer questions that remain regarding VMS deposits. This talk will explore our current understanding of VMS deposits, and how integrated research, including comparisons with SMS, field, microanalytical, geochemical and geochronological studies are facilitating, and will continue to facilitate, advances in our understanding of metal endowment, setting, genesis of, and exploration for, VMS deposits.

Acknowledgements

I would like to acknowledge particular collaborators over the years and all-out rock stars in the field of VMS research and exploration who have had significant impact on my work and the work presented herein – H. Gibson, S. Piercey, M. Hannington, P. Mercier-Langevin A. Bailes, A. Galley, R. Allen and J. Franklin.

References

Allen RL, Weihed P, and the global VMS research project team (2002) Global comparison of volcanic-associated massive sulphide districts: Geological Society of London, London, Special Publication 204, 13−37.

Allen RL, Tornos F, Peter JM (2011) A thematic issue on the geological setting and genesis of volcanogenic massive sulfide (VMS) deposits. Mineralium Deposita 46, 429−430.Allen et al., 2002, 2011

Franklin JM, Gibson HL, Jonasson IR, Galley AG (2005) Volcanogenic Massive Sulfide Deposits. In: Hedenquist, J.W., Thompson, J.F.H., Goldfarb, R.J., and Richards J.P. (Eds.) Econ. Geol. 100th Anniversary Volume, 523–560.

Galley AG, Hannington MD, Jonasson I (2007) Volcanogenic massive sulphide deposits: Geological Association of Canada, Mineral Deposits Division, Special Publication 5, 141−161.

Hannington MD (2014) Volcanogenic massive sulfide deposits. Treatise on Geochemistry (Second Edition). 13: 463–488.

Lydon JW (1984) Ore deposits models: Volcanogenic massive sulfide deposits. Part 1: A descriptive model: Geoscience Canada 11, 195–202.

Mercier-Langevin P, Gibson HL, Hannington MD, Gouthier J, Monecke T, Dube B, Houlé M (2014) A Special Issue on Archean Magmatism, Volcanism, and Ore Deposits: Part 2. Volcanogenic Massive Sulfide Deposits. Econ. Geol. 109, 1–9.

Ohmoto H (1996) Formation of volcanogenic massive sulfide deposits: The Kuroko perspective: Ore Geol. Reviews10, 135-177.

Constraints on magma evolution at the epithermally mineralized Conical Seamount, Papua New Guinea

Louis-Maxime Gautreau[1], Philipp A. Brandl[1], Thor Hansteen[1], Maxim Portnyagin[1]
[1]GEOMAR Helmholtz Centre for Ocean Research Kiel, Germany

Abstract. The Tabar-Lihir-Tanga-Feni island chain in northeastern Papua New Guinea is host to highly alkaline magmatism and Au-rich porphyry-epithermal systems. Two examples are the Ladolam deposit on Lihir island that is the world's largest alkalic epithermal Au deposit and Conical Seamount, south of Lihir, which is the site where epithermal-style mineralization was first discovered at the modern seafloor. It has been interpreted as a juvenile analogue of the onland deposit. Previous studies focused on the mineralization process itself, but the origin and evolution of the host magmas and their contribution to the metal enrichment remain so far poorly constrained. Here we characterize the magmatic system underneath Conical Seamount and explain how the melt contributes to the gold endowment. We present new petrographic and geochemical analyses of whole rock samples, minerals and glass inclusions. The glass inclusions offer a new perspective on magma evolution at Conical Seamount. The melt within the magma chamber beneath the volcano is of tephri-phonolitic composition. Periodic replenishment includes pulses of compositionally diverse melts. The magma at Conical Seamount seems to possess a very specific ore potential, directly linked to its high alkaline content and redox evolution, which involves degassing processes influencing sulfur speciation.

1 Introduction

The Tabar-Lihir-Tanga-Feni island chain (TLTF) formed independent of the arc volcanism related to active subduction at the New Britain Trench. Its magma ascended through crust that occupied a forearc location at the time of active subduction along the Manus-Kilinailau Trench. More than half of the gold deposits within the Melanesian Arc are found in the TLTF island chain. Two deposits (Ladolam, Simberi) are actively exploited but at least six further prospects indicate the high Au potential of the region (Brandl et al. 2020).

One of them is located at Conical Seamount, a submarine volcano south of Lihir, which is also the first site where an epithermal-style mineralization was discovered at the seafloor (Petersen et al. 2002). It has been interpreted as a potential juvenile analogue of the world-class Ladolam deposit on Lihir island (Müller et al. 2003).

While many submarine volcanoes are present around Lihir (Figure 1), only Conical Seamount is found to host a significant gold mineralization. Our study thus aims to investigate the specific magmatic and epithermal conditions at Conical that promoted such a mineralization.

2 Methods

Several cruises with the German research vessel SONNE have investigated and recovered samples in the surroundings of Lihir: SO-94 in 1994, SO-133 in 1998 and SO-166 in 2002. Other expeditions like the Australian SHAARC in 2000 also recovered samples from the area.

Figure 1. Map of Lihir with location of the Ladolam deposit on the main island and of the surrounding seamounts.

We chose 24 representative samples for thin sections and further petrographic, mineralogical and geochemical studies. We also used polished mineral separates for the analysis of glass inclusions from eight representative rock samples.

Electron microprobe analysis was performed on the JEOL JXA-8200 at GEOMAR, Kiel, in wavelength dispersive (WDS) mode. The instrument was operated with 15 kV acceleration voltage and a focused beam (~1 µm diameter for plagioclase, pyroxene, sulfide and magnetite, 3 µm for mica and amphibole). The beam current was set to 10 nA for amphibole and mica, to 20 nA for plagioclase as well as pyroxene and to 50 nA for sulfide and magnetite. In the same thin sections, the composition of glass (formerly melt) inclusions in pyroxenes was analyzed using the same instrument. The beam current was set to 10 nA and the diameter to 5 µm.

The volatile content (H_2O, F, Cl, S, CO_2) of glass inclusions in clinopyroxene crystals embedded in indium mounts was analyzed using Secondary Ion Mass Spectrometry (SIMS) at the SwissSIMS in Lausanne. The machine was set to point analyses mode to determine the element concentration in

local spots. A primary Cs^+. source was used to generate secondary negative ions. Several elements could be measured at the same time in multicollection mode. The secondary ions measured were $^{12}C^-$, $^{16}O^1H^-$, $^{19}F^-$, $^{32}S^-$ and $^{35}Cl^-$ with $^{30}Si^-$ as reference.

The FeTiMM-oxybarometer (Arató and Audétat 2017) was used to calculate the oxygen fugacity. As the method involves the compositions of magnetite and melt (glass) in equilibrium, the composition of magnetite in contact with glass, all included in clinopyroxene crystals, was used.

3 Petrographic and geochemical overview

The rocks from Conical Seamount all possess a characteristic grey to dark grey color with a clinopyroxene-phyric texture. Clinopyroxene comprises 10-30 % of the total rock volume. Individual crystals have sizes ranging from 100 µm to several millimeters at Conical Seamount. Most of the clinopyroxene crystals at Conical Seamount contain distinct cores and show repeated growth zonation and/or sector zonation.

Other main mineral phases are plagioclase (5-15 %, 100-500 µm in size), magnetite (up to 5 %, 20-200 µm in size), and subordinate olivine (<1 %, approximately 50 µm in size) and sulfide (much less than 1 %).

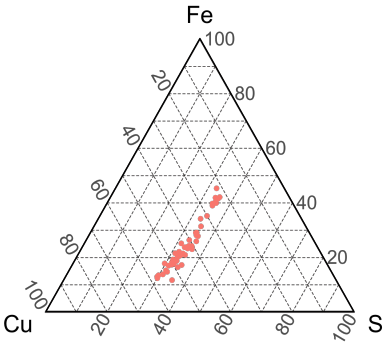

Figure 2. Composition of magmatic sulfides from Conical Seamount in the Fe-S-Cu ternary.

The Mg-number of clinopyroxene (Mg# = Mg / (Mg + Fe) x 100) ranges between 74 and 78 and generally decrease from the core to the rim of the minerals. However, this trend is periodically interrupted by several compositional bands of Mg# above 80.

Glass inclusions are frequently present in clinopyroxene. Most of them have an irregular shape and are typically distributed across one zone of the mineral in a grid-like pattern.

Magmatic sulfide occurs in almost every sample from Conical Seamount. Sulfide blebs are associated with magnetite, possess a subrounded shape and range in sizes between 10 and 50 µm) or occur isolated in the groundmass with a spherical, droplet shape (sizes of 10-20 µm). They correspond to intermediate solid solution-type sulfides with compositions ranging from the stochiometric composition of chalcopyrite to cubanite (Figure 2).

At Conical Seamount, glomerophyric mineral aggregates including clinopyroxene crystals are very common and present in all samples. Some consist of just two intergrown pyroxene crystals, others appear as bigger, flower-like intergrowths, where three to six pyroxene crystals, have grown in several directions from a central core that itself consists of one or several small pyroxene grains (Figure 3).

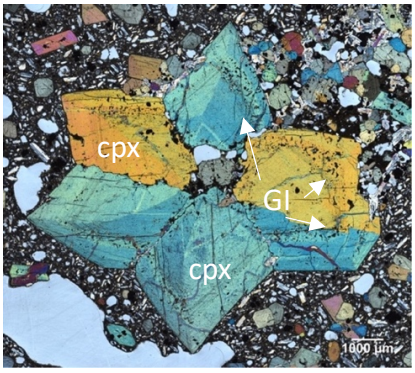

Figure 3. Flower-like glomerocrysts at Conical Seamount (sample 42RD10-22). Glass inclusions (GI) enriched zones occur within the clinopyroxenes (cpx).

The whole rock samples have a trachybasaltic composition. However, the glass (groundmass and inclusions) plots within the tephriphonolitic field in the TAS diagram.

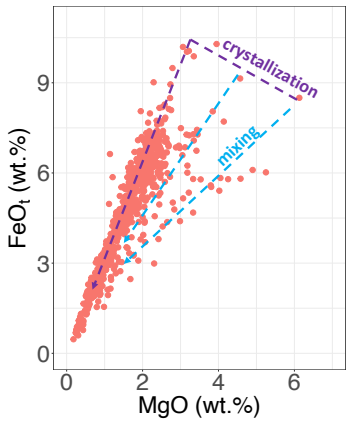

Figure 4. FeO_t vs MgO of melt inclusions data. Inferred crystallization (purple) and magma mixing (blue) trends and clusters are highlighted.

Several compositional trends are recorded in the glass inclusion data from Conical Seamount. The MgO contents decrease linearly with increasing SiO_2, Na_2O, K_2O and Al_2O_3 and FeO_t, CaO and TiO_2 are positively corelated with MgO. At higher MgO values (>3.8 wt. %), the glass inclusions show significant difference in FeO_t contents (Figure 4). For a MgO content of 4 wt. %, one glass inclusion has an FeO_t content at around 5.9 wt. %, one at 7.5 wt. % and the third one at 10.0 wt. %. The major element data systematically show a wide compositional

range at any given MgO content. Fractional crystallization alone cannot explain these observations.

The CO_2 contents of the glass inclusions is systematically below 400 ppm, whereas the H_2O contents vary between 0.2 and 4.5 wt.%. The concentration of sulfur is up to 3600 ppm, 6800 ppm for chlorine as well as 2500 ppm for fluorine in the glass inclusions.

4 The magma chamber at Conical Seamount

The comparatively high abundance of clinopyroxene megacrysts, partly showing repeated zonation patterns, is consistent with extensive crystal growth in a convecting magma chamber underlying Conical Seamount. The frequent occurrence of glomerophyric mineral textures further indicates an efficient circulation/convection of magmas within the magma chamber, leading to mineral accumulation (Vance 1969).

The observed grid-like distribution of glass inclusions is interpreted to be the result of repeated growth and resorption periods for clinopyroxene (Dungan and Rhodes 1978), that reflect periodic disequilibrium between crystals and the surrounding melt. This disequilibrium may be the consequence of a rapid change in the local melt composition compared to the parental melt in which the crystal grew originally. Additionally, the peaks in Mg-number (>80) within the pyroxene profiles highlight several events in which the crystals continued to grow in a temporarily more primitive melt environment.

These observations as well as repetitive zonation patterns in pyroxene phenocrysts indicate convection in a heterogeneous magma chamber (with at least two different melts) and several magma recharging events.

While the trachybasaltic nature of the whole rocks has been reported in previous studies (Stracke and Hegner 1998; Müller et al. 2003), our new glass inclusion analyses indicate a tephriphonolitic melt composition. This is consistent with groundmass glass compositions and confirms a dominantly tephriphonolitic melt composition in the magma chamber.

The broad range in the glass inclusion chemical compositions from Conical Seamount and especially their distinct variations of FeO contents at high MgO, indicate a diversity of melts present in the magma chamber. Therefore, we assume different magmatic sources prior to pooling and mixing in a shallow magma chamber.

The flower-like intergrowths of glomerocrysts as well as normally zoned core compositions are consistent with early crystal growth prior to storage in a magma chamber, where radial growth dominates over nucleation. The negative Al_2O_3 and positive CaO correlation with MgO within the glass and the whole rock samples point towards clinopyroxene as the dominant fractionating phase. This is consistent with petrographic observations and confirms previous studies (e.g., Müller et al. 2003).

Involving a pressure between 1.4 and 2.1 kbar (calculated after Papale et al. 2006), the H_2O and CO_2 contents confirm the shallow crustal level (approximately 4-6 km depth) of the magma chamber as suggested previously (Müller et al. 2003; Kamenov et al. 2005).

5 The melt fertility

At Conical Seamount, the absence of a volatile-bearing magmatic mineral phase such as amphibole or phlogopite, promotes the progressive enrichment of volatiles during fractional crystallization. Thus, early pyroxene fractionation increased the alkalinity of the melt, and also the volatile contents in the magma increased. Such high volatile contents allow for an optimal solubility of Au within the melt (Zajacz et al. 2012) and a high potential to exsolve a fluid phase with a high metal carrying capability (Hogg et al. 2023).

Lead (Kamenov et al. 2005) as well as sulfur (Gemmell et al. 2004) isotopic measurements indicate a significant magmatic volatile contribution in the hydrothermal ore forming process at Conical Seamount.

At Conical Seamount, the calculated values for the oxidation state of the melt (Figure 5) range between 0.6 and 3.3 log units above FMQ. These conditions correspond to the conditions of coexistence of reduced S^{2-} and oxidized S^{6+} sulfur species, (at fO_2 between 0 and 2 log units above the FMQ buffer (Jugo et al. 2010)) and existence of S^{6+} only at higher fO_2. This also overlaps with the range of high Au solubility in the melt (at fO_2 between 0.5 and 1.5 log units above FMQ (Zajacz et al. 2012)).

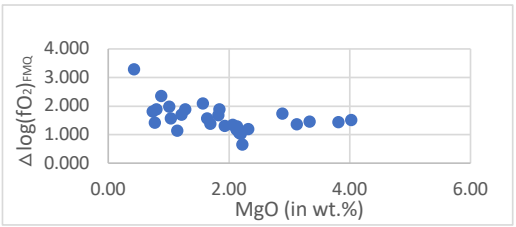

Figure 5. Melt oxidation state ($\Delta\log(fO_2)_{FMQ}$) calculated from magnetite-glass inclusion pairs following the method of Arató and Audétat (2017).

However, it is important to note that our constrains on melt oxidation state is limited to low MgO values (<4.5 wt.%), where magnetite is crystallizing. Magnetite crystallization consumes iron from the residual melt. This may reduce the sulfur solubility and trigger sulfide saturation (Brandl et al. 2022) and consequently the sequestration of chalcophile elements (Au, Cu, Ag) (e.g., Jenner et al. 2010). The common association of magnetite and

sulfide confirms the strong link between crystallization of the two mineral phases.

Our combined observations are consistent with an efficiently convecting magma chamber being present at shallow crustal levels underneath Conical Seamount that underwent several cycles of replenishment. We assume that the recharging magma and the chemical buffering through fractional crystallization in the chamber is maintaining the oxidation state in the range where the reduced and oxidized sulfur species coexist.

When the melt reaches the magma chamber, the subsequent fractional crystallization and the low pressure are likely to trigger fluid oversaturation. This exsolution of a magmatic volatile phase leads to the formation of a metal-bearing fluid. The remaining metals staying in the melt are sequestrated in immiscible sulfides, as the oxygen fugacity stays below FMQ+2.

The sulphide phase, associated to vapor bubbles, may be transported to the top of the magma chamber as compound drops. The metals would progressively, but almost completely, move from the sulphide melt to the vapor (Mungall et al. 2015) and thus contribute to the metal enrichment of the following exsolving fluid. The cyclic magmatic replenishment resupplies the magma chamber in metals and leads thus to the optimal and repeated formation of metal enriched fluids from the magma chamber at shallow level.

The most evolved melt, with low MgO values, seems to erupt from the magma chamber with a very high fO_2 (up to above FMQ+3), thus in less favorable sulfide precipitation conditions and consequently has a very highly chalcophile element carrying capability. At the same time, we assume that rising melt leaving the magma chamber entrains already precipitated sulfides on the way to the surface.

6 Conclusion

Here we demonstrate that the range of melts related to epithermal-style mineralization at Conical Seamount has tephriphonolitic composition. This contrasts with previous studies that solely used whole rock samples with variable contents of mafic minerals and thus assumed a trachybasaltic melt composition.

We show that clinopyroxene crystallization exerts an important control on melt composition. The alkalinity of the melt is rising, the mineral phases concentrate compatible elements and avoids the sequestration of volatiles in a crystal phase.

We provide evidence for the existence of shallow crustal magma reservoir that is undergoing continuous convection, fractional crystallization, frequent magma replenishment and continuous degassing.

Sulfide precipitation associated with fluid exsolution are optimal conditions for the metal transfer from the melt to the hydrothermal system.

Acknowledgements

A special thank is given to Sven Petersen and Colin Devey for their valued advice and support as well as to the SwissSIMS team in Lausanne and Mario Thöner for their valuable help during SIMS and electron microprobe analyses respectively. This study is funded by the German Research Foundation (DFG) through grant BR 5297/4-1.

References

Arató R, Audétat A (2017) FeTiMM - A new oxybarometer for mafic to felsic magmas. Geochemical Perspect Lett 5:19–23. https://doi.org/10.7185/geochemlet.1740

Brandl PA, Hannington MD, Geersen J, et al (2020) The submarine tectono-magmatic framework of Cu-Au endowment in the Tabar-to-Feni island chain, PNG. Ore Geol Rev 121:103491. https://doi.org/10.1016/j.oregeorev.2020.103491

Brandl PA, Portnyagin M, Zeppenfeld H, et al (2022) The Origin of Magmas and Metals at the Submarine Brothers Volcano, Kermadec Arc, New Zealand. Econ Geol 1–28. https://doi.org/10.5382/econgeo.4973

Dungan MA, Rhodes JM (1978) Residual glasses and melt inclusions in basalts from DSDP Legs 45 and 46: Evidence for magma mixing. Contrib to Mineral Petrol 67:417–431. https://doi.org/10.1007/BF00383301

Gemmell JB, Sharpe R, Jonasson IR, Herzig PM (2004) Sulfur Isotope Evidence for Magmatic Contributions to Submarine and Subaerial Gold Mineralization : Conical Seamount and the Ladolam Gold Deposit , Papua New Guinea. Econ Geol 99:1711–1725

Hogg OR, Edmonds M, Blundy J (2023) Water-rich magmas optimise volcanic chalcophile element outgassing fluxes. Earth Planet Sci Lett 611:118153. https://doi.org/10.1016/j.epsl.2023.118153

Jenner FE, O'Neill HSC, Arculus RJ, Mavrogenes JA (2010) The magnetite crisis in the evolution of arc-related magmas and the initial concentration of Au, Ag and Cu. J Petrol 51:2445–2464. https://doi.org/10.1093/petrology/egq063

Jugo PJ, Wilke M, Botcharnikov RE (2010) Sulfur K-edge XANES analysis of natural and synthetic basaltic glasses: Implications for S speciation and S content as function of oxygen fugacity. Geochim Cosmochim Acta 74:5926–5938. https://doi.org/10.1016/j.gca.2010.07.022

Kamenov GD, Perfit MR, Jonasson IR, Mueller PA (2005) High-precision Pb isotope measurements reveal magma recharge as a mechanism for ore deposit formation: Examples from Lihir Island and Conical seamount, Papua New Guinea. Chem Geol 219:131–148. https://doi.org/10.1016/j.chemgeo.2005.02.013

Müller D, Franz L, Petersen S, et al (2003) Comparison between magmatic activity and gold mineralization at Conical Seamount and Lihir Island, Papua New Guinea. Mineral Petrol 79:259–283. https://doi.org/10.1007/s00710-003-0007-3

Mungall JE, Brenan JM, Godel B, et al (2015) Transport of metals and sulphur in magmas by flotation of sulphide melt on vapour bubbles. Nat Geosci 8:216–219. https://doi.org/10.1038/ngeo2373

Papale P, Moretti R, Barbato D (2006) The compositional dependence of the saturation surface of H 2O + CO 2 fluids in silicate melts. Chem Geol 229:78–95. https://doi.org/10.1016/j.chemgeo.2006.01.013

Petersen S, Herzig PM, Hannington MD, Jonasson IR (2002) Submarine Gold Mineralization Near Lihir Island , New Ireland Fore-Arc , Papua New Guinea. 97:1795–1813

Stracke A, Hegner E (1998) Rifting-related volcanism in an oceanic post-collisional setting: The Tabar-Lihir-Tanga-Feni (TLTF) island chain, Papua New Guinea. Lithos 45:545–560. https://doi.org/10.1016/S0024-4937(98)00049-8

Vance JA (1969) On synneusis. Contrib to Mineral Petrol 24:7–29. https://doi.org/10.1007/BF00398750

Zajacz Z, Candela PA, Piccoli PM, et al (2012) Gold and copper in volatile saturated mafic to intermediate magmas: Solubilities, partitioning, and implications for ore deposit formation. Geochim Cosmochim Acta 91:140–159. https://doi.org/10.1016/j.gca.2012.05.033

SEDEX deposits in the Graz Paleozoic, Eastern Alps, Austria

Annika Geringer[1], Sandro Rohrhofer[2], Frank Melcher[2], Christian Benold[1], Heinz Reitner[1], Ralf Schuster[1]
[1]GeoSphere Austria, Vienna, Austria
[2]Montanuniversität Leoben, Leoben, Austria

Abstract. The Pb-, Zn-, barite- and Ag-bearing SEDEX deposits in the Graz Paleozoic (Eastern Alps, Austria) are hosted by polyphase deformed, greenschist facies metasediments and metavolcanics of upper Silurian to Lower Devonian stratigraphic age. The stratiform mineralization is characterized by pyrite, pyrrhotite, galena and sphalerite as the predominant sulphide phases, accompanied by chalcopyrite, arsenopyrite, freibergite, marcasite, pyrargyrite, tetradymite, cobaltite, ullmannite, breithauptite and others. Whole rock major and trace element data show metal enrichment in the adjacent host rocks. A detailed local geochemical survey to identify anomalies in stream sediments, in stream waters and headwaters reveals coincidence with former surveys, but also identified additional anomalies with elevated contents of Pb, Zn and Ba and in traces of Cu, Ni, As and Cd, which can be interpreted as indications of former unknown occurrences.

1 Introduction

In the Graz Paleozoic (Drauzug-Gurktal nappe system, Eastern Alps) in Austria sedimentary exhalative (=SEDEX) deposits are known within an area of about 35 x 20 km. They constitute the metallogenetic district "Lead-zinc-barite district Graz Paleozoic – Schönberg Formation (Arzberg)" and form the most important ore district of non-ferrous metals in Paleozoic units of the Eastern Alps. These deposits are stratiform and occur exclusively in the Schönberg Formation (Weber 1990). They carry raw materials that have been important for basic supply for a long time (Pb, Zn and Ag), as well as raw materials (barite, Co, In, Sb) that have been put on the list of critical raw materials by the European Commission (European Commission 2020). Many of these deposits have been sites of mining for Ag, Pb and Zn for about 680 documented years. After several closures and restarts, mining was terminated in 1927. Since then, there has been repeated research work as well as an exploration phase with drilling activity in the 1970s to 1980s (Weber 1990).

2 Geological Overview

The Graz Paleozoic nappe stack consists of low- to medium-grade metamorphic Paleozoic (meta)sediments and metavolcanics (Flügel and Neubauer 1984). It is part of the Drauzug-Gurktal nappe system of the Austroalpine Unit and is located in the eastern part of the Eastern Alps (Figure 1). Covering an area of about 30 x 50 km, the thickness of the Graz Paleozoic is expected to be only about 1.5 km (Gasser et al. 2010). It is surrounded and underlain by epidote-amphibolite facies to eclogite facies metamorphic units of the Koralpe-Wölz nappe system, some of which are referred to by local names such as Anger crystalline or Radegund crystalline (Krenn et al. 2008). The western part of the nappe stack is locally overlain by Upper Cretaceous sediments of the Gosau Group (Kainach-Subgroup). Neogene sediments of the Styrian and Passail basins cover along the southern margin and close to Arzberg respectively (Fritz et al. 1992).

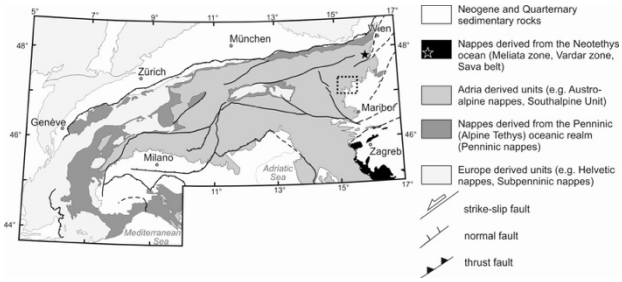

Figure 1. Overview map of the Alps showing the paleogeographic origin of the main tectonic units after Schmid et al. (2004). The dotted square indicates the Graz Paleozoic.

There are two concepts for the internal tectonic subdivision of the Graz Paleozoic: Fritz et al. (1992) divide the nappe stack into a lower, middle and upper nappe group, with the Rannach nappe and Hochlantsch nappe in the upper, the Laufnitzdorf nappe and Gschwendt (Kalkschiefer) nappe in the middle and the Schöckel nappe in the lower nappe group. In the concept of Gasser et al. (2010) only a lower and upper nappe system separated by the Rannach Thrust are subdivided, whereby the upper nappe system includes the Rannach nappe and Hochlantsch nappe. According to recent work the lower nappe group is formed by the Gschnaidt nappe, Schöckel nappe and Gasen nappe (Schuster et al. 2016) (Figure 2).

The lithostratigraphic subdivision of the Graz Paleozoic comprises five different sedimentological facies units termed the Laufnitzdorf, Kalkschiefer, Schöckel, Rannach and Hochlantsch facies (Gasser et al. 2010). However, these facies units

are not identical with the tectonic units and therefore overlap. The successions start with lower Silurian to Lower Devonian volcanoclastics and siliciclastics, followed by Middle Devonian carbonate platform sediments. The end is defined by pelagic limestones

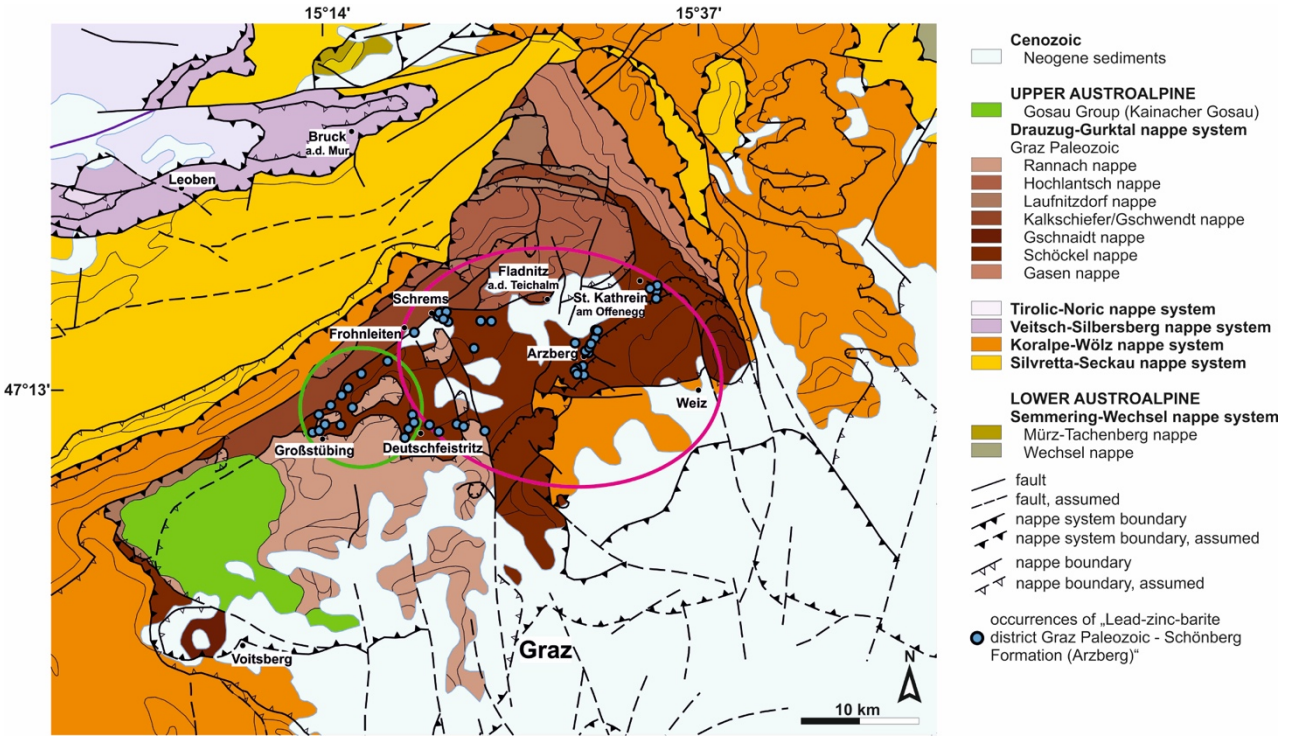

Figure 2. Tectonic map of the Graz Paleozoic in the Austroalpine with the occurrences of the investigated metallogenic district “Lead-zinc-barite district Graz Paleozoic – Schönberg Formation (Arzberg)”. Green circle indicates the western part and pink circle indicates the eastern part of the ore district. Map according to ADB 500 of GeoSphere Austria 1.3.2023.

and slates of Upper Devonian to lower Carboniferous age (Flügel and Neubauer 1984; Fritz and Neubauer 1988; Flügel and Hubmann 2000; Gasser et al. 2010; Schantl et al. 2015). Thirty-five formations belonging to the above-mentioned sedimentological facies units are described by Flügel and Hubmann (2000).

According to the concept of Gasser et al. (2010) the nappe pile below the Rannach Thrust is characterised by a penetrative schistosity, isoclinal folds and an E-W trending stretching lineation. In the thrust zone the deformation is dominated by a stretching lineation that progressively turns from E-W to SE-NW. Krenn et al. (2008) describe open folds with NE-SW trending fold axes throughout the whole nappe pile. The Graz Paleozoic is crosscut by several brittle strike slip faults and a normal fault between the lower nappe group and the Rannach nappe, which creates a potential metamorphic break (Neubauer 1989). The borders of the nappe stack constitute a normal fault in the southwest and northeast, a transtensional strike slip fault in the northwest and a system of strike slip, normal and thrust faults in the south (Fritz et al. 1992; Neubauer et al 1995; Krenn et al. 2008).

Metamorphic conditions range from sub-greenschist to lower-most greenschist facies conditions in the middle and upper nappe group (Hasenhüttl 1994; Russegger 1996; Rantitsch et al. 2005, Krenn et al. 2008). Interestingly there is an inverted metamorphic gradient within the lower nappe group, with garnet bearing assemblages appearing in the uppermost Gschnaidt nappe. The garnet shows a polyphase growth and eoalpine temperatures for the Glöselhof Lithodeme

(Gschnaidt nappe), calculated with the garnet-chlorite and garnet-amphibole thermometer, range between 510-530°C for an assumed pressure of 0.8 GPa (Schantl et al. 2015).

The age of metamorphism and deformation within the Graz Paleozoic is the basis of a long discussion. Different models ascribe the main imprint either to the Variscan or the Eoalpine (Cretaceous) tectonometamorphic events (Frank 1981; Flügel et al. 1980; Fritz 1988; Hasenhüttl 1994; Russegger 1996; Neubauer et al. 1999; Krenn et al. 2008; Gasser et al. 2010). According to the occurrence of polyphase garnet, a pre-Alpine (Variscan or Permian) metamorphic imprint is proven at least for some parts of the Graz Paleozoic (Schantl et al. 2015). However, the major metamorphic and structural overprint occurred during the Eoalpine event in the Early Cretaceous at about 125 Ma (Fritz et al. 1992; Schuster et al. 2016).

3 SEDEX mineralization

There are two (eastern part) to three (western part) sulphide- and/or barite-dominated ore horizons („Lager“) developed (Table 1) (Weber 1990; Feichter 2005). Pyrite, pyrrhotite, galena and sphalerite are

the predominant sulphide phases, accompanied by chalcopyrite, arsenopyrite, freibergite, marcasite, pyrargyrite, tetradymite, cobaltite, ullmannite, breithauptite and others. At the type locality Arzberg (Figure 3, Figure 4), Au-Ag-Hg alloys (66-84% Ag) have also been described (Feichter and Mogessie 2003). Host rocks are polyphase deformed, greenschist facies metasediments (often black shale and carbonates) and metavolcanics (greenschist) of the Schönberg Formation (Flügel and Hubmann 2000), which are placed in the upper Silurian to Lower Devonian (Weber 1990; Gasser et al. 2010). A genetic model of sedimentary massive sulphides deposited in channel-like structures on the seafloor is widely accepted, similar to the SEDEX deposits at Rammelsberg and Meggen, Germany.

Table 1. Ore mineralization of the western and eastern part of the ore district (Weber 1990).

	Western part	Eastern part
Lower horizon "Liegendlager"	Barite, (galena), pyrite	Galena, sphalerite, fahlore
Middle horizon "Mittellager"	Galena, sphalerite, some barite, pyrite	-
Upper horizon "Hangendlager"	Galena, sphalerite, pyrite	Barite, galena, little sphalerite

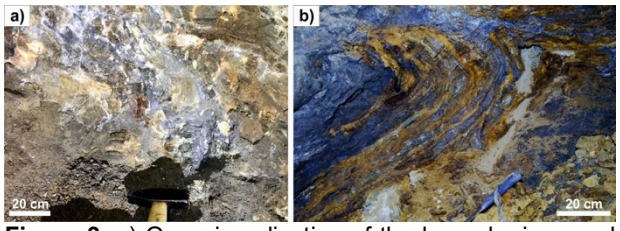

Figure 3. a) Ore mineralization of the lower horizon and b) folded ore mineralization of the upper horizon in the eastern part of the ore district (type locality Arzberg).

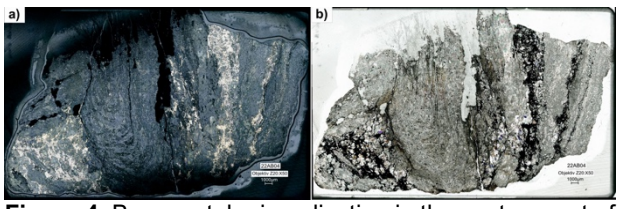

Figure 4. Base metal-mineralization in the eastern part of the ore district (type locality Arzberg). a) Reflected light, plane polarizers and b) transmitted light, plane polarizers. The scale bar represents 1000 µm.

In the inactive Arzberg mine, mineralization styles comprise Pb-Ag and Fe-Cu assemblages. The latter consists of major pyrrhotite, pyrite and chalcopyrite, with minor sphalerite, galena and cobaltite hosted by greenschist (Figure 4). The sulphide phases are accompanied by siderite and dolomite-ankerite as gangue minerals. Fluorapatite and monazite are connected to the ore forming processes. The sedimentary structures are partially preserved and in mica-rich areas the ore is strongly deformed.

LA-ICP-MS trace element data of Fe-Cu and Zn sulphides from the Graz Paleozoic reveal a high variability between single deposits (Onuk 2018): median Fe concentrations in sphalerite from different former mining areas range from 0.6 to 7.3 wt.%; concentrations of Mn, Co, Ga, Ag, Cd, In and Sb vary significantly, with slight In enrichment in some of the ancient mines. Sphalerites from Arzberg appear to be most enriched in Ag, those from Haufenreith carry highest In concentrations, and those from Deutschfeistritz (Elisabethbau, Friedrichbau, Ottilienstollen) are highest in Sb and Ga. Pyrite in the ores is generally enriched in Co over Ni (md Co/Ni = 1.28) and has low to moderate, but variable As contents (median 176 ppm). Chalcopyrite carries Ag, In and Sn.

First results from whole rock geochemistry by fusion ISP-OES/ICP-MS show that in the host rocks adjacent to the ore, Pb reaches up to >1 wt.%, Zn up to 2940 ppm, Ba up to 11750 ppm and Ag up to 19 ppm. The ore is characterized by Pb and Zn over 1 wt.%, Ba up to 4871 ppm and Ag exceeding 100 ppm. Sb (up to >200 ppm) and Cu contents (up to 190 ppm) in the ore are moderate and in the host rocks low to moderate (Sb up to 38 ppm, Cu up to 100 ppm). In the ore, As and Ni are below detection limit (As 5 ppm, Ni 20 ppm), but up to 140 ppm As and up to 130 ppm Ni were detected in the host rocks. Co reaches 12 ppm, In 0.8 ppm and Ga 21 ppm in the ore, whereas Co is up to 327 ppm, In below detection limit (0.2 ppm) and Ga up to 36 ppm in the host rocks.

4 Geochemical anomalies in stream sediments and waters

In the surroundings of deposits in the western part of the ore district a detailed local geochemical survey was carried out to identify anomalies in stream sediments and in waters of streams and headwaters. The geochemical analyses (major and trace elements) of stream sediment were obtained using the RFA and of water samples using the IC (for anions) and ICP-MS. These analyses show strong dependencies to regional geological settings, i.e. regarding hydrochemical water types. Although a number of water samples are directly related to sites of historic mining of sulphide ores, no acid mine waters were observed. Because of the prevalent carbonate content in the surrounding lithological units the waters are buffered showing near neutral or weakly basic pH-values. Regarding metal contents our first results confirm the vast majority of characteristics already shown in a previous regional geochemical survey. Nevertheless, some additional anomalies of Pb, Zn and Ba and in traces Cu, Ni, As and Cd can be interpreted as indications of former unknown occurrences which will justify further investigation.

Acknowledgements

The authors are very grateful to Ing. Christian Auer, Univ.-Prof. Dr. Bernhard Grasemann, Ao.Univ.-Prof. Dr. Bernhard Hubmann, Priv.-Doz. Mag. Dr. Kurt Krenn, Dr. Duncan Large, Dr. Holger Paulick and Univ.-Prof. Dr. Leopold Weber for providing their great support and expertise. The Federal Ministry for Education, Science and Research of the Republic of Austria is thanked for funding the project by the “Initiative GBA-Forschungspartnerschaften Mineralrohstoffe – MRI”.

References

European Commission (2020) Study on the EU’s list of Critical Raw Materials – Final report. 158 pp.

Feichter MM and Mogessie A (2003) Die Sulfidmineralisation von Arzberg (Steiermark): Ergebnisse petrographischer, mineralchemischer und geochemischer Untersuchungen. Mitt. Österr. Mineral. Ges., 148, 133-135.

Feichter MM (2005) Die sedimentgebundene Pb-Zn-Ba-Lagerstätte Arzberg (Steiermark, Österreich): Mineralisation und Genese. Dissertation, Karl-Franzens-Universität Graz, 230 pp.

Flügel HW, Mauritsch H, Heinz H and Frank W (1980) Paläomagnetische und radiometrische Daten aus dem Grazer Paläozoikum. Mitteilungen der Österreichischen Geologischen Gesellschaft, 71/72, 201-211.

Flügel HW and Neubauer F (1984) Erläuterungen zur geologischen Karte der Steiermark. Verlag der Geologischen Bundesanstalt, Wien, 127 pp.

Flügel HW and Hubmann B (2000) Die lithostratigraphische Gliederung des Paläozoikums von Graz (Österreich). Österreichische Akademie der Wissenschaften/Schriftenreihe der Erdwissenschaftlichen Kommissionen, 13, 7-59.

Frank W (1981) Geochronologische Datierung frühalpiner Metamorphosevorgänge in den Ostalpen (Jahresbericht 1980 des Geochronologischen Labors). In: Die frühalpine Geschichte der Ostalpen Jahresbericht, Montanuniversität Leoben, 2, 9-43.

Fritz H (1988) Kinematics and geochronology of Early Cretaceous thrusting in the northwestern Paleozoic of Graz (Eastern Alps). Geodinamica Acta, 2, 53-62. http://dx.doi.org/10.1080/09853111.1988.11105156.

Fritz H and Neubauer F (1988) Geodynamic aspects of the Silurian and Early Devonian Sedimentation in the Paleozoic of Graz (Eastern Alps). Schweizer Mineralogische Petrographische Mitteilungen, 68, 359-367.

Fritz H, Ebner F and Neubauer F (1992) The Graz thrust complex (Paleozoic of Graz). In: ALCAPA field guide, Karl-Franzens-Universität Graz, 83-92.

Gasser D, Stüwe K and Fritz H (2010) Internal structural geometry of the Paleozoic of Graz. International Journal of Earth Sciences, 99, 1067-1081. http://dx.doi.org/10.1007/s00531-009-0446-0.

Hasenhüttl C (1994) Eine Wärmegeschichte des Grazer Berglandes. Inkohlung, Illitkristallinität, Tonmineralogie und Conodont Colour Alteration Index im nördlichen Teil des Grazer Deckenkomplex (Grazer Paläozoikum). Dissertation, Karl-Franzens-Universität Graz, 182 pp.

Krenn K, Fritz H, Mogessie A and Schaflechner J (2008) Late Cretaceous exhumation history of an extensional extruding wedge (Graz Paleozoic Nappe Complex, Austria). International Journal of Earth Sciences, 97, 1331-1352. http://dx.doi.org/10.1007/s00531-007-0221-z.

Neubauer F (1989) Lithostratigraphie und Strukturen an der Basis der Rannachdecke im zentralen Grazer Paläozoikum (Ostalpen). Jahrbuch der Geologischen Bundesanstalt, 132, 459-474.

Neubauer F, Dallmeyer RD, Dunkl I and Schirnik D (1995) Late Cretaceous exhumation of the metamorphic Gleinalm dome. Eastern Alps: kinematics, cooling history and sedimentary response in a sinistral wrench corridor. Tectonophysics, 242, 79-98. http://dx.doi.org/10.1016/0040-1951(94)00154-2.

Neubauer F, Hoinkes G, Sassi FP, Handler R, Höck V, Koller F and Frank W (1999) Pre-Alpine metamorphism in the Eastern Alps. Schweizer Mineralogische Petrographische Mitteilungen, 79, 41-62.

Onuk P (2018) High-tech metal potential of sphalerite from Eastern Alpine lead-zinc deposits and development of a matrix-matched sphalerite (ZnS) calibration material (MUL-ZnS-1) for calibration of in-situ trace element measurements by laser ablation inductively coupled plasma mass spectrometry (LA-ICP-MS). Dissertation, Montanuniversität Leoben, 196 pp.

Rantitsch G, Sachsenhofer R, Hasenhüttl C, Russegger B and Rainer T (2005) Thermal evolution of an extensional detachment as constrained by organic metamorphic data and thermal modelling: Graz Paleozoic Nappe Complex (Eastern Alps). Tectonophysics, 411, 57-72. http://dx.doi.org/10.1016/j.tecto.2005.08.022.

Russegger B (1996) Niedrigst- bis niedriggradige Metamorphose im südlichen Grazer Paläozoikum (Ostalpen). Jahrbuch der Geologischen Bundesanstalt, 139, 93-100.

Schantl P, Schuster R, Krenn K and Hoinkes G (2015) Polyphase metamorphism at the southeastern margin of the Graz Paleozoic and the underlying Austroalpine basement units. Austrian Journal of Earth Sciences, 108, 219-238.

Schmid SM, Fügenschuh B, Kissling E and Schuster R (2004) Tectonic map and overall architecture of the Alpine orogen. Eclogae Geologicae Helvetiae, 97, 93-117. http://dx.doi.org/10.1007/s00015-004-1113-x.

Schuster R, Schantl P and Nowotny A (2016) Tektonik, Metamorphose und Abkühlgeschichte des Grazer Paläozoikums auf Kartenblatt GK50 Blatt 135 Birkfeld. In: Arbeitstagung 2015 der Geologischen Bundesanstalt Geologie der Kartenblätter GK50 ÖK 103 Kindberg und ÖK 135 Birkfeld, Mitterdorf im Mürztal 21.-25. September 2015. Verlag der Geologischen Bundesanstalt, Wien, 71-87.

Weber L (1990) Die Blei-Zinkerzlagerstätten des Grazer Paläozoikums und ihr geologischer Rahmen. Archiv für Lagerstättenforschung der Geologischen Bundesanstalt, Wien, 12, 289 pp.

Textures of Cu-Fe sulphides in hydrothermal seafloor massive sulphide deposits: indications of a new metastable mineral phase $Cu_2Fe_3S_5$

Simon Goldmann[1], Sebastian Fuchs[1]
[1]Federal Institute for Geosciences and Natural Resources (BGR), Stilleweg 2, D-30655 Hannover, Germany

Abstract. Seafloor massive sulphide deposits are present globally along the spreading axis of mid ocean ridges, arc volcanoes and back-arc basins. The major ore minerals are sulphides, such as pyrite, marcasite, chalcopyrite, sphalerite, and galena that occur in various proportions, assemblages and textures. In Cu-rich ore samples from the ultramafic rock-hosted Kaimana vent field from the Central Indian Ridge, the peculiar texture of the Cu-Fe sulphide mineral association of isocubanite and non-stoichiometric chalcopyrite together with a yet unnamed Cu-Fe sulphide phase of intermediate composition of $Cu_2Fe_3S_5$ occurs. The latter mineral was previously described as "Y-Phase". In this study, the texture, mineralogical assemblage, and the chemical composition of the associated sulphides were investigated in detail using polarized reflected light microscopy and electron probe microanalysis. We present new data on mineral chemistry not only of $Cu_2Fe_3S_5$, but also of associated isocubanite and chalcopyrite.

1 Introduction and previous work

On behalf of the German Federal Government, the Federal Institute for Geosciences and Natural Resources (BGR) holds one exploration license from the International Seabed Authority (ISA) of the United Nations for massive sulphides in the Central Indian Ocean. The exploration program comprises the outline of potential ore deposits including resource assessment, but also baseline studies for the sustainable protection of the marine environment.

In comparison to the observations during this study, similar Cu-Fe sulphide assemblages and textures were previously reported from a number of seafloor massive sulphide occurrences (e.g., Mozgova et al. 2005; Bogdanov et al. 2008; Borodaev et al. 2010; Firstova et al. 2016) as well as from the metalliferous sediments of Atlantis II Deep in the Red Sea (e.g., Missack et al. 1989).

For the first time, Rambaldi et al. (1986) identified a sulphide mineral with the formula of $Cu_2Fe_3S_5$ from one inclusion within the Qingzhen (EH3) chondritic meteorite. Beside its occurrence in meteorites, this $Cu_2Fe_3S_5$ mineral (that received the generic name "Y-Phase") was only found within the mineral assemblages of notably ultramafic rock-hosted seafloor massive sulphide deposits. Its chemical composition is close to $Cu_2Fe_3S_5$, which is intermediate between isocubanite and chalcopyrite.

2 Geological Setting

The hydrothermal vent field and associated massive sulphide occurrences are situated in the license area of the central Indian Ocean (Fig. 1). The samples are retrieved from the new, yet undescribed, Kaimana vent field. This vent field occurs along the Central Indian Ridge (CIR), in close vicinity to the Rodriguez Triple Junction (Fig. 1). The Kaimana vent field is located in geotectonic setting that differs from most other hydrothermal fields, which are commonly located off-axis, associated with prominent faults, and hosted by basaltic rocks. At Kaimana vent field, hydrothermal activity occurs on a tectonic massif on the slow-spreading western flank of the CIR and is associated with the exposure of mantle and lower crustal rocks. Active and inactive vent sites are scattered along the sedimented, axis-facing slope of the tectonic massif. The black smokers exhaust high-salinity fluids at a number of active vent sites in water depths ranging from 2625 to 3020 m. Highest fluid temperature measured at Kaimana vent field reached up to 349 °C. The fluid temperature measured at the investigated chimney reached 328 °C.

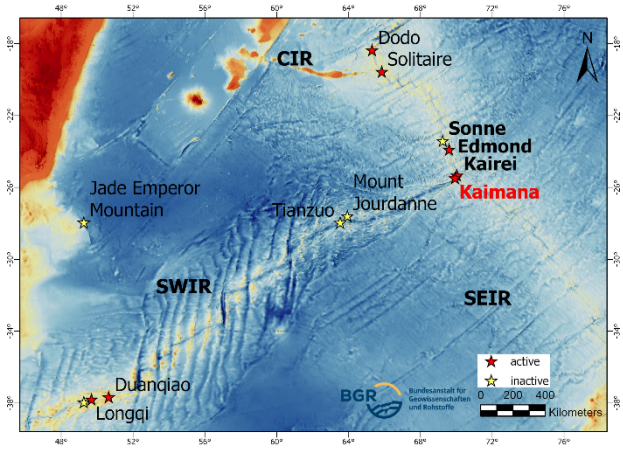

Figure 1. Bathymetric map of the central Indian Ocean showing the Central Indian Ridge (CIR), South-East Indian Ridge (SEIR), and South-West Indian Ridge (SWIR). Red and yellow stars indicate active and inactive vent sites, respectively. The Kaimana site (highlighted in red font colour) is close to the Rodriguez Triple Junction, where the three mid-ocean ridges converge

The samples were collected during the INDEX2018 marine expedition with the research vessel Pelagia and was conducted within the scope

of BGR's exploration work for polymetallic massive sulphide deposits. An entire suite of massive sulphide, rock and sediment samples were retrieved using the remotely operated vehicle (ROV) ROPOS. The two samples (99ROPOS-H and 99ROPOS-K) in focus of the current study were snapped from two actively venting chimneys. Both chimney fragments are composed of predominant chalcopyrite and pyrite/marcasite, minor sphalerite, isocubanite, bornite, galena, and silica plus native gold. Both samples are mineralogically zoned and form numerous conduits.

3 Materials and Methods

Polished sections of Cu-Fe sulphide-rich chimney samples 99ROPOS-H and 99ROPOS-K were selected for detailed analysis. Minerals and their textural relationships were investigated under reflected light using a LEICA DM4P polarization microscope.

Major element compositions of the respective Cu-Fe sulphide minerals were determined by electron probe microanalysis (EPMA) using a JEOL JXA-8350F microprobe. The instrument was set to accelerating voltage of 25 kV, beam current of 20 nA, and focussed electron beam. For spot analysis, the respective X-ray line, spectrometer crystal, measuring time in seconds, and reference material for each element were as follows (ordered by atomic number): S Kα (PET, 10 s, chalcopyrite), Fe Kα (LIFL, 10 s, cubanite), Cu Kα (LIFH, 10 s, chalcopyrite).

4 Results

4.1 Petrography

The mineral assemblage and texture were investigated by reflected light microscopy (Figs. 2 & 3). The mineral texture of this unusual mineral assemblage is characterised by isocubanite matrix with two sets of Cu-Fe sulphide lamellae, which differ in orientation and appearance.

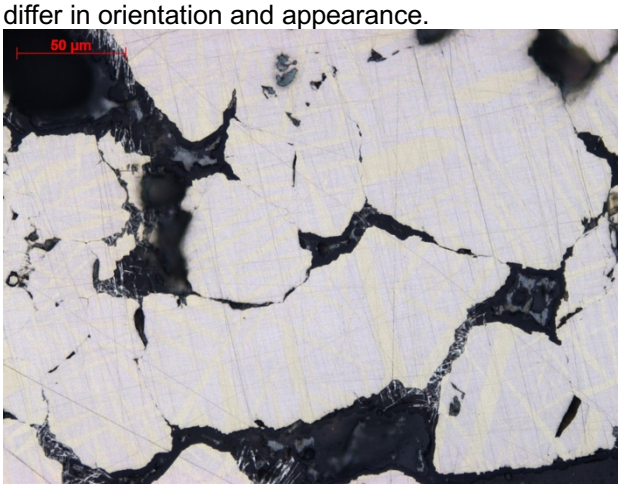

Figure 2. Micrograph under plane polarized reflected light showing the texture with isocubanite (cream) matrix and two sets of lamellae (yellow). Image width about 250 µm, sample 99ROPOS-K

Both sets of lamellae are oriented in parallel patterns, but of different orientation. One set forms acicular lamellae, which are oriented in two directions presumably following crystallographic structure of the isocubanite host, whereas the other set is lenticular or spindle-shaped and oriented independently from the former set of lamellae.

In reflected light, both sets of lamellae show similar optical characteristics resembling chalcopyrite with distinct yellow colour, but without any anisotropy. These lamellae are optically different from the host mineral, which is cream-coloured and isotropic as well. Chalcopyrite is also present as overgrowth along the rim of isocubanite followed by sphalerite of later stage in the paragenetic sequence (Fig. 3).

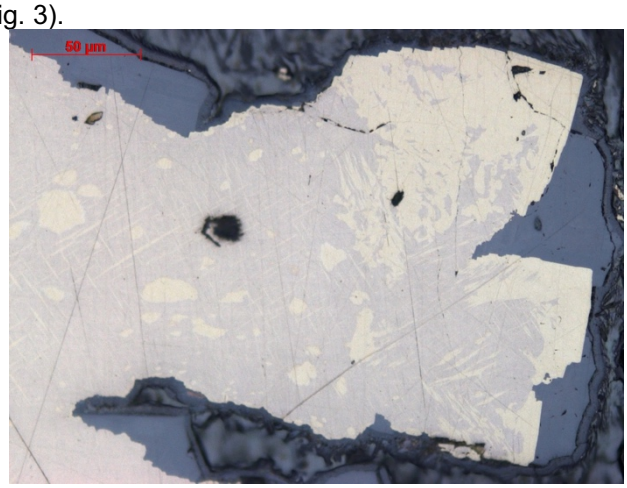

Figure 3. Micrograph under plane polarized reflected light showing the texture with isocubanite (cream) matrix, spindle-shaped $Cu_2Fe_3S_5$ (yellow), and chalcopyrite lamellae (yellow). This assemblage is overgrown by chalcopyrite along the rim (right) and late-stage sphalerite (grey). Image width about 250 µm, sample 99ROPOS-H

4.2 Mineral chemistry

The host mineral is isocubanite with an average composition (n=11) of 21.26 wt% Cu, 42.71 wt% Fe, and 35.99 wt% S, resulting in a slightly un-stoichiometric $Cu_{0.90}Fe_{2.07}S_{3.03}$ formula based on Z=6 atoms per formula unit (Fig. 4, red ellipse).

The acicular lamellae within isocubanite and the overgrowth on isocubanite are both chemically chalcopyrite with an average composition (n=14) of 30.60 wt% Cu, 34.28 wt% Fe, and 35.49 wt% S resulting in an non-stoichiometric $Cu_{0.87}Fe_{1.11}S_{2.01}$ formula based on Z=4 atoms per formula unit (Fig. 4, yellow ellipse). In comparison, the chalcopyrite from overgrowth is closer to its ideal stoichiometry than the acicular lamellae and plots between ideal $CuFeS_2$ and ideal $Cu_{0.9}Fe_{1.1}S_2$ (Fig. 4, top left within yellow ellipse).

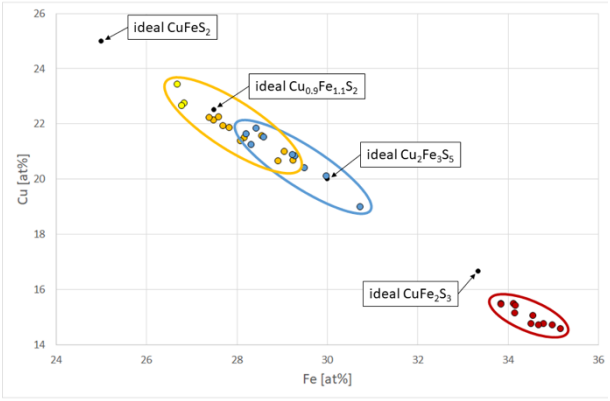

Figure 4. Binary diagram for Fe atomic% versus Cu atomic% showing the chemical composition of Cu-Fe sulphides (red circle: isocubanite, yellow: chalcopyrite, blue: $Cu_2Fe_3S_5$).

The chemical composition of spindle-shaped lamellae is close to $Cu_2Fe_3S_5$ (probably representing "Y-Phase"), but still mostly non-stoichiometric. Average composition (n=9) is 29.21 wt% Cu, 35.88 wt% Fe, and 35.38 wt% S resulting in a $Cu_{2.08}Fe_{2.91}S_{5.00}$ formula based on Z=10 atoms per formula unit (Fig. 4, blue ellipse). The chemical composition of $Cu_2Fe_3S_5$ was also reported by previous studies (Mozgova et al. 2005; Bogdanov et al. 2008; Borodaev et al. 2008; Firstova et al. 2016), but results were rather variable among each other at much lower Cu contents compared to our data.

Nevertheless, it has to be kept in mind that due to the very limited dimension of the lamellae, it cannot be excluded that analytical data may be affected by the chemistry of the enclosing host mineral creating the observed non-stoichiometric composition of chalcopyrite and $Cu_2Fe_3S_5$ lamellae with tendencies towards lower Cu and higher Fe contents.

5 Discussion

In seafloor massive sulphide deposits, isocubanite is a common mineral phase and represents the face-centred cubic polymorph of $CuFe_2S_3$, and is only stable at temperatures above 210 °C (Fleet 1971; Cabri et al. 1973; Caye et al. 1988; Pruseth et al. 1999). Authors of preceding experimental studies demonstrated the decomposition of isocubanite into stable chalcopyrite and pyrrhotite upon cooling below temperatures of 210 °C. This transformation is regarded as solid-state reaction, which does not require the presence of fluids. Because high temperatures can be easily maintained at active vent sites in modern hydrothermal systems on the seafloor, metastable mineral phases such as isocubanite can still be preserved, and are a characteristic mineral phase for recent seafloor massive sulphides (Borodaev et al. 2010). Consequently, isocubanite is only rarely reported within analogue ancient massive sulphide deposits on land (e.g., Maslennikov et al., 2017).

Chalcopyrite is generally slightly non-stoichiometric in composition. At temperatures between 300 and 350 °C, the chalcopyrite solid solution field extends from $CuFeS_2$ to $Cu_{0.9}Fe_{1.1}S_2$ (Sugaki et al. 1975), and the non-stoichimetric chalcopyrite form our study probably represents the Fe-rich and Cu-poor end-member of the solid solution field. However, as anisotropy is not observed, the present chalcopyrite may represent the isotropic variety formed at high temperatures (Missack et al. 1989). Previous studies report chalcopyrite of similar composition and coined the generic name "X-Phase" (Mozgova et al. 2005; Borodaev et al. 2010), but this may also simply represent chalcopyrite solid solution.

A first explanation for the presence of the "Y-Phase" ($Cu_2Fe_3S_5$) was provided by Bogdanov et al. (2008), who interpret this mineral phase as "a protosubstance, in which solid-phase reactions resulted in the formation of textures of the solid solution decomposition under slow cooling."

Based on our observations and analyses, we propose an updated model for the formation and preservation $Cu_2Fe_3S_5$ and its associated mineral assemblage. The occurrence of $Cu_2Fe_3S_5$ is confined to those samples that are collected from two active chimneys, where venting fluids reach high temperatures of at least 328 °C. The temperatures maintained within the chimneys have to be significantly higher than the measured ones, because hydrothermal fluids quickly cool during mixing with ambient seawater at the exhausts of the chimneys (where the temperature measurements have been conducted). This observed association with high-temperature hydrothermal fluids is in agreement with the observation from the Rainbow field, where $Cu_2Fe_3S_5$ occurs as homogenous segregations in active zonal copper-rich chimneys (Mozgova et al. 2005).

In this environment, elevated temperatures are maintained during and after mineral precipitation from the emanating fluid over long time periods, permitting the preservation of temperature-sensitive metastable mineral phases. As we also found isocubanite in absence of $Cu_2Fe_3S_5$ in other massive sulphide samples, we propose that the $Cu_2Fe_3S_5$ becomes unstable and decomposes even at higher temperatures than isocubanite.

Similar to Bogdanov et al. (2008), we suggest that $Cu_2Fe_3S_5$ represents a high-temperature proto-phase, which converts into isocubanite and chalcopyrite upon the cooling to lower temperatures according to the reaction:

$$Cu_2Fe_3S_5 = CuFe_2S_3 + CuFeS_2.$$

The observation of $Cu_2Fe_3S_5$ limited to small lentoid or spindle-shaped forms within isocubanite host mineral provides an indication that the vast majority of this mineral has already been consumed. Within this assemblage of $Cu_2Fe_3S_5$ and isocubanite, remarkably low proportions of chalcopyrite are

observed in form thin acicular lamellae. The preservation of only small volumes of chalcopyrite are explained by selective dissolution of chalcopyrite back into the vent fluid immediately after its formation. Geochemical model simulations have already shown that vent fluids in similar ultramafic rock-hosted settings are undersaturated in chalcopyrite at temperatures of 350 °C and higher (e.g., Fuchs et al. 2019). Under these conditions, chalcopyrite will dissolve into the fluid forming aqueous copper chloride and bisulphide complexes, whereas isocubanite remains stable. The vent fluids likely re-mobilize the Cu (plus Fe and S) on a limited spatial scale (within mm to cm) and re-precipitate chalcopyrite in cooler areas at temperatures below 350 °C. Such overgrowths textures of chalcopyrite have been widely observed in the studied samples and is represented by chalcopyrite of less non-stoichiometric compositions.

As temperatures cool down below 210 °C, the isocubanite host crystals become in turn unstable and transform into the final products chalcopyrite and pyrrhotite, according the solid-state reaction:

$$CuFe_2S_3 = CuFeS_2 + FeS.$$

Isocubanite lamella preserved within chalcopyrite host crystals and vice versa has been observed in many seafloor massive sulfide occurrences (including Kaimana) and provide evidence for the decomposition process of isocubanite. Pyrrhotite is, however, absent in the studied samples of Kaimana. This is again likely due to geochemical properties and temperatures of the vent fluid. If the redox state (oxygen fugacity) of the fluids are above the pyrrhotite-pyrite-magnetite (PPM) redox buffer and/or H_2S concentrations are high, pyrrhotite would dissolve back into the fluid and likely precipitate other Fe-bearing minerals instead (e.g., pyrite).

6 Conclusion

The metastable mineral phase $Cu_2Fe_3S_5$ is a very rare Cu-Fe sulphide, which is until now only observed in meteorites and active high-temperature hydrothermal systems at seafloor. We propose that $Cu_2Fe_3S_5$ is the high-temperature precursor of the investigated mineral assemblage and exsolves into the two Cu-Fe sulphides isocubanite and chalcopyrite during cooling, likely at initial fluid temperatures significantly above 350 °C. The currently measured fluid temperature of 328 °C at the associated black smokers are lower, however, higher temperatures reaching 349 °C are confirmed at neighbouring chimneys, suggesting that high temperatures of ≥ 349 °C are maintained within the chimneys. Chalcopyrite dissolved back into the vent fluid leaving small non-stoichiometric residues (lamellae) behind, with a composition of close to $Cu_{0.9}Fe_{1.1}S_2$. The majority of chalcopyrite and is re-mobilized on mm- to cm-scale, and precipitated with a composition closer to its ideal stoichiometry. Isocubanite decomposed in turn into even more chalcopyrite and unstable pyrrhotite, when fluids further cool down to temperatures below 210 °C.

As an outlook, we are currently preparing a new publication addressing crystal structural properties and micro- to nano-textures of these Cu-Fe sulphides using transmission electron microscopy (TEM), especially to characterise $Cu_2Fe_3S_5$ and to verify the occurrence of isotropic chalcopyrite. Furthermore, we apply geochemical model simulations to empirically investigate the role of the vent fluids in the dissolution and re-precipitation of this mineral assemblage.

Acknowledgements

Many thanks to the colleagues at the BGR in Hannover. Andreas Heiner ably produced polished sections and Christian Wöhrl is thanked for excellent support on electron probe microanalysis.

References

Bogdanov YA, Lein AY, Maslennikov VV, Syaoli L, Ul'yanov AA (2008) Mineralogical-geochemical features of sulfide Ores from the Broken Spur hydrothermal vent field. Oceanology 48:679-700

Borodaev YS, Mozgova NN, Uspenskaya TY (2010) Typomorphic features of modern oceanic sulfides. Moscow University Geology Bulletin 65:66-75

Cabri LJ, Hall HT, Szymanski JT, Stewart JM (1973) On the transformation of cubanite. Canadian Mineralogist 12:33-38

Caye R, Cervelle B, Cesbron F, Oudin E, Picot P, Pillard F (1988) Isocubanite, a new definition of the cubic polymorph of cubanite $CuFe_2S_3$. Mineralogical Magazine 52:509-514

Firstova A, Stepanova T, Cherkashov G, Goncharov A, Babaeva S (2016) Composition and formation of gabbro-peridotite hosted seafloor massive sulfide deposits from the Ashadze-1 hydrothermal field, Mid-Atlantic Ridge. Minerals 6:19

Fleet ME (1971) Refinement of crystal structure of cubanite and polymorphism of $CuFe_2S_3$. Zeitschrift für Kristallographie 132:276-287

Fuchs S, Hannington MD, Petersen S (2019) Divining gold in seafloor polymetallic massive sulfide systems. Mineralium Deposita 54:789-820

Maslennikov VV, Maslennikova SP, Large RR, Danyushevsky LV, Herrington RJ, Ayupova NR, Zaykov VV, Lein AY, Tseluyko AS, Melekestseva IY, Tessalina SG (2017) Chimneys in Paleozoic massive sulfide mounds of the Urals VMS deposits: Mineral and trace element comparison with modern black, grey, white and clear smokers. Ore Geology Reviews 85:64-106

Missack E, Stoffers P, El Goresy A (1989) Mineralogy, parageneses, and phase relations of copper-iron sulphides in the Atlantis II deep, Red Sea. Mineralium Deposita 24:82-91

Mozgova NN, Borodaev YS, Gablina IF, Cherkashev GA, Stepanova TV (2005) Mineral assemblages as indicators of the maturity of oceanic hydrothermal mounds. Lithology and Mineral Resources 40:293-319

Pruseth KL, Mishra B, Bernhardt HJ (1999) An experimental study on cubanite irreversibility: Implications for natural chalcopyrite-cubanite intergrowths. European Journal of Mineralogy 11:471-476

Sugaki A, Shima H, Kitakaze A, Harada H (1975) Isothermal phase relations in the system Cu-Fe-S under hydrothermal conditions at 350°C and 300°C. Economic Geology 70:806-823

Magmatic metal contribution to volcanic arc seafloor massive sulfides: case study of the Kolumbo volcano

Hector S. [1], Patten C.G.C. [1], Kolb J. [1], Kilias S.P. [2], Nomikou P. [2]
[1]*Institute of Applied Geosciences, Chair of Geochemistry and Economic Geology, KIT, Karlsruhe, Germany*
[2]*National and Kapodistrian University of Athens, Athens, Greece*

Abstract. Seafloor massive sulfides (SMS) form in various marine hydrothermal environments, including volcanic arcs, where magmatic fluids can contribute to the metal budget of the hydrothermal system. Here we study the Kolumbo volcano, a submarine volcano in the central Aegean Volcanic Arc, hosting an active hydrothermal system. Sulfate-sulfides chimneys forming a Zn-Pb SMS show elevated As, Ag, Au, Hg, Sb and Tl contents. These elements belong to the "epithermal suite of elements" and are usually related to magmatic input to the hydrothermal fluid. Combining volcanic whole rock chemistry, numerical modelling and in-situ magnetite analysis, we reconstruct the magmatic history and particularly, the behaviour of metals relative to sulfide saturation, magnetite crystallisation and degassing. Despite early sulfide saturation, chalcophile element concentrations in the magma do not decrease until water saturation, implying that magmatic sulfides remain in the magma and are not removed. Formation of sulfide-volatile compounds and magmatic degassing lead to metal transfer to the volatiles, depleting Cu, Au, Ag, Sn, Sb and Pb in the magma while Zn, As and Tl do not show specific behaviour.

1 Introduction

Arc-related hydrothermal systems differ in many aspects from those located along the mid-oceanic ridge and mature back-arc spreading centres, most notably by the shallow environment and importance of a magmatic source for fluids and metals (e.g. Hannington et al. 2005).

Magmatic volatiles in arc-related submarine hydrothermal systems indicate that ore deposits mineralization style form a continuum from volcanogenic massive sulfide to porphyry and epithermal deposits (Keith et al. 2018). In porphyry and epithermal deposits, metals are considered to be mostly carried by magmatic fluids that exsolve from hydrous magmas in the mid- to upper crust (Richards 2011). Thus, magmatic processes such as sulfide saturation, degassing and sulfide volatile compound formation are key parameters for controlling the formation of metal-rich magmatic fluids in arc-related submarine hydrothermal systems (Fontboté et al. 2017). Sulfide saturation in the melt will extract most of the chalcophile and siderophile elements (including As, Ag, Au, Hg, Sb and Tl) and concentrate them into an immiscible sulfide phase (Jenner et al. 2010). Because of its density, the sulfide phase tends to sink at the bottom of the magma chamber, physically removing the metals from the magma.

Similarly, degassing leads to formation of an aqueous fluid rich in volatiles such as S, Cl, F and CO_2, which can extract metals from the magma if it is still fertile (i.e. before sulfide saturation) (Fontboté et al. 2017). If the melt reached sulfide saturation before degassing, most of the chalcophile and siderophile metals will be already extracted by the sulfide melt, leaving too little metals available for the aqueous fluids and volatiles to generate metal-rich magmatic-hydrothermal fluids. However, formation of sulfide-volatile compounds and interaction between the two phases can favour metal transfer to the volatile despite early sulfide saturation (Mungall et al. 2015). Therefore, investigating the timing of sulfide saturation, water saturation in the system is crucial to understand the behaviour of metals during magmatic differentiation. To do so, detailed petrographic and whole rock analysis have been carried on volcanic rock samples from Kolumbo, coupled with magmatic differentiation and sulfur concentration at sulfide saturation (SCSS) modelling. Additionally, in-situ magnetite trace element analysis allows monitoring the metal content of the melt and refining the understanding of the metal behaviour during differentiation.

2 Kolumbo volcano and its SMS

The submarine Kolumbo volcano in the Anhydros basin belongs to the Christiana-Santorini-Kolumbo Volcanic Field in the centre of the Aegean Volcanic Arc, southern Aegean Sea. The last eruption of 1650CE shaped the volcanic edifice, forming a 7 kilometres wide cone with a 2.7 kilometres wide crater in its centre (Fouqué 1879; Sigurdsson et al. 2006). The seafloor of the crater is 500 meters below sea level and hosts a hydrothermal field in its northern part (Sigurdsson et al. 2006). The hydrothermal field contains active and fossil sulfate-sulfide chimneys, forming a polymetallic Zn-Pb-(As, Ag, Au, Hg, Sb, Tl)-rich SMS associated with CO_2-dominated fluids venting with temperature up to 220°C (Kilias et al. 2013; Sigurdsson et al. 2006). Kolumbo' s volcanic cone is formed by a superposition of 5 cone-shaped stratigraphic units labelled K1 to K5 interbedded with volcano-sedimentary units (Hübscher et al. 2015). Due to lack of drill cores at the time and limitation of remotely operated vehicle (ROV) sampling, only the

outcropping units K2 and K5 units are available for study.

3 Methodology

Major element composition was measured on glass beads by X-ray fluorescence with a S4 Explorer at LERA. In-situ trace element analysis by laser ablation-inductively coupled plasma mass spectrometry (LA-ICP-MS) on pressed powder pellets of representative volcanic rocks and on magnetite in thin sections was carried out at the Laboratory of Environmental and Raw Materials Analysis (LERA), KIT using a Teledyne 193 nm Excimer Laser coupled to an Element XR ThermoFisher ICP-MS. Reference materials BHVO-2, BHVO-2G, BIR-1 and NIST-612 were used for calibration and monitoring. Pellets and magnetite analysis were carried out in separate runs. Low detection limit Au analysis was carried out on the same apparatus, using the method from Patten et al. (accepted).

4 Results

The volcanic rock samples from Kolumbo belong to units K2 and K5. They are pumices and lavas and commonly contain mafic enclaves. Major element composition of the pumice, lava and mafic enclaves show that the K2 and K5 eruptions record similar differentiation processes, from basaltic andesite to rhyolite (own data; Cantner et al. 2014; Klaver et al. 2016). The compositional range of volcanic rocks of Kolumbo is considered to reflect continuous magmatic differentiation and magma mixing (Klaver et al. 2016). The pumices are mostly rhyolitic and exceptionally trachytic or andesitic. Magmatic enclaves in rhyolite and trachyte and mafic lavas are basaltic andesite to andesite. Detailed petrography shows that magmatic magnetite and sulfides are ubiquitous in the samples, independently of their differentiation stage.

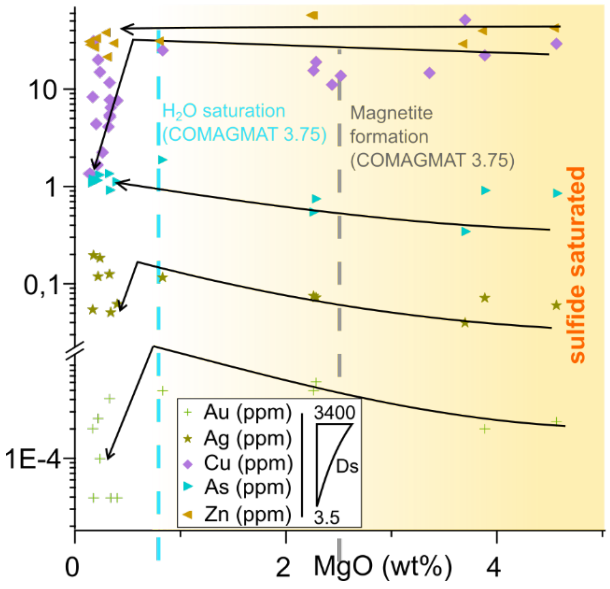

Figure 1. Different behaviour of metals in volcanic rocks during magmatic differentiation related to their chalcophile affinity. Ds is the partition coefficient between a sulfide liquid and the silicate melt (Patten et al. 2013 and references therein).

Trace element analysis of the volcanic rocks show that Ag, As, Au, Cu, Pb, Sb, Sn and Tl contents are slightly increasing during magmatic differentiation, while Co, Fe, Ni, Ti, V and Zn contents remain relatively constant until reaching 0.7 wt.% MgO, then Ag, Au, Cu, Pb, Sb, Sn are locally depleted (Figure 1). The TiO_2 and Fe_{tot} contents remain relatively stable during the early magmatic differentiation, until ~2.5 wt.% MgO (~62 wt.% SiO_2), before decreasing strongly (Figure 2-A and B).

Trace elements content in magnetite is varying depending on the differentiation

state of the host rock. As magnetite is hosted in more felsic rocks, Al, Co, Cr, Cu, Ga, Mg, Ni, Sc and V contents are decreasing while Ge, Hf, Mn, Mo, Nb, P, Pb, Sn, Ta, Ti, W, Y, Zn and Zr contents are increasing in comparison to mafic rock-hosted magnetite.

5 Discussion

5.1 Modelling of magmatic differentiation in Kolumbo

Using an average primitive composition of the melt based on the composition of the most mafic samples (n=3), the evolution the melt composition during differentiation is modelled using COMAGMAT 3.75 (Ariskin and Barmina 2004) and compared to the major oxide composition of the volcanic rocks. The parameters modelling a melt composition evolution fitting best to the major oxide composition of the samples are fO_2 FMQ + 1 and 2 wt.% H_2O with a pressure variation from 2.0 to 0.9 kbar. The pressure decrease is meant to reflect conditions for an ascending melt in an upper reservoir located at between 6- and 3-kilometres depth. The evolution of the SCSS during differentiation was modelled according to Smythe et al. (2017) using melt compositions calculated by COMAGMAT 3.75. Modelling predicts the following magmatic processes: (1) extensive magnetite crystallisation at ~2.5 wt.% MgO; (2) the melt is sulfide-saturated from the beginning of the differentiation; (3) water saturation starts at 0.87 wt.% MgO (Figure 1). The model is fitting well with the observations, correctly predicting early sulfide saturation and evolution of the major oxide composition during differentiation. However, it does not predict early magnetite formation, as observed in the most mafic samples. The absence of early magnetite crystallization in the model is likely caused by the higher Fe^{2+}/FeO_{tot} used in the calculation to stay within range of use for COMAGMAT 3.75. Nonetheless, the model predicts correctly the magnetite crystallization observed in

the samples and reflected by the drop in TiO_2 and Fe_2O_3 content in the rocks around ~2.5 wt.% MgO.

5.2 Metal content evolution during magmatic differentiation

Depletion in V, Ni, Co and to some extent Fe and Ti is related to crystallization and settling of magnetite in the magma chamber (Dare et al. 2014). Demixing of a sulfide melt after sulfide saturation should result in depletion of chalcophile and siderophile elements (Jenner et al. 2010; Patten et al. 2013). However, despite early sulfide saturation, there is no significant depletion in chalcophile elements in the samples before water saturation and magmatic degassing, implying more complex metal behaviour during the evolution of the melt than sulfide exsolution and settling (Figure 1).

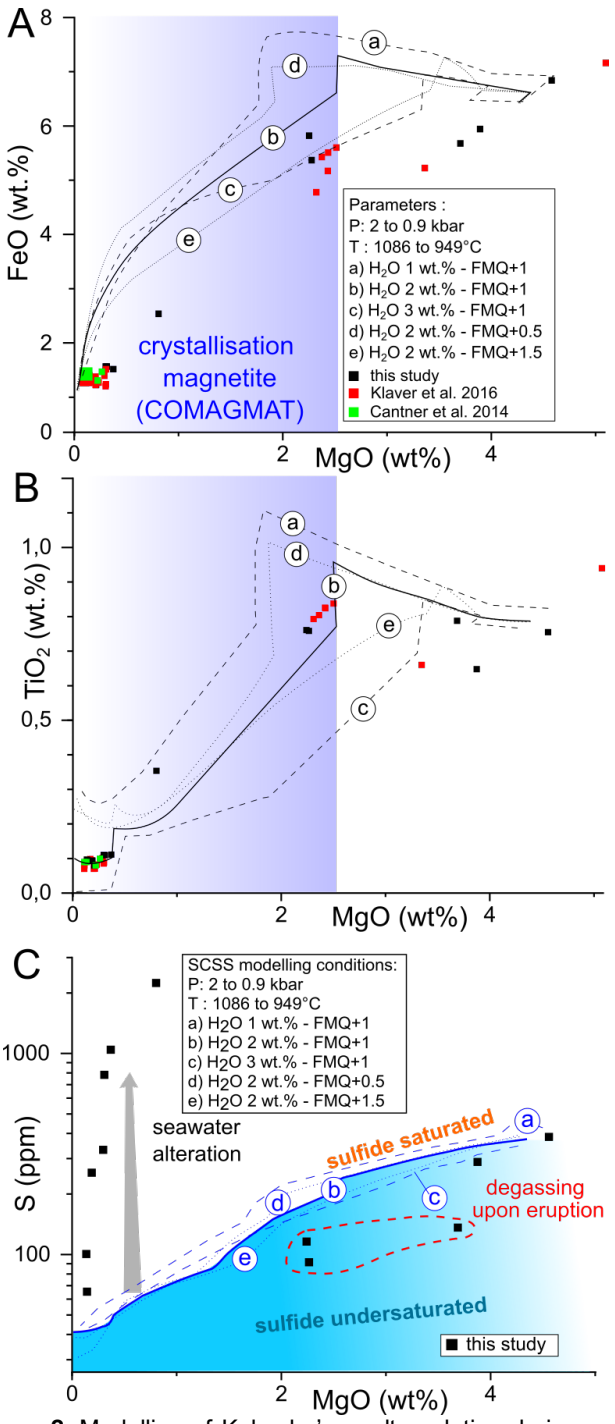

Figure 2. Modelling of Kolumbo' s melt evolution during magmatic differentiation. A) Modelled evolution of FeO content in the melt compared to volcanic samples for varying H_2O initial content and fO_2 using COMAGMAT 3.75 (Ariskin and Barmina 2004); B) Modelled evolution of TiO_2 content in the melt compared to volcanic samples for varying H_2O initial content and fO_2 settings using COMAGMAT 3.75; C) Modelled evolution of the SCSS (according to Smythe et al. 2017) using five different melt compositions calculated by COMAGMAT 3.75 with varying H_2O initial content and fO_2 compared to S content in the volcanic samples.

5.3 Insight on metal behaviour from magnetite and sulfides

Chalcophile element content in magnetite reflects their availability in the melt at time of crystallization.

Before magmatic degassing, the Cu content in magnetite decreases constantly during magmatic differentiation. Conversely, the corresponding whole rock Cu content remains relatively constant in the whole rock during magmatic differentiation (29±12 ppm on average) (Figure 3). This indicates that less and less Cu is available in the melt for magnetite during magmatic differentiation. Copper is likely trapped in magmatic sulfides, as the melt is sulfide saturated since at least formation of basaltic andesite, as observed petrographically and supported by SCSS modelling (Figure 2-C). However, the constant Cu content in the whole rock indicates that magmatic sulfides are not removed from the magma. The limited size of the sulfide phases observed in the samples and the increasing viscosity of the melt as it differentiates are greatly reducing their mobility, likely preventing them to sink and conserving the metal content of the system (Holzheid 2010).

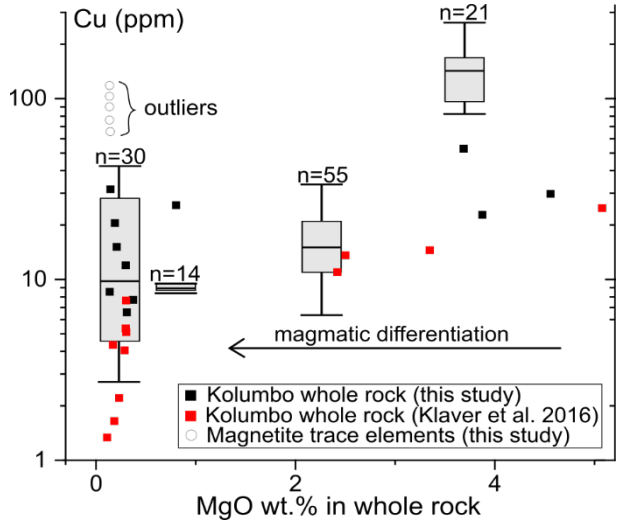

Figure 3. Evolution of the Cu content in volcanic rocks and their respective magnetite during magmatic differentiation.

5.4 Metal flux during magmatic degassing

According to the modelling, water saturation starts at 0.87 wt.% MgO, which correspond to formation of trachyte by magma mixing/differentiation. Upon degassing, the most chalcophile elements (i.e. Cu, Ag and Au and to some extend Sn, Sb and Pb) are the most depleted in the whole rock while the least chalcophile (i.e. As, Tl and Zn) are not affected (Figure 3). However, in Kolumbo' s magma, the most chalcophile elements are concentrated in the magmatic sulfide phases which remain in the magma. Thus, leaching of the sulfide phases by the degassing volatiles is required for efficient mobilization of the chalcophile metals. Volatile phase nucleation on magmatic sulfides and formation of sulfide-volatile compounds (Mungall et al., 2015) would be a very efficient mechanism for mobilizing metals from the sulfides during degassing.

5.5 Magmatic input in Kolumbo' s SMS

The sulfide-sulfate chimneys at Kolumbo' s SMS are Zn-Pb-rich and show elevated As, Ag, Au, Hg, Sb and Tl content, while being relatively Cu poor (Ahmad 2018; Kilias et al. 2013). Enrichment in Au, Ag, Sb and Pb is agrees with a magmatic source, as these elements are mobilized from the magma upon degassing and can be transferred to the magmatic-hydrothermal fluids. The low Cu content in the chimneys indicates that it is most likely trapped in the deeper, hotter part of the mineralized system, as frequently observed in VMS and epithermal/porphyry systems (Hannington et al. 2005).

Conversely, As, Zn and Tl are enriched in the chimneys but do not seem to be lost during magmatic degassing, indicating another metal mobilizing mechanism is likely involved. Hydrothermal leaching can mobilize As, Ag, Au, Cu, Pb, Sb, Sn, Tl, Zn from the host rocks in VMS deposits, especially in felsic environment, and can represent an additional process occurring at Kolumbo (Shikazono 2003).

Conclusion

Combining in-situ magnetite trace element analysis with whole rock analysis and modelling allows to track metal behaviour in the magma during magmatic differentiation. It indicates that chalcophile elements are scavenged by sulfide phases but remain in the magma. Sulfide-volatile compounds formation and magmatic degassing appear to be an important process to transfer Cu, Au, Ag, Sb, Sn and Pb from the magma to the magmatic-hydrothermal system by leaching of the sulfide phases by volatiles. However, hydrothermal leaching of the basement also provides metals to the system, especially Zn, As and Tl.

Acknowledgements

This work is funded by the German Research Foundation (DFG - Priority Program DOME SPP 2238 and INST 121384/213-1 FUGG).

References

Ahmad Q (2018) The source of metals in the recent polymetallic seafloor massive sulfide mineralization at the Kolumbo arc-volcano, Greece. M.Sc. thesis, Karlsruhe Institute of Technology

Ariskin AA, Barmina GS (2004) COMAGMAT: Development of a magma crystallization model and its petrological applications. Geochemistry International 42:1–157

Cantner K, Carey S, Nomikou P (2014) Integrated volcanologic and petrologic analysis of the 1650AD eruption of Kolumbo submarine volcano, Greece. Journal of Volcanology and Geothermal Research 269:28–43

Dare SAS, Barnes S-J, Beaudoin G, Méric J, Boutroy E, Potvin-Doucet C (2014) Trace elements in magnetite as petrogenetic indicators. Miner Deposita 49:785–796

Fontboté L, Kouzmanov K, Chiaradia M, Pokrovski GS (2017) Sulfide Minerals in Hydrothermal Deposits. ELEMENTS 13:97–103

Fouqué F (1879) Santorin et ses éruptions. G. Masson, Paris
Hannington M, de Ronde CEJ, Petersen S (2005) Sea-Floor Tectonics and Submarine Hydrothermal Systems. In: Hedenquist J, Thompson JFH, Goldfarb RJ, Richards JP (eds) One Hundredth Anniversary Volume. Society of Economic Geologists
Holzheid A (2010) Separation of sulfide melt droplets in sulfur saturated silicate liquids. Chemical Geology 274:127–135
Hübscher C, Ruhnau M, Nomikou P (2015) Volcano-tectonic evolution of the polygenetic Kolumbo submarine volcano/Santorini (Aegean Sea). Journal of Volcanology and Geothermal Research 291:101–111
Jenner FE, St. O'Neill HC, Arculus RJ, Mavrogenes JA (2010) The Magnetite Crisis in the Evolution of Arc-related Magmas and the Initial Concentration of Au, Ag and Cu. Journal of Petrology 51:2445–2464
Keith M, Haase KM, Klemd R, Smith DJ, Schwarz-Schampera U, Bach W (2018) Constraints on the source of Cu in a submarine magmatic-hydrothermal system, Brothers volcano, Kermadec island arc. Contrib Mineral Petrol 173
Kilias SP, Nomikou P, Papanikolaou D, Polymenakou PN, Godelitsas A, Argyraki A, Carey S, Gamaletsos P, Mertzimekis TJ, Stathopoulou E, Goettlicher J, Steininger R, Betzelou K, Livanos I, Christakis C, Bell KC, Scoullos M (2013) New insights into hydrothermal vent processes in the unique shallow-submarine arc-volcano, Kolumbo (Santorini), Greece. Sci Rep 3:2421
Klaver M, Carey S, Nomikou P, Smet I, Godelitsas A, Vroon P (2016) A distinct source and differentiation history for Kolumbo submarine volcano, Santorini volcanic field, Aegean arc. Geochem Geophys Geosyst 17:3254–3273
Mungall, J. E.; Brenan, J. M.; Godel, B.; Barnes, S. J.; Gaillard, F. (2015) Transport of metals and sulphur in magmas by flotation of sulphide melt on vapour bubbles. In : Nature Geoscience, vol. 8, n° 3, p. 216–219. DOI: 10.1038/NGEO2373.
Patten CGC, Barnes S-J, Mathez EA, Jenner FE (2013) Partition coefficients of chalcophile elements between sulfide and silicate melts and the early crystallization history of sulfide liquid: LA-ICP-MS analysis of MORB sulfide droplets. Chemical Geology 358:170–188
Patten, CGC; Beranoaguirre, A; Hector, S; Gudelius, D; Kolb, J; Eiche, E (accepted) Improved whole rock low detection limit of gold by LA-ICP-MS utilizing pressed-powder-pellets. In : International Journal of Mass Spectrometry.
Richards JP (2011) Magmatic to hydrothermal metal fluxes in convergent and collided margins. Ore Geology Reviews 40:1–26
Shikazono N (2003) Geochemical and tectonic evolution of arc-backarc hydrothermal systems: Implication for origin of Kuroko and epithermal vein-type mineralizations and the global geochemical cycle, 1st ed. Developments in geochemistry, vol 8. Elsevier, Amsterdam, Boston
Sigurdsson H, Carey S, Alexandri M, Vougioukalakis G, Croff K, Roman C, Sakellariou D, Anagnostou C (2006) Marine investigations of Greece's Santorini volcanic field. Eos, Trans. Am. Geophys. Union 87:337–342
Smythe DJ, Wood BJ, Kiseeva ES (2017) The S content of silicate melts at sulfide saturation: New experiments and a model incorporating the effects of sulfide composition. American Mineralogist 102:795–803

Distribution of Characteristic Elements in Pore Waters, Sediments and Nodules from the Eastern Part of the Clarion-Clipperton Fractures Zone, NE Pacific

Atanas Hikov[1], Zlatka Milakovska[1], Irena Peytcheva[1], Valcana Stoyanova[2], Elitsa Stefanova[1], Tomasz Abramowski[2], Silvia Chavdarova[1], Milen Stavrev[1], Dimitrina Dimitrova[1]
[1] Geological Institute, Bulgarian Academy of Sciences, Bulgaria
[2] Interoceanmetal Joint Organization, Poland

Abstract. The geochemical characteristics of pore waters, bottom sediments and polymetallic nodules from the Interoceanmetal exploration area in the eastern part of the Clarion-Clipperton Fractures Zone (CCZ), NE Pacific were studied. Manganese has a positive correlation with Fe in pore waters but a negative correlation in the sediments and polymetallic nodules. The results suggest that Mn precipitates faster than Fe in sediments and especially in nodules that are enriched in Mn, Ni and Cu compared to the host sediments. PAAS-normalized REE patterns of pore water layers, sediments layers, bulk nodules and nodule growth layers show gradual enrichment resulting of several factors, including low sedimentation rate, high REE of the bottom seawater, oxidation conditions, certain bottom current conditions and the presence of Fe–Mn oxyhydroxides.

1 Introduction

The development of modern society and new emerging technologies are resulting in growing demand for rare and trace elements defined as critical raw materials (CRMs). The deep-sea metalliferous sediments and Fe-Mn polymetallic nodules formed in modern environment at the deep-sea ocean floor (>4000 m depth) were evaluated as promising new raw materials, especially for high-tech elements as Co, Ni and rare earth elements (REE) (Kato et al. 2011; Pak et al. 2019). The Clarion-Clipperton Fe-Mn Nodule Zone (CCZ) in the NE Pacific is the area of greatest economic interest for nodules and sediments (Kato et al. 2011; Hein et al. 2013).

In the present study we compare geochemical characteristics of pore waters, sediments and polymetallic nodules from the Interoceanmetal (IOM) exploration area located in the eastern part of the CCZ, NE Pacific. Our aim is to assess the main factors that control metal deposition and Fe-Mn polymetallic nodule enrichment in some CRMs.

2 Geological setting and sampling

The studied area covers 630 km^2 of the seafloor in the eastern part of the Clarion-Clipperton fractures Zone, NE Pacific between 11°06'–11°26'N latitude and 119°25'–119°42'W longitude at depth varying from 4300 to 4500 m (Figure 1). Box-core samples

from six stations were collected during the 2019 Interoceanmetal cruise. The explored stations are distributed among various morphological types of the bottom relief, mostly represented by the undulating hilly plain, intersected by longitudinal ridges and sub-parallel volcanic massifs.

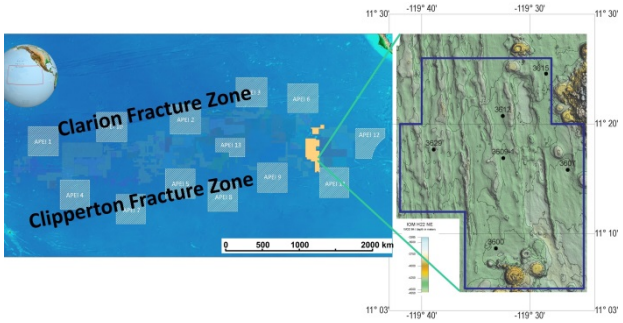

Figure 1. Geomorphological map of the seafloor and location of the sampling area in the IOM exploration area in the eastern part of the CCZ.

The polymetallic nodules were observed on the top of, and partly buried in the seabed sediments. The sediment composition is dominated by light brown siliceous silty clay down to 45-cm. The top semiliquid dark brown clay variety (thickness of 7–12 cm) was denoted as a geochemically active layer (GAL), i.e. it is the medium for main processes of polymetallic nodule formation. An amorphous phase (biogenic opal, authigenic Fe-Mn hydroxides and clay minerals) predominates in the mineral composition. The crystalline phases are illite, kaolinite, chlorite, quartz, andesine, halite, cristobalite and barite (Hikov et al. 2022a).

A box corer was used to yield relatively undisturbed bottom samples up to 50 cm in depth. After collecting the nodules from the surface four sediment layers at depths 0–3, 3–5, 5–10, 10–20 cm were sampled. The sediment samples for pore water extraction were collected on-board from the depth intervals 0–5, 10–15, 25–30 and 35–40 cm following the recommendations of ISBA/19/LTC/8. The water samples were stabilized by concentrated nitric acid and stored in plastic bottles.

3 Analytical techniques

The chemical analyses of the water samples were carried out at the Faculty of Chemistry and Pharmacy, Sofia University using ICP-MS (Perkin-Elmer SCIEX Elan DRC-e) with a cross-flow nebulizer, following the analytical techniques of Lyubomirova et al. (2020). The concentrations of 69 elements were determined. Working standard solutions were prepared from ICP-MS multi-element calibration standard solution-2 (Ultra Scientific) and ICP-MS Multielement Standard B (High Purity Standards).

Major element composition of the sediment samples was determined by ICP-OES at AQUATERATEST LTD, Sofia. Trace element content was measured on fused pellets by LA-ICP-MS at the Geological Institute of Bulgarian Academy of Sciences (BAS), using laser ablation system New Wave UP193FX coupled to a PerkinElmer ELAN DRC-e ICP-MS. The laser beam diameter was 100 µm and laser pulse frequency - 10 Hz. The NIST 610 was used for external standard and SiO_2, determined by ICP-OES as internal standard.

The major element composition of the main minerals in the nodules was determined by SEM-EDS (SEM JEOL JSM-6610LV at Belgrade University, Serbia). The chemical composition of bulk nodule samples was measured on pressed pellets with LA-ICP-MS at the Geological Institute, BAS. Laser spot of 35 µm and 6 Hz pulse rate were applied. External standardization was made on NIST 610 glass and Mass1 polymetallic standards. The total major element oxides (100 wt.%) was used as standardization method for the pressed pellets after subtracting the loss of ignition (LOI). The *in situ* trace element composition was measured on polished sections, whereas Mn concentration from SEM-EDS analyses was used as internal standard.

4 Results

4.1 Pore waters

The major elements in the pore water are Na, Mg, Ca and K, and Na is clearly prevailing. The concentrations of elements of interest are as follows (in µg/L): Fe (241.4–2236.1), Mn (1.8–137.8), Co (1.73–6.09), Ni (11.6–38.8), Cu (9.0–41.7), Zn (21.1–95.1), As (39.0–82.9), Mo (5.4–34.0), Cd (0.21–44.9). Most of the stations have maximum values of Fe and Mn in the second (10–15 cm) or the first (0–5 cm) layers. Ni, Cu and Co show similar trends while As distribution is clearly opposite. The ΣREE in the pore water samples varies from 3.56 to 94.34 µg/L. Maximum REE values were observed for the first (0–5 cm) or for the second (10–15 cm) layers. A negative Ce anomaly predominates and increases with depth. The Eu anomaly is highest in the second layer in the most of the stations.

4.2 Sediments

The chemical composition of the sediment samples is similar with small differences depending on the station and depth interval. Iron content ranges from 4.10% to 4.99% (mean 4.60%) and increases with depth. Manganese varies from 0.16% to 0.70% (mean 0.49%), and Mn/Fe ratio - from 0.03 to 0.16. Both values are the highest in GAL and decrease with depth. Characteristic element contents in the sediments are as follows (ppm): Co (41.6–86.8), Ni (80.2–216.8), Cu (280–429.5) and Zn (105.5–132). Cobalt, Ni, Cu and Ba have the highest contents in the GAL that decrease with depth, while Zn does not show such a trend. The ΣREE in the sediments varies from 195.84 to 357.79 ppm (mean 245.79 ppm) without any significant variations between the sediment layers. PAAS-normalized REE patterns

show enrichment of MREE and HREE. All samples reveal strong negative Ce anomaly, positive Eu and weak positive Y anomalies.

4.3 Polymetallic nodules

Bulk nodule samples show Mn content variation from 22.62 to 35.59 wt.% (mean 31.36%) and Fe one - from 3.51 to 8.26 wt.% (mean 5.38%). The Mn/Fe ratio varies from 2.74 to 10.12. The characteristic elements concentrations are as follows: Ni (0.58–1.70 wt.%), Cu (1.07–1.50 wt.%), Co (0.12–0.30 wt.%), Zn (0.09–0.26 wt.%), Mo (430–872 ppm), W (55–111 ppm), Li (77–205 ppm), Tl (53–410 ppm), Pb (247–616 ppm), Y (42–83 ppm), Ba (2197–5775 ppm). The ΣREE range is 316.33–677.49 ppm (mean 472.08 ppm). The PAAS-normalized REE patterns show enrichment of all REE, especially of middle REE (MREE) and heavy REE (HREE). The studied nodules have mainly positive or weak negative Ce anomaly, positive Eu and negative Y anomalies.

Most of the studied polymetallic nodules have high Mn/Fe ratio (>5) and are diagenetic nodules according to Kotlinski and Stoyanova (2012). Some nodules with Mn/Fe ratio 3–5 are of mixed, hydrogenetic-diagenetic type, and only one nodule (sample 3607) is hydrogenetic with Mn/Fe ratio <3. The diagenetic nodules reveal high ΣNi+Cu. The nodule 3607 has the lowest ΣNi+Cu and the highest Co content. Hikov et al. (2022b) suggested that most of the nodules are of mixed hydrogenetic-diagenetic type using different discrimination criteria.

The SEM-EDS analyses of nodule layers show Mn and Fe content variations from 10.75 to 57.63%, and from 0.10 to 24.12%, respectively. The range of the Mn/Fe ratio is 0.76–491.75.The *in situ* LA-ICP-MS analyses show high contents for Ni (0.13–3.58 wt.%), Cu (0.20–3.21 wt.%), Co (0.005–1.04 wt.%), Zn (0.03–0.85 wt.%), Ba (0.04–2.64 wt.%), Mo (195–2114 ppm), W (23–607 ppm), Li (15.5–1046 ppm), Tl (26–1101 ppm), Pb (24–2917 ppm), Y (14.8–196.6 ppm). The ΣREE varies from 119.3 to 2312.8 ppm.

The PAAS-normalized REE patterns of *in situ* nodule analyses show MREE and HREE enrichment. Approximately half of the layers reveal patterns with a negative Ce anomaly while the others are characterized with positive Ce anomaly. Most of the analyses show weak positive Eu anomaly and all have negative Y anomaly. All *in situ* analyses of nodule 3607 have positive Ce anomaly which corresponds to the low Mn/Fe ratio and low ΣNi+Cu contents in the bulk analysis.

4.4 Correlations

Table 1 shows the positive and negative correlations of Mn and Fe with other elements in the pore waters, bottom sediments, polymetallic nodules and nodule layers. Copper is the only element which has positive correlation with Mn in all studied components of the deep ocean floor environment. Five elements – Ni, Zn, Mo, Sb and Ba have positive correlation with Mn in sediments, bulk nodules and nodule layers. Other elements correlate either positively (Cd, W and Tl) or negatively (Si, Ti and Pb) with Mn in two components. Manganese has variable (+/-) correlations with Fe, Co and Na in different components. Iron has positive correlation with Ti, P, Zr, Nb and Pb in sediments, nodules and nodule layers and with REE, Y and Th in sediments and nodule layers.

comp	pore waters		sediments		bulk nodules		nodule layers	
corr	+	-	+	-	+	-	+	-
Mn	Al, Fe ***Co, Y*** Cu		Co Ni Cu ***Zn*** ***Mo,W*** **Na, Sr** **Sb, Ba**	***Ti, Pb*** **Al, Fe** **K**	Sn Sb, Zn ***Li,*** ***Ni,Cu*** ***Mo*** ***Cd, Tl*** **V, Ag** **Ba**	Si, Al Fe ***Na,Co*** ***Hf,*** **Zr, In**	Cu,Cd Tl ***Mg,Na*** ***Ni,Zn*** ***Mo*** **Sb, *Ba*** **Li, V,** **Sr, W**	Si, Fe P, Zr Sn,Pb ***Ti, Sc*** ***As, Y*** ***Te,* Ce** **REE** **Co**
Fe	Al Mn ***Ba***		Al, Ti Ca, K Mg ***P, Y*** ***REE*** **Ga, Zr** **Nb,** **Pb Th**	***Si, Ni*** ***As,Mo*** ***W*** **Mn**	Si, Al Na,Co Zr, Hf ***P, As*** ***In, Nb*** ***Pb, W*** **Ti, Ce**	Mn Sn,Sb ***Li, Zn*** ***Cd,Mo*** **Ni, Cu** **Ba, Tl**	P, Co As, Zr Ce,*Pb* ***Si, Ti*** ***Y, Nb*** ***REE*** ***Bi, U*** ***Th,* Sc**	Mn Cu ***Ni, Cd*** **Zn, Ga** **Mo,Ba** **Sb, W** **Tl**

Table 1. Correlations of Mn and Fe in pore waters, sediments, bulk nodules and nodule layers. Abbreviations: comp – component, corr – correlation, **Al (bold)** - strong (0.7-1) correlation, *Co (Italic)* - moderate (0.5-0.69) correlation, Sr (normal) - weak (0.3-0.49) correlation, Cu - correlation in all components , Ni - correlation in 3 components .

5 Discussion and conclusions

The natural environment for the nodules formation (bottom sediments, pore waters, organic matter) is a result of diagenetic processes (biogeochemistry, adsorption, desorption, transformation and migration), sedimentation rate, bioturbation, oxidation conditions, and certain bottom current conditions (Kotlinski and Stoyanova 2012; Hein and Koschinsky 2014).

In the pore water, Mn and Fe have the highest concentration in the geochemically active layer (Milakovska et al. 2022).The pore waters accumulate metals from oxidation of organic matter in the deep-ocean sediments resulting in the reduction and dissolution of Mn oxides and associated elements (Ni, Cu, Li). Owing to concentration gradients in the sediment, these metals diffuse upwards and, on contact with oxygen-rich ocean water, are reoxidized and precipitate as 7Å and 10Å Mn oxides (disordered phyllomanganates) (Hein et al. 2020). Manganese has positive correlation with Fe in pore waters but the correlation becomes negative in the sediments and polymetallic nodules.

The results suggest that Mn precipitates faster than Fe in the sediments and especially in nodules.

The latter are enriched in Mn, Ni and Cu compared to the host sediments. This trend can be traced on the Fe–Mn–(Co+Ni+Cu)x10 ternary diagram of Bonatti et al. (1972) (Figure 2.).

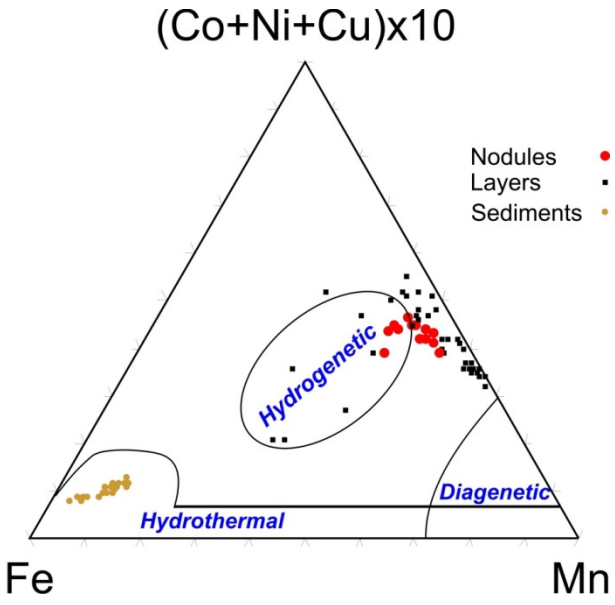

Figure 2. Ternary Fe–Mn–(Co+Ni+Cu)x10 diagram (Bonatti et al. 1972) for discrimination of polymetallic nodules and sediments.

The concentration of metals in the pore water depends mainly on the accumulation rate of sediments and the processes of dissolution, reduction and oxidation. In the sediments and nodules the metal deposition depends on the presence of nucleus (fragments of old nodules, sediment material, volcanoclastic rocks, bioclastic material), well oxygenated bottom waters, semi-liquid surface layer and bioturbation (Kotlinski and Stoyanova 2012). Two main types of nodule formation were distinguished – hydrogenetic and diagenetic precipitation, but often a mixed hydrogenetic-diagenetic type of precipitation was suggested (Hein et al. 2013).

The REE content in the studied pore waters is at least one order of magnitude higher than in the average bottom sea water (Li and Schoonmaker 2014) and shows MREE and HREE enrichment (Figure 3.). In contrast, the host sediments have two orders of magnitude higher REE contents than the pore waters and comparatively flat patterns. The nodules reveal 2-3 times higher REE contents than the host sediments, and in the richest nodule layers REEs are 2-3 times higher than their average content in bulk nodules.

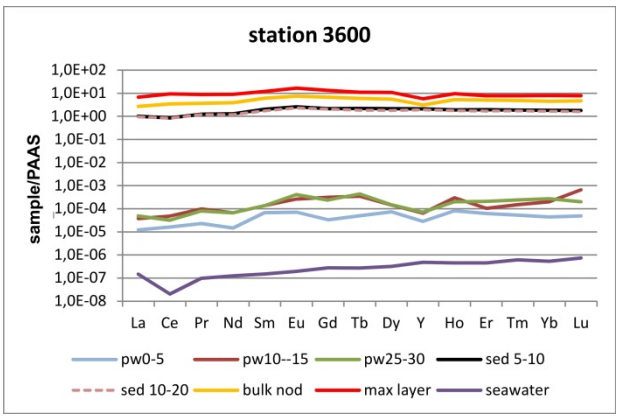

Figure 3. PAAS-normalized REE patterns of pore water layers (pw 0-5, pw 10-15, pw 25-30), sediments layers (sed 5-10, sed 10-20), bulk nodules (bulk nod) and the richest nodule layers (max layer) of station 3600 compared to average deep oceanic water (seawater) (Li and Schoonmaker 2014).

REE enrichment in deep-sea sediments is explained as the result of the interaction of several factors, including low sedimentation rate, presence of phosphate component near the seawater/sediment interface, high REE of the bottom seawater, oxidation conditions, and certain bottom current conditions (Ren et al. 2021). Generally, the REE accumulate mainly on Fe–Mn oxyhydroxide particulates (Dubinin 2014), and in a small degree incorporate into authigenic apatite. Our samples show positive correlation of REE with Fe and P. Negative Ce anomalies are characteristic for diagenetic Fe hydroxides, whereas a positive Ce anomaly is typical for hydrogenic nodules (Dubinin 2014; Hein and Koschinsky 2014). Our bulk analyses show no or weak positive Ce anomalies that is in line with the suggestion for a mixed hydrogenetic-diagenetic type. In the nodule layers the varying Ce anomalies suggest changing oxic/suboxic conditions. The Ce anomaly variations correlate with the Mn/Fe ratio and the genetic type (diagenetic or hydrogenetic) and could be a useful indicator for the nodule growth mechanisms (Hein and Koschinsky 2014).

The comparison of the results for the bottom sediments, pore waters and polymetallic nodules argue for a complexity of the processes that influence the formation of these deposits. The changing oxic/suboxic and anoxic conditions are well documented in the chemistry of the studied nodule layers. Probably the most important controlling factors are sedimentation rate, bioturbation, adsorption, desorption and oxidation.

Acknowledgements

The study was supported by Bulgarian National Science Fund grant KP-06-N34/6.

References

Bonatti E, Kraemer T, Rydell H (1972) Classification and genesis of submarine ironmanganese deposits. In: Horn D (Ed), Ferromanganese Deposits on the Ocean Floor, Natl. Sci. Found., Washington, pp 149–165

Dubinin A (2004) Geochemistry of Rare Earth Elements in the ocean. Lithology and Mineral Resources 39:289–307

Hein J, Koschinsky A (2014) Deep-Ocean Ferromanganese Crusts and Nodules. Treatise on Geochemistry 2nd Edition 7, pp. 273–291

Hein J, Mitzell K, Koschinsky A, Conrad T (2013) Deep-ocean mineral deposits as a source of critical metals for high- and green-technology applications: Comparison with land-based resources. Ore Geology Reviews 51:1–14

Hein J, Koschinsky A, Kuhn T (2020) Deep-ocean polymetallic nodules as a resource for critical materials. Nature Reviews Earth & Environment 1:158–169

Hikov A, Milakovska Z, Stoyanova V, Stefanova E, Abramowski T, Chavdarova S, Stavrev M (2022a) REE and trace elements distribution in the deep-sea sediments from the Interoceanmetal (IOM) polymetallic nodule exploration area in the Clarion-Clipperton fractures zone, NE Pacific. Compt Rend Acad Bulg Sci 75:1018–1027

Hikov, A, Stefanova E, Stoyanova V, Milakovska Z, Abramowski T, Chavdarova S, Stavrev M, Peytcheva I (2022b) Genetic types and REE composition of polymetallic nodules from the eastern part of the Clarion–Clipperton Fractures zone, NE Pacific. In: Christie, A. (ed.) Proceedings of the 16th SGA Biennial Meeting, 28-31 March 2022, 1, pp.129–132

ISBA/19/LTC/8 recommendations – (c) For chemical oceanography (i) Collect information on background water column chemistry, including water overlying the resource, in particular on metals and other elements that may be released during the mining process.

Kato Y, Fujinaga F, Nakamura K, Takaya Y, Kitamura K, Ohta J, Toda R, Nakashima T, Iwamori H (2011) Deep-sea mud in the Pacific Ocean as a potential resource for rare-earth elements. Nature Geoscience 4:535–539

Kotlinski R, Stoyanova V (2012) Nodule coverage, morphology and distribution in the Eastern CCZ. In: ISA, Technical Study No 6: Prospector's Guide for Polymetallic Nodule Deposits in the Clarion-Clipperton Fracture Zone, pp 34–42

Li Y-H, Sc hoonmaker J (2014) Chemical Composition and Mineralogy of Marine Sediments. Treatise on Geochemistry 2nd Edition 7, pp 1–35

Lyubomirova V., Mihaylova V., Djingova R. 2020. Chemical characterization of Bulgarian bottled mineral waters. Journal of Food Composition and Analysis, 93, 103595

Milakovska Z, Hikov A, Stoyanova V, Peytcheva I, Lyubomirova V, Abramowski T (2022) REY in pore waters of sediments hosting Fe-Mn nodules of the Interoceanmetal exploration area in the Clarion-Clipperton Fracture Zone, NE Pacific. Geologica Balcanica 51 (2):27–35

Pak S, Seo I, Lee K, Hyeong K (2019) Rare Earth Elements and Other Critical Metals in Deep Seabed Mineral Deposits: Composition and Implications for Resource Potential. Minerals 9 (1) 3:1–19

Ren J, Liu Y, Wang F, He G, Deng X, Wei Z, Yao H (2021) Mechanism and Influencing Factors of REY Enrichment in Deep-Sea Sediments. Minerals 11(2) 196:1–16

Inter- and intra-caldera, stratiform Zn-Pb-Ag and iron formation at Nyberg, Bergslagen, Sweden

Nils F Jansson[1], Anton Fahlvik[2], Rodney L Allen[3], Jenny Andersson[4]
[1]Division of Geosciences and Environmental Engineering, Department of Civil, Environmental and Natural Resources Engineering, Luleå University of Technology, 971 87 Luleå, Sweden
[2]Exploration Department, Boliden Mines, 776 98 Garpenberg, Sweden
[3]Volcanic Resources AB, Nås 230, 776 92 Hedemora, Sweden
[4]Geological Survey of Sweden, 751 28 Uppsala, Sweden

Abstract. The Nyberg Zn-Pb-Ag deposit is poorly known in comparison with some other, metamorphosed, c. 1.9 Ga stratiform Zn-Pb-Ag deposits in Bergslagen, Sweden (e.g., Zinkgruvan, Lovisa). Based on facies analysis, whole-rock lithogeochemistry, U-Pb zircon geochronology and sulphur isotope analysis, we argue that the deposit formed in a redox-stratified submarine intra-caldera basin which developed after a major, felsic, pyroclastic caldera-forming event at 1900±5 Ma. The widespread (>10km) host succession of mudstone, iron formation, sulphide mineralisation and limestone accumulated during a quiescent period prior to a resurgence in volcanism at c. 1890±3 Ma, during which a younger phase of intense, caldera-forming felsic volcanism ensued. Geochemical evidence points to an association between the waning stage 1900±5 Ma volcanism and the Nyberg mineralisation, whereas the 1890±3 Ma phase volcanism is associated with coeval porphyritic intrusions and granitoids which in turn are associated with, metasomatic Zn-Pb-Ag deposits elsewhere in the area.

1 Introduction

Stratiform Zn-Pb-Ag mineralisation in fine-grained volcaniclastic, siliciclastic and calcareous strata (e.g., Zinkgruvan, Lovisa) is one of the main types of c. 1.9 Ga, metamorphosed base metal sulphide deposits in Bergslagen, Sweden. Several deposits exhibit an intimate relationship with magnetite iron formation; the relatively unknown Nyberg deposit in central Bergslagen being a prime example. Here, a gradational is observed along and across strata from a banded iron formation of magnetite, amphibole and chlorite, into stratiform Zn-Pb-Ag mineralisation. The iron formation is more widespread than the sulphide mineralisation and has been correlated over a distance of more than 10 km along the folded and faulted stratigraphy in the area (Fig. 1). A progressively higher content of hematite and calcite is observed away from Nyberg.

This contribution presents a geological overview of the Nyberg deposit, focusing on the genesis of the sulphide deposit and its relation to adjacent iron oxide mineralisation.

2 Results

2.1 Structure and stratigraphy

The Nyberg deposit occurs in a belt of c. 1.91–1.89 Ga, mainly felsic metavolcanic rocks. This supracrustal succession is intruded by c. 1.89 Ga granite in the south (Fig.1). The deposit is hosted by the Jugansbo formation: An approximately 100 m thick succession of pelitic siliciclastic and volcaniclastic rock with minor intervals of marble and laminated-banded magnetite and sulphide mineralisation (pyrrhotite-sphalerite>galena) in skarns with amphibole (grunerite, actinolite), garnet (almandine-dominant) and chlorite (ripidolite). The deposit is interpreted to occupy a gently–moderately plunging, isoclinal F_1 syncline based on younging reversals (Figs. 1 and 2A), albeit the stratigraphy differs on each limb of the F_1 fold. The northern part of the deposit is affected by complex faulting and shearing.

Facies analysis show that the footwall to the mineralisation on the southern limb consists of a >500 m thick unit of massive rhyolitic pumice breccia with several normal graded juvenile volcaniclastic beds at the top (Högberget formation). At Nyberg, these rocks are pervasively albitized and silicified, with a sharp alteration contact towards the more alkali-depleted rocks of the Jugansbo formation. They overlie a succession of mainly fine-grained, reworked and re-sedimented felsic volcaniclastic deposits with limestone interbeds (Armanbo formation)(Fig.1).

A unit of massive, quartz-phyric rhyolitic silt-sandstone (IBM = 'in-between member') overlies the Nyberg deposit in the core of the F_1 syncline. Lithological zoning in the southern and northern parts of the Nyberg deposit is perfectly mirrored on each side of the IBM, albeit the footwall on the northern limb comprises a package of chloritic mudstone with bands and dissemination of calc-silicates and sulphides, underlain by organic-rich (graphitic) mudstone with local interbeds of limestone (calcite marble)(Fig 2A).

Further north, a tectonic contact exists towards a strongly foliated lens of chlorite+sericite-altered rhyolite (intra-shale rhyolite member). This unit is geochemically similar to the Högberget formation volcanic rocks (Fig. 2D), and is likely a tectonic sliver of these. A repetition of the Jugansbo formation is found further north, which is stratigraphically overlain by coarse-grained, rhyolitic volcaniclastic rocks of the Gransjön formation (Fig. 1). These differ from the Högberget formation in a higher abundance of quartz phenocrysts and a frequent occurrence of limestone clasts and interbeds. The contact to the Gransjön formation is marked by a vertical fault (GK fault) in Fig. 2A.

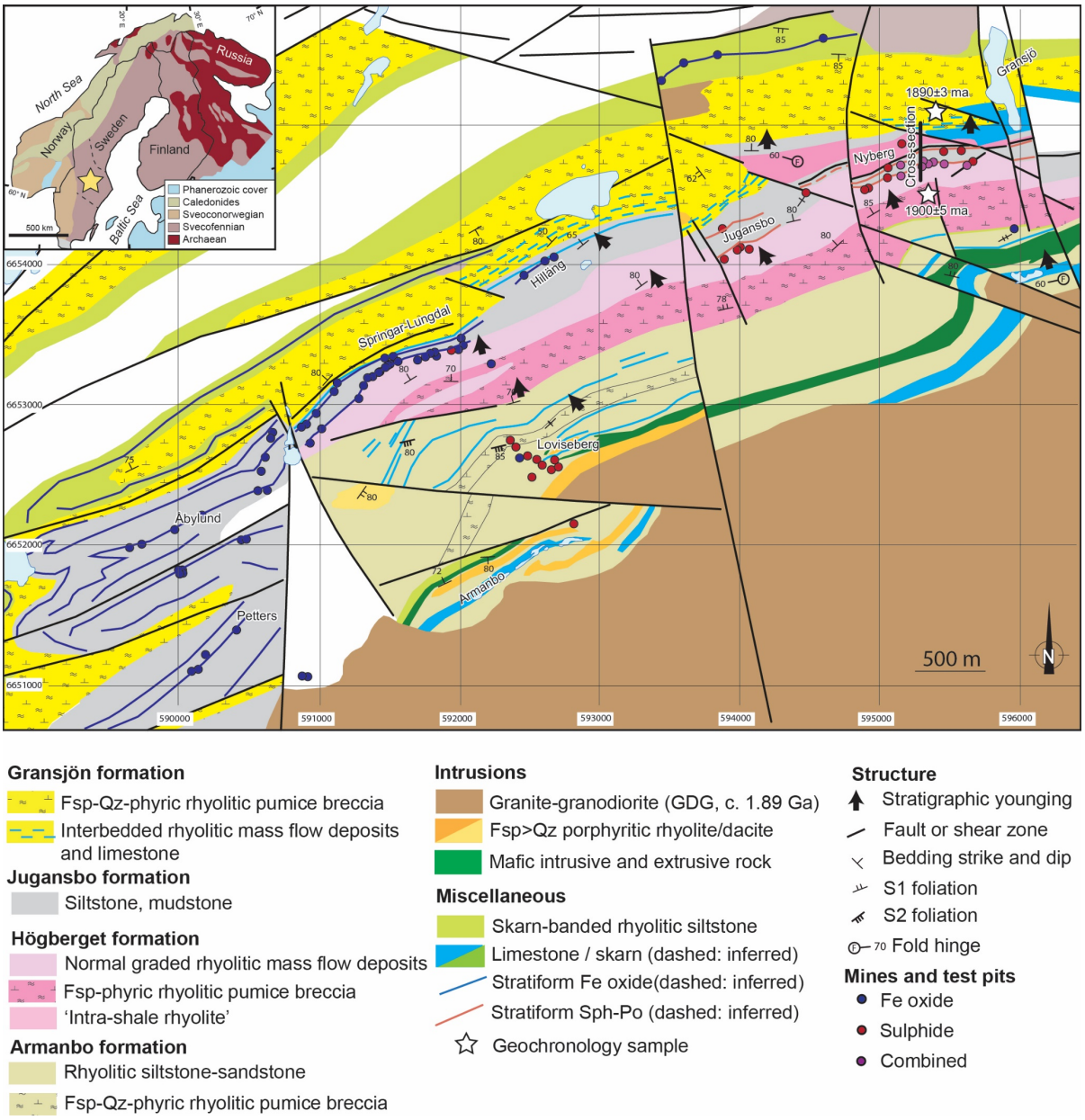

Figure 1. Geological map of the Jugansbo-Nyberg area, showing part of the extent of the Jugansbo formation and adjacent units. Grid is old Swedish national grid RT90. The cross-section in Figure 2 is indicated. Inset shows the location of Jugansbo in the Fennoscandian shield (Yellow star, the dashed lines show the northern and southern boundaries of Bergslagen).

2.2 Mineralisation

Sphalerite and pyrrhotite are the main sulphide minerals, with lesser galena and pyrite. The sulphides range from bedding-concordant laminae and dissemination to remobilized mineralisation in cross-cutting veins and breccias. The banded iron formation exhibits distinct stratification defined by interbedded magnetite, amphibole and chlorite (Fig. 2G). Hematite is entirely lacking but occurs in stratigraphically equivalent iron formation distal to Nyberg (e.g., Hilläng, Fig. 1). Iron formation at Nyberg is characterized by pronounced positive Eu anomalies (Eu/Eu^*_{PAAS} = 1.13–4.43) and negative Ce anomalies (Fig. 2D), whereas iron formation distal (>1km) to known sulphide mineralisation lack Eu anomalies. The Nyberg iron formation exhibits elevated contents of Mn, Zn, Co, Cu, Pb, Tl, Cs, Sn, Cd and S.

With regards to immobile element ratios, ore zone skarns exhibit ratios of Zr, TiO_2 and Al_2O_3, intermediate between Högberget and Gransjön volcanic rocks, and end-member mudstone such as Post-Archaean Australian Shale (PAAS, McDonough and Sun, 1995)(Fig. 2E). This is interpreted to reflect that many of the ore zone rocks are hybrid volcaniclastic-siliciclastic rocks.

2.3 Geochronology

Two juvenile rhyolitic pumice breccias were selected for U–Pb zircon Secondary Ion Mass

Spectrometry (SIMS) analysis (Fig. 2C): one from the Högberget formation pumice breccia below the sulphide deposit, and one from the Gransjön formation pumice breccia that overlies the sulphide deposit. Eleven concordant analyses with a Concordia age of 1896±5 Ma and a weighted average $^{207}Pb/^{206}Pb$ age of 1900±5 Ma set the maximum age for deposition of the Högberget formation pumice breccia. Ten concordant analyses with a Concordia age of 1892±3 Ma and a weighted average $^{207}Pb/^{206}Pb$ age of 1890±3 Ma for zircon in the Gransjön formation pumice breccia bracket the age of the Jugansbo formation. The age and lithogeochemistry of the Gransjön formation rhyolite are identical to that of the Sala granite (1891±6 Ma, Ripa et al. 2022).

2.5 Sulphur isotope geochemistry

Analysis of hand-picked concentrates of pyrite, sphalerite and pyrrhotite yielded consistently negative $\delta^{34}S_{V\text{-}CDT}$ values (-10.60 to -0.25 per mil)(Fig. 2F). A mixture of sulphur derived from leaching of volcanic rocks at $\delta^{34}S_{V\text{-}CDT} \approx 0$ per mil, and isotopically lighter sulphur derived thermochemical or bacteriogenic reduction of seawater sulphate can explain the sulphur isotope pattern at Nyberg. The latter processes are consistent with the presence of graphitic mudstone in the Jugansbo formation at Nyberg, which suggest that the depositional environment at the time of sulphide deposition was at times anoxic.

3 Discussion

The stratigraphy of the Armanbo and Högberget formations is similar to the footwall of many other mineralized units in Bergslagen in the sense that a several 100 meter-thick unit of pumiceous pyroclastic debris overlie shallow marine limestone strata. Allen et al. (1996) invoked caldera subsidence to explain the space needed to accommodate rapid deposition of voluminous, relatively homogeneous pyroclastic material.

In detail, ore zone skarns and chlorite schist exhibit compositions intermediate between PAAS and Högberget volcanic rocks. This is consistent with formation of the Nyberg deposit during the waning stage of Högberget volcanism. The positive Eu anomalies in the Nyberg iron formation are indicative of a hydrothermal origin of the iron formations and an oxic depositional environment, whereas the sulphur isotope data and the presence of graphite are more consistent with anoxic environment. These variations can be explained by fluctuations in the redox state of the basin over time. A sharp decrease in the redox state of the basin can explain the distinct shift from early Fe-rich non-sulphide mineralisation (now magnetite) to stratiform and disseminated sphalerite-pyrrhotite mineralisation on both limbs of the syncline. Absence of sulphides and graphite in a stratigraphically equivalent hematite-bearing iron formation west of Nyberg (e.g. Springar-Lungdal, Fig. 1) suggest lateral facies variations in what was likely a stratified marine, intra-caldera basin with depth variations. We suggest that the part of the Jugansbo formation which hosts the Nyberg deposit likely formed in a fault-bounded, relatively deep part of this basin, pointing to that post-eruptive, basinal processes controlled mineralisation. Lateral facies variations may explain the different footwall stratigraphies on the northern and southern limb of the Nyberg syncline.

The caldera model is also applicable to the Gransjön formation, which similar to Högberget formation is a several 100 thick pumiceous unit overlying shallow marine limestone strata (Fig. 2). This suggests that the Jugansbo formation formed during a pause in volcanism, which was favourable for the deposition of a hybrid succession of siliciclastic, volcaniclastic, ferrugineous and calcareous sediment. Resurgent volcanism at 1890±3 Ma (Gransjön volcanism) marks the end of the syngenetic mineralizing event described above. The IBM may possibly mark the onset of this event, as indicated by similarity in immobile elements to Gransjön volcanic rocks (Fig. 2D). The Gransjön volcanic rocks are remarkably geochemically similar to the bordering granite in the south, pointing to an intimate relationship between volcanic resurgence and plutonism. Together with incremental burial due to caldera subsidence, the magmatic resurgence may have induced a transition to skarn-type, metasomatic mineralizing systems associated with emplacement of granites and porphyritic intrusions as elsewhere in the area (e.g. Jansson et al. 2021).

Acknowledgements

This research has been carried out within the strategic innovation program Swedish Mining Innovation, a joint venture by Vinnova, Formas and the Swedish Energy Agency, with additional financial support from Boliden Mines and Björka Mineral. Martin Whitehouse and Kerstin Lindén (NordSIMS, NRM) are thanked for help during the SIMS analytical session. Jaroslaw Majka (UU) is thanked for assistance during EPMA session.

References

Allen RL, Lundström I, Ripa M, Simeonov A, Christofferson H (1996): Facies analysis of a 1.9 Ga, continental margin, back-arc, felsic caldera province with diverse Zn-Pb-Ag-(Cu-Au) sulfide and Fe oxide deposits, Bergslagen region, Sweden. Economic Geology 91:979-1008.

Jansson NF, Allen RL, Skogsmo G, Turner T (2021): Origin of Palaeoproterozoic, sub-seafloor Zn-Pb-Ag skarn deposits, Sala area, Bergslagen, Sweden. Miner Deposita:1-26.

McDonough WF, Sun SS (1995): The composition of the Earth. Chemical geology 120, 223-253.

Ripa M, Kübler L, Persson L, Göransson M (2002): Beskrivning till berggrundskartan 11G Västerås NO. Geological Survey of Sweden Af:70.

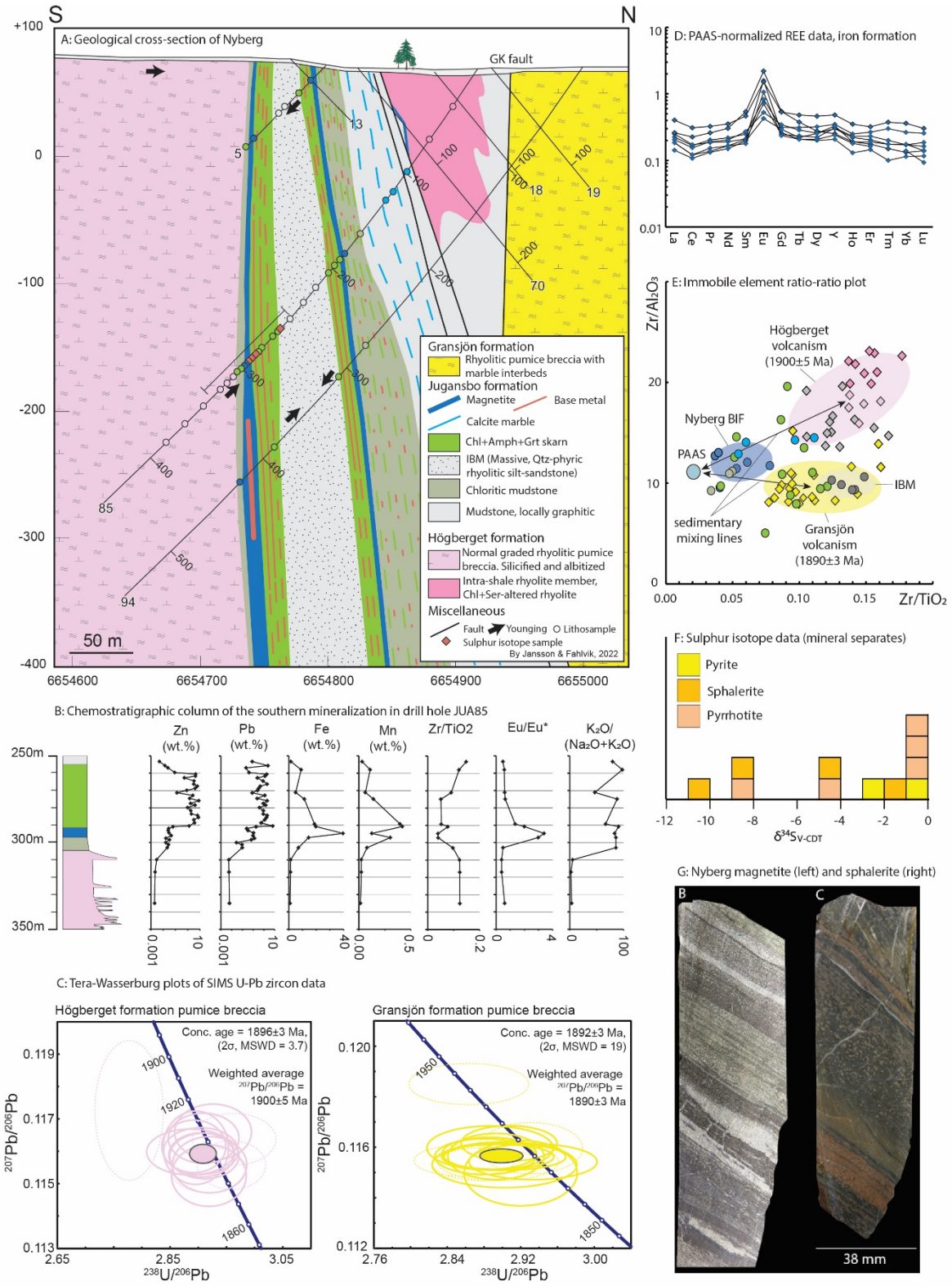

Figure 2. The Nyberg deposit, A: Geological cross-section, B: Whole-rock lithogeochemistry chemostratigraphy, C: Tera-Wasserburg plots of SIMS U-Pb zircon data and weighted average $^{207}Pb/^{206}Pb$ ages, D: Iron formation normalized to post-Archean Australian Shale (PAAS), using value of McDonough and Sun (1995), E: Immobile element ratio-ratio plot of key units, F: Sulphur isotope data (see Jansson et al. 2021 for method), G: Representative example of banded magnetite-tremolite-chlorite iron formation (left) and banded sphalerite mineralisation (right) from Nyberg. Dashed error ellipse in 2C indicate data omitted due to discordance or significant common Pb correction.

Lead isotope systematics of VMS deposits from Oman

Ana P Jesus' Thomas M Belgrano[2], André Cravinho[1], Bernhard Pracejus[3], Fatma Kourim[4], Kuo-Lang Wang[4], Mathieu Benoit[5], Mário A Gonçalves[1,6]

[1] *Instituto Dom Luiz, University of Lisbon, Portugal*
[2] *National Oceanography Centre, University of Southampton, UK*
[3] *Sultan Qaboos University, Oman.*
[4] *Institute of Earth Sciences, Academia Sinica, Taiwan*
[5] *Geoscience-Environment Toulouse, France*
[6] *Faculty of Science, University of Lisbon, Portugal*

Abstract. The Samail ophiolite in Oman, represents one of the most well-preserved remnants of the Tethyan oceanic crust, and hosts numerous mafic-hosted volcanogenic massive sulfide (VMS) deposits. In this work we present Pb isotopic data from 13 VMS deposits in Oman, in different volcanostratigraphic positions, as well as pristine volcanic glasses from the ophiolite main volcanic units. Our data shows that the volcanic units and VMS deposits in Oman exhibit a wide range of Pb isotopic compositions. The volcanic glasses show an increasingly radiogenic Pb isotopic composition from the Geotimes lava unit (V1) into the uppermost Boninitic Alley unit (V2), supporting significant isotopic modification of the mantle source trough time. The VMS deposits isotopic composition generally reflects that of their host volcanic units, indicating that the footwall represents the major source of Pb for each deposit. Some deposits hosted in the uppermost Tholeiitic and Boninitic Alley units, however, show highly variable isotopic signatures, possibly due to leaching of Pb from different volcanic units at depth. These results demonstrate shallower metal sourcing than is typically considered for VMS deposits and highlights the importance of the footwall volcanic architecture in controlling the metal endowment of the VMS deposits.

1 Introduction

The Cretaceous (*ca.* 95 Ma) Samail ophiolite in Oman, is the largest exposed remanent of the Tethyan oceanic lithosphere and has been intensely researched to unravel processes of formation and alteration of the oceanic crust and mantle. The Samail lavas hosts 17 known VMS deposits, totalling 58 Mt of ore with a weighted average grade of 1.5 wt% Cu, of which 6 deposits totalling 22 Mt of ore remain unmined (Fig. 1). Exploration is ongoing throughout much of the ophiolite. Although most VMS deposits in Oman are classified as Au-poor, there is growing evidence that deposits hosted in the Boninitic Alley units are Au-enriched (Gilgen et al. 2014).

Recently, significant effort has been devoted to refine the mapping of the volcanic sequence (Belgrano et al. 2019) and accurately locate the deposits within the volcanostratigraphy (Gilgen et al. 2014). Pb isotope compositions of samples recently collected from drill core and ore body outcrop from 13 deposits for Pb isotopes are presented here. This work aims to assess Pb sources of Oman VMS deposits relative to their host lavas, shedding light to the evolution of the ophiolite mantle source through time and the architectural source of metals within the Samail VMS mineral system.

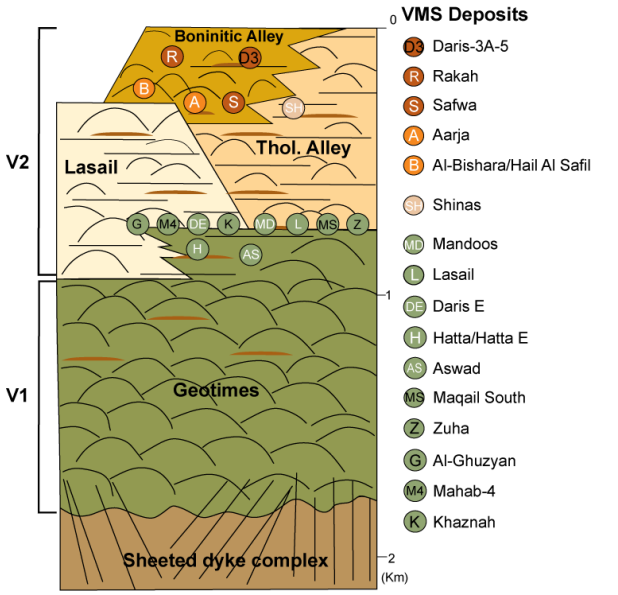

Figure 1. Schematic volcanostratigraphy of the Samail ophiolite showing the location of VMS deposits based on Belgrano et al. (2019), Gilgen et al. (2014) and Cravinho et al. (in press). Deposits are colour coded according to their footwall. Sampled deposits are labelled in white.

1.1 Samples and methods

Samples were collected from volcanic rocks and sulfide ore from throughout the Samail volcanostratigraphy (Figure 1). Samples include pristine glasses from each volcanic unit except for Geotimes, for which weakly hydrated but otherwise fresh, vitreous glass is the freshest material available. Massive ores are predominantly composed of pyrite (*Py*), chalcopyrite (*Ccp*), quartz, and minor sphalerite (*Sph*), with occasional magnetite, hematite, tennantite, and bornite.

Pb isotopes were analysed at the Institute of Earth Sciences, Academia Sinica (Taiwan) following the procedures reported in Wu and Huang (2021).

2 Results and discussion

Preliminary Pb isotope results are summarized in Figure 2. These results show a concomitant increase in radiogenic Pb in both the lavas and the

VMS deposits they host upwards through the stratigraphy.

2.1 Sources of Pb in Oman VMS deposits

With few exceptions, the isotopic signatures of the VMS ores broadly reflect the signature of their assigned footwall unit. The isotopic ratios of the pristine V2 glass samples, particularly the Boninitic Alley Unit, provide the necessary components to account for the most radiogenic sulfide signatures of the VMS deposits hosted by these lavas. These constraints have two main implications. One, is that Pb in the VMS ores was predominantly leached from shallow footwall lavas, which for the upper deposits requires sourcing from within the 0.5–2km thickness of the host volcanic units (Belgrano et al. 2019). Secondly, the trend from the Geotimes (V1) towards the Boninitic Alley (V2) unit requires a highly radiogenic component that defines a mixing line through the tight isotopic array ores and lavas. Such component could be acquired through assimilation of sediments via incorporation in a subduction zone, with consequent modification of the Samail mantle source zone.

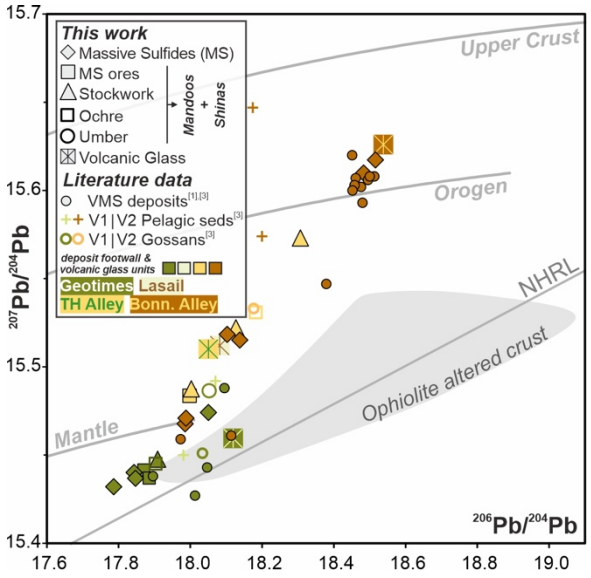

Figure 2. 207Pb/204Pb - 206Pb/204Pb isotopic systematics for the Samail rocks and VMS deposits. Plumbotectonic model curves for the evolution of the mantle, upper continental crust and orogen from Zartman and Doe (1981); North Hemisphere Regression Line (NHRL) from Hart (1984). Literature data (including "Ophiolite Crust"): [1] Chen and Pallister (1981); [2] Hamelin et al. (1984) and; [3] Calvez and Lescuyer (1991).

VMS deposits hosted in the V1 Geotimes lavas are less radiogenic than the Geotimes volcanic rocks. This feature may be tentatively related with the absence of pristine V1 rocks or volcanic glasses, whereas the sulfides, that do not incorporate significant radiogenic U, preserve their original Pb isotopic signatures. V1-hosted deposits may thus represent the best proxies for the original Pb isotopic composition of the Samail mantle source, prior to its modification during the V2 stage.

Deposits hosted in the Alley units show greater isotopic variation, which could be explained by hydrothermal fluids leaching a heterogenous footwall volcanic sequence. Similar reasoning can also explain the large-scale heterogeneities in the Boninitic Alley VMS deposits. Some of these present mixed compositions such as Safwa and Al-Bishara/Hail Al Safil, while others have solely compositions as unradiogenic as the Tholeiitic Alley (Daris 3) or Geotimes (Aarja) units (Figures 1 and 2). The proximity to V1 or Lasail lavas (Aarja), or the existence of deep faulting (Al-Bishara/Hail Al Safil) have been suggested as enabling leaching of lavas from more than one unit, resulting in a very large span of Pb compositions. The local crustal architecture underlying each deposit should thus be decisive to determine the pathways and metal endowment of VMS deposits in Oman.

Acknowledgements

This project has received funding from the European Union's Horizon 2020 research and innovation programme under the Marie Sklodowska-Curie grant agreement No 894599 and Portuguese Fundação para a Ciência e a Tecnologia (FCT) I.P./MCTES through national funds (PIDDAC) - UIBD/50019/2020-IDL.

References

Belgrano TM, Diamond LW, Vogt Y, Biedermann AR, Gilgen S, Al-Tobi K (2019) A revised map of volcanic units in the Oman ophiolite: insights into the architecture of an oceanic proto-arc volcanic sequence. Solid Earth 10:1181-1217.

Calvez JY, Lescuyer JL (1991) Lead Isotope Geochemistry of Various Sulphide Deposits from the Oman Mountains In: Peters T, Nicolas A, Coleman RG (eds) Ophiolite Genesis and Evolution of the Oceanic Lithosphere. Springer Netherlands, pp 385-397.

Chen JH, Pallister JS (1981) Lead isotopic studies of the Samail Ophiolite, Oman. Journal of Geophysical Research: Solid Earth 86:2699-2708. doi: 10.1029/JB086iB04p02699.

Cravinho A, Jesus A, Moreira B, Mateus A, Pracejus B, Figueiras J, Benoit M, Bauer W, Rocha F (in press) Contrasting Features and Volcanostratigraphy of the Mafic-Hosted Mandoos and Shinas Volcanogenic Massive Sulfide Deposits, Samail Ophiolite, Oman. Economic Geology.

Gilgen SA, Diamond LW, Mercolli I, Al-Tobi K, Maidment DW, Close R, Al-Towaya A (2014) Volcanostratigraphic Controls on the Occurrence of Massive Sulfide Deposits in the Semail Ophiolite, Oman. Economic Geology 109:1585-1610. doi: 10.2113/econgeo.109.6.1585.

Hamelin B, Dupré B, Allègre CJ (1984) The lead isotope systematics of ophiolite complexes. Earth and Planetary Science Letters 67:351-366. doi: http://dx.doi.org/10.1016/0012-821X(84)90174-2.

Hart SR (1984) A large-scale isotope anomaly in the Southern Hemisphere mantle. Nature 309:753-757. doi: 10.1038/309753a0.

Wu P-C, Huang K-F (2021) Tracing local sources and long-range transport of PM10 in central Taiwan by using

chemical characteristics and Pb isotope ratios. Scientific Reports 11:7593.
Zartman RE, Doe BR (1981) Plumbotectonics—the model. Tectonophysics 75:135-162. doi: https://doi.org/10.1016/0040-1951(81)90213-4.

Modelling of zinc mobilization by magmatic-hydrothermal circulation in the sub-seafloor

Benoit Lamy-Chappuis[1], Thomas Driesner[1]
[1]Institut of Geochemistry and petrology, ETH Zürich, Switzerland

Abstract. We present simulations of hydrothermal circulation triggered by the emplacement of magmatic intrusions in the sub-seafloor, we aim to understand and evaluate the processes controlling metal leaching from the host rock and transport to the seafloor. The simulations are conducted using a transport simulator allowing us to explicitly represent magmatic intrusions up to temperatures of 1000°C. We use water-NaCl as a proxy for the fluid chemical composition. To gain insights into metal mobilization, a basic zinc solubility model is added to the transport simulator, which considers the dissolution reactions of sphalerite. We present two sets of simulations, one with simplified setups and one with the real, albeit simplified topography of the seafloor resembling the TAG area of the mid-Atlantic oceanic ridge. The results show that the size and depth of the intrusion, as well as the depth of the seafloor, play a significant role in controlling the metal mobilization potential of hydrothermal fluxes. The simulations also highlighted the importance of understanding the complex interplay of structural and magmatic controls to better estimate the size and grades of seafloor resources.

1 Introduction

Magmatic intrusions emplaced in the sub-seafloor give rise to powerful and transient hydrothermal activity. The resulting hydrothermal fluxes can vary but the quantitative effect of possible controls such as ocean floor depth and topography, and the size and depth of intrusions have remained poorly constrained. Time-integrated fluxes may be decisive for the size of seafloor massive sulphide (SMS) deposits and more generally in determining the metal budgets of the oceans. As water is heated up in contact with the intrusion it can form a focused and hot (300-400°C) rising plume that can leach metals from the host rock. Metal solubilities strongly depend on temperature and salinity (among other parameters), which, in turn, depend on the characteristics of the hydrothermal fluxes and their complex evolution. Reactive transport modelling is a tool that can allow us to better apprehend these processes.

We conducted simulations of hydrothermal circulation driven by magmatic intrusions in generic setups and more realistic, “TAG-like” scenarios. To evaluate the metal mobilization potential of the hydrothermal fluxes we added a simplified zinc solubility model to the transport simulator. We aim to understand and evaluate the structural and magmatic controls on metal leaching of the host rock and transport to the seafloor. This might ultimately help understanding the systematics behind location, size, and grades of SMS deposits.

2 Concept and methods

We conduct simulations testing various scenarios of magma emplacement in the sub-seafloor to determine the controlling parameters of the metal mobilization processes. Our in-house transport simulator, developed on the CSMP++ platform allows us to explicitly represent the magmatic intrusions up to temperatures of 1000°C (Weis et al. 2014). We use water-NaCl as a proxy for the fluid properties and phase relations; this is particularly relevant for the systems under study since the fluid recharge will be of oceanic origin. Although this is probably still a crude approximation of the fluid compositions at depth, it is a fundamental improvement over simulations using pure water, in particular because we can capture salinity variations resulting from phase separation and the resulting metal fractionation as zinc will preferentially partition into the more saline liquid rather than into the low-salinity vapor phase.

We added a basic zinc solubility model to our transport simulator based on the equilibrium constants for sphalerite as $ZnCl^{+}, ZnCl_2^0, ZnCl_3^-$, and $ZnCl_4^{2-}$ as derived from the Supcrt92 database. We take advantage of the fact that the logarithms of equilibrium constants are linearly dependent on temperature when following water isochores. In practice, this allows us to use simple parametrization of the sphalerite solubility in function of temperature, density (a proxy for pressure), chloride activity, pH and sulphur activity. We make some major simplifications: chloride activity coefficients are not considered, and we do not simulate the evolution of pH and sulphur activity, instead we chose constant, plausible values that lead to solubilities in excess of the concentrations measured at active black smokers. In addition, we consider the case of 100% metal leaching efficiency.

Two sets of simulations are presented, the first one deals with simplified setups where an intrusion is emplaced at depth below a flat seafloor and where the host rock permeability does not exhibit heterogeneities. We use two intrusion sizes (4 and 16 km^3) and two different depths for the roof of the intrusion (3 and 5 km). The second set is derived from geophysical interpretation of the TAG area on

the mid-Atlantic oceanic ridge (deMartin et al. 2007). Here we use the real, albeit simplified topography of the seafloor and include a large detachment fault that dips steeply in the crust and terminates at approximately 10 km depth near a hypothetical magmatic region. We also investigate another "TAG-like" scenario where a smaller intrusion is emplaced at a shallower level (7 km) just below the current TAG vent field and below the detachment fault.

3 Simulations of zinc leaching triggered by the emplacement of a magmatic intrusion in the sub-seafloor

With these simulations using simple geometries, we aim to gain a first order understanding of the factors controlling metal fluxes to the seafloor. The models' dimensions are 10x10x10 km. The host rock permeability k decreases with depth according to $\log(k) = \log(k_b) - \alpha \log(z+1)$ where k_b is the baseline permeability and z the depth in km. The factor α controls the rate of decrease of permeability with depth. The permeability can be further reduced to impermeable values (10^{-22} m^2) once the rock reaches a temperature of 550°C. The rock porosity is constant at 5%, we assume a homogeneous initial distribution of zinc in the rock, with a mass fraction of 40 ppm. We use a heat flux bottom boundary condition of 100 $mW.m^{-2}$. The top boundary conditions are 6°C and a pressure that depends on the assumed seafloor depth (we calculate the expected hydrostatic pressure at the seafloor). Three seafloor depths are considered, 1, 2 and 3 km. At time t=0, the intrusion is instantaneously emplaced. The intrusions have a cubic shape and sizes of 4 or 16 km^3, the roof of the intrusions is either at 3 or 5 km depth.

Given the variations in ocean depth and intrusion size and depth, a total of 12 simulations were run. Figure 1 shows a time series of major parameters for one of the simulations. In this simulation, as in the others, we observe the formation of an intermediate density supercritical fluid directly above the intrusion, this fluid rises buoyantly towards the seafloor for as long as the intrusion is cooling. Phase separation into a low salinity vapor and high salinity brine can occur during the initial rise of the plume, particularly at lower pressures (shallower ocean) and for intrusions closer to the seafloor. The up flow remains focused directly above the intrusion for several thousands of years, its size is comparable to the size of the intrusion's roof. Figure 1 shows a constant stream of zinc-enriched fluid being established between the intrusion and the seafloor. As the hot fluids migrate towards the surface, they encounter a cold oceanic downflow, this results in a "funnel-like" zinc leaching pattern where the area of leaching gets narrower the further away from the intrusion. A direct consequence of mixing with cold oceanic water is that zinc is re-precipitated on the edge of this funnel, all the way from the intrusion to the seafloor, although this reduces the total amount of zinc reaching the seafloor it also has the effect of further focussing the zinc fluxes. This is possibly a necessary condition for obtaining high ore grades.

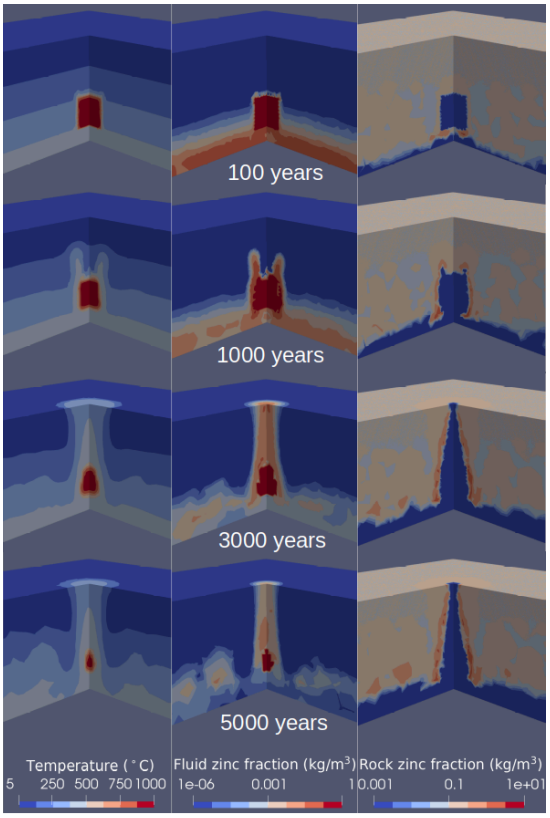

Figure 1. Time series of temperature, zinc mass fractions (in the rock and fluid) for the case of a 16 km^3 intrusion emplaced at 5 km and with a seafloor depth of 2 km.

In Figure 2 we show the total mass of zinc that exited the model on the seafloor boundary, this might be a good proxy for estimating the possible size of a deposit at the vent site. In most cases, the transport of zinc to the surface occurs over a short time frame with respect to the total magma cooling duration, it principally takes place during the initial flushing of hot fluids. This effect is most likely reinforced by our possibly unrealistic assumption of 100% leaching efficiency.

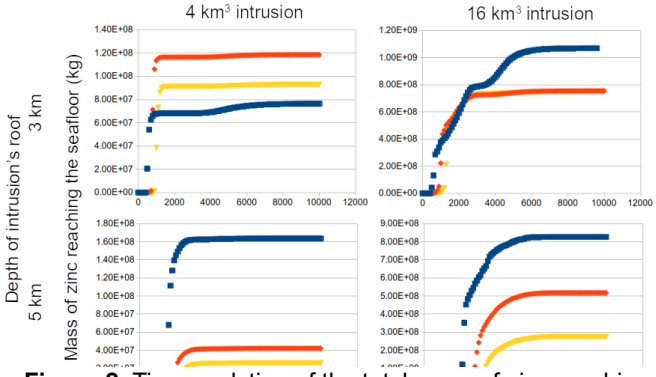

Figure 2. Time evolution of the total mass of zinc reaching the seafloor for 12 simulations with varying ocean depth and intrusion size and depth.

The total integrated zinc mass fluxes vary by two orders of magnitude, ranging from $2x10^7$ to $1.1x10^9$ kg. They approximately increase by one order of magnitude for the larger intrusions (despite the fact that the volume is only multiplied by 4 and the cross-sectional area by 2). For intrusions emplaced at 5 km depth, there is a clear trend of more zinc reaching the seafloor for shallower oceans, our interpretation is that this results from the driving force for oceanic fluid downflow being decreased. This would result in an enlargement of the leaching funnel (this is mostly visible in Figure 3 for the 16 km3 intrusion case at 5 km depth). This simple interpretation is insufficient to explain the results of the shallower intrusions (3 km depth) where there are no obvious trends. Further data processing will be necessary to properly explain the results from these simulations. It is apparent that shallower intrusions will have stronger hot plumes which will possibly override the counteracting downwards oceanic flows in non-trivial ways (depending on the oceanic depth or other parameters). It is for instance interesting to observe that shallower intrusions do not result in significantly lower total zinc mass fluxes even though there would be less rock available to be leached. Another important effect of oceanic depth not yet fully analysed here is the possibly to drastically change the density of the fluids present in the subsurface (due to pressure change). For instance, much more phase separation (via condensation of a supercritical fluid) occurs for shallower intrusions and oceans, this would directly affect the zinc carrying capacity of the fluids.

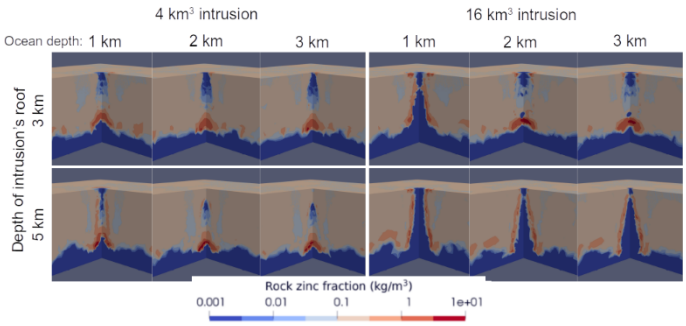

Figure 3. Rock zinc fractions in the centre of the models after 10000 years for all simulations.

4 Simulations of zinc leaching in "TAG-like" scenarios

We applied our model to a more realistic scenario. Following the interpretations of deMartin et al. (2007) and Canales et al. (2007), we designed a model aimed at resembling the TAG area on the mid-Atlantic oceanic ridge. We used bathymetric data to build a simplified geometry of the seafloor. The controls on hydrothermal fluxes towards the TAG vent field are still uncertain but one possible interpretation, put forward by deMartin et al. (2007) is that the fluids are channelled along a large detachment fault before being diverted in the hanging wall. A possible driver for the hydrothermal circulation is a large magma body at 10 km depth. It is particularly interesting to evaluate the importance of the structural and magmatic controls on the hydrothermal fluxes and consequently the metal fluxes. Is it possible to focus hydrothermal fluids with a setup such as the one shown in Figure 4? If yes, would they carry significant amounts of metals?

In our "TAG-like" setup, the permeability is behaving similarly to the previous simulations, the porosity and initial zinc rock fractions are also the same. The assumed damage area of the detachment fault is volumetrically meshed and has a permeability of 10-14 m2 and a thickness of 100m. We ran the simulations for 10000 years; the results are shown in Figure 5 and 6. We observe no strong up flow of zinc at the seafloor with this setup; however, we observe the slow development of a focused up-flow zone in the fault. This might develop further if the simulation were run for longer. Alternatively, a larger fault permeability might lead to faster and stronger up-flow and potentially zinc reaching the surface.

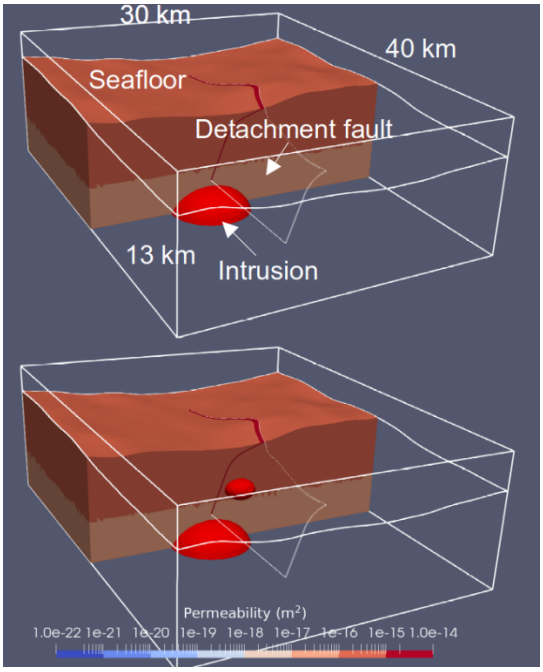

Figure 4. Geometry of the detachment fault, seafloor and initial intrusions for the two "TAG-like" setups.

In a second simulation, we added a hypothetical intrusion, smaller and at a shallower level, below the TAG area (see Figure 4). After 10000 years, there is now a clear zinc fingerprint at the seafloor, where the TAG main vent should be located (Figure 6). This is clearly a direct consequence of having an intrusion directly below and at a shallower level. Interestingly, the presence of the fault only had a very marginal impact on the fluid and metal fluxes which simply traversed the fault vertically.

5 Discussion and conclusions

Intrusions can lead to the transport of metals and energy towards a focused area on the seafloor. In our simulations, the total amount of ore depends on parameters such as ocean depth, intrusion size and depth. It is now necessary to constrain the results of these simulations with real data to gain better insights into the subsurface processes acting in the real world.

Faults can also participate in focussing the fluids and enhancing mass fluxes due to their high permeability; however, a fault dominated hydrothermal system might not enable the significant enrichment of a seafloor deposit since one can expect that the amount of source rock would be greatly limited if fluids were to principally be transported through faults. More simulations are required to understand the effect of variations in the fault and host rock permeability.

In the case of TAG, we envision that the intermittent rise of magma batches from 10 km depth to shallower levels could explain the transient presence of anomalously high temperature flows having the capacity to carry zinc. In our scenario (second TAG-like setup), the presence of the large detachment fault has an impact on the hydrothermal fluxes but is not responsible of the zinc accumulation on the seafloor. It would be valuable to further study the relative strengths and the interplay of the structural and magmatic controls in more realistic scenarios.

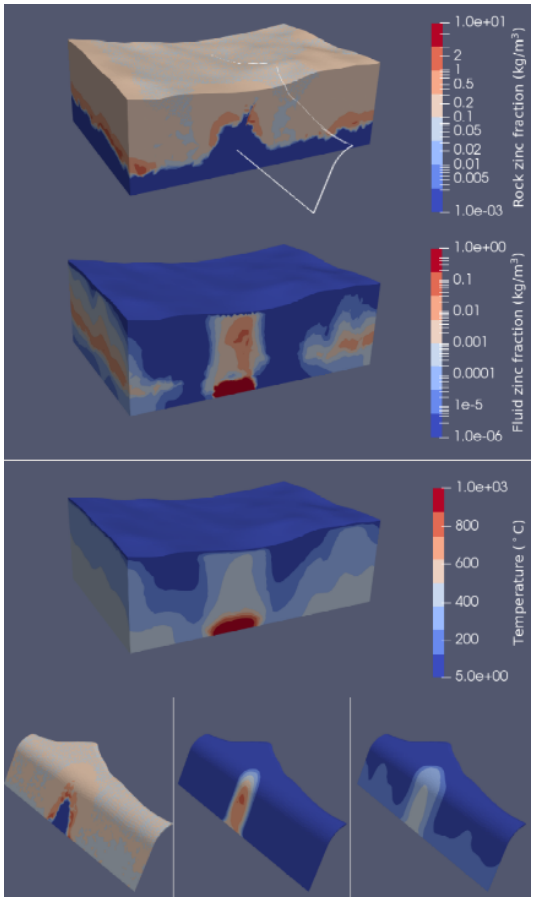

Figure 5. Result after 10000 years of the "TAG-like" simulation in the first setup, shown in a cross-section and on the detachment fault plane.

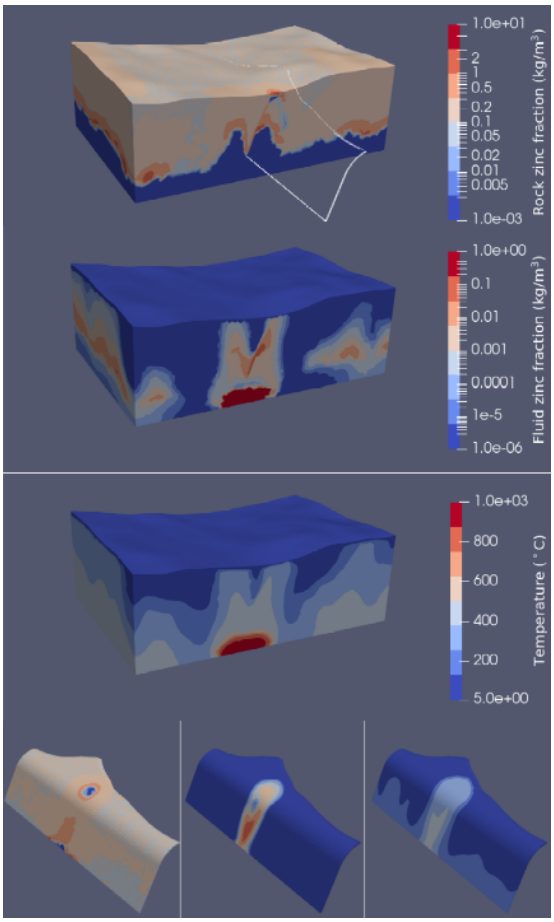

Figure 6. Result after 10000 years of the "TAG-like" simulation in the second setup (with a shallower intrusion added), shown in a cross-section and on the detachment fault plane.

Acknowledgements

We would like to thank Equinor Energy AS for funding this research.

References

Canales, J.P., Sohn, R.A., Demartin, B.J. (2007): Crustal structure of the Trans-Atlantic Geotraverse (TAG) segment (Mid-Atlantic Ridge, 26 degrees 10-Minutes-N): Implications for the nature of hydrothermal circulation and detachment faulting at slow spreading ridges. Geochemistry Geophysics Geosystems, 8: 18.

deMartin, B.J., Canales, R.A.R., Canales, J.P., Humphris, S.E. (2007): Kinematics and geometry of active detachment faulting beneath the Trans-Atlantic Geotraverse (TAG) hydrothermal field on the Mid-Atlantic Ridge. Geology, 35(8): 711-714.

Weis, P., Driesner, T., Coumou, D., Geiger, S. (2014): Hydrothermal, multiphase convection of H2O-NaCl fluids from ambient to magmatic temperatures: a new numerical scheme and benchmarks for code comparison. Geofluids, 14(3): 347-371.

Fluid overprinting in an oceanic detachment fault: micro-analysis of pyrite from 13°30' N on the Mid-Atlantic Ridge

Andrew J. Martin[1], John W. Jamieson[2], Sven Petersen[3], Mostafa Fayek[4]
[1]Geoscience, University of Nevada, Las Vegas, USA
[2] Department of Earth Sciences, Memorial University of Newfoundland, Canada
[3]GEOMAR – Helmholtz Centre for Ocean Research Kiel, Germany
[4]Department of Earth Sciences, University of Manitoba, Canada

Abstract. Detachment faults are crustal-scale normal faults that can exhume mantle lithologies at the seafloor. Hydrothermal fluids in detachment fault hosted hydrothermal systems have been shown to be more oxidizing than those observed in a typical basalt-hosted system. Oxidizing fluids produce a hydrothermal mineral assemblage characterised by hematite, magnetite and pyrite. Microtextural and in-situ geochemical as well as isotopic ($\delta^{34}S$) analysis of pyrite from 13°30'N on the Mid-Atlantic Ridge illustrate the effect of fluctuating fluid redox on the distribution and enrichment of metals across individual mineral grains. Nickel and Co are remobilized from the grain margin toward the core during fluid overprinting, forming distinct enrichment fronts that overprint primary micron-scale oscillatory zonations that formed in response to temporal variations in the composition of primary hydrothermal fluids. Sulphur isotope ratios systematically increase (up to 9.2‰) toward the grain margin where secondary zonations are present. This increase indicates that larger amounts of sulphur are derived from thermochemical sulphate reduction of seawater, likely related to periods of fault movement and seawater ingress in the shallow subsurface. Thus, the presence of oxidizing fluids, which may be analogous to the waning stage of hydrothermal venting in many deposits, can remobilize and concentrate metals across individual sulphide grains.

Formation age of Kosaka Uchinotai-West Kuroko Deposit, NE Japan, determined by Re-Os isotope analysis

Mizuki Ogasawara[1], Junichiro Ohta[2,3], Mizuki Ishida[1], Moei Yano[3,1], Kazuhide Mimura[3,1], Kazutaka Yasukawa[2,1], and Yasuhiro Kato[1,3].

[1] *Department of Systems Innovation, School of Engineering, The University of Tokyo*

[2] *Frontier Research Center for Energy and Resources, School of Engineering, The University of Tokyo*

[3] *Ocean Resources Research Center for Next Generation, Chiba Institute of Technology*

Abstract. The north-eastern (NE) Honshu arc of Japan is the type locality of the Kuroko-type volcanogenic massive sulphide (VMS) deposits. Major Kuroko deposits in Japan are distributed in the Hokuroku District in the NE Honshu arc, approximately 40 km × 40 km in size. This study applied rhenium (Re)-osmium (Os) radiometric dating to determine the formation age of the Kosaka Uchinotai-West deposit. The Re-Os isochron age of 13.314 ± 0.070 Ma with initial $^{187}Os/^{188}Os$ ratio of 0.7568 was obtained. The initial $^{187}Os/^{188}Os$ ratio is consistent with the Miocene seawater $^{187}Os/^{188}Os$ ratio. The isochron age implies that the Kosaka Uchinotai-West deposit was formed at the end of Nishikurosawa stage. During this period, the deep-sea environment in the Sea of Japan is considered to have been depleted in oxygen, which could have contributed to the preservation of the Kuroko deposits formed on the seafloor.

1 Introduction

The volcanogenic massive sulphide (VMS) deposits are defined as strata-bound massive sulphide-sulphate deposits associated with submarine volcanic activities. Because of its economic significance for producing copper and other critical metals, VMS deposits are under exploration in several countries (e.g., Tornos et al. 2015).

The north-eastern (NE) Honshu arc of Japan is the type locality of the Kuroko-type VMS deposits. Kuroko deposits in Japan are found in the Green Tuff region. Although Green Tuff is widely distributed in Japan, major Kuroko deposits are distributed in the Hokuroku District, approximately 40 km × 40 km in size (Figure 1).

Previous studies have suggested that the formation of the Kuroko deposits in Japan is associated with back-arc bimodal volcanism which formed the Sea of Japan in the early to middle Miocene (e.g., Jolivet et al. 1994; Yamada and Yoshida 2011). Direct and precise dating of the Kuroko ores will provide important constraints to understand the ore genesis in detail by correlating with the geologic events relating to the back-arc extension.

The Re-Os geochronology is an effective tool to directly determine the formation ages of sulphide deposits (e.g., Nozaki et al. 2013). Terakado (2001) analysed one to three samples from each of the four Kuroko-type deposits in the Hokuroku District (Fukazawa, Kosaka, Shakanai, and Hanaoka deposits) and reported a single isochron age of 14.32 ± 0.51 Ma with the initial $^{187}Os/^{188}Os$ ratio of 0.7563 ± 0.0047 by combining all the data for these deposits. However, individual age for each deposit has not been determined. Further analyses focusing on each deposit are necessary for discussing the Kuroko ore genesis more in detail. Here, as a first step, we implemented Re-Os isotope analysis of ore samples from the Kosaka Uchinotai-West deposit and determined its formation age.

2 Geological Background

Kuroko deposits in the Hokuroku District, including the Kosaka deposit, are hosted in middle Miocene Nishikurosawa Unit, which is composed of acidic tuff and rhyolite lava. Nishikurosawa Unit is conformably overlain by middle Miocene Onnagawa Unit, which consists of acidic pumice tuff and basaltic to rhyolitic lava. The inferred age of the boundary between the Nishikurosawa and Onnagawa Units is 16.7–12.4 Ma based on zircon U-Pb dating and biostratigraphy (Yoshioka et al. 2021).

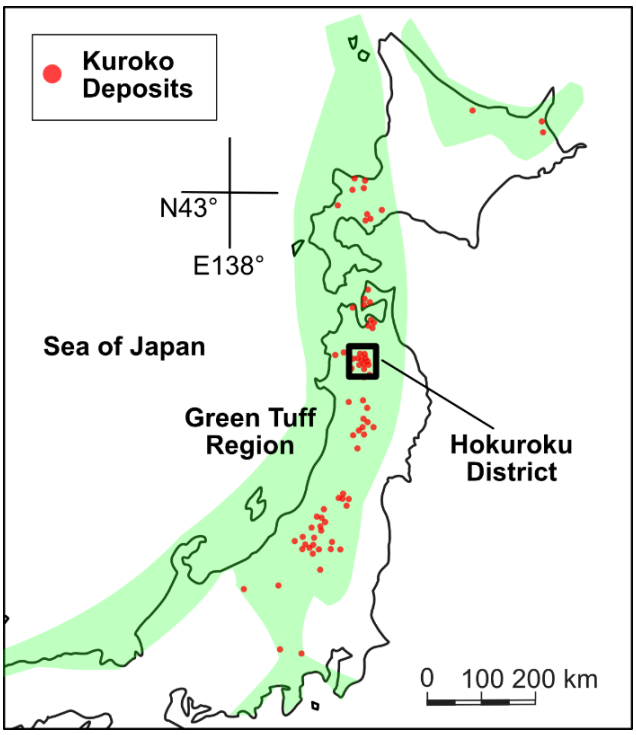

Figure 1. Distribution of Kuroko deposits in Japan and location of the Hokuroku District (modified after Shikazono 2003).

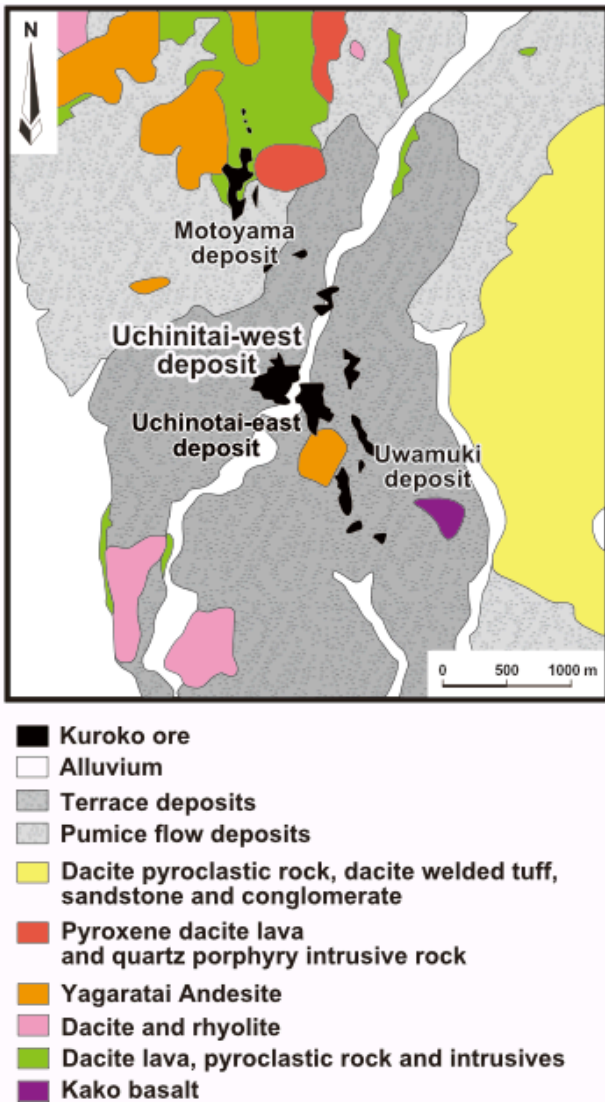

Figure 2. Geological map of Kosaka deposit (modified after Nakajima 1988).

The Kosaka deposit is a Kuroko-type Cu-Pb-Zn-Au-Ag deposit located at the eastern margin of the Hokuroku District. Its reserves are estimated to be about 9.2 million tons of ore (Cu 2.5 %, Pb 1.3 %, Zn 4.2%). The Kosaka deposit, covering about 2 km × 4 km in size, consists mainly of Motoyama, Uchinotai, and Uwamuki ore deposits (Figure 2). The Uchinotai deposit, discovered in 1959, is composed of two large orebodies called Uchinotai-West and Uchinotai-East and one small orebody called Otarube. The Uchinotai-West and Uchinotai-East deposits have a total reserve of about four million tons of sulphide ore (Urabe and Sato 1978).

3 Samples

The ores from the Kuroko deposits are classified into two types based on their mineral assemblages. Kuroko ores (black ores) consist mainly of sphalerite, galena, barite and contain minor quantities of chalcopyrite, pyrite and tetrahedrite. Oko ores (yellow ores) consist mainly of chalcopyrite and pyrite. Five black ores and three yellow ores from

Figure 3. Kuroko and Oko ore samples from Kosaka Uchinotai-West Deposit analysed in this study.

Kosaka Uchinotai-West deposit (Figure 3) were selected and split into 10 black ore and five yellow ore subsamples in total. This study analysed these 15 subsamples from the Kosaka Uchinotai-West deposit.

4 Methods

After crushing the samples, the sulphide grains were hand-picked and powdered using an agate mortar and pestle.

The Re-Os isotope analyses were performed using a multiple collector-inductively coupled plasma-mass spectrometer (MC-ICP-MS) at Ocean Resources Research Center for Next Generation (ORCeNG), Chiba Institute of Technology, Japan, following the analytical procedures by Ohta et al. (2022). Approximately 0.4 g of sulphide sample was weighed, spiked with ^{185}Re and ^{190}Os, and digested with 4 mL of inverse aqua regia and 1 mL of $HClO_4$ in a sealed Carius tube heated at 220° C for 24 h. The analytical procedures applied in this study is

shown in Figure 4. Two samples, one black ore sample and one yellow sample, were analysed as duplicate to check analytical reproducibility.

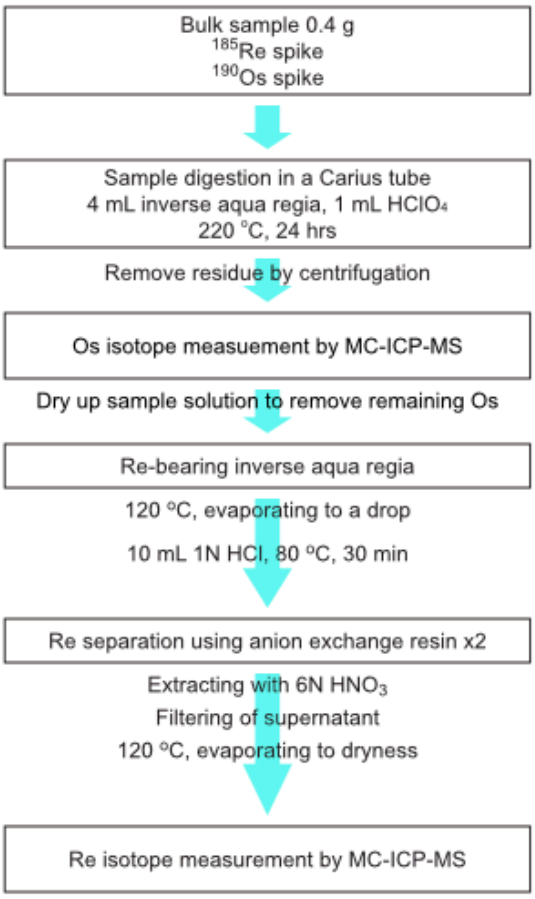

Figure 4. Analytical procedure for Re-Os isotope analysis in this study.

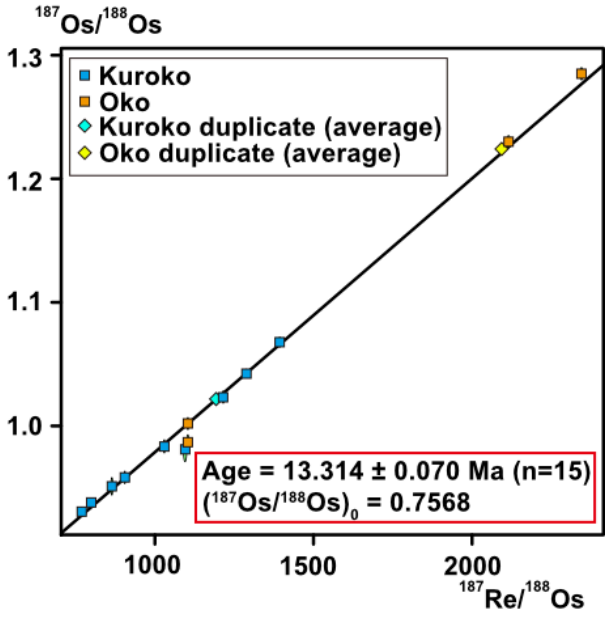

Figure 5. Re-Os isochron for Kosaka Uchinotai-West deposit obtained in this study. Online version for IsoplotR (Vermeesch 2018) was used.

5 Results

The black ore samples showed Re and Os concentrations of 10–56 ppb and 54–299 ppt, respectively. The yellow ore samples showed Re and Os concentrations of 16–50 ppb and 80–123 ppt, respectively. The duplicated analysis resulted in almost identical values, and thus we consider that the influence of analytical error on the isochron age is negligible.

$^{187}Re/^{188}Os$ and $^{187}Os/^{188}Os$ ratios of the 15 data points ranged 769.2–2345 and 0.9305–1.2849, respectively. The 15 data points yielded an isochron age of 13.314 ± 0.070 Ma with initial $^{187}Os/^{188}Os$ ratio of 0.7568 (Figure 5).

6 Discussion

Considering the inferred age of the boundary of Nishikurosawa/Onnagawa Units (see Geological background), the Re-Os age obtained by this study shows that the Kosaka Uchinotai-West deposit is likely to have been formed at the end of Nishikurosawa stage.

The initial $^{187}Os/^{188}Os$ ratio obtained by this study is 0.7568, which falls in the range of $^{187}Os/^{188}Os$ isotope ratio of the middle Miocene seawater, approximately 0.73–0.83 (e.g., Goto et al. 2023). It is generally accepted that VMS deposits like Kuroko deposits are produced on seafloor, with mixing of hot hydrothermal fluids and cold seawater causing precipitation of sulfides (e.g., Ohmoto 1996; Franklin et al. 2005). Therefore, the obtained initial $^{187}Os/^{188}Os$ ratio may indicate that the ores of Kosaka Uchinotai-West deposit preserve $^{187}Os/^{188}Os$ ratio of middle Miocene seawater, with relatively small influence of hydrothermal fluid, under a condition similar to the present-day submarine hydrothermal systems (Urabe and Sato 1978).

At the Nishikurosawa/Onnagawa boundary, the deep-sea environment in the Sea of Japan changed from oxic to reducing condition (e.g., Kimura et al. 2004). Since exposure to oxygenated seawater before burial into sediments would oxidize and dissolve sulphide ores, low-oxygen conditions in the water column would have played an important role in the preservation of sulphide ores of the VMS deposits (e.g., Otake et al. 2021). Therefore, the deoxygenation of seawater at the Nishikurosawa/Onnagawa boundary could have contributed to the effective preservation of the Kosaka Uchinotai-West deposit.

7 Conclusion

In this study, Re-Os geochemistry of the samples from Kosaka Uchinotai-West deposit were analysed using a MC-ICP-MS. The Re-Os isochron age of 13.314 ± 0.070 Ma with initial $^{187}Os/^{188}Os$ ratio of 0.7568 was obtained. The initial $^{187}Os/^{188}Os$ ratio is consistent with $^{187}Os/^{188}Os$ of the middle Miocene seawater. This may support that they originated from

seafloor hydrothermal activity in the middle Miocene. Further studies on the formation ages of each deposit would contribute to elucidating the relations between Kuroko ore formation in the Hokuroku District and the opening of the Sea of Japan more in detail.

Acknowledgements

This research was financially supported by Japan Society for the Promotion of Science (JSPS) KAKENHI Grants No. JP20H05658 to Y.K. and No. JP20J22038 to M.I. The authors thank Mr. Kaoru Kiyota of the University Museum, the University of Tokyo, for providing us with the samples of Kosaka deposit. We also thank Ms. Kana Ashida of ORCeNG, Chiba Institute of Technology, for supporting us with the laboratory equipment.

References

Franklin JM, Gibson HL, Jonasson IR, and Galley AG (2005) Volcanogenic Massive Sulfide Deposits. In JW Hedenquist, JFH Thompson, RJ Goldfarb and JP Richards (Eds.), One Hundredth Anniversary Volume (pp. 0). Society of Economic Geologists. 10.5382/AV100.17

Goto KT, Tejada MLG, Tajika E., and Suzuki K (2023) Enhanced magmatism played a dominant role in triggering the Miocene Climatic Optimum. Communications Earth and Environment 4(1):21-8. doi: 10.1038/s43247-023-00684-x

Jolivet L, Tamaki K, and Fournier M (1994) Japan Sea, opening history and mechanism: A synthesis. Journal of Geophysical Research - Solid Earth 99(B11):22237-22259. doi: 10.1029/93JB03463

Kimura S, Shikazono N, Kashiwagi H, and Nohara M (2004) Middle Miocene–early Pliocene paleo-oceanic environment of Japan Sea deduced from geochemical features of sedimentary rocks. Sedimentary Geology 164(1):105-129. doi: 10.1016/j.sedgeo.2003.08.003

Nakajima T (1988) Geological map for mineral resources assessment of the Hokuroku district. Geological Survey of Japan.

Nozaki T, Kato Y, and Suzuki K (2013) Late Jurassic ocean anoxic event: evidence from voluminous sulphide deposition and preservation in the Panthalassa. Scientific Reports 3(1):1889. doi: 10.1038/srep01889

Ohmoto H (1996) Formation of volcanogenic massive sulfide deposits: The Kuroko perspective. Ore Geology Reviews 10(3):135-177. doi: 10.1016/0169-1368(95)00021-6

Ohta J, Nozaki T, Sato H, Ashida K, and Kato Y (2022) A precise and accurate analytical method for determination of osmium isotope ratios at the 1-15 pg level by using a MC-ICP-MS equipped with sparging introduction and high-sensitivity discrete dynode-type ion-counting detectors. Journal of Analytical Atomic Spectrometry 37(8):16-161. doi: 10.1039/d2ja00089j

Otake T, Yamada R, Suzuki R, Nakamura S, Ito A, Shin K, and Sato T (2021) Large Fe isotope fractionations in sulfide ores and ferruginous sedimentary rocks from the Kuroko volcanogenic massive sulfide deposits in the Hokuroku district, northeast Japan. Geochimica et Cosmochimica Acta 295:49-64. doi: 10.1016/j.gca.2020.12.009

Shikazono N (2003) Geochemical and tectonic evolution of arc-backarc hydrothermal systems: implications for the origin of Kuroko and epithermal vein-type mineralizations and the global geochemical cycle. Elsevier Science.

Terakado Y (2001) Re-Os dating of the Kuroko ore deposits from the Hokuroku district, Akita Prefecture, Northeast Japan. Chishitsugaku Zasshi 107(5):354-357. doi: 10.5575/geosoc.107.354

Tornos F, Peter JM, Allen R, and Conde C (2015) Controls on the siting and style of volcanogenic massive sulphide deposits. Ore Geology Reviews 68:142-163. doi: 10.1016/j.oregeorev.2015.01.003

Urabe T, and Sato T (1978) Kuroko deposits of the Kosaka Mine, Northeast Honshu, Japan; products of submarine hot springs on Miocene sea floor. Economic Geology and the Bulletin of the Society of Economic Geologists 73(2):161-179. doi: 10.2113/gsecongeo.73.2.161

Vermeesch P (2018) IsoplotR: A free and open toolbox for geochronology. Geoscience Frontier 9(5):1479-1493. doi: 10.1016/j.gsf.2018.04.001

Yamada R, and Yoshida T (2011) Relationships between Kuroko volcanogenic massive sulphide (VMS) deposits, felsic volcanism, and island arc development in the northeast Honshu arc, Japan. Mineralium Deposita 46(5-6):431-448. doi: 10.1007/s00126-011-0362-7

Yoshioka J, Kuroda J, Takahata N, Sano Y, Matsuzaki KM, Hara H, Auer G, Chiyonobu S, and Tada R (2021) Zircon U-Pb dating of a tuff layer from the Miocene Onnagawa Formation in Northern Japan. Geochemical Journal 55(3): 185-191. doi: 10.2343/geochemj.2.0622

Geological settings, distribution, and resource potential of seafloor hydrothermal systems

Sven Petersen[1], Mark D. Hannington[2], John Jamieson[3], Thomas Monecke[4], Meike Klischies[1],
[1] *GEOMAR – Helmholtz Centre for Ocean Research Kiel, 24148 Kiel, Germany*
[2] *Department of Earth and Environmental Sciences, University of Ottawa, Canada*
[3] *Department of Earth Sciences, Memorial University of Newfoundland, Canada*
[4] *Department of Geology and Geological Engineering, Colorado School of Mines, Colorado, USA*

Abstract. Over the past decades, the main target areas for exploration for seafloor massive sulfides (SMS) have shifted from fast spreading ridges, to back-arc basins and recently to ultra-slow and slow-spreading ridges. These changes are often linked to changes in our understanding of the importance of certain processes in the formation of large sulfide deposits on the modern ocean floor. Similarly, the growing body of information on the deposits themselves, the increasing resolution of geophysical, topographic, geological, and geochemical datasets is influencing our view on SMS formation and resource potential. This more detailed information allows us to investigate the importance of the local geological setting in deposit formation, helping us to understand the processes responsible for the formation of large and economically interesting deposits.

1 Introduction

Seafloor massive sulfides occurrences (SMS) have become a target of increased global exploration activity due to their presumed resource potential. Recent investigations have shown that these occurrences are more variable than previously thought (incl. native sulphur springs as well as talc-rich deposits) and that this variability is not necessarily reflected in volcanogenic massive sulfide deposits preserved in the ancient rock record.

The regional geological setting has profound impacts on water depth, source rocks, permeability, vent fluid chemistry and hence on the geochemical composition and mineralogy of the sulfides deposited at or below the seafloor. Spreading rate tends to be one of the major factors affecting the accumulation, distribution, and ultimately the resource potential of seafloor massive sulfides at spreading centers. Currently, 435 sulfide-bearing or high-temperature hydrothermal sites have been reported throughout the global ocean, indicating the widespread occurrence of this type of seafloor mineralization (Figure 1). Most of these occurrences are, however, hydrothermally active and tend to be in an early stage of development. Following the classification of Jamieson and Gartman (2020) nearly 75 % of the known sites are either actively venting high-temperature fluids (Figure 2) or they have been described as being hydrothermally active, either with low-T venting or the exit temperatures were not measured. Additionally, active vent sites commonly host chemosynthetic faunal communities that will receive strong protection by the regulation of

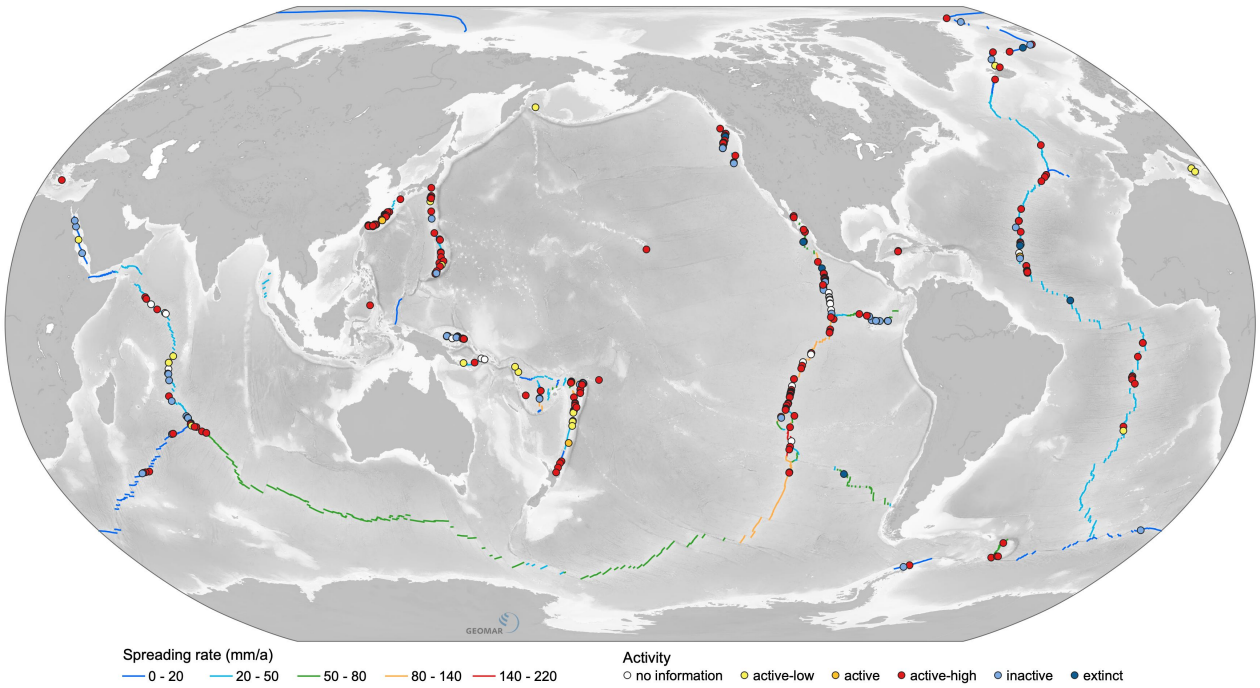

Figure 2. Global distribution of seafloor hydrothermal systems with respect to reported activity and spreading rate (N=435). Note that the scarcity of sites in the southern oceans is related to a lack of exploration.

mining activities in areas beyond national jurisdiction. Around 22 % of the known sites are described as being inactive. They are commonly located close to active vent sites or in an environment where a renewal of hydrothermal activity is possible or even likely. A few sites are considered to be extinct because they are located far off-axis with no evidence of any recent magmatic or hydrothermal activity in their surroundings. Inactive and extinct sites, that have gone through a full life-cycle of metal deposition, where hydrothermal activity has ceased, and where vent-specific macrofaunal communities have disappeared, are seen as a possible mining target. These systems lack the prominent water column signature and are more difficult to locate. Many extinct sites are considered to be located at even greater distance to the neovolcanic zone increasing the area that needs to be explored to several million km^2 (Petersen et al., 2018)

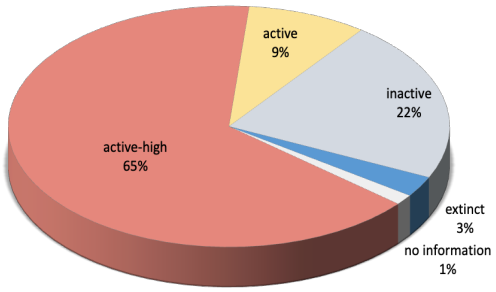

Figure 2. Style of activity of known SMS occurrences (N=435).

2 Global settings of SMS occurrences

Most of the known SMS occurrences are associated with basaltic host rocks formed at mid ocean ridges (54%; Figure 3). Additional 7 % of the currently known sites are associated with exposed mantle and/or lower crustal rocks (UM), usually at slow-spreading mid-ocean ridges. Intraoceanic back-arc basins are another important setting (15 %), followed by subduction-related arc volcanoes (12 %). Recent exploration in the Okinawa Trough, the only known intracontinental hosting seafloor massive sulfides, resulted in a large number of discoveries in this extensional setting.

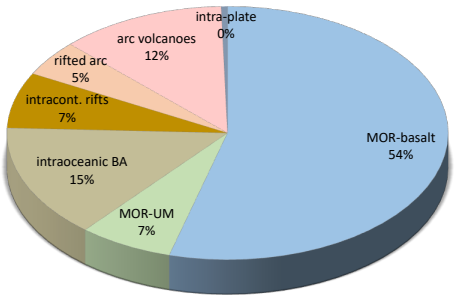

Figure 3. Regional geological setting of known SMS occurrences (BA = back-arc; MOR = mid-ocean ridge; UM = ultramafic).

Occurrences associated with rifted arc crust account for 5 % of the known sites. Currently, only two sulfide-bearing sites are associated with intraplate volcanism.

3 The importance of slow-spreading ridges

Over the past years considerable effort has focused in exploring ultra-slow- and slow-spreading mid-ocean ridges, but also slow-spreading segments within back-arc basins such as the Mariana Trough or the Lau Basin. New discoveries of large sulfide occurrence have been made, especially in the Indian Ocean (Pak et al., 2017; Wang et al., 2017; Kim et al., 2020; Tao et al., 2020; Yang et al., 2023; Schwarz-Schampera, in prep), often as a result of ongoing exploration activities of contractors to the International Seabed Authority.

These discoveries extend the variability of regional and local geological settings of SMS formation even further, providing evidence for substantial mineralization also in non-transform offsets or associated with large off-axis volcanic plateaus. Another area of intense exploration is located in the Okinawa Trough, a region with extensional volcanism and a plate separation velocity similar to those of slow-spreading ridges. Here, numerous hydrothermal sites have been discovered, with some of them of possible economic potential (Kawano and Furuya, 2022).

One of the main reasons for the intense exploration in slow-spreading environments is the favorable metal content (Cu, Au) and size of many of the documented occurrences at slow-spreading ridges (Hannington et al., 2011; German et al., 2016).

Slow-spreading ridges are, overall, tectonically very active, including the formation of deep-reaching faults in the neovolcanic zone and at some distance to it. Along some shallow-dipping faults (detachment faults) tectonic forces expose rocks of lower crustal or mantle origin in tectonic massifs and at oceanic core complexes and allow the interaction of hydrothermal fluids with these source rocks.

The presence of such large-scale faulting has been suggested to be responsible for long-lived and even periodic hydrothermal activity at some sites, possibly explaining why most of the large known SMS occurrences are located at slow-spreading ridges (Hannington et al., 2011). This includes a number of vent fields, such as the TAG and Semyenov vent fields on the Mid-Atlantic Ridge, that contain a number of individual large vent sites or mounds, each of which could be considered a possible mining target (Cherkashov et al., 2013; Graber et al., 2020).

At both these sites, some of the massive sulfide mounds occur in the hanging wall of the detachment faults and are associated with intense extensional faulting. This specific geological setting may account for the large size of these deposits. Overall, the concentration of the sulfide tonnage into smaller

areas seems to be more common at slow-spreading ridges when compared to their faster equivalents.

Available ship-based bathymetry and advances in geological interpretation indicate that a simple tectonic vs. magmatic classification (German et al., 2016) does not capture all of the important settings of SMS formation. Instead, several distinct settings for SMS formation can be classified in mid-ocean ridge environments (Klischies et al., this volume). Similar distinct classes of different deposit types can also be considered for the subduction related settings. Based on published geochemical analyses of SMS occurrences globally, an enrichment of copper, gold and other trace metals is apparent in many of the sites associated with slower spreading rates, especially those associated with the exposure of lower crustal and mantle rocks. At the same time, slow- and ultra-slow spreading ridges are a major portion of the global ridge system (36% and 24% of the global ridge length; Fig. 1) that is still under-explored, thereby representing a large permissive area.

4 Resource potential

The resource potential of seafloor massive sulfides is a consequence of their bulk chemical composition and their size. Geochemical data is available for over 180 sites, however, published datasets are commonly missing data for some trace elements. Still, the data shows a high variability on a regional scale reflecting plate tectonic settings and associated source rock controls. Seafloor massive sulfide deposits associated with rifted arc crust or with ultramafic host rocks at mid-ocean ridges often contain higher concentrations of copper compared to basalt-hosted deposits at mid-ocean ridges, (Fig. 4).

Gold and silver are also enriched in some settings, especially in intraoceanic back-arc basins, volcanic arcs, and at ultramafic-hosted mid-ocean ridge systems, where concentrations of these precious metals can reach several tens of ppm for gold and hundreds of ppm for silver (Fig. 4). Certain trace elements, some of which of growing importance for modern society occur in concentrations of only a few tens of ppm, but can be significantly enriched in some deposits.

Some of the uncertainty in global resource estimates for SMS lies in the enormous range in the perceived sizes (tonnage) of many modern seafloor massive sulfides. These deposits are three-dimensional but information from the subseafloor are sparse. Visual inspection of their surface morphology and from sampling indicates that some may reach a thickness of several tens of meters. However, most known sites have a diameter of less than a few tens of meters and, thus, contain only a small amount of sulfide material (a few thousand tons to 100,000 tons).

Some occurrences on the global mid-ocean ridges, however, are estimated to contain between 100,000 tons and 1 million tons of massive sulfide (Hannington et al., 2011).

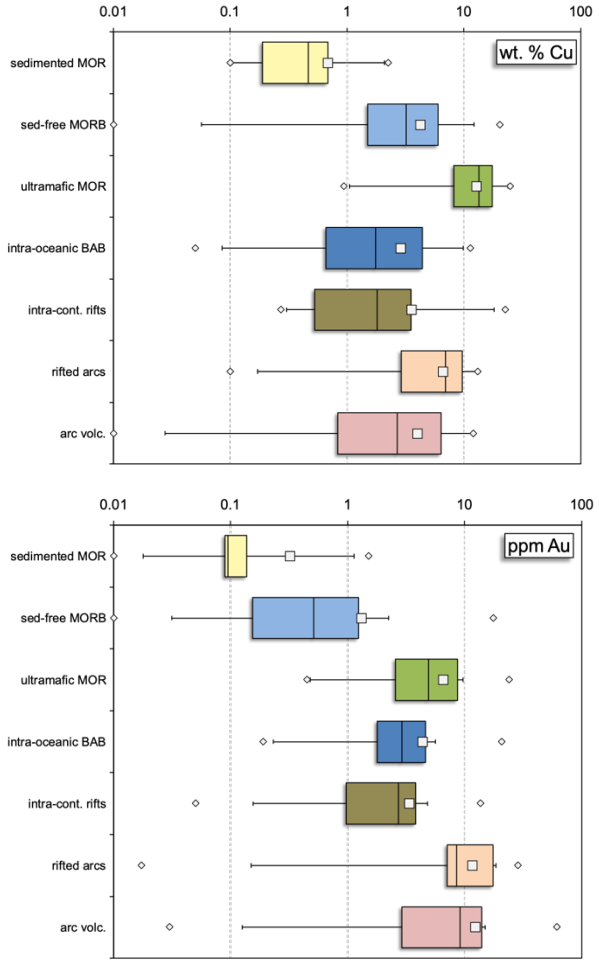

Figure 4. Box-and-Whisker-plot showing the range, average, and median of Cu and Au in SMS sites from various geological settings (N=185 averages of SMS occurrences; MOR = mid-ocean ridge; BAB = back-arc basin).

Very few are thought to be as large as 10 million tons. Hence, only a small number of known massive sulfide deposits are large enough to be considered as economically interesting. This contrasts with the size distribution of ancient deposits, which are generally much larger (Hannington 2014). The data for land-based deposits, however, is strongly biased towards large deposits because it includes only data for deposits that were large enough to be mined or to justify drilling. Many small sulfide occurrences are not included in resource data.

5 Global Exploration

At present the International Seabed Authority, responsible for administering seafloor resource in areas beyond national jurisdiction (ABNJ, “the Area”), has issued seven fifteen-year contracts for exploration of seafloor massive sulfides since 2011.

As a consequence of the presumed larger potential of SMS at slow-spreading ridges, these contract areas are all located along slow- to ultraslow-spreading ridges. All contractors are representatives of national governments (China, Russia, South Korea, France, India, Germany, and Poland). Four contract areas are located in the Indian Ocean, the remaining three in the Central Atlantic. Each original contract area covered 10.000km^2, however, due to mandatory relinquishments after 8 and 10 years, the area currently under contract by ISA is only 55.000km^2.

In addition to the work performed by the various contractors to the ISA, the last years have seen intensified exploration within the exclusive economic zones of selected countries. In Japan, a multi-year R&D project on marine mineral resources intensified seabed exploration. Within this project successful mining tests were performed at seafloor massive sulfide occurrences in the Okinawa Trough in 2012, 2015, and 2017.

In recent years, Norway has engaged in deep sea exploration within their EEZ through activities of the Norwegian Petroleum Directorate and is currently considering to open its EEZ for exploration.

Acknowledgements

We thank the Marine Mineral Resources group at GEOMAR and the Metal Oceans team at the University of Ottawa for discussions. Numerous colleagues contributed over the years by sharing their knowledge and observations. M. Hannington was also supported through a Discovery Grant from the Natural Sciences and Engineering Research Council of Canada.

References

Cherkashev GA, Ivanov VN, Bel'tenev V, et al (2013) Massive sulfide ores of the northern equatorial Mid-Atlantic Ridge. Oceanology 53: 607–619. https://doi.org/10.1134/S0001437013050032

German CR, Petersen S, Hannington MD (2016) Hydrothermal exploration of mid-ocean ridges: Where might the largest sulfide deposits be forming? Chemical Geology 420:114–126. https://doi.org/10.1016/j.chemgeo.2015.11.006

Graber S, Petersen S, Yeo I, et al (2020) Structural Control, Evolution, and Accumulation Rates of Massive Sulfides in the TAG Hydrothermal Field. Geochem Geophys Geosyst 21. https://doi.org/10.1029/2020GC009185

Hannington M, Jamieson J, Monecke T, et al (2011) The abundance of seafloor massive sulfide deposits. Geology 39: 1155–1158. https://doi.org/10.1130/G32468.1

Hannington MD (2014) Volcanogenic Massive Sulfide Deposits. Treatise on Geochemistry, Vol. 2 13, 463–488. http://doi.org/10.1016/B978-0-08-095975-7.01120-7

Jamieson JW, Gartman A (2020) Defining active, inactive, and extinct seafloor massive sulfide deposits. Marine Policy 117:103926. https://doi.org/10.1016/j.marpol.2020.103926

Kawano S, Furuya H (2022) Mining and processing of seafloor massive sulfides: experiences and challenges. In, Sharma R Perspective on Deep-Sea Mining. Springer Verlag. Switzerland. https://doi.org/10.1007/978-3-030-87982-2_7

Kim J, Son SK, Kim D, et al (2020) Discovery of active hydrothermal vent fields along the Central Indian Ridge, 8–12°S. Geochem Geophys Geosyst 21. https://doi.org/10.1029/2020GC009058

Klischies M, Petersen S, Schwarz-Schampera U et al (2023) Deposit models for seafloor massive sulfides from remote sensing data. This volume.

Pak S-J, Moon J-W, Kim J, et al (2017) Widespread tectonic extension at the Central Indian Ridge between 8°S and 18°S. Gondwana Research 45, 163–179. http://doi.org/10.1016/j.gr.2016.12.015

Petersen S, Lehrmann B, Murton BJ (2018) Modern Seafloor Hydrothermal Systems: New Perspectives on Ancient Ore-Forming Processes. Elements 14:307–312. https://doi.org/10.2138/gselements.14.5.307

Schwarz-Schampera U (in prep.) The INDEX exploration concept – introduction and rationale. In: U. Schwarz-Schampera (ed), Exploration of Marine Minerals – First results from the INDEX Campaign on Polymetallic Massive Sulfides.

Tao C, Seyfried WE, Lowell RP, et al (2020) Deep high-temperature hydrothermal circulation in a detachment faulting system on the ultra-slow spreading ridge. Nature Communications 1–9. http://dx.doi.org/10.1038/s41467-020-15062-w

Wang Y, Han X, Petersen S, et al (2017) Mineralogy and trace element geochemistry of sulfide minerals from the Wocan Hydrothermal Field on the slow-spreading Carlsberg Ridge, Indian Ocean. Ore Geology Reviews 84, 1–19. http://doi.org/10.1016/j.oregeorev.2016.12.020

Yang W, Liao S, Dias A, et al (2023) Geochemistry, sulfur and lead isotopic composition of hydrothermal sulfide from the Duanqiao hydrothermal field on the Southwest Indian Ridge: implications for ore genesis. International Geolology Review 65(3), https://doi.org/10.1080/00206814.2022.2081937

Reconstructing the formation of volcanic-associated Lahn-Dill-type iron ores from fluid venting to seafloor deposition

Leanne Schmitt[1,2], Thomas Kirnbauer[1], Thomas Angerer[3], Sabine Klein[4,2], Dieter Garbe-Schönberg[5], Vladimir Roddatis[6]

[1]Faculty of Georesources and Process Engineering, TH Georg Agricola, Bochum, Germany
[2]Institute of Geology, Mineralogy and Geophysics, Ruhr-Universität Bochum, Germany
[3]GeoSphere Austria, Wien, Austria
[4]Deutsches Bergbau-Museum Bochum, Germany
[5]Institute of Geosciences, Christian-Albrechts-Universität, Kiel, Germany
[6]Interface Geochemistry Section, Helmholtz Centre Potsdam, Germany

Abstract. Volcanic-associated Fe-oxide mineralisation of the Lahn-Dill-type formed in pre-Variscan restricted, shallow marine basins. They are located in the hanging wall of thick volcaniclastic rocks marking the Middle to Upper Devonian boundary. One of the largest Lahn-Dill-type iron ore mines (Fortuna mine) has been sampled in order to elucidate the interplay of genetic processes leading to ore formation as well as the environment in which ores formed. Petrography revealed that ores most likely formed from a Fe-Si gel. Primary and diagenetic gel textures include spherules and aggregates composed of nanocrystalline hematite dispersed in quartz, or of hematite accumulations that are associated with pores in quartz. Local post-depositional Fe(III) reduction within the gel is indicated by siderite replacing hematite. In-situ mineralogical and textural microdomain (md) chemistry analysed by laser ablation ICP-MS displays four different source and formational trace element signatures related to (1) syngenetic apatite nanoinclusions, (2) scavenging by Fe-(oxyhydr)oxides, (3) (volcani)clastic contamination and (4) diagenetic mobilisation of REY in pore water. These signatures imply that ores formed related to diffused venting of a low-T fluid and subsequent rapid Fe-(oxyhydr)oxide precipitation. These processes were favoured in Silurian to Carboniferous restricted shallow marine basins that were characterised by extensive volcanic and hydrothermal activity.

1 Introduction

Marine volcanic-associated Fe-oxide mineralisation formed from the Precambrian until today. They are interpreted to have formed related to an interplay of volcanic-, hydrothermal-, marine- and microbial processes and therefore represent archives of basin sedimentation and marine environmental conditions, and are also important sources for iron.

Volcanic-associated Fe-oxide mineralisation of the Lahn-Dill-type formed in the restricted and shallow Rhenohercynian-, Saxothuringian- and Moravo-Silesian marine basins. They have been described mainly from the eastern Rhenish Massif, the Harz Mountains, central Saxothuringia and the Eastern Sudetes, but similar volcanic-associated marine Fe-oxide mineralisation also occur in western and southeastern Europe. Lahn-Dill-type iron ores are associated with Middle to Upper Devonian alkali basaltic volcanic and volcaniclastic rocks (Quade 1976). Ores formed either related to chemical precipitation (sedimentary-type) or to metasomatic replacement of wall rocks (replacement-type).

Lahn-Dill-type iron ores (sedimentary-type) are usually composed of hematite and quartz, with minor siderite and magnetite. Their Fe grade ranges from 30 to 40 wt.%. Due to low metamorphic overprint (< 300°C), ores display many primary and early diagenetic textures making them favourable to study mineral transformation and textural changes from sedimentation to metamorphism.

Whole rock geochemistry of marine Fe-oxide mineralisation is a conventional tool to decipher ocean chemistry and variations of the redox state. Mineral-specific minor and trace element geochemistry may however, provide a more detailed image of element fractionation during mineral formation. Trace elements in Fe-(oxyhydr)oxides are for instance interpreted to reflect the solution from which they precipitated (Bau 1999), whereas syngenetic apatites rather record ocean chemistry (Alibert 2016). Detecting these mineral-specific element fractionation mechanisms may provide insights that are masked in whole rock geochemistry.

We therefore, sampled one of the largest Lahn-Dill-type iron ores mines (Fortuna mine) and conducted a systematic petrography from the micro- to nano-scale (optical microscopy, REM, TEM) and microdomain chemistry (LA-ICP-MS) to reconstruct the unique depositional environment and venting mechanisms during Lahn-Dill-type ore formation.

2 Fortuna mine geology

The Fortuna mine is located within the Lahn-syncline (eastern Rhenish Massif, Germany) which is part of the Rhenohercynian Zone of the Variscan orogenic belt. Lithostratigraphy within the Fortuna mine is mainly characterised by a thick volcanic succession composed of green (distal to ore) and purple (proximal to ore) volcaniclastic rocks (Fig. 1a). Several thin (0.1 to 0.5 m) ore lenses are intercalated with purple volcaniclastic rocks near the top of the succession (position A ores; Fig. 1a, b). The main ore body is ~5 m thick and located on top of the volcaniclastic succession (position B ores; Fig. 1a, c). Sampled ore types are composed either of hematite and quartz forming sedimentary-type hematite-quartz ores, or subordinately of siderite, hematite and quartz forming sedimentary-type siderite-hematite ores. The latter occur rather at the

top of the position B ore body. Hanging wall rocks are composed of volcaniclastic and clastic sedimentary rocks with occasionally intercalated limestone. The above described stratigraphic sequence was overprinted by Variscan low-grade metamorphism, regional to local thrusting and folding and local hydrothermal carbonate-quartz-hematite-(chlorite-apatite) veins.

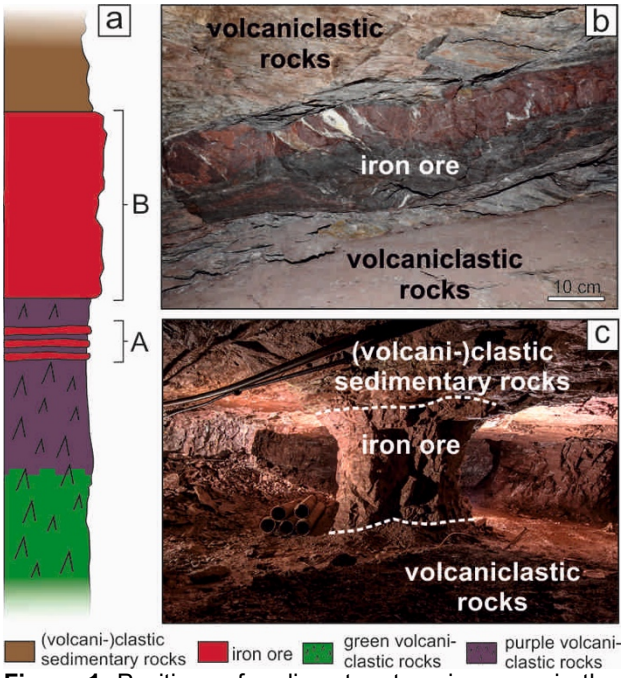

Figure 1. Positions of sedimentary-type iron ores in the Fortuna mine. **a** Lithostratigraphic profile depicting position A and B ores. Note that depicted thicknesses of drawn stratigraphic units do not correspond with true thicknesses due to graphic reasons. **b** Photo of position A ores and **c** of position B ores (iron ore layer ~5 m; image in **c** by courtesy of Roger Lang/Geowelt Fortuna e.V).

3 Methods

Fortuna mine position A and B ores were sampled and analysed using a reflected light microscope and a scanning electron microscope (SEM). High-resolution microscopy down to the nano-scale was carried out with a Thermo Fisher Scientific (former FEI) Tecnai F20 G2 and Themis Z 80-300 transmission electron microscope (TEM). For in-situ bulk microdomain geochemical analysis, a 193 nm ArF excimer laser ablation system (GeoLasPro Plus, Coherent) coupled to an Agilent 8900 inductively coupled plasma mass spectrometer (LA-ICP-MS/MS) was used. Rare earth elements and Y (REY) have been normalised to OIB, related to footwall volcaniclastic rocks displaying an OIB signature.

4 Petrography

4.1 Micro-scale petrography

Mineralogy of Fortuna mine position A and B sedimentary-type ores is simple and characterised by hematite, quartz and minor siderite. Internal textures, however, are complex and can be divided into three types of microdomains (md) - quartz-hematite-, hematite- and quartz md - in hematite-quartz ores and three types - siderite-hematite-, minor hematite- and quartz md - in siderite-hematite ores.

Quartz-hematite md are composed of microcrystalline quartz with finely dispersed tabular hematite crystals (< 200 nm; Fig. 2a). These md form specific mineral textures such as spherules often surrounded by crescent-shaped shrinking cracks, aggregates and tube- and filamentous stalk-like textures. Hematite md are characterised by accumulations of tabular hematite crystals (50 nm – 1 µm; Fig. 2a). Quartz md are completely constituted by quartz forming the fine-crystalline matrix and filling cracks around spherules. Siderite-hematite md are composed of large siderite single crystals (0.1 – 2 mm) with finely dispersed tabular hematite crystals (< 500 nm) forming aggregates and spherules. Hematite- and quartz md in siderite-hematite ores are similar to those in hematite-quartz ores.

4.2 Nano-scale petrography

TEM analysis of selected md in hematite-quartz- and siderite-hematite ores revealed that interfaces between quartz-hematite- and hematite md are characterised by abundant pores. Hematite from hematite md is accumulated in these pores, whereas hematite from quartz-hematite md is evenly distributed within microcrystalline quartz grains (Fig. 2a). TEM analysis also shows that at the interface between hematite- and siderite-hematite md, tabular hematite crystals are replaced by nanocrystalline siderite (Fig. 2b).

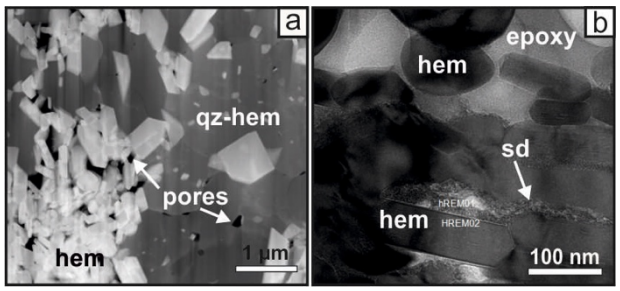

Figure 2. Photomicrographs of md in Fortuna mine ores. **a** Hematite md associated with pores at the interface to the quartz-hematite md (TEM HAADF). **b** Hematite replaced by nanocrystalline siderite (BFSTEM). qz = quartz; hem = hematite; sd = siderite.

5 Microdomain-specific geochemistry

Quartz-hematite md are dominated by total Fe_2O_3 and SiO_2 averaging 20 and 79 wt.%, respectively. Most transition metals are below 25 ppm, though V can reach 144 ppm. High field strength elements (HFSE) show individual averages < 15 ppm. ΣREE (avg. 2 ppm) correlates positively with P_2O_5. OIB-normalised REY patterns are characterised by negative Ce and Eu, and positive Y anomalies.

Hematite md in hematite-quartz- and siderite-hematite ores are differentiated into two types based

on Al_2O_3, TiO_2, K_2O and HFSE concentrations as indicator for (volcani)clastic contamination: Type 1 ("pristine") is characterised by total Fe_2O_3 and SiO_2 averaging 99 wt.% and 1 wt.%, respectively (type 1). Transition metals and HFSE are enriched about tenfold compared to quartz-hematite md. ΣREE generally does not correlate with other elements in hematite md. OIB-normalised REY pattern displays negative Eu and Y anomalies, and in some samples negative La anomalies. Cerium anomalies are usually absent, but in some md weakly positive. Type 2 ("contaminated") hematite md display higher Al_2O_3, TiO_2, K_2O and HFSE concentrations, and depict different REY patterns with variable Eu, Ce and Y anomalies.

Siderite-hematite md display total Fe_2O_3 ranging between 62 and 74 wt.%, and SiO_2 averaging 0.5 wt.%. CaO, MgO, MnO and P_2O_5 usually account together for less than 5 wt.%. Transition metal and HFSE contents are in the same range as in type 1 hematite md. Several siderite-hematite md are characterised by absence of positive ΣREE correlations, whereas some show a positive correlation of ΣLREE with P_2O_5. OIB-normalised REY patterns for all siderite-hematite md are however, uniform charactersied by a negative Eu and absence of other anomalies.

6 Discussion

6.1 Hematite-quartz- and siderite-hematite ore formation

In hematite-quartz ores, quartz-hematite md spherules surrounded by crescent-shaped cracks are a common feature and regarded as primary textures. They are interpreted to be a product of inorganic consolidation and dehydration of a Si-Fe gel (Grenne and Slack 2003). Aggregates formed by quartz-hematite- and hematite md are either primary textures that may have formed by fluctuating vent activity or are early diagenetic textures formed related to diagenetic gel maturation. During transient periods of high hydrothermal venting rates, Si partitions readily onto Fe-(oxyhydr)oxides (the likely precursor to hematite) forming primary quartz-hematite md. This, however, leaves temporary zones of Si depletion in the water column (Sherrell et al. 1999) through which Fe-(oxyhydr)oxides settle leading to primary hematite md formation. Hematite associated with quartz pores implies that md also formed due to diagenetic gel maturation. Uptake of silica onto Fe-(oxyhydr)oxides causes formation of a silica gel with "floating" Fe-(oxyhydr)oxides (precursor to quartz-hematite md). During diagenesis, silica transforms through coupled dissolution and reprecipitation via several steps from opal to quartz (Williams and Crerar 1985). Textures suggest that this is accompanied by dehydration, shrinking, liberation of Fe-(oxyhydr)oxides from silica polymorphs and subsequent accumulation of Fe-(oxyhydr)oxides in pores. Ferrihydrite to hematite transformation likely occurs during early diagenesis as it is triggered by Fe-(oxyhydr)oxide accumulation (Schwertmann et al. 1999). Ultimately, (incomplete) separation of Fe-(oxyhydr)oxides/hematite from silica polymorphs may led to formation of early diagenetic quartz-hematite-, hematite- and quartz md.

Siderite-hematite md in siderite-hematite ores may have either formed related to redox change in the water column or to post-depositional Fe(III) reduction. Nano-crystalline siderite replacing hematite crystals in siderite-hematite md supports the latter process. Fe(III) reduction is described from other Fe-oxide mineralisation and usually interpreted to have occurred during diagenesis (Heimann et al. 2010).

6.2 Microdomain-specific trace element fractionation

Most quartz-hematite- and one type 1 hematite md display REY fractionation features that are characteristic for Devonian seawater (neg. Ce_{OIB}, pos. Y_{OIB} anomalies; Fig. 3; Nothdurft et al. 2004). Due to ΣREE correlating positively with P_2O_5 in these md, it is inferred that REY are associated with phosphates (likely apatite). These apatites are petrographically not visible. They likely occur as syngenetic nanoinclusions within these md, which is in good agreement with seawater sourced P and REY that are readily scavenged by Fe-(oxyhydr)oxides in modern vent systems (Feely et al. 1991).

Contrastingly, positive correlations of ΣREE with P and other elements are absent in the majority of type 1 hematite- and few quartz-hematite md. Therefore, REY are rather associated with hematite in these md. This is also evident from their REY fractionation pattern displaying typical features detected in Fe-(oxyhydr)oxides that scavenge REY in a simulated marine environment (negative La_{OIB} and Y_{OIB}, and no to weak positive Ce_{OIB} anomalies; Fig. 3; Bau 1999).

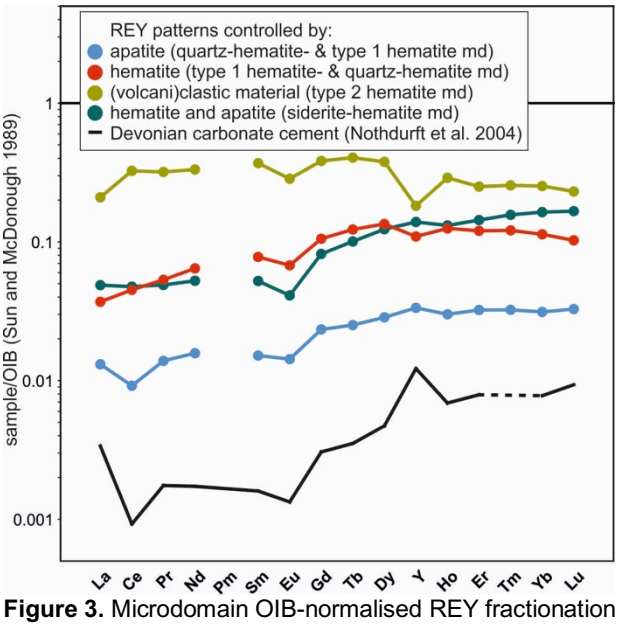

Figure 3. Microdomain OIB-normalised REY fractionation

patterns, grouped related to mineralogical control, and in comparison with Devonian carbonate cement. Note that the patterns displayed here, only show the average of the respective md which may lead to disappearance of several anomalies that only occur in some samples.

Type 2 hematite md that show higher Al_2O_3, TiO_2 and K_2O display distinctly different REY fractionation patterns. They are controlled by finely dispersed (volcani)clastic material, which is supported by OIB-normalised REY slopes being relatively flat (Fig. 3).

Trace elements of siderite-hematite md are likely controlled by a mix of apatite (LREE) and hematite (HREE) related to several md displaying a positive correlation between ΣLREE and P_2O_5. They show, however, a different REY pattern compared to those controlled by hematite and apatite (Fig. 3). This may be related to mobilisation of REY during diagenetic Fe(III) reduction (see previous section). During diagenetic dissolution and reprecipitation of hematite and likely simultanous apatite, trace elements may have been released into pore water resulting in trace element excess (Chetty and Gutzmer 2012; Alibert 2016). Those processes may have led to homogenisation of REY_{OIB} patterns in all siderite-hematite md.

6.2 Reconstruction of venting dynamics and depositional environment

Microdomain chemistry controlled by hematite and apatite show a uniform negative Eu anomaly that is consistent with low-T (<250 °C) fluids interacting with basaltic rocks (Giese and Bau 1994).

A weak positive Ce anomaly in several hematite md may be evidence for rapid Fe(II) oxidation subsequent to fluid venting. In precipitation experiments in oxidised seawater-like conditions, Ce(IV) sorption onto Fe-(oxyhydr)oxides is highest in the first few minutes and then drastically decreases (Bau 1999). Rapid Fe-(oxyhydr)oxide formation likely occurred in an environment characterised by high seawater to vent fluid ratio. This is evident from quartz-hematite- and hematite md displaying REY fractionation patterns typical for marine environments (see previous section) that rather developed during Fe-(oxyhydr)oxide- and apatite trace element scavenging from seawater and not from the vent fluid.

This may be consistent with diffused fluid venting and low fluid flux, and not with high fluid flux in focused vent systems. Diffused venting is a far more abundant venting process than focused fluid venting (Bemis et al. 2012) and may be the driving mineralisation process in all Lahn-Dill-type iron ores within the Rhenohercynian-, Saxothuringian- and Moravo-Silesian basins.

7 Conclusion

Lahn-Dill-type iron ores in the Fortuna mine include hematite-quartz- and minor siderite-hematite ores. The former formed related to formation of a Fe-Si gel on the seafloor. Microdomains in these ores preserve primary to early diagenetic textures that recorded vent fluid fluctuation, and gel maturation. Siderite-hematite ores formed most likely related to diagenetic Fe(III) reduction. Trace element geochemistry of md is compatible with diffused venting of a low-T fluid and subsequent rapid Fe-(oxyhydr)oxide formation. These ore forming processes appear to have been favoured during the Silurian to Carboniferous during which restricted pre-Variscan shallow marine basins have been linked to extensive volcanic and hydrothermal activity.

Acknowledgements

We would like to thank the TH Georg Agricola for financial support. We also would like to say thank you to the “Fortuna mine” team for their support during sampling campaigns.

References

Alibert C (2016) Rare earth elements in Hamersley BIF minerals. Geochim Cosmochim Acta 184:311–328.

Bau M (1999) Scavenging of dissolved yttrium and rare earths by precipitating iron oxyhydroxide: experimental evidence for Ce oxidation, Y-Ho fractionation, and lanthanide tetrad effect. Geochim Cosmochim Acta 63:67–77.

Bemis K, Lowell RP and Farough A (2012) Diffuse Flow: On and Around Hydrothermal Vents at Mid-Ocean Ridges. Oceanography 25:182–191.

Chetty D, Gutzmer J (2012) REE redistribution during hydrothermal alteration of ores of the Kalahari Manganese Deposit. Ore Geol Rev 47:126–135.

Feely RA, Trefry JH, Massoth GJ and Metz S (1991) A comparison of the scavenging of phosphorus and arsenic from seawater by hydrothermal iron oxyhydroxides in the Atlantic and Pacific Oceans. Deep Sea Research Part A. Oceanographic Research Papers 38:617–623.

Giese U and Bau M (1994) Trace Element Accessibility in Mid-Ocean Ridge and Ocean Island Basalt: An Experimental Approach. Mineral mag 58A:329–330.

Grenne T, Slack JF (2003) Bedded jaspers of the Ordovician Løkken ophiolite, Norway: seafloor deposition and diagenetic maturation of hydrothermal plume-derived silica-iron gels. Miner Deposita 38:625–639.

Heimann A, Johnson CM, Beard BL, Valley JW, Roden EE, Spicuzza MJ, Beukes NJ (2010) Fe, C, and O isotope compositions of banded iron formation carbonates demonstrate a major role for dissimilatory iron reduction in ~2.5 Ga marine environments. Earth Planet Sc Lett 294:8–18.

Nothdurft LD, Webb GE, Kamber BS (2004) Rare earth element geochemistry of Late Devonian reefal carbonates, Canning Basin, Western Australia: confirmation of a seawater REE proxy in ancient limestones. Geochim Cosmochim Acta 68:263–283.

Quade H (1976) Genetic problems and environmental features of volcano-sedimentary iron ore deposits of the Lahn-Dill Type. In: Wolf KH (ed) Handbook of strata-bound and stratiform ore deposits. Elsevier, Amsterdam, pp 255–294.

Schwertmann U, Friedel J, Stanjek H (1999) From Fe(III) Ions to Ferrihydrite and then to Hematite. J Colloid Interf Sci 209: 215–223.

Sherrell RM, Field MP and Ravizza G (1999) Uptake and fractionation of rare earth elements on hydrothermal plume particles at 9°45′N, East Pacific Rise. Geochim Cosmochim Acta 63:1709–1722.

Sun S-s and McDonough WF (1989) Chemical and isotopic systematics of oceanic basalts: implications for mantle composition and processes. Geological Society, London, Special Publications 42:313–345.
Williams LA, Crerar DA (1985) Silica Diagenesis, II. General Mechanisms. J Sediment Petrol 55:312–321.

Reconstructing the formation of volcanic-associated Lahn-Dill-type iron ores from fluid venting to seafloor deposition

Leanne Schmitt[1,2], Thomas Kirnbauer[1], Thomas Angerer[3], Sabine Klein[4,2], Dieter Garbe-Schönberg[5], Vladimir Roddatis[6]

[1]Faculty of Georesources and Process Engineering, TH Georg Agricola, Bochum, Germany
[2]Institute of Geology, Mineralogy and Geophysics, Ruhr-Universität Bochum, Germany
[3]GeoSphere Austria, Wien, Austria
[4]Deutsches Bergbau-Museum Bochum, Germany
[5]Institute of Geosciences, Christian-Albrechts-Universität, Kiel, Germany
[6]Interface Geochemistry Section, Helmholtz Centre Potsdam, Germany

Abstract. Volcanic-associated Fe-oxide mineralisation of the Lahn-Dill-type formed in pre-Variscan restricted, shallow marine basins. They are located in the hanging wall of thick volcaniclastic rocks marking the Middle to Upper Devonian boundary. One of the largest Lahn-Dill-type iron ore mines (Fortuna mine) has been sampled in order to elucidate the interplay of genetic processes leading to ore formation as well as the environment in which ores formed. Petrography revealed that ores most likely formed from a Fe-Si gel. Primary and diagenetic gel textures include spherules and aggregates composed of nanocrystalline hematite dispersed in quartz, or of hematite accumulations that are associated with pores in quartz. Local post-depositional Fe(III) reduction within the gel is indicated by siderite replacing hematite. In-situ mineralogical and textural microdomain (md) chemistry analysed by laser ablation ICP-MS displays four different source and formational trace element signatures related to (1) syngenetic apatite nanoinclusions, (2) scavenging by Fe-(oxyhydr)oxides, (3) (volcani)clastic contamination and (4) diagenetic mobilisation of REY in pore water. These signatures imply that ores formed related to diffused venting of a low-T fluid and subsequent rapid Fe-(oxyhydr)oxide precipitation. These processes were favoured in Silurian to Carboniferous restricted shallow marine basins that were characterised by extensive volcanic and hydrothermal activity.

1 Introduction

Marine volcanic-associated Fe-oxide mineralisation formed from the Precambrian until today. They are interpreted to have formed related to an interplay of volcanic-, hydrothermal-, marine- and microbial processes and therefore represent archives of basin sedimentation and marine environmental conditions, and are also important sources for iron.

Volcanic-associated Fe-oxide mineralisation of the Lahn-Dill-type formed in the restricted and shallow Rhenohercynian-, Saxothuringian- and Moravo-Silesian marine basins. They have been described mainly from the eastern Rhenish Massif, the Harz Mountains, central Saxothuringia and the Eastern Sudetes, but similar volcanic-associated marine Fe-oxide mineralisation also occur in western and southeastern Europe. Lahn-Dill-type iron ores are associated with Middle to Upper Devonian alkali basaltic volcanic and volcaniclastic rocks (Quade 1976). Ores formed either related to chemical precipitation (sedimentary-type) or to metasomatic replacement of wall rocks (replacement-type).

Lahn-Dill-type iron ores (sedimentary-type) are usually composed of hematite and quartz, with minor siderite and magnetite. Their Fe grade ranges from 30 to 40 wt.%. Due to low metamorphic overprint (< 300°C), ores display many primary and early diagenetic textures making them favourable to study mineral transformation and textural changes from sedimentation to metamorphism.

Whole rock geochemistry of marine Fe-oxide mineralisation is a conventional tool to decipher ocean chemistry and variations of the redox state. Mineral-specific minor and trace element geochemistry may however, provide a more detailed image of element fractionation during mineral formation. Trace elements in Fe-(oxyhydr)oxides are for instance interpreted to reflect the solution from which they precipitated (Bau 1999), whereas syngenetic apatites rather record ocean chemistry (Alibert 2016). Detecting these mineral-specific element fractionation mechanisms may provide insights that are masked in whole rock geochemistry.

We therefore, sampled one of the largest Lahn-Dill-type iron ores mines (Fortuna mine) and conducted a systematic petrography from the micro- to nano-scale (optical microscopy, REM, TEM) and microdomain chemistry (LA-ICP-MS) to reconstruct the unique depositional environment and venting mechanisms during Lahn-Dill-type ore formation.

2 Fortuna mine geology

The Fortuna mine is located within the Lahn-syncline (eastern Rhenish Massif, Germany) which is part of the Rhenohercynian Zone of the Variscan orogenic belt. Lithostratigraphy within the Fortuna mine is mainly characterised by a thick volcanic succession composed of green (distal to ore) and purple (proximal to ore) volcaniclastic rocks (Fig. 1a). Several thin (0.1 to 0.5 m) ore lenses are intercalated with purple volcaniclastic rocks near the top of the succession (position A ores; Fig. 1a, b). The main ore body is ~5 m thick and located on top of the volcaniclastic succession (position B ores; Fig. 1a,

c). Sampled ore types are composed either of hematite and quartz forming sedimentary-type hematite-quartz ores, or subordinately of siderite, hematite and quartz forming sedimentary-type siderite-hematite ores. The latter occur rather at the top of the position B ore body. Hanging wall rocks are composed of volcaniclastic and clastic sedimentary rocks with occasionally intercalated limestone. The above described stratigraphic sequence was overprinted by Variscan low-grade metamorphism, regional to local thrusting and folding and local hydrothermal carbonate-quartz-hematite-(chlorite-apatite) veins.

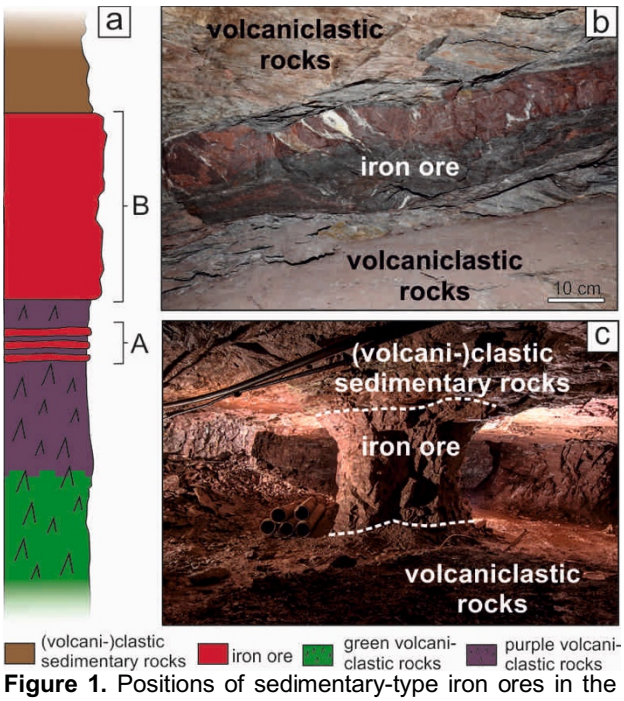

Figure 1. Positions of sedimentary-type iron ores in the Fortuna mine. **a** Lithostratigraphic profile depicting position A and B ores. Note that depicted thicknesses of drawn stratigraphic units do not correspond with true thicknesses due to graphic reasons. **b** Photo of position A ores and **c** of position B ores (iron ore layer ~5 m; image in **c** by courtesy of Roger Lang/Geowelt Fortuna e.V).

3 Methods

Fortuna mine position A and B ores were sampled and analysed using a reflected light microscope and a scanning electron microscope (SEM). High-resolution microscopy down to the nano-scale was carried out with a Thermo Fisher Scientific (former FEI) Tecnai F20 G2 and Themis Z 80-300 transmission electron microscope (TEM). For in-situ bulk microdomain geochemical analysis, a 193 nm ArF excimer laser ablation system (GeoLasPro Plus, Coherent) coupled to an Agilent 8900 inductively coupled plasma mass spectrometer (LA-ICP-MS/MS) was used. Rare earth elements and Y (REY) have been normalised to OIB, related to footwall volcaniclastic rocks displaying an OIB signature.

4 Petrography

4.1 Micro-scale petrography

Mineralogy of Fortuna mine position A and B sedimentary-type ores is simple and characterised by hematite, quartz and minor siderite. Internal textures, however, are complex and can be divided into three types of microdomains (md) - quartz-hematite-, hematite- and quartz md - in hematite-quartz ores and three types - siderite-hematite-, minor hematite- and quartz md - in siderite-hematite ores.

Quartz-hematite md are composed of microcrystalline quartz with finely dispersed tabular hematite crystals (< 200 nm; Fig. 2a). These md form specific mineral textures such as spherules often surrounded by crescent-shaped shrinking cracks, aggregates and tube- and filamentous stalk-like textures. Hematite md are characterised by accumulations of tabular hematite crystals (50 nm – 1 µm; Fig. 2a). Quartz md are completely constituted by quartz forming the fine-crystalline matrix and filling cracks around spherules. Siderite-hematite md are composed of large siderite single crystals (0.1 – 2 mm) with finely dispersed tabular hematite crystals (< 500 nm) forming aggregates and spherules. Hematite- and quartz md in siderite-hematite ores are similar to those in hematite-quartz ores.

4.2 Nano-scale petrography

TEM analysis of selected md in hematite-quartz- and siderite-hematite ores revealed that interfaces between quartz-hematite- and hematite md are characterised by abundant pores. Hematite from hematite md is accumulated in these pores, whereas hematite from quartz-hematite md is evenly distributed within microcrystalline quartz grains (Fig. 2a). TEM analysis also shows that at the interface between hematite- and siderite-hematite md, tabular hematite crystals are replaced by nanocrystalline siderite (Fig. 2b).

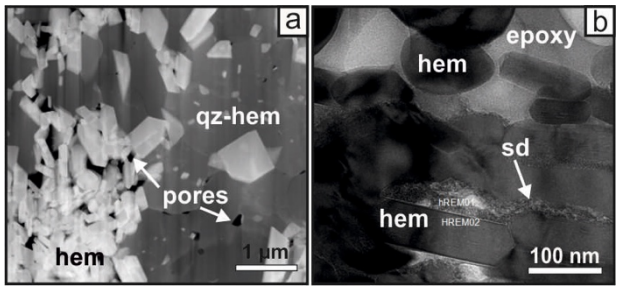

Figure 2. Photomicrographs of md in Fortuna mine ores. **a** Hematite md associated with pores at the interface to the quartz-hematite md (TEM HAADF). **b** Hematite replaced by nanocrystalline siderite (BFSTEM). qz = quartz; hem = hematite; sd = siderite.

5 Microdomain-specific geochemistry

Quartz-hematite md are dominated by total Fe_2O_3 and SiO_2 averaging 20 and 79 wt.%, respectively. Most transition metals are below 25 ppm, though V can reach 144 ppm. High field strength elements (HFSE) show individual averages < 15 ppm. ΣREE

(avg. 2 ppm) correlates positively with P_2O_5. OIB-normalised REY patterns are characterised by negative Ce and Eu, and positive Y anomalies.

Hematite md in hematite-quartz- and siderite-hematite ores are differentiated into two types based on Al_2O_3, TiO_2, K_2O and HFSE concentrations as indicator for (volcani)clastic contamination: Type 1 ("pristine") is characterised by total Fe_2O_3 and SiO_2 averaging 99 wt.% and 1 wt.%, respectively (type 1). Transition metals and HFSE are enriched about tenfold compared to quartz-hematite md. ΣREE generally does not correlate with other elements in hematite md. OIB-normalised REY pattern displays negative Eu and Y anomalies, and in some samples negative La anomalies. Cerium anomalies are usually absent, but in some md weakly positive. Type 2 ("contaminated") hematite md display higher Al_2O_3, TiO_2, K_2O and HFSE concentrations, and depict different REY patterns with variable Eu, Ce and Y anomalies.

Siderite-hematite md display total Fe_2O_3 ranging between 62 and 74 wt.%, and SiO_2 averaging 0.5 wt.%. CaO, MgO, MnO and P_2O_5 usually account together for less than 5 wt.%. Transition metal and HFSE contents are in the same range as in type 1 hematite md. Several siderite-hematite md are characterised by absence of positive ΣREE correlations, whereas some show a positive correlation of ΣLREE with P_2O_5. OIB-normalised REY patterns for all siderite-hematite md are however, uniform charactersied by a negative Eu and absence of other anomalies.

6 Discussion

6.1 Hematite-quartz- and siderite-hematite ore formation

In hematite-quartz ores, quartz-hematite md spherules surrounded by crescent-shaped cracks are a common feature and regarded as primary textures. They are interpreted to be a product of inorganic consolidation and dehydration of a Si-Fe gel (Grenne and Slack 2003). Aggregates formed by quartz-hematite- and hematite md are either primary textures that may have formed by fluctuating vent activity or are early diagenetic textures formed related to diagenetic gel maturation. During transient periods of high hydrothermal venting rates, Si partitions readily onto Fe-(oxyhydr)oxides (the likely precursor to hematite) forming primary quartz-hematite md. This, however, leaves temporary zones of Si depletion in the water column (Sherrell et al. 1999) through which Fe-(oxyhydr)oxides settle leading to primary hematite md formation. Hematite associated with quartz pores implies that md also formed due to diagenetic gel maturation. Uptake of silica onto Fe-(oxyhydr)oxides causes formation of a silica gel with "floating" Fe-(oxyhydr)oxides (precursor to quartz-hematite md). During diagenesis, silica transforms through coupled dissolution and reprecipitation via several steps from opal to quartz (Williams and Crerar 1985). Textures suggest that this is accompanied by dehydration, shrinking, liberation of Fe-(oxyhydr)oxides from silica polymorphs and subsequent accumulation of Fe-(oxyhydr)oxides in pores. Ferrihydrite to hematite transformation likely occurs during early diagenesis as it is triggered by Fe-(oxyhydr)oxide accumulation (Schwertmann et al. 1999). Ultimately, (incomplete) separation of Fe-(oxyhydr)oxides/hematite from silica polymorphs may led to formation of early diagenetic quartz-hematite-, hematite- and quartz md.

Siderite-hematite md in siderite-hematite ores may have either formed related to redox change in the water column or to post-depositional Fe(III) reduction. Nano-crystalline siderite replacing hematite crystals in siderite-hematite md supports the latter process. Fe(III) reduction is described from other Fe-oxide mineralisation and usually interpreted to have occurred during diagenesis (Heimann et al. 2010).

6.2 Microdomain-specific trace element fractionation

Most quartz-hematite- and one type 1 hematite md display REY fractionation features that are characteristic for Devonian seawater (neg. Ce_{OIB}, pos. Y_{OIB} anomalies; Fig. 3; Nothdurft et al. 2004). Due to ΣREE correlating positively with P_2O_5 in these md, it is inferred that REY are associated with phosphates (likely apatite). These apatites are petrographically not visible. They likely occur as syngenetic nanoinclusions within these md, which is in good agreement with seawater sourced P and REY that are readily scavenged by Fe-(oxyhydr)oxides in modern vent systems (Feely et al. 1991).

Contrastingly, positive correlations of ΣREE with P and other elements are absent in the majority of type 1 hematite- and few quartz-hematite md. Therefore, REY are rather associated with hematite in these md. This is also evident from their REY fractionation pattern displaying typical features detected in Fe-(oxyhydr)oxides that scavenge REY in a simulated marine environment (negative La_{OIB} and Y_{OIB}, and no to weak positive Ce_{OIB} anomalies; Fig. 3; Bau 1999).

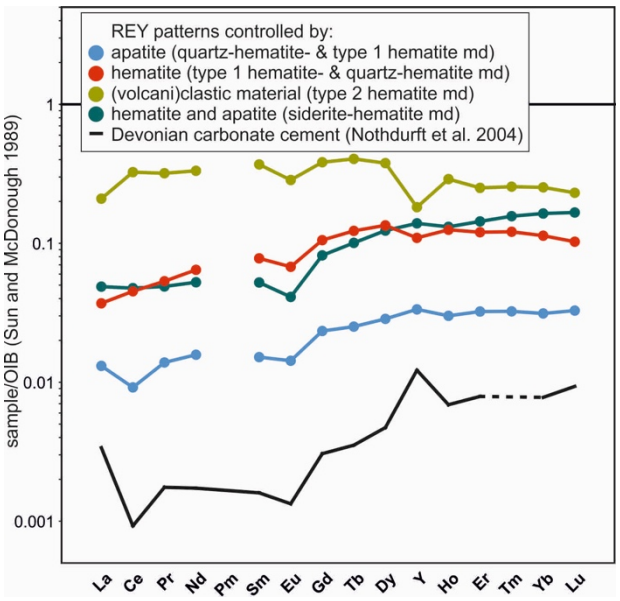

Figure 3. Microdomain OIB-normalised REY fractionation patterns, grouped related to mineralogical control, and in comparison with Devonian carbonate cement. Note that the patterns displayed here, only show the average of the respective md which may lead to disappearance of several anomalies that only occur in some samples.

Type 2 hematite md that show higher Al_2O_3, TiO_2 and K_2O display distinctly different REY fractionation patterns. They are controlled by finely dispersed (volcani)clastic material, which is supported by OIB-normalised REY slopes being relatively flat (Fig. 3).

Trace elements of siderite-hematite md are likely controlled by a mix of apatite (LREE) and hematite (HREE) related to several md displaying a positive correlation between ΣLREE and P_2O_5. They show, however, a different REY pattern compared to those controlled by hematite and apatite (Fig. 3). This may be related to mobilisation of REY during diagenetic Fe(III) reduction (see previous section). During diagenetic dissolution and reprecipitation of hematite and likely simultanous apatite, trace elements may have been released into pore water resulting in trace element excess (Chetty and Gutzmer 2012; Alibert 2016). Those processes may have led to homogenisation of REY_{OIB} patterns in all siderite-hematite md.

6.2 Reconstruction of venting dynamics and depositional environment

Microdomain chemistry controlled by hematite and apatite show a uniform negative Eu anomaly that is consistent with low-T (<250 °C) fluids interacting with basaltic rocks (Giese and Bau 1994).

A weak positive Ce anomaly in several hematite md may be evidence for rapid Fe(II) oxidation subsequent to fluid venting. In precipitation experiments in oxidised seawater-like conditions, Ce(IV) sorption onto Fe-(oxyhydr)oxides is highest in the first few minutes and then drastically decreases (Bau 1999). Rapid Fe-(oxyhydr)oxide formation likely occurred in an environment characterised by high seawater to vent fluid ratio. This is evident from quartz-hematite- and hematite md displaying REY fractionation patterns typical for marine environments (see previous section) that rather developed during Fe-(oxyhydr)oxide- and apatite trace element scavenging from seawater and not from the vent fluid.

This may be consistent with diffused fluid venting and low fluid flux, and not with high fluid flux in focused vent systems. Diffused venting is a far more abundant venting process than focused fluid venting (Bemis et al. 2012) and may be the driving mineralisation process in all Lahn-Dill-type iron ores within the Rhenohercynian-, Saxothuringian- and Moravo-Silesian basins.

7 Conclusion

Lahn-Dill-type iron ores in the Fortuna mine include hematite-quartz- and minor siderite-hematite ores. The former formed related to formation of a Fe-Si gel on the seafloor. Microdomains in these ores preserve primary to early diagenetic textures that recorded vent fluid fluctuation, and gel maturation. Siderite-hematite ores formed most likely related to diagenetic Fe(III) reduction. Trace element geochemistry of md is compatible with diffused venting of a low-T fluid and subsequent rapid Fe-(oxyhydr)oxide formation. These ore forming processes appear to have been favoured during the Silurian to Carboniferous during which restricted pre-Variscan shallow marine basins have been linked to extensive volcanic and hydrothermal activity.

Acknowledgements

We would like to thank the TH Georg Agricola for financial support. We also would like to say thank you to the “Fortuna mine” team for their support during sampling campaigns.

References

Alibert C (2016) Rare earth elements in Hamersley BIF minerals. Geochim Cosmochim Acta 184:311–328.

Bau M (1999) Scavenging of dissolved yttrium and rare earths by precipitating iron oxyhydroxide: experimental evidence for Ce oxidation, Y-Ho fractionation, and lanthanide tetrad effect. Geochim Cosmochim Acta 63:67–77.

Bemis K, Lowell RP and Farough A (2012) Diffuse Flow: On and Around Hydrothermal Vents at Mid-Ocean Ridges. Oceanography 25:182–191.

Chetty D, Gutzmer J (2012) REE redistribution during hydrothermal alteration of ores of the Kalahari Manganese Deposit. Ore Geol Rev 47:126–135.

Feely RA, Trefry JH, Massoth GJ and Metz S (1991) A comparison of the scavenging of phosphorus and arsenic from seawater by hydrothermal iron oxyhydroxides in the Atlantic and Pacific Oceans. Deep Sea Research Part A. Oceanographic Research Papers 38:617–623.

Giese U and Bau M (1994) Trace Element Accessibility in Mid-Ocean Ridge and Ocean Island Basalt: An Experimental Approach. Mineral mag 58A:329–330.

Grenne T, Slack JF (2003) Bedded jaspers of the Ordovician Løkken ophiolite, Norway: seafloor deposition and diagenetic maturation of hydrothermal plume-derived silica-iron gels. Miner Deposita 38:625–639.

Heimann A, Johnson CM, Beard BL, Valley JW, Roden EE, Spicuzza MJ, Beukes NJ (2010) Fe, C, and O isotope compositions of banded iron formation carbonates demonstrate a major role for dissimilatory iron reduction in ~2.5 Ga marine environments. Earth Planet Sc Lett 294:8–18.

Nothdurft LD, Webb GE, Kamber BS (2004) Rare earth element geochemistry of Late Devonian reefal carbonates, Canning Basin, Western Australia: confirmation of a seawater REE proxy in ancient limestones. Geochim Cosmochim Acta 68:263–283.

Quade H (1976) Genetic problems and environmental features of volcano-sedimentary iron ore deposits of the Lahn-Dill Type. In: Wolf KH (ed) Handbook of strata-bound and stratiform ore deposits. Elsevier, Amsterdam, pp 255–294.

Schwertmann U, Friedel J, Stanjek H (1999) From Fe(III) Ions to Ferrihydrite and then to Hematite. J Colloid Interf Sci 209: 215–223.

Sherrell RM, Field MP and Ravizza G (1999) Uptake and fractionation of rare earth elements on hydrothermal plume particles at 9°45′N, East Pacific Rise. Geochim Cosmochim Acta 63:1709–1722.

Sun S-s and McDonough WF (1989) Chemical and isotopic systematics of oceanic basalts: implications for mantle composition and processes. Geological Society, London, Special Publications 42:313–345.

Williams LA, Crerar DA (1985) Silica Diagenesis, II. General Mechanisms. J Sediment Petrol 55:312–321.

Linking Lithofacies and Chemostratigraphy, Rävliden North VHMS deposit, Skellefte district, Sweden

Filip Simán[1], Nils Jansson[1], Foteini Liwicki[1], Tobias Hermansson[2], Erik Nordfeldt[2], Mac Fjellerad Persson[2], Paul McDonnell[2], Sean Johnson[2], Jon Gustafsson[2]
[1]Luleå University of Technology, Luleå, Sweden
[2]Boliden Mines, Boliden, Sweden

Abstract. The recently discovered Rävliden North Zn-Pb-Ag-Cu deposit, located in the western Skellefte district, northern Sweden, is classified as a volcanic hosted massive sulphide (VHMS) and occurs at the contact between the Skellefte group (SG) metavolcanic rocks and the overlying predominantly metasiliciclastic rocks of the Vargfors group (VG). Alteration, metamorphism and complex internal stratigraphy makes classifying and spatially relating rocks in the area difficult, but chemostratigraphy utilising immobile elements may be a useful tool for overcoming some of these challenges. However, few comprehensive studies exist for the Rävliden North stratigraphy that link lithofacies and chemostratigraphy. This contribution advances the stratigraphic understanding of the crucial SG-VG contact at Rävliden North by linking lithofacies and immobile element signatures, resulting in the discrimination of two rhyolitic units. This study interprets a volcaniclastic facies for rhyolitic rocks located in a “transitional zone” between SG and VG rocks, whereas the footwall and immediate hanging wall rocks relate to a different rhyolitic unit, which due to high alteration intensities has more elusive facies, which are locally volcaniclastic and locally coherent. Given the complex structural relationships and discontinuous stratigraphy, this demonstrates the value in linking lithofacies to chemostratigraphy to aid core logging in altered rocks.

1 Introduction

The Rävliden North Zn-Pb-Ag-Cu deposit (8.4 Mt grading 4.17 % Zn, 0.64 % Pb, 81 g/t Ag, 0.98 % Cu, and 0.25 g/t Au; Boliden 2020) is located in the western part of the economically significant Skellefte district, northern Sweden (Figure 1). The deposit is classified as a volcanic hosted massive sulphide (VHMS) similar to most other deposits in the district. These deposits occur at the contact between two lithostratigraphic units: 1) the c. 1.89 – 1.88 Ga Skellefte group (SG) metavolcanic rocks, and 2) the overlying c. 1.89 – 1.87 Ga Vargfors group (VG) comprising predominantly metasiliciclastic rocks. The internal stratigraphies of the two groups and their contact relationships are highly variable throughout the district (Allen et al. 1996 and Skyttä et al. 2012), which is challenging for exploration. Furthermore, alteration and metamorphism cause difficulty in classifying rocks and, for this reason, immobile element lithogeochemistry is a useful technique for assisting classification. Previous workers have defined precursor rock-types based on immobile elements (Barrett et al. 2005 and Chmielowski et al. 2016), and some work with chemostratigraphy has been done for the footwall to the Rävliden deposit (Schlatter et al. 2003 and Årebäck et al. 2005). However, few comprehensive studies have been conducted on the full stratigraphy (Mataruga 2016), and even fewer have aimed at linking lithofacies and chemostratigraphy. This contribution aims to advance the detailed stratigraphic understanding at Rävliden North by linking lithofacies of least-altered samples to their immobile element signatures. By proxy, the possible lithofacies of more altered counterparts with similar immobile element signatures can be discussed. This approach is also useful at Rävliden North for further defining the complicated SG-VG contact where a “transitional zone” of volcanosedimentary rocks and intrusions occur.

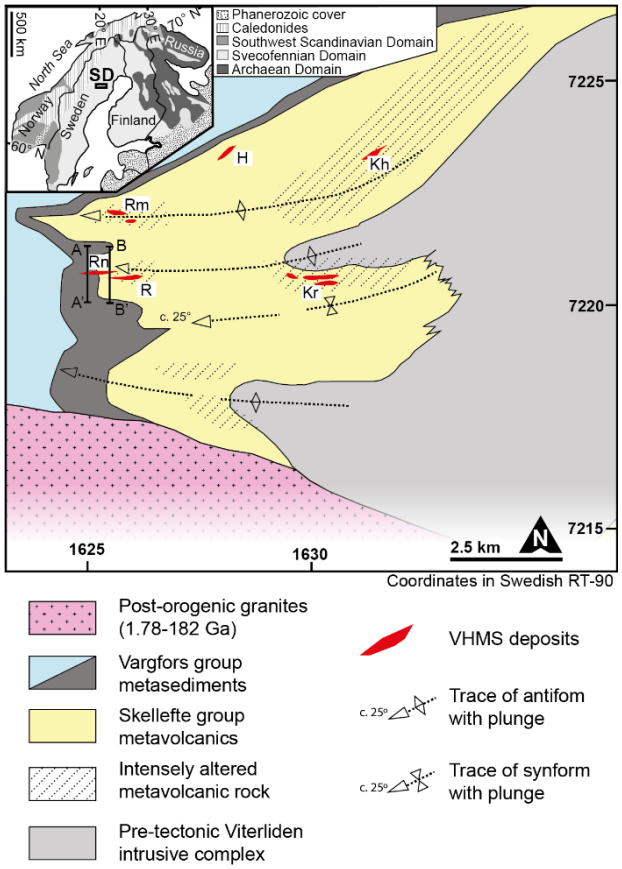

Figure 3. Geological map of the Kristineberg area with cross section traces A–A' and B–B' indicated, inset map of Fennoscandian Shield, H=Hornträsk, Kh=Kimheden, Rm=Rävlidmyran, Rn=Rävliden North, R=Rävliden, and Kr=Kristineberg. Modified after Skyttä et al. (2012).

1.1 Geological background

The Skellefte district belongs to the Bothnia-Skellefteå lithotectonic unit of the c. 2.0–1.8 Ga Svecokarelian orogen located in the Fennoscandian Shield (inset in Figure 1).

A continental intra-arc basin palaeoenvironment is widely accepted for the district based on the dominantly felsic composition and the calc-alkaline magmatic affinity of the SG (Allen et al. 1996 and Skyttä et al. 2020). This volcanic arc formed between c. 1.90 and 1.88 Ga (Skyttä et al. 2020) and an extensional tectonic regime, which lasted from c. 1.89 – 1.88 Ga and resulted in D1 deformation, caused subsidence with associated subaqueous SG volcanism forming intermediate to felsic volcaniclastic rocks, minor lavas and minor sedimentary rocks in half-graben fault bound compartments (Allen et al. 1996; Skyttä et al. 2012; Årebäck et al. 2005). Coeval with the formation of the SG, granitoids of the Jörn suite were emplaced (Skyttä et al. 2020). The c. 1.89 – 1.87 Ga VG overlies the SG with a diachronous contact, which is a result of differential uplift and subsidence. Partly coeval with the VG are 1.88–1.86 Ga metavolcanic rocks that belong to the Arvidsjaur group, and several granitoids. At c. 1.88–1.87 Ga a transpressional tectonic regime with associated D2 deformation took over, which resulted in the closure of the intra-arc basin at c. 1.86 Ga. The corresponding peak metamorphism reached upper amphibolite facies (Weihed et al. 1992). For brevity and simplicity the prefix "meta-" is omitted in further geological descriptions.

In terms of regional stratigraphy, the Rävliden North VHMS deposit is at the top of the SG felsic volcanic rocks. The footwall to the deposit is a weakly porphyritic rhyolite that locally exhibits texturally destructive sericite-silica±chlorite alteration. Footwall rocks proximal to mineralisation in the local stratigraphy are intensely chlorite-sericite altered with minor calc-silicate rocks that is locally tremolite rich (Barrett et al. 2005 and Årebäck et al. 2005). The ore lenses comprises semi-massive to massive sphalerite-galena-pyrite mineralisation, structurally above vein-hosted chalcopyrite-pyrrhotite-pyrite (Rincon 2022). A discontinuous graphitic phyllite, named by local workers as "Bonus shale", locally directly overlies the mineralisation. The lower hanging wall, herein referred to as the "transitional zone", comprises mainly rhyolitic rocks with widely unknown facies, coherent andesite with volcaniclastic margins with andesitic and dacitic composition, and a volcanosedimentary breccia-conglomerate with clasts of andesite, dacite and graphitic phyllite in a calc-silicate rich matrix. Upper hanging wall rocks comprise thick successions of graphitic phyllite, siltstone and sandstone, which are typically recognisable VG siliciclastic rocks.

2 Results

Legacy data from whole-rock lithogeochemical samples (n=652), taken by Boliden geologists from 44 drill cores in the Rävliden North host stratigraphy, show local intense alteration. In order to link lithofacies to chemostratigraphy the least-altered samples had to be identified, since important textures for determining lithofacies, such as phenocrysts, are better preserved in these rocks. Criteria for least altered samples are defined by the alteration box plot, where Ishikawa alteration index (AI) is plotted against the carbonate-chlorite-pyrite index (CCPI; Large et al. 2001), in tandem with criteria for LOI <4 vol.% and Na >2 vol.%, and qualitative description of alteration intensities. With these criteria, only 163 (25%) samples were classified as least altered. Two drill cores were relogged, RAVLD663 and RAVLD673. In drill core RAVLD663, there were eight least altered samples, five of which were described as volcaniclastic, two as coherent, and one as unidentifiable facies. In drill core RAVLD673, there were eleven least altered samples, four of which were described as volcaniclastic, five as coherent, and two as unidentifiable facies.

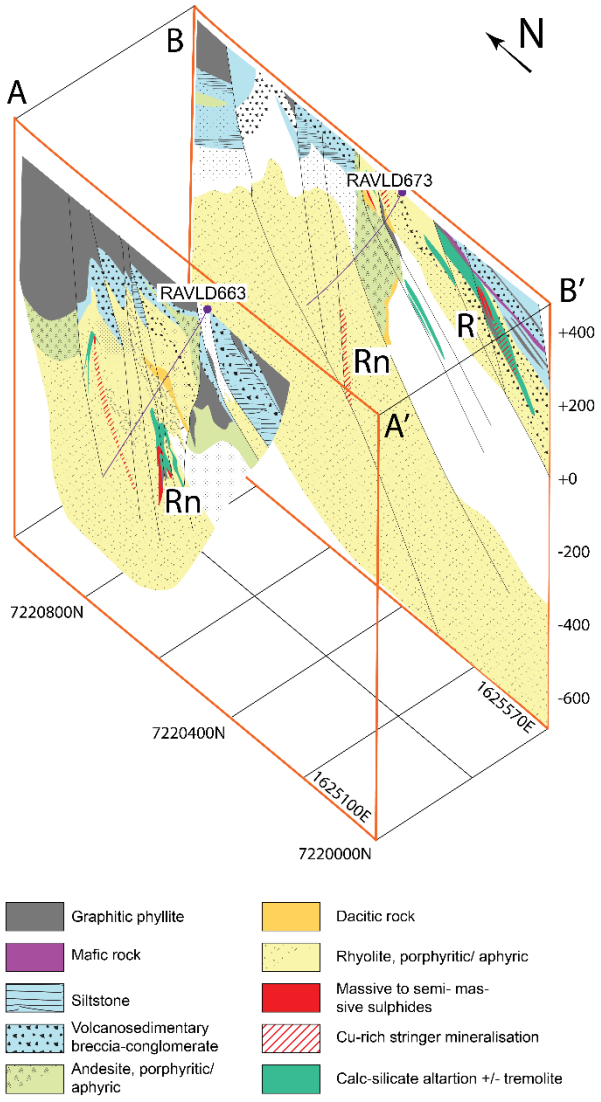

Figure 4. Cross sections A–A' and B–B' (see also Figure 1) with drill core traces RAVLD663 and RAVLD673 indicated. Rn=Rävliden North and R=Rävliden.

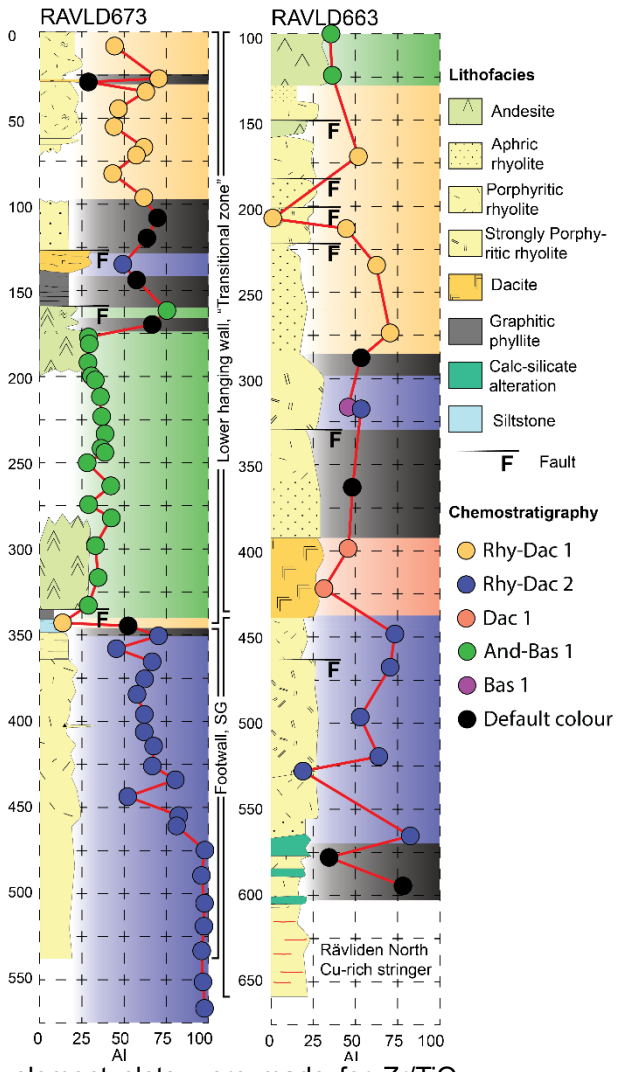

Immobile element plots were made for Zr/TiO_2 against Al_2O_3/TiO_2 for all data (altered and least-altered, n=652) to identify protolith compositions. Six clusters were identified by using the heat-map function in ioGAS. These were then labelled by petrographic descriptions of samples in tandem with TAS classification (Maitre et al. 2004) of the least altered counterparts (Figure 3). The "Bas 1" cluster (n=45), "And-Bas 1" cluster (n=46) and "Dac 1" cluster (n=27) likely correspond to mafic, andesitic and dacitic rocks, respectively. The "Rhy-Dac 1" (n=264) and "Rhy-Dac 2" (n=122) clusters likely both correspond to different rhyolitic-dacitic rocks. The sixth cluster, "Rhy 1" (n=12), corresponds to rhyolites in TAS classification and it did not occur in any samples from the logged drill cores.

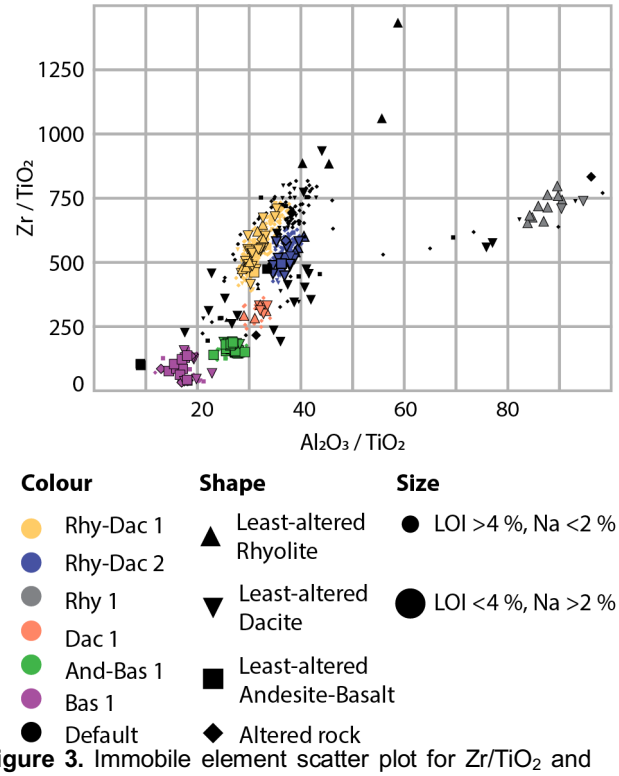

Figure 3. Immobile element scatter plot for Zr/TiO_2 and Al_2O_3/TiO_2 ratios for all drill cores. Colour labelling by apparent clusters, shape labelling by alteration box plot (AI vs CCPI) and size labelling by LOI and Na values.

Logged facies from RAVLD673 and RAVLD663 are linked to their respective chemostratigraphic units for both altered and least altered samples (Table 1). For "Rhy-Dac 1" no coherent facies were observed. Facies of "Rhy-Dac 2" are mostly unknow due to high alteration intensities, but both volcaniclastic and coherent facies are observed.

The "Rhy-Dac 1" chemostratigraphic unit occurring in RAVLD673 (0–100 metres, Figure 4) has weak to moderate sericite-chlorite alteration (average AI= 55 and average CCPI= 60). Only one of the samples was classified as least altered and its facies was described as volcaniclastic. Three "Rhy-Dac 1" samples found to be altered were also identified as volcaniclastic.

The "Rhy-Dac 1" chemostratigraphic unit occurring in RAVLD663 (130–280 metres) relates to strongly sericite altered rock (average AI= 57 and average CCPI= 48; excluding a carbonate altered sample with anomalous Ca values), where two samples were classified as least altered. Of these two, one was recognised as volcaniclastic facies and the other had unidentified facies. In addition, one altered sample could also be identified as volcaniclastic.

Table 1. Facies of the chemostratigraphic units in drill cores RAVLD673 and RAVLD663.

	Volccl.	Coherent	Sed.	Unknown
Rhy-Dac 1	6 (55%)	0 (0%)	1 (9%)	5 (42%)
Rhy-Dac 2	8 (30%)	2 (7%)	0 (0%)	17 (63%)
Dac 1	1 (50%)	1 (50%)	0 (0%)	0 (0%)
And-Bas 1	4 (40%)	5 (50%)	1 (10%)	0 (0%)
Bas 1	0 (0%)	1 (100%)	0 (0%)	0 (0%)
Default	3 (33%)	0 (0%)	0 (0%)	6 (66%)

The "Rhy-Dac 2" chemostratigraphic unit, occurring in RAVLD673, has largely altered rocks with alteration intensities increasing downhole, from AI= 62 and CCPI= 48 at 350 metres to AI= 97 and CCPI= 63 at 530 metres. Here, two samples are classified as least altered, where one could be recognised as a volcaniclastic facies and the other had unidentified facies. Taking altered samples into account, seven could be identified as volcaniclastic.

The "Rhy-Dac 2" chemostratigraphic unit occurring in RAVLD663 (460–550 metres) is phenocryst-rich (10–15 vol.%, Fsp>Qz) with locally uneven crystal distributions; however, lithofacies determination is challenged by moderate sericite-chlorite alteration and patchy strong calc-silicate alteration (average AI= 60 and average CCPI= 53). Here, one sample is classified as least altered and, despite this, its facies could not be determined. At c. 300 to 330 metres in RAVLD663, another sample classified as least altered plots as "Rhy-Dac 2"; its facies was determined to be coherent.

Figure 4. Downhole core logs of RAVLD673 and RAVLD663 linked to chemostratigraphy, AI is plotted above with red line.

3 Discussion and conclusion

A key finding is that immobile elements reveal two different rhyolitic units at different stratigraphic positions. The "Rhy-Dac 2" unit belongs to the footwall and immediate hanging wall of the Rävliden North mineralisation and, consequently, to the SG. The "Rhy-Dac 1" unit belongs to the "transitional zone" between the SG and VG. Alteration makes determining facies difficult, but by identification of what is defined as least altered samples, it is suggested that "Rhy-Dac 1" is exclusively volcaniclastic, whereas the facies of "Rhy-Dac 2" remains elusive. Taking altered samples into account for "Rhy-Dac 2", several volcaniclastic and no coherent facies are found in RAVLD673, whereas in RAVLD663 coherent and volcaniclastic textures were both observed.

With immobile element chemostratigraphy, a better stratigraphic understanding of the Rävliden North host rocks is achieved. Rhyolitic rocks in the "transitional zone" have been linked spatially between drill cores, as well as to a respective volcaniclastic facies. However, footwall alteration is generally strong, and finding least altered samples is difficult. Further work, with more samples, should be done with this technique to establish a stronger link between lithofacies and chemostratigraphy, and to help guide exploration efforts in these altered rocks.

Acknowledgements

Thank you to all the geologists at the Boliden core archive and staff who have been helpful with logistics and discussions during visits for core logging.

References

Allen RL, Weihed P, Svenson SA (1996) Setting of Zn-Cu-Au-Ag massive sulfide deposits in the evolution and facies architecture of a 1.9 Ga marine volcanic arc, Skellefte District, Sweden. Econ Geol 91-6:1022–1053. https://doi.org/10.2113/gsecongeo.91.6.1022

Barrett TJ, MacLean WH, Åreback H (2005) The Palaeoproterozoic Kristineberg VMS deposit, Skellefte district, northern Sweden; Part II, Chemostratigraphy and alteration. Miner Deposita 40-4: 368–395. https://doi.org/10.1007/s00126-005-0001-2

Boliden (2021) Boliden Summary Report, Resources and Reserves 2021, Kristineberg. 1–42. https://www.boliden.com/490e8a/globalassets/operations/exploration/mineral-resources-and-mineral-reserves-pdf/2021/bol_main-1848472-v1-resources-and-reserves-kristineberg-2021-12-31.pdf. Accessed 1 February 2023

Chmielowski RM, Jansson N, Persson MF, Fagerström P (2016) 3D modelling of hydrothermal alteration associated with VHMS deposits in the Kristineberg area, Skellefte district, northern Sweden. Miner Deposita 51-1: 113–130. https://doi.org/10.1007/s00126-014-0572-x

Large RR, Gemmell JB, Paulick H (2001) The alteration box plot; a simple approach to understanding the relationship between alteration mineralogy and lithogeochemistry associated with volcanic-hosted massive sulfide deposits. Econ Geol 96-5: 957–971. https://doi.org/10.2113/gsecongeo.96.5.957

Maitre R, Streckeisen A, Zanettin B, Le Bas M, Bonin B, Bateman P (2004) Igneous Rocks: A Classification and Glossary of Terms. Cambridge University Press, Cambridge

Mataruga Z (2016) Determining host rock protolith in an altered VMS deposit in the Rävliden area, North Sweden. Bachelor thesis, Uppsala universitet, Institutionen för geovetenskaper http://proxy.lib.ltu.se/login?url=https://search.ebscohost.com/login.aspx?direct=true&db=edsbas&AN=edsbas.4A64FBDB&lang=sv&site=eds-live&scope=site

Rincon J (2022) Textural and chemical characterization of sulphide minerals at the Rävliden North VMS deposit, Skellefte district, Sweden. Licentiate thesis, Luleå University of Technology

Schlatter DM, Barrett T (2003) Chemostratigraphy of metamorphosed and altered Paleoproterozoic volcanic rocks associated with massive sulfide deposits at Rävliden and Kristineberg West, Skellefte district, Sweden Seventh Biennial SGA Meeting, Mineral exploration and sustainable development, Athens, Greece.

Skyttä P, Bauer TE, Tavakoli S, Hermansson T, Andersson J, Weihed P (2012) Pre-1.87 Ga development of crustal domains overprinted by 1.87 Ga transpression in the Palaeoproterozoic Skellefte district, Sweden. Precambrian Res 206-207:109–136. https://doi.org/10.1016/j.precamres.2012.02.022

Skyttä P, Weihed P, Högdahl K, Bergman S, Stephens MB (2020) Paleoproterozoic (2.0–1.8 Ga) syn-orogenic sedimentation, magmatism and mineralization in the Bothnia–Skellefteå lithotectonic unit, Svecokarelian orogen. In: Stephens MB and Weihed JB (ed) Sweden - Lithotectonic framework, tectonic evolution and mineral resources. Geological Society of London, pp 83–130.

Weihed P, Bergman J, Bergström U (1992) Metallogeny and tectonic evolution of the early Proterozoic Skellefte District, northern Sweden. Precambrian Res 58-1-4:143–167. https://doi.org/10.1016/0301-9268(92)90117-7

Årebäck H, Barrett TJ, Abrahamsson S, Fagerström P (2005) The Palaeoproterozoic Kristineberg VMS deposit, Skellefte district, northern Sweden, part I: Geology. Miner Deposita 40-4:351–367. https://doi.org/10.1007/s00126-005-0476-x

The Hydrothermal History of the VOLPA Seafloor Massive Sulphide Deposit, SW Pacific

Jonathan Umbsaar, Melissa Anderson, Daniel Gregory
[1]*University of Toronto, Department of Earth Sciences*

Abstract. The VOLPA deposit is a previously uncharacterized Seafloor Massive Sulphide (SMS) deposit on the Niua Volcanic Complex; an arc volcano located at the northernmost end of the Tofua Volcanic Arc, SW Pacific. SMS deposits form through circulating hydrothermal fluids in the oceanic crust, which are driven by anomalous geothermal gradients. Circulating fluids reach elevated temperatures, acidity, and REDOX potential, which are favourable conditions for the transport of metal cations. These deposits are enriched in a variety of critical metals, and represent a modern analogue to Volcanogenic Massive Sulphide (VMS) deposits, which are a valuable base and precious metal source. VOLPA is composed of especially barite-rich chimneys, in sulphur-encrusted trachyandesitic host rocks of variable permeability, resulting in deposit scale zonation of mineral abundances. Petrography, elemental mapping, and whole-rock geochemistry have facilitated subclassification of SMS chimneys, with implications for hydrothermal processes such as boiling, seawater mixing, magmatic volatile influx, as well as the pH, temperature, and REDOX conditions of the hydrothermal vent fluids. The conclusions of this research indicate that the distribution of critical metals across VOLPA are largely dependent on host rock permeability, depth, and the influx of magmatic volatiles, in addition to adsorption, colloidal gold transport, and structural influences.

1 Introduction

1.1 Seafloor Massive Sulphides

Seafloor massive sulphide (SMS) deposits are the modern equivalent to continental volcanogenic massive sulphide (VMS) deposits which are actively mined across the globe for Cu, Zn, Pb, Au, and Ag, with the capacity for enrichments in a host of other critical metals, including As, Bi, Co, Ga, Ge, In, Mn, Mo, Ni, Sb, Sn, and W (Robb 2005; Boschen et al. 2013). SMS deposits form on the ocean floor due to anomalous geothermal gradients generated by intruding magma bodies, and thus, tend to be localized along plate margin boundaries (Barrie 2012). The heat from these magma bodies triggers circulation of seawater (and injected magmatic volatiles), which become locally high-temperature, acidic, saline, and reducing, which are favourable conditions for the transport of metal cations, that are leached from the host rocks, and extracted from the cooling magma (Robb 2005; Barrie 2012). These metal cations precipitate out of solution when the hydrothermal fluids mix with the cold seawater, or otherwise when these fluids reach critical temperatures, resulting in boiling (Herzig and Hannington 1995). Fluid mixing destabilizes the metal complexes, causing the cations to be dropped out of solution (de Ronde et al. 2003).

To date, more than 700 hydrothermal vents have been identified, of which ~300 contain measurable quantities of metal-bearing sulphides (Beaulieu et al. 2013).

1.2 The VOLPA Deposit

The Volcano P Site A (VOLPA) deposit is a previously uncharacterized deposit located on the southern end of the Niua Volcanic Complex; an irregular, rectangularly-shaped arc volcano composed of multiple coalescing volcanic ridges, with accompanying, fissures, cones, and volcaniclastic mounds (Moum, unpublished thesis). This volcano is located at the northern end of the Tofua volcanic arc, along the Tonga-Kermadec trench in the SW Pacific (Figure 1).

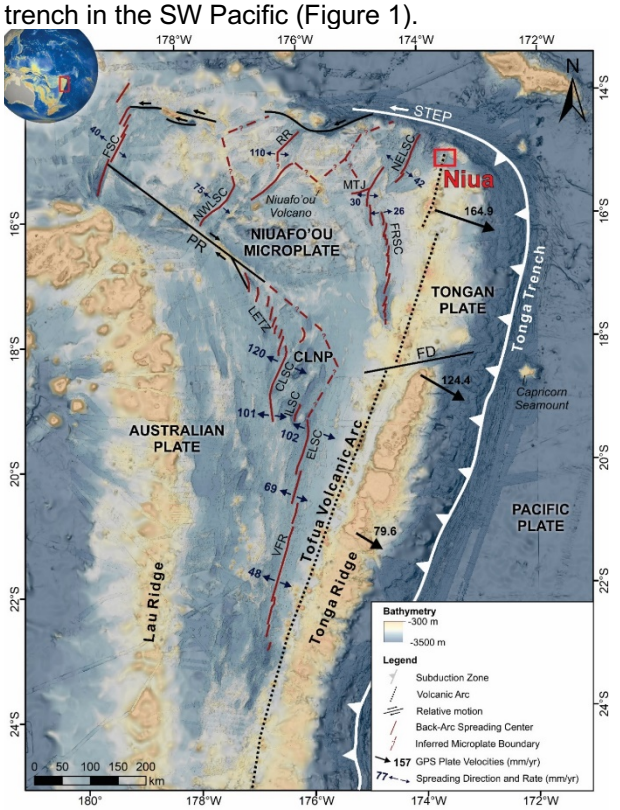

Figure 1. Bathymetric map of the Lau Basin. The Niua Volcanic Complex is highlighted in red.

The VOLPA deposit is situated in a volcanic crater at 1100 m depth and is roughly 1 km in diameter. It can be locally subdivided into eastern and western vent fields, with the west being composed of trachyandesitic, permeable volcaniclastics, and the east being composed of imposing trachyandesitic lava flows (Figure 2; Moum, unpublished thesis). Active venting and

seafloor boiling has been documented at the VOLPA deposit (Moum, unpublished thesis).

2 Methods

Samples and bathymetric data were collected by Nautilus Minerals Inc. during commercial exploration between 2011–2012, and additional bathymetric data was collected from the Niua volcanic complex in 2018 during the SO-263 cruise on board the R/V Sonne (Haase et al., 2018). 69 hand sample were selected for processing into thin sections and rock powders for bulk geochemical analysis. Thin sections were analysed using a Nikon Optiphot petrographic microscope in both reflected and transmitted light. Based on the whole rock geochemistry and petrography, samples were classified into chimney types (Sphalerite-barite, sphalerite-tennantite, chalcopyrite-pyrite, and chalcopyrite-tennantite). Twenty-five samples were then selected for electron microprobe analysis, and ten of those samples were later used to generate 1mm x 1mm laser ablation inductively coupled mass spectrometric (LA-ICP-MS) element maps.

3 Results and Discussion

3.1 Permeability of the Substrate

The VOLPA deposit is compositionally zoned in accordance with the permeability of the substrate. The west is composed of permeable volcaniclastic cover, and thus, oceanic seawater can more easily infiltrate the subsurface and interact with the hydrothermal fluids before reaching the ocean floor (Galley 1993; Andersen et al. 2015). The result is a cooler venting system that contains more sphalerite, galena, Pb-sulfosalts (gratonite, semseyite), and barite. The western vent field is compositionally enriched in Ba, Pb, Tl, and Ag. In contrast, the eastern vent field is covered by relatively impermeable lava flows, and thus, hydrothermal vents exhibit more focussed and less diffuse venting, resulting in higher temperature fluids with a greater capacity for surficial boiling. These eastern vents are enriched in Cu, Au, In, Co, and S, and generally contain more chalcopyrite and tennantite (Figure 2).

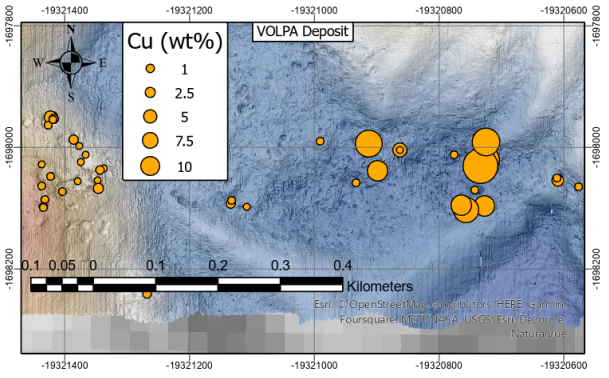

Figure 2. Bathymetric map of the VOLPA crater. Orange circles indicate copper wt% of SMS chimney samples

These observations complicate the classification of SMS deposits, because despite both the eastern and western vent fields being located on the same volcanic crater, they are compositionally very different.

3.2 Magmatic Volatile Input

There is evidence to suggest that magmatic volatiles have contributed to the formation of the VOLPA deposit.

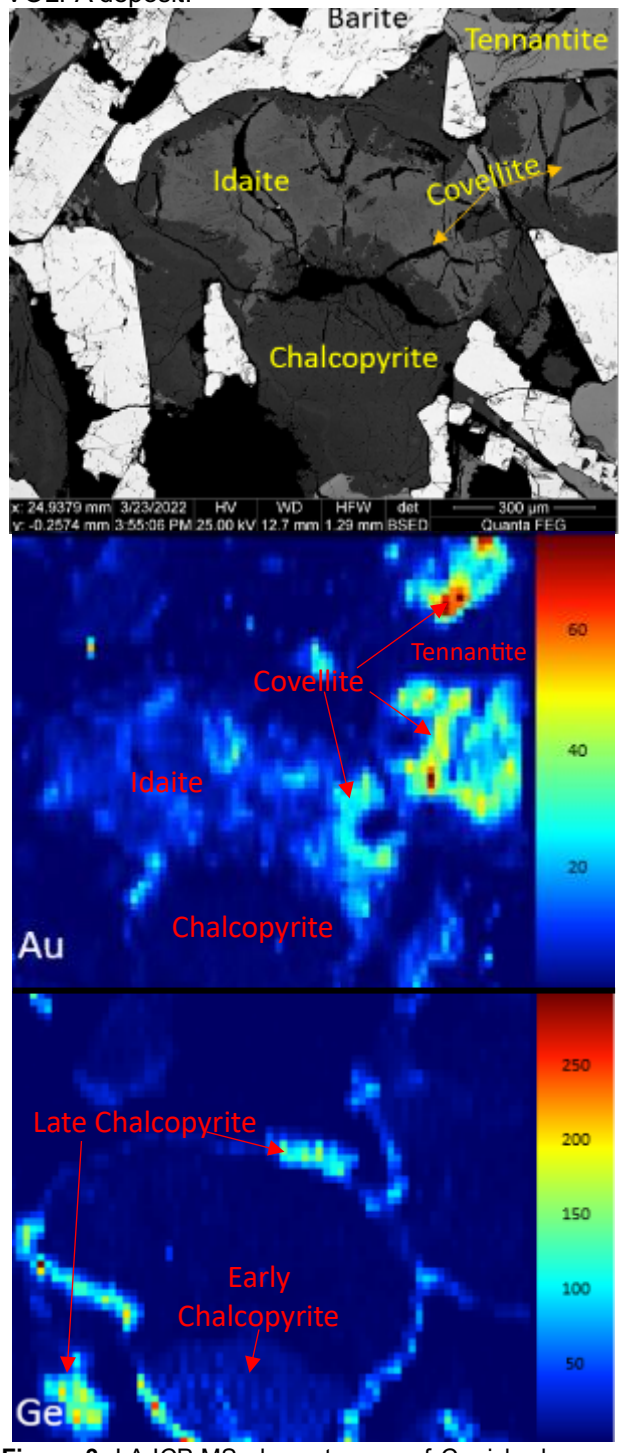

Figure 3. LA-ICP-MS element maps of Cu-rich phases, with chalcopyrite replaced by covellite-idaite, and late tennantite, with critical metal enrichments associated with these later phases of growth. Au and Ge element maps are shown with concentrations in ppm.

Magmatic volatiles are characterized by high-sulfidation mineral phases such as enargite, tennantite-tetrahedrite, covellite, orpiment, realgar, and native sulphur: all of which were identified at the VOLPA deposit, and consistently correlated with elevated concentrations of characteristically epithermal-associated elements (Au, Ag, As, Sb, Hg) among other critical metals (Wohlgemuth-Ueberwasser et al. 2015; Fuchs et al. 2019). Characteristics that are diagnostic of magmatic volatile flux, are ones that demonstrate changing fluid conditions to a more oxidizing, and Cu-rich system. This is evidenced in chalcopyrite-diseased sphalerite that is rimmed with tennantite.

Additionally, this phenomenon is also evident in replacement textures of chalcopyrite into idaite-covellite (representing a loss of iron, and gain in copper), with a subsequent back-reaction and exsolution of chalcopyrite from the idaite-covellite (Figure 3). Replacement, dissolution, and exsolution features are key when investigating for critical metals because these textures demonstrate rapidly changing fluid conditions. Under steady conditions, trace metal capture is low, as evidenced by depleted massive and biomineralized sulphides.

3.3 Comparisons to Niua South

The VOLPA deposit is adjacent to the Niua South SMS deposit, which is similarly hosted on the Niua Volcanic Complex. Relative to VOLPA, Niua South is compositionally enriched in Cu, Au, Co, In, Se, Mo, Sn, Fe, Mn, Si, Ca, and S, while VOLPA is enriched in Ba, Sr, Zn, Cd, Ge, Pb, Ag, As, and Sb. Based on these elemental enrichments and depletions, it seems that VOLPA represents a lower-temperature system, with more abundant seawater infiltration. In contrast, Niua South appears to contain more high-temperature phases like chalcopyrite, but does not contain the same high-sulfidation mineral phases that are present at VOLPA.

Although no dates have yet been calculated from the VOLPA deposit, Rb-Sr isotope age dating from Niua South indicates that the barite content of the SMS chimneys correlates with age, due to the prolonged exposure to seawater as hydrothermal activity wanes. The average Ba concentration at VOLPA is 22.98%, while only 12.69% at Niua South; therefore, it is likely that the VOLPA deposit is older than Niua South. This is further evidenced by the presence of amorphous silica at Niua South, whereas the same silica content is very rare at VOLPA. There is evidence to suggest that an amorphous silicate host housed early spheroidal pyrites (Si and O are well correlated as elemental inclusions in these pyrites), but has since been dissolved in accordance with the retrograde solubility of quartz. The abundance of silica at Niua South may indicate that the advancement of this siliceous cap is an ongoing process.

Thia age difference between VOLPA and Niua South may provide rationale for why high-sulfidation minerals associated with magmatic volatiles are much more common at VOLPA. Magmatic volatiles may have been introduced to this volcanic system relatively early, while Niua South was not yet actively venting. These observations are generally supported by the paragenetic sequences of chimney samples from VOLPA and have implications for comparisons to other SMS deposits.

3.4 Co-Precipitation of Phases

In addition to the aforementioned textures indicating a fluctuating hydrothermal environment, it is equally important that multiple phases are present in the system in order to accommodate the cations that are actively precipitating. The partition coefficients

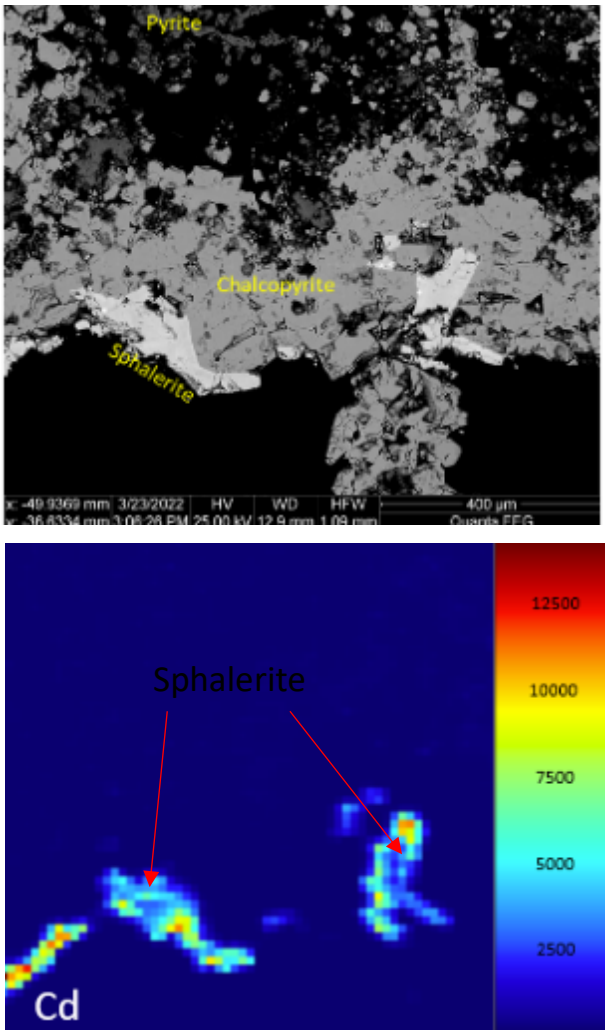

of metals from solution varies for the different sulphides present in the system. For example, at VOLPA, sphalerite is an excellent sink of Hg, Ga, Ge, and Cd (Figure 4).

Figure 4. LA-ICP-MS element map of Cd concentrations in a Cu-Fe-rich SMS chimney with minimal sphalerite demonstrates the importance of multi-phase systems for metal capture. Concentrations are in ppm.

Chalcopyrite is less likely to be enriched in these elements, but can generally accommodate more In, Mo, and Se. Multi-phase systems are ideal for critical metal capture, but overlapping stability fields of multiple sulphide phases can be rare. Boiling is an ideal mechanism for co-precipitating multiple phases because the system is already destabilized by the introduction of a gaseous phase.

4 Conclusions

The hydrothermal history of the VOLPA deposit highlights how nuanced the conditions of SMS deposit formation can be, and illustrates the difficulties in rigidly classifying and differentiating deposits based on tectonic setting and host lithology. Two distinct SMS deposits (Niua South and VOLPA) located on the same volcanic complex contain variable geochemical enrichments, petrologies, textures, and conditions of formation. There is evidence to suggest that VOLPA is an older deposit, and may have been subject to early magmatic volatile fluxes. Moreover, the VOLPA deposit can be further subdivided on the basis of the permeability of the substrate, which results in deposit-scale zonation, with low-temperature phases being enriched in regions with higher permeability.

There is reason to believe that magmatic volatiles have contributed to the critical metal endowment of the VOLPA deposit based on the high-sulfidation mineral phases and correlations of critical and precious metals with these phases.

Important textures to investigate for critical metal abundances are those that indicate fluctuating hydrothermal conditions, such as adsorption, resorption, replacement, and exsolution textures, as well as the co-precipitation of multiple sulphide phases. Finally, not all critical metals are affinitive of high-temperature systems. Some elements like Pb, Tl, and Ag, are generally more common in low-temperature venting systems, demonstrating the challenges associated with high resolution element mapping and resource estimations.

The ongoing research into these SMS deposits is indispensable for prospective private companies and government agencies attempting to navigate the burgeoning field of seafloor mining. Likewise, these insights into SMS deposits can be translated to the ancient rock record, to aid in paleoenvironmental reconstruction and investigations of the previously overlooked critical metal abundances in VMS deposits.

Acknowledgements

Thanks to Nautilus Minerals (now SM2) for assisting with sample collection.

Thanks to NSERC-iMAGE Create and the coordinators (Dr. Mark Hannington, Dr. Alan Baxter, and Dr. Erin Bethell) for providing funding for research and learning activities.

Thanks to David Diekrup, Alexander Voinot, Matthew Laybourne and Agatha Dobosz for help with EPMA and LA-ICP-MS analyses.

Thanks to Dr. Jan Peters, Dr. Shu Xu, and Dr. Cornell Dr Ronde for guidance in this research.

Thanks to Actlabs, the University of Toronto, University of Ottawa, Queen's University, and Vancouver Petrographics for all assisting with sample preparation and analytical work.

References

Andersen C, Rüpke L, Hasenclever J, Grevemeyer I, Petersen S. 2015. Fault geometry and permeability contrast control vent temperatures at the Logatchev 1 hydrothermal field, Mid-Atlantic Ridge. Geology. 43(1):51–54. doi:10.1130/G36113.1.

Barrie CT. 2012. Volcanogenic massive sulfide occurrence model. Economic Geology. 107(5):1073–1073. doi:10.2113/econgeo.107.5.1073.

Beaulieu SE, Baker ET, German CR, Maffei A. 2013. An authoritative global database for active submarine hydrothermal vent fields. Geochemistry, Geophysics, Geosystems. 14(11):4892–4905. doi:10.1002/2013GC004998.

Boschen RE, Rowden AA, Clark MR, Gardner JPA. 2013. Mining of deep-sea seafloor massive sulfides: A review of the deposits, their benthic communities, impacts from mining, regulatory frameworks and management strategies. Ocean and Coastal Management. 84:54–67. doi:10.1016/j.ocecoaman.2013.07.005.

Fuchs S, Hannington MD, Petersen S. 2019. Divining gold in seafloor polymetallic massive sulfide systems. Mineralium Deposita. 54(6):789–820. doi:10.1007/s00126-019-00895-3.

Galley AG. 1993. Characteristics of semi-conformable alteration zones associated with volcanogenic massive sulphide districts. Journal of Geochemical Exploration. 48(2):175–200. doi:10.1016/0375-6742(93)90004-6.

Herzig PM, Hannington MD. 1995. Polymetallic massive sulfides at the modern seafloor a review. Ore Geology Reviews. 10(2):95–115. doi:10.1016/0169-1368(95)00009-7.

Moum T. Geology and geochemistry of the newly-discovered VOLPA seafloor massive sulfide deposit, Niua volcanic arc complex , Tonga , SW Pacific. Unpublished Thesis.

Robb L. 2005. Introduction to Ore-Forming Processes. Blackwell Publishing (1-373).

Wohlgemuth-Ueberwasser CC, Viljoen F, Petersen S, Vorster C. 2015. Distribution and solubility limits of trace elements in hydrothermal black smoker sulfides: An in-situ LA-ICP-MS study. Geochimica et Cosmochimica Acta. 159:16–41. doi:10.1016/j.gca.2015.03.020.

Iron, boron and sulfur isotope constraints on ore-forming process of the subseafloor replacement-style volcanogenic massive sulfide systems

Bing Xiao[1], Huayong Chen[1, 2, 3], Fang Huang[4], Yuzhou Feng[1], Xia Hu[4]
[1]Key Laboratory of Mineralogy and Metallogeny, Guangzhou Institute of Geochemistry, Chinese Academy of Sciences, Guangzhou 510640, China
[2]University of Chinese Academy of Sciences, Beijing 100049, China
[3]Guangdong Provincial Key Laboratory of Mineral Physics and Materials, Guangzhou 510640, China
[4]CAS Key Laboratory of Crust-Mantle Materials and Environments, School of Earth and Space Sciences, University of Science and Technology of China, Hefei 230026, Anhui, China

Abstract. A combined systematic Fe, B and S isotope investigation has been applied in the well-preserved Ashele subseafloor replacement-style VMS deposit, which comprises two stages of Cu mineralization, i.e., early massive sulfides, which were replaced by late vein-dominated chlorite-chalcopyrite assemblages. Boron isotopes of tourmaline and sulfur isotopes of sulfides indicate significant seawater participated during the formation of massive sulfides and increasing contribution of magmatic sulfur from the early to late stages. In addition, δ^{56}Fe values of pyrite gradually increase outwards from the mineralization center, which is likely related to the different extent of isotopic exchange and formation temperature. The new two-stage ore-forming model shows that at the early stage, rapid mixing of hydrothermal fluid from underlying magma chamber with abundant cold seawater led to rapid deposition of pyrite and associated Cu mineralization. Long-term hydrothermal activities in relatively closed systems would promote the formation of upper massive ores, which resulted in an equilibrium system between sulfides and associated fluid with wide ranges of δ^{56}Fe in sulfides. The late hydrothermal activities in relatively open system would contribute to stringer sulfides or stockworks underlying the massive ore with heavier Fe isotope compositions in sulfides.

1 Introduction

The subseafloor replacement-type VMS deposits are formed by the fully to partially hydrothermal replacement of subseafloor rocks and commonly have large metal reserves and economic values (Galley et al. 1995; Piercey 2015). However, their detailed sulfide precipitation processes are not well constrained by existing geochemical tracers. Furthermore, the relative proportion of fluid sources (e.g., seawater and magmatic fluid) in different alteration and mineralization stages is still unknown. In this study, we report a complete suite of B, Fe and S isotope data for whole-rocks and Fe bearing minerals, including pyrite, chalcopyrite, and chlorite from the Ashele VMS deposit. These results are used to understand sulfide precipitation processes, as well as B, Fe and S isotope compositions and behaviors in the subseafloor hydrothermal systems, and discuss the entire alteration/mineralization process of VMS deposits.

2 Deposit Geology

The Ashele deposit, the largest known VMS Cu-Zn deposit in the Chinese Altay, contains significant Cu (1.08 Mt. @ 2.46%), Zn (0.43 Mt. @ 0.41%) and Au (27.2 t @ 0.36 g/t; Zheng et al., 2016). Mineralization and hydrothermal alteration is generally hosted by the Ashele Formation, which mainly comprises tuff, breccia tuff, volcanic breccia, agglomerate, dacite, andesite, basalt, sedimentary tuff, and limestone (Zheng et al. 2016).

Based on previous study and our new observations, hydrothermal alteration and mineralization zonation at the Ashele deposit are well presented in the hanging wall of volcanic tuff, which can be divided into five zones (outwards from the mineralization center), i.e., the massive sulfides (I), quartz-pyrite (II), chlorite-chalcopyrite-quartz-pyrite (III), quartz-chlorite-sericite-pyrite (IV), and quartz-sericite-pyrite zones (V), and the Cu mineralization is mainly hosed in zone I and III.

3 Results

δ^{56}Fe values for the basalt and dacite porphyry show similar and small variations (0.01‰–0.06‰ and 0.03‰–0.06‰), while the tuff has a larger range of δ^{56}Fe (-0.1‰–0.24‰). Pyrite from zone I (Py1), zone II (Py2), zone III (Py3) and zone V (Py4) have δ^{56}Fe of -0.46‰–-0.02‰, -0.09‰–0.07‰, 0–0.21‰ and -0.02‰–0.29‰, respectively. Chalcopyrite from zone I (Ccp1) and zone III (Ccp2) have δ^{56}Fe of -1.56‰–-0.49‰ and -0.60‰–-0.04‰, respectively. Chlorite from zone III has δ^{56}Fe of -0.48‰ to -0.12‰ (Fig. 1).

The δ^{34}S values of Py1 ranges from -2.62‰ to 5.94‰. Compared with Py1, Py2, Py3, and Py4 have higher δ^{34}S values of 1.28‰–5.00‰, 1.25‰–9.76‰, and 3.13‰–6.25‰, respectively. The δ^{34}S values of Ccp1 and Ccp2 have δ^{34}S values of 0.01‰–4.15‰ and 2.18‰–3.05‰, respectively (Fig. 2).

Boron isotope compositions (δ^{11}B) of Mg-rich tourmaline in the zone I are of -5.57‰ to -2.73‰.

4 Source contribution in two stages ore-forming fluids

Boron in VMS systems could originate from seawater and magmatic fluids. Seawater usually has

heavy B isotope compositions with $\delta^{11}B$ value of about +40‰, while the average $\delta^{11}B$ value of igneous rock is around -10‰ (Trumbull et al. 2020), which therefore provides a sensitive indicator for mixing of seawater and magmatic fluid. The modal calculations indicate that the fraction of B from seawater relative to B of hydrothermal fluid would be 19% to produce an average $\delta^{11}B$ value of -1.53‰, suggesting that significant seawater participated in the processes of tourmaline and massive sulfide formation, which is also confirmed by Mg-rich characteristic of tourmaline.

Previous studies have shown that reduced sulfur (H_2S) for VMS systems comes from (1) bacterial sulfate reduction (BSR) of seawater sulphate, (2) thermochemical sulfate reduction (TSR) of sulfate from seawater or hydrothermal alteration products, and (3) igneous sulfur either via leaching from footwall volcanic rocks and/or direct contributions from magmatic fluids/volatiles (Seal 2006). Most of $\delta^{34}S$ values obtained from sulfides in this study are basically above 0‰, and lacking of framboidal pyrite in the Ashele deposit with relatively high temperatures (above 200 °C), indicating BSR is not a significant source of reduced sulfur in the Ashele deposit. Model calculations were undertaken to evaluate the relative contribution of igneous and TSR sulfur for sulfides, and the results show the increasing contribution of magmatic sulfur from the early (35%) to late (76%) stages.

5 Ore-forming process in the early massive sulfides and late vein-dominated chlorite-chalcopyrite stages

The calculated $\delta^{56}Fe$ isotope compositions of hydrothermal fluid associated with early stage Ccp1 range from -1.65‰ to -0.71‰ (avg. -1.01‰), which is lighter than the typical sub-seafloor hydrothermal fluids (-0.67‰–-0.09‰) and magmatic rocks (basalt, tuff, and dacite porphyry) in the ore district (~ 0‰). Based on Rayleigh fractionation modeling results, if Py1 and associated fluid have reached equilibrium in an open system, removal of 100% of the initial iron in the fluid as pyrite only lead to about 0.8‰ $\delta^{56}Fe$ drop of fluid, which could not explain $\delta^{56}Fe$ value of -1.65‰, however, in a closed system, the removal of 80% of the initial iron in the fluid as pyrite could shift the $\delta^{56}Fe$ of fluid from -0.30‰ towards -1.65‰. In addition, The studies of stratigraphic sequence and zircon U-Pb ages in the Ashele district have shown that basaltic magmatic activity occurred immediately after the formation of the massive ores and isolated them from oxygenated seawater. The underlying quartz-pyrite zone and the compact texture feature of massive ores would cause limited circulation between massive sulfides and the external fluid. As a result, the wide range of $\delta^{56}Fe$ in Py1 and Ccp1 of the Ashele deposit may have recorded the isotopic change controlled by pyrite-fluid equilibrium in a relatively closed system.

The calculated Fe isotope compositions of hydrothermal fluid associated with late stage Ccp2 range from -0.75‰ to -0.19‰ (avg. -0.53‰) based on the theoretical equilibrium calculation (Fujii et al. 2014), which is similar to that of seafloor hydrothermal fluids. The modal calculations indicate Fe isotope fractionations between Py2, Py3, Py4 and associated fluid have not reached equilibrium. In this study, the extent of Fe isotope exchange (F) relative to the equilibrium value for pyrite was simply calculated, and the results indicate the extent of Fe isotope exchange is gradually increasing from Py2, Py3 to Py4, represented by the increasing ^{56}Fe values in an open system.

The proposed model based on Fe, B and S isotope suggests long-term hydrothermal activities in the relatively closed systems promote the formation of upper massive ores at the early stage, and late hydrothermal activities in relatively open system would contribute to underlying stringer sulfides or stockworks.

Acknowledgements

This study was funded by the National Natural Science Foundation of China (41725009, 42173065, U1603244, 41921003, 42003033), and the Strategic Priority Research Program of the Chinese Academy of Sciences (XDB42020404), the Science and Technology Planning of Guangdong Province, China (2020B1212060055), and the Guang Dong Major Project of Basic and Applied Basic Research (2019B030302013).

References

Fujii, T., Moynier, F., Blichert-Toft, J. and Albarède, F. (2014): Density functional theory estimation of isotope fractionation of Fe, Ni, Cu, and Zn among species relevant to geochemical and biological environments; Geochimica et Cosmochimica Acta, v. 140, p. 553-576.

Galley, A.G., Watkinson, D.H., Jonasson, I.R. and Riverin, G. (1995): The subsea-floor formation of volcanic-hosted massive sulfide; evidence from the Ansil Deposit, Rouyn-Noranda, Canada: Economic Geology, v. 90, p. 2006-2017.

Piercey, S.J. (2015): A semipermeable interface model for the genesis of subseafloor replacement-type volcanogenic massive sulfide (VMS) deposits; Economic Geology, v. 110, p. 1655-1660.

Seal, R.R., II (2006): Sulfur Isotope Geochemistry of Sulfide Minerals; Reviews in Mineralogy and Geochemistry, v. 61, p. 633-677.

Trumbull, R.B., Codeço, M.S., Jiang, S.Y., Palmer, M.R. and Slack, J.F. (2020): Boron isotope variations in tourmaline from hydrothermal ore deposits: A review of controlling factors and insights for mineralizing systems; Ore Geology Reviews, v. 125, p. 103682.

Zheng, Y., Wang, Y.J., Chen, H.Y., Lin, Z.W., Hou, W.S. and Li, D.F. (2016): Micro-textural and fluid inclusion data constraints on metallic remobilization of the Ashele VMS Cu-Zn deposit, Altay, NW China; Journal of Geochemical Exploration, v. 171, p. 113-123.

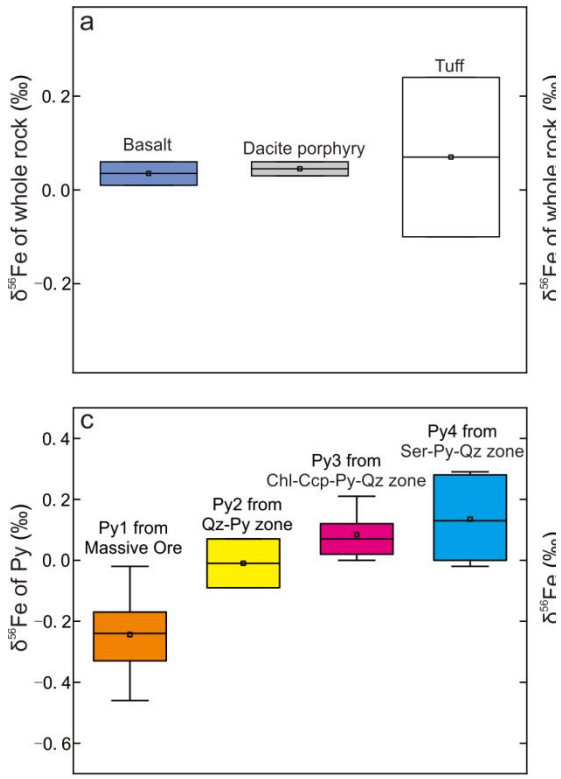

Figure 1. The ranges of Fe isotope for basalt, dacite porphyry and tuff (a); whole-rock from the massive ores, quartz-pyrite and chlorite-quartz-chalcopyrite-pyrite zones (b); pyrite from the massive ores, quartz-pyrite, chlorite-quartz-chalcopyrite-pyrite and sericite-pyrite-quartz zones(c); chalcopyrite and chlorite from the massive ores and chlorite-quartz-chalcopyrite-pyrite zones (d) in the Ashele Cu-Zn deposit

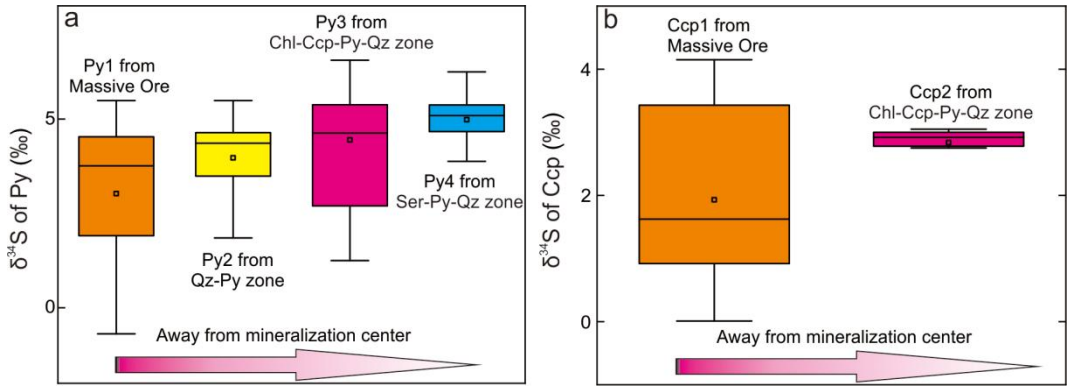

Figure 2. The ranges of S isotope for pyrite (a) and chalcopyrite (b) from the Ashele Cu-Zn deposi
t

The Tectonic Evolution of the North New Hebrides Backarc Troughs: A Remote-Predictive Mapping Approach

David J. Summer[1], Melissa O. Anderson[1], Philipp A. Brandl
[1]Department of Earth Sciences, University of Toronto, Canada [2]GEOMAR Helmholtz Centre for Ocean Research, Kiel, Germany

Abstract. Extensional backarc basins are the modern analogue for the tectonic setting of many ancient Volcanogenic Massive Sulphide deposits and are the sites of modern Seafloor Massive Sulphide deposition. However, little is known about the tectonic processes involved in the opening of nascent backarc basins prior to the establishment of seafloor spreading. This study addresses the question: what is the tectonic evolution of the over-riding plate during the early stages of backarc basin development? To answer this, the ~3 Ma geodynamic history of the North New Hebrides Backarc (NNHB) is evaluated with respect to regional tectonic complexities. A 1:100,000 lineament map of the NNHB has been produced via integration of available bathymetry datasets. Morphotectonic and lineament classifications are accomplished via visualization in an ArcGIS workflow. Lineament mapping is used to resolve fault kinematics of centroid moment tensor data in seismically active areas. Lineament analysis, fault kinematics, seafloor morphology and crosscutting relationships of mapped features are used to assess stress regime changes in the North New Hebrides Backarc. Preliminary results reveal three stages of backarc basin opening: initial arc breakup, east-west directed rifting and ongoing transtensional rifting.

1 Introduction

Volcanogenic Massive Sulphide (VMS) deposits formed in a variety of submarine tectonic settings, including mid-ocean ridges, continental rifts, and backarc basins. However, most VMS deposits are interpreted to have formed in a rifted arc setting, which progress to deep backarc basins before basin closure and accretion onto continental margins (Hannington et al. 2005). In the modern seafloor setting, many Seafloor Massive Sulphide (SMS) deposits have been identified and described, including deposits located in extensional oceanic convergence zones. While the tectonic environment and local geologic controls on magmatism and hydrothermal systems are described, little is known about the early stages of arc rifting and nascent backarc basin opening in the context of magmatic-hydrothermal evolution. Specifically, it is unknown whether the magma plumbing in rifted backarc basins is inherited from the migrating arc and whether this scenario contributes to long-lived hydrothermal systems. These are fundamental gaps in our understanding about where large SMS deposits can be found.

The New Hebrides subduction zone (NHSZ) is uniquely suited to investigating the early stages of backarc basin formation. The New Hebrides Arc formed ~10 Ma, with backarc rifting commencing ~3 Ma as a result of complex tectonic events (detailed below). The recent availability of yet unexplored high- resolution bathymetry datasets provides the opportunity to visualize the backarc in detail. By developing a remote-predictive mapping approach unique to the region, interpretation of geologic features is made possible, culminating in the development of a detailed spatio-temporal model of the regional tectonic evolution.

Tectonic Setting

The NHSZ is a ~10 Ma oceanic convergent boundary accommodating subduction of the Australia Plate beneath the North Fiji Basin (NFB) in the SW Pacific (Figure 1). Stretching from ~9.5-23°S, the subduction zone formed as a result of a

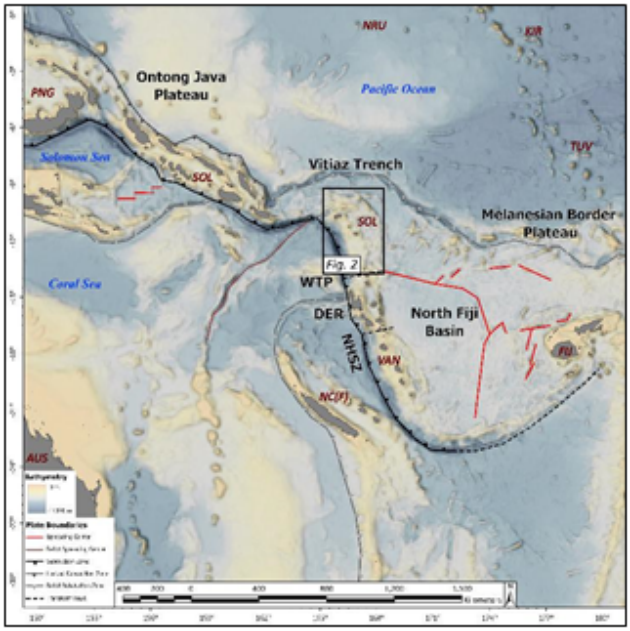

Figure 1. Regional map of the SW Pacific. The North New Hebrides Arc and Backarc are outlined by the Figure 2 box. Bathymetry data is from the Global Multi-Resolution Topography data syntheses.

subduction polarity reversal initiated by the arrival of the Ontong Java Plateau at the Vitiaz Trench (Petterson et al. 1999). Following subduction initiation, asymmetric rollback of the Australia Plate caused the opening of the NFB and clockwise rotation of the NHSZ (Schellart et al. 2006). Beginning ~3 Ma, arrival of the D'Entrecasteaux

Ridge (DER) at the New Hebrides Trench (NHT) between 15-16°S caused segmentation of the NHSZ with a central compression belt separating extensional zones to the north and south (Calmant et al. 2003). Extension in the North New Hebrides Subduction Zone (NNHSZ) resulted in the opening of NNHB. The NNHB widens and deepens northward from ~13.5°S, reaching depths of up to ~4000 m and terminating abruptly at a ~2 km high escarpment, the San Gerónimo Fault (SGF) at ~10°S. Collision of the DER with the New Hebrides Arc was followed by the arrival of the West Torres Plateau (WTP) at ~0.7-1.0 Ma directly north of the DER (Meffre and Crawford 2001).

2 Methods

2.1 Bathymetry Data

Seafloor visualization was achieved via the compilation of available ship-track bathymetry and the production of hillshade and slope raster datasets in an ArcGIS workflow. Raster resolutions ranges from 25- 150 m. Areas lacking ship-track bathymetry coverage are underlain by the Global Multi-Resolution Topography data synthesis.

2.2 Lineament mapping

Mapping of lineament feature was accomplished using a remote-predictive mapping approach, a process whereby bathymetric features are interpreted based on previously ground-truthed morphological properties. The most frequently observed lineament features observed in the NNHB are normal faults, which are characterized by an abrupt change in relief across a lineament (i.e. fault scarp), and volcanic fissures, which are characterized by symmetrical slopes on either side of the feature.

Mapped lineaments vary in length from ~100 m to several kilometers. To ensure proportional representation in lineament analysis using rose diagrams, all line segments are divided up into 100 m segments. The line segments are classified into eight different categories based on trend in order to produce a lineament orientation map (Figure 2).

2.2 Centroid moment tensor data

Centroid moment tensor (CMT) data for earthquake with Mw >5.0 were acquired from the global CMT project. CMTs up to a depth of 30 km were included to capture all crustal earthquakes. The dataset was imported into ArcGIS using the Arcbeachball tool. Each CMT has two possible focal planes. Where possible, the focal planes were resolved using local lineament features, assuming that fault plane of an earthquake will have a strike subparallel to the structures at surface. Where the focal plane of a CMT could not be resolved, CMTs were classified as general fault types.

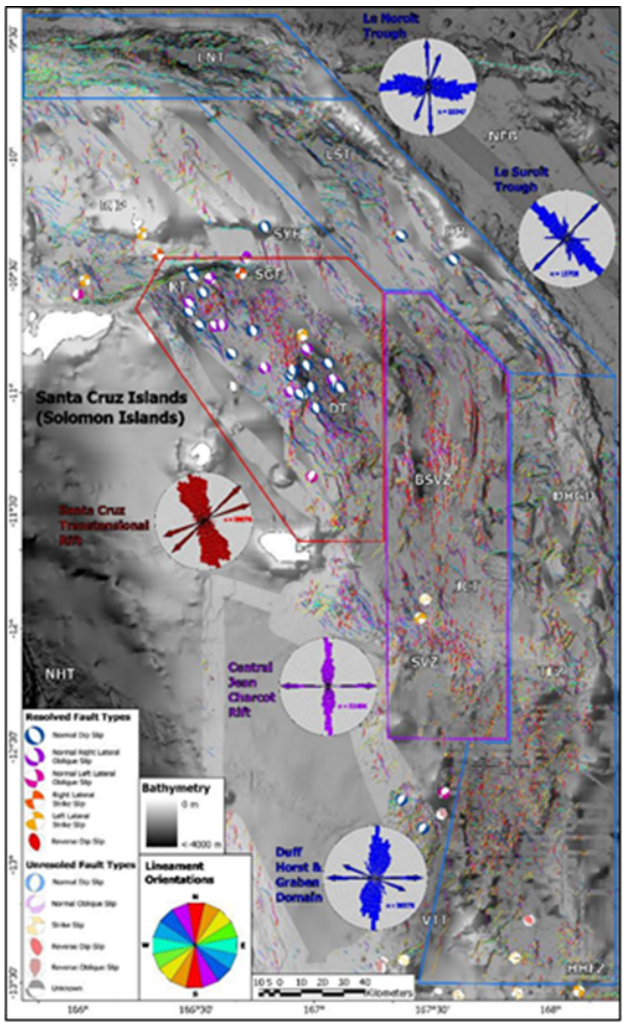

Figure 2. Lineament orientation map of the NNHSZ. Polygons and rose diagrams are colour-coded based on stage of backarc opening: blue = initial arc breakup, purple = central JCT rift, red = SCTR. Arrows on rose diagrams represent principal extension directions (perpendicular to lineament orientations). See in-text for acronym meanings.

3 Morphology and Lineament Analysis

3.1 North New Hebrides Arc Break-up

The Duff Ridge (DR) is arcuate ridgeline that forms the northern boundary of the NNHB, separating it from the NFB. It is a relict arc recording the position of the North New Hebrides Arc (NNHA) prior to the rift initiation (Auzende et al., 1995). Trench-ward from the DR are two sedimented, flat-bottomed rift basins elongated parallel to the ridgeline. The E-W oriented Le Noroît Trough (LNT) reaches depths of ~4300 m and is bound to the south by a series of fault scarps with a cumulative throw of ~3000 m that rise to the floor of the Reef Islands Plateau (RIP), a region of relict arc/forearc rifted from the DR. The NW-SE oriented Le Suroît Trough (LST) reaches depths of ~3600 m and is bound by a ~500 m footwall to the SW, from which the RIP shoals westward towards the Reef Islands.

At its southeast end, ~11°S, the DR curves to a N-S trend where the ridge morphology yields to the Duff Horst and Graben Domain (DHGD). The horst and graben fragmentation of the relict arc is characterized by an arrangement of tilted horst structures with prominent, anastomosing W- to WNW-dipping fault scarps which bound discontinuous sedimented half- graben basins extending south to the Tikopia Fracture Zone (TFZ). The TFZ is an E-W trending structure in the NFB that intersects the backarc at ~12.2°S. South of the TFZ, the relict arc is more heavily fragmented and consists of smaller horst structures and lower relief footwall scarps. The exception to this is a single, prominent ~100 km long escarpment which is a boundary fault separating the relict arc DHGD from a single narrow basin, the Vot Tande Trough (VTT).

Lineament analysis reveals two peak lineament orientation frequencies at 0-5° and 20-25° in the DHGD. Lineament orientations combined with left-lateral offset ridgelines indicate a transtensional stress regime with conjugate normal-oblique to oblique-strike slip faulting. From its northern extent at ~11°S, the DHGD widens from ~20 km to ~65 km at ~13.5°S where the NNHB abruptly terminates and intersects the Hazel Holme Fracture Zone (HHFZ), a slow E-W trending spreading centre in the NFB. The geometry of the DHGD together with indicators for transtensional tectonics reveals that deformation in this region accommodated clockwise rotation of the NNHA.

Lineament analysis of the troughs paralleling the DR reveal peak lineament orientation frequencies of 85-90° and 110-115° in the LNT and 140-145° in the LST. This indicates SW-directed rifting of the RIP with respect to the DR and NFB. The timing of the rifting with respect to the DHGD formation is unclear.

3.2 Central Jean Charcot Rift

The central NNHB is characterized by uniform N-S-trending lineament orientations, suggesting a transition from transtensional to E-W extensional tectonics. The seafloor morphology, however, is highly variable within this zone. To the north of the VTT the Starfish Volcanic Zone (SVZ) occupies an area of ~1500 km2 at the western termination of the TFZ. The SVZ has high relief relative to the surrounding basins and is characterized by high density of volcanic cones (<3 km in width) and volcanic fissures (<3 km in length) and a central large volcanic edifice, the Starfish Volcano (~10 km wide) at about 12.2°S.

To the north of the SVZ, is the sedimented Jean Charcot Trough (JCT), which lacks volcanism and has a sparsity of lineaments. The JCT reaches a maximum depth of ~3200 m and is bound to the west by rifted arc volcanic crust and to the west by an oceanic core complex (OCC). The OCC rises to a depth of 1900m and lies just to the west of the DHGD. Striations on the exhumed OCC record an extension direction consistent with the principal WNW-ESE extension indicated by lineament analysis in the DHGD.

In the north end of the JCT is the Brittle Star Volcanic Zone (BSVZ) with an area approximately the same as the SVZ. This area features prominent N-S striking normal faults with scarp lengths of up to ~80 km. At the centre of the volcanic zone is a ~10 km wide rift valley reaching up to ~3500 m in depth with ridge crests up to 1500 m high. The axial valley has a hummocky floor indicating recent volcanic activity. To the east, a parallel, long and narrow rift valley has a sedimented floor, suggesting that rifting has migrated from east to west. North of the BSVZ, the main rift valley deepens to a maximum depth of ~4000 m. North of ~10.8°S, N-S trending lineaments become sparse in hummocky terrain that shoals northward to depths of 2200-1700m.

3.3 Santa Cruz Transtensional Rift

To the east of BSVS lies the Santa Cruz Transtensional Rift (SCTR). The southwestern end of this zone features the Dolphin Trough (DT), a ~65 km long, ~20 km wide sigmoidal shaped basin. The morphology of this basin is characteristic of transtensional basins (cf. Wu et al. 2009). The basin footwall scarps reach maximum throws of ~1700 m and ~2600 m on the eastern and western flanks, respectively. The two bounding horsts have been offset oblique to the cross-basin axis of the basin. South from the western basin footwall, the escarpment fans out into a series of en echelon normal faults. To the southwest of the basin, a sequence of parallel NNW-SSE trending faults produces a terraced morphology, stepping up towards an arc-front volcano. To the northwest of the basin is the Kaiyo Trough (KT), which deepens northward, has a hummocky and heavily faulted morphology and is populated with numerous volcanic fissures and rifted volcanic edifices. The KT terminates at the E-W trending SGF. The SCTR is the most seismically active location in the NNHB. The resolved focal planes of the CMT data reveal prevalent NW-SE striking normal dip slip to left lateral oblique slip fault kinematics. Lineament analysis of the region reveals two peak lineament orientation at 145-150° and 160-165°. The morphology of the basin, lineament analysis, and the fault kinematics in both the KT and DT indicate transtensional tectonics accommodating counter-clockwise rotation of the northernmost region of the arc (i.e., the Santa Cruz Islands). As indicated by CMTs, the SGF and a parallel fault to the north, the Santa Ysabel Fault (SYF) are crustal-scale faults that accommodate dextral displacement of the active NNHA from the dismembered, relict arc RIP segment.

4 Discussion and Conclusion

The opening of the NNHB troughs began ~3 Ma (Monjaret et al., 1991), coeval the DER collision. The resultant compression in the central NHSZ and continued retreat of the subducting plate to the north created the conditions for arc segmentation and rifting in the NNHB. The timing of the opening of the LNT and LST relative to the formation of the DHGD is unclear but occurred earlier than rifting in the JCT as indicated by the sedimented basin floor in the former as compared to the hummocky morphology indicating relatively recent volcanism in the latter. Rifting of the RIP from the DR can be attributed to continued retreat of the subducting slab. The RIP had been the northern most extent of the NNHA but had translated away from the subducting slab during the earlier ~10-3 Ma clockwise arc rotation and no longer experienced the force of slab suction. Slab retreat induced the crustal- scale rupturing that formed the SYF and SGF, suspended extension in the LNT and LST, and dislocated the RIP from the rest of the arc.

Formation of the SGF boundary likely permitted the JCT rift stage of backarc opening by accommodating dextral motion in the north. Rifting was accompanied by profuse volcanism in the SVZ and the BSVS, with the latter developing a deep axial valley reminiscent of slow ocean spreading centers. Dating of dredged seafloor samples with backarc basin basalt signatures from the SVZ indicate opening of the JCT at ~2.3 Ma (Monjaret et al. 1991; Maillet et al. 1995). It is unknown how volcanically active the JCT rift is currently, however seismic quiescence in the region suggests reduced volcanism in the region.

Transtension in the seismically active SCTR was likely induced by the arrival of the WTP at the NHT at ~0.7-1.0 Ma. Incipient compressional tectonics inboard of the trench is evidenced by forearc uplift (West Torres Islands; Calmant et al. 2003) and may explain discontinuation of rifting in the JCT. Arrival of the WTP likely caused emplacement of a rotation hinge point in the NNHA. This agrees with a pole of rotation just south of the SVZ as determined Bergeot et al. (2009). Current convergence rates at the north end of the NNHSZ are ~150-170 mm/yr, with ongoing slab retreat being accommodated by ~80 mm/yr of backarc extension (Calmant et al. 2003). The asymmetry in convergence caused by compression induced by the arc-plateau collision in the south and slab retreat in the north can explain the current transtensional tectonics in the SCTR.

Acknowledgements

The authors gratefully acknowledge IFREMER, Neptune Minerals Inc., and Nautilus Minerals Inc. for contributing bathymetry data to this study. Funding for this project was provided by OGS and NSERC-CREATE grants awarded to D.J.S.

References

Auzende JM, Pelletier B, Eissen JP (1995) The North Fiji Basin geology, structure, and geodynamic evolution. In: Taylor B (ed) Backarc basins: Tectonics and magmatism: 139-75.

Bergeot N, Bouin MN, Diament M, Pelletier B, Régnier M, Calmant S, Ballu V (2009) Horizontal and vertical interseismic velocity fields in the Vanuatu subduction zone from GPS measurements: Evidence for a central Vanuatu locked zone. J Geophys Res: Solid Earth 114: B6.

Calmant S, Pelletier B, Lebellegard P, Bevis M, Taylor FW, Phillips DA (2003) New insights on the tectonics along the New Hebrides subduction zone based on GPS results. J Geophys Res: Solid Earth 108: B6.

Hannington MD, de Ronde CEJ, Petersen S (2005) Sea-Floor Tectonics and Submarine Hydrothermal Systems. In: Hedenquist JW, et al. (eds) 100th Anniv Vol Econ Geol, SEG, Littleton, CO: 111–141.

Maillet P, Ruellan E, Gérard M, Person A, Bellon H, Cotten J, Joron JL, Nakada S, Price RC (1995) Tectonics, magmatism, and evolution of the New Hebrides backarc troughs (Southwest Pacific). In Taylor B (ed) Backarc basins: Tectonics and magmatism: 177-235.

Meffre S, Crawford AJ (2001) Collision tectonics in the New Hebrides arc (Vanuatu). Island Arc 10: 33-50.

Monjaret MC, Bellon H, Maillet P (1991) Magmatism of the troughs behind the New Hebrides island arc (RV Jean Charcot SEAPSO 2 cruise): K-Ar geochronology and petrology. J of Volcanol and Geotherm Res 46: 265-80.

Petterson MG, Babbs T, Neal CR, Mahoney JJ, Saunders AD, Duncan RA, Tolia D, Magu R, Qopoto C, Mahoa H, Natogga D (1999) Geological–tectonic framework of Solomon Islands, SW Pacific: crustal accretion and growth within an intra-oceanic setting. Tectonophys 301: 35-60.

Schellart WP, Lister GS, Toy VG (2006) A Late Cretaceous and Cenozoic reconstruction of the Southwest Pacific region: tectonics controlled by subduction and slab rollback processes. Earth-Sci Rev 76:191-233.

Taylor FW, Bevis MG, Schutz BE, Kuang D, Recy J, Calmant S, Charley D, Regnier M, Perin B, Jackson M, Reichenfeld C (1995) Geodetic measurements of convergence at the New Hebrides island arc indicate arc fragmentation caused by an impinging aseismic ridge. Geology 23: 1011-4.

